Metal implant artifact reduction in magnetic resonance imaging

Metal Implant Artifact Reduction in Magnetic Resonance Imaging

Chiel den Harder

ISBN: 978-90-5335-962-4

The research and the technological design of the prototype presented in this thesis were performed at and made possible by:
Philips Healthcare, Best, the Netherlands

Printing:
Ridderprint BV, www.ridderprint.nl

Printing was financially supported by:
Technische Universiteit Eindhoven (TU/e), Eindhoven, the Netherlands

Metal Implant Artifact Reduction in Magnetic Resonance Imaging

PROEFONTWERP

ter verkrijging van de graad van doctor
aan de Technische Universiteit Eindhoven,
op gezag van de rector magnificus prof.dr.ir. C.J. van Duijn,
voor een commissie aangewezen door het College voor Promoties,
in het openbaar te verdedigen
op woensdag 21 januari 2015 om 16:00 uur

door

Johan Michiel den Harder

geboren te Oss

De documentatie van het proefontwerp is goedgekeurd door de promotiecommissie:

voorzitter:	prof.dr. H.J.H. Clercx
1e promotor:	prof.dr.ir. P.F.F. Wijn
2e promotor:	prof.dr.ir. M. Breeuwer
copromotor:	dr. C. Bos (UMCU)
leden:	prof.dr. K. Nicolay
	prof.dr.ir. E.J.E. Cottaar
	prof.dr. A.G. Webb (LUMC)
	prof.dr. F.E. Lecouvet (UCL)

Table of Contents

1. Introduction

Since the first studies of nuclear magnetic resonance (NMR) effects [1,2] and their applications for imaging [3] and diagnosis [4] in the late 1960's and early 1970's, Magnetic Resonance Imaging (MRI, Figure 1.1) has vastly evolved, improved, and expanded to disciplines including neurology [5,6], orthopedics [7], oncology [8], and cardiology [9]. With its proven diagnostic value for many clinical applications, and its wide range of possible tissue contrasts, MRI is a valuable imaging modality for tissue evaluation. While bone tissue is generally evaluated using X-ray imaging or Computed Tomography (CT), MRI and ultrasound (US) imaging are commonly used for the evaluation of soft tissue. Ultrasound imaging on the one hand is a widely available low-cost portable modality. MRI on the other hand provides a higher signal to noise ratio (SNR) and higher and more flexible contrast. Functionality of organs can be diagnosed using nuclear medicine or MRI. As opposed to nuclear medicine and X-ray modalities, MRI does not expose the patient to ionizing radiation.

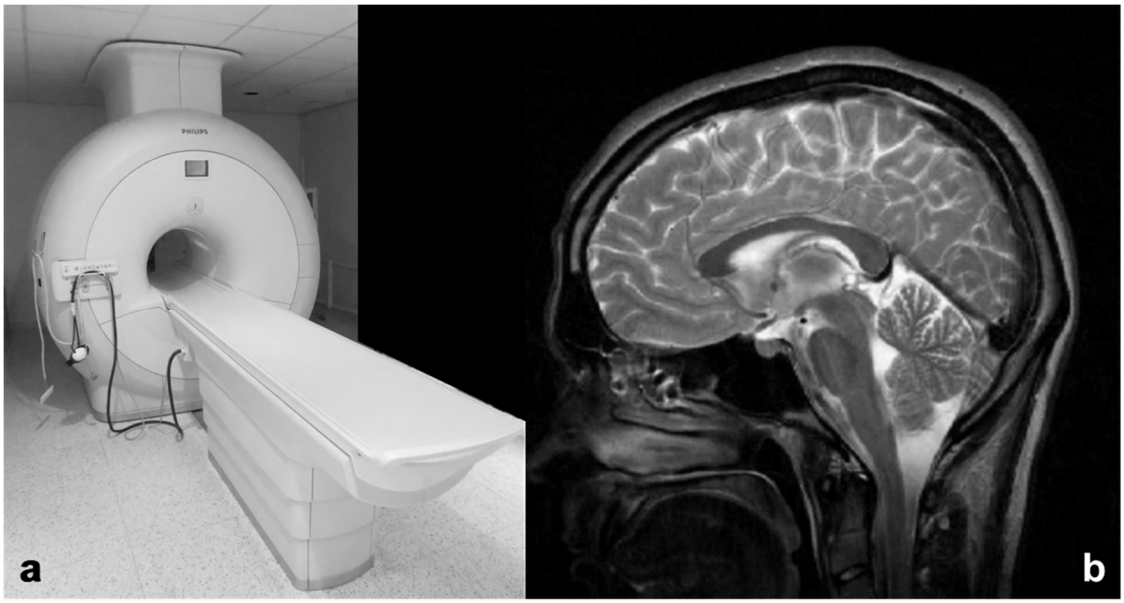

Figure 1.1: Example MRI scanner (a) and example MR image (b).

Though the relevance and applicability of MRI is clear for many patients, contraindications exist. Especially metal objects may be dangerous in the scanner. Even if safe, metal compromises image quality, because it influences the magnetic field.

1.1. Purpose of this thesis

An increasing number of patients are treated with joint replacements, many of which contain metal implants. This leads to the clinical need for diagnosis of potentially diseased tissue near metal, often as a consequence of complications caused by the implant itself. However, due to the influence of the metal on the main magnetic field of the scanner, MR imaging near metal is associated with image distortions and artifacts that complicate

diagnosis using these images. Artifacts are features added by the imaging system or the imaging process that compromise the intention of imaging to provide a reliable representation of the patient's anatomy.

This thesis describes the artifacts in MR imaging due to the presence of metal and the mechanisms that cause these artifacts. An inventory is made of existing and novel artifact reduction techniques, and of the clinical and technical requirements for artifact reduction. A prototype is described that includes a selection of these techniques for evaluation.

1.2. Thesis setup

This first chapter gives an overview of the thesis purpose and setup and provides a short introduction to basic MRI principles and applications.

Chapter 2 provides a brief overview of safety aspects when metal objects enter the MRI scanner. The influence of metal on the signal excitation, imaging and encoding process of MRI is explained, as well as the clinical impact of the image artifacts, leading to the clinical need to reduce these artifacts. A number of currently widely available techniques may address metal artifacts to some extent, but residual artifacts remain. The mechanisms behind these techniques are described, as well as their limitations. The clinical impact of metal artifacts is described, based on interviews with radiologists and orthopedists.

Recent research efforts focused on further reduction of metal implant artifacts in MRI. Chapter 3 provides an overview of advanced scanning techniques and discusses their strengths and limitations. In particular, a number of these advanced techniques enable substantial artifact reduction and imaging very close to the metal, but at the cost of a substantially prolonged scan-time. This scan-time increase needs to remain within limits to enable practical clinical use.

Chapter 4 describes the requirements for a solution that meets the clinical need described in chapter 2, from the perspective of the different stakeholders. Interviews with radiologists and orthopedists formed the basis for defining the clinical requirements.

Based on the requirements identified in chapter 4, modifications to the methods described in chapter 3 were proposed that resulted in novel MRI acquisition techniques. Chapter 5 explains how a tunable trade-off between scan-time and metal artifact reduction can be provided to the user. Chapter 6 describes the mechanism behind a residual artifact which is typical for one of the more recent and promising techniques, as well as a measure to reduce that residual artifact. These two chapters were published as articles in Magnetic Resonance in Medicine (MRM). Therefore, the content of these chapters –in particular the introduction and discussion– overlaps with other parts of the thesis.

A prototype was built for evaluation of the most suitable advanced techniques described in chapter 3 as well as the extensions described in chapters 5 and 6. The requirements for and the description of this prototype can be found in chapter 7. Phantom experiments were used to verify that the artifact reduction obtained with the prototype's functionality –as well as the residual artifact– behaves as expected based on theory, and to validate whether the

achieved artifact reduction is sufficient according to what is required to meet the clinical needs. The verification and validation are described in chapter 8.

Finally, based on the validation results as well as initial experience in academic hospitals in among others Sweden [10,11] and Korea [12], chapter 9 provides recommendations for product implementation of the functionality as well as an outlook to the future.

In all, the scope of the work described in this thesis is limited to the technical feasibility of the metal artifact techniques. Clinical validation of the techniques is beyond that scope, but is part of studies that are being performed using the prototype.

Please enjoy reading this thesis as much as I enjoyed developing the functionality and the prototype that formed the basis for this thesis.

1.3. Magnetic Resonance Imaging

An MRI examination usually consists of a number of diagnostic scans, each of which results in images of a specific contrast between different tissues. To ensure that the diagnostic images are acquired at the intended position and orientation, a low resolution survey or scout scan is acquired first, covering a sufficiently large area around the anatomy of interest. The MRI scanner operator then uses the survey images to plan the size, location and orientation of the subsequent diagnostic scans. Multiple contrasts may help for optimal visualization of different tissues or abnormalities. Images are often acquired in several orientations as this helps for optimal coverage of the anatomy of interest and for imaging the anatomy structures at the angle they are best recognized and resolved, given that the in-plane resolution is usually better than the resolution in the through-plane direction.

1.3.1. Image formation

The principles of magnetic resonance image formation have been explained in many comprehensive books e.g. by Mansfield and Morris [13], Haacke and Brown [14], and Vlaardingerbroek and Den Boer [15], as well as in other material. This section only a briefly summarizes these principles and defines the terminology used in this thesis.

1.3.1.1. Magnetization and precession

Tissue, as any other material, consists of atoms with a positively charged nucleus and negatively charged electrons moving around the nucleus. Spin is a property of the nucleus. In the classical mechanical model, spin may be considered a rotation of the nucleus around its axis. Its electrical charge turns into a circular electrical current, which induces a tiny magnetic field along the axis of the nucleus, effectively functioning as a tiny electromagnet. This microscopic magnetic field is called the magnetic moment of the nucleus. On a macroscopic scale, there is generally no effect of the nuclear magnetic moments, as all magnetic moments have random and independent orientations and their magnetic fields cancel mutually.

The main component of an MRI scanner is a strong magnet with a field strength of a few Tesla (T), which is roughly 100,000 times as strong as the earth's magnetic field. As a patient enters the MRI scanner, nuclear magnetic moments in the patient have a slight preference

for orientation in the direction of the applied magnetic field, which results in a macroscopic magnetization aligned with the applied magnetic field. With increasing applied magnetic field strength, the magnetization increases as well.

Nuclear spins do not align exactly with the applied magnetic field, but remain at an angle and precess around the applied magnetic field, very similarly to the axis of a spinning top precessing around the vertical axis of the earth's gravity field (Figure 1.2). The precession frequency of the nucleus is called the Larmor frequency f_0 which is proportional to the magnetic field strength B_0 and which depends on the nucleus type:

$$f_0 = \gamma B_0. \qquad (1.1)$$

Here, γ is the gyromagnetic ratio. In common clinical MRI, nuclei that contribute to an MR image are mainly hydrogen atoms in fat and water. For hydrogen atoms, which consist of one proton each, γ = 42.58 MHz/T.

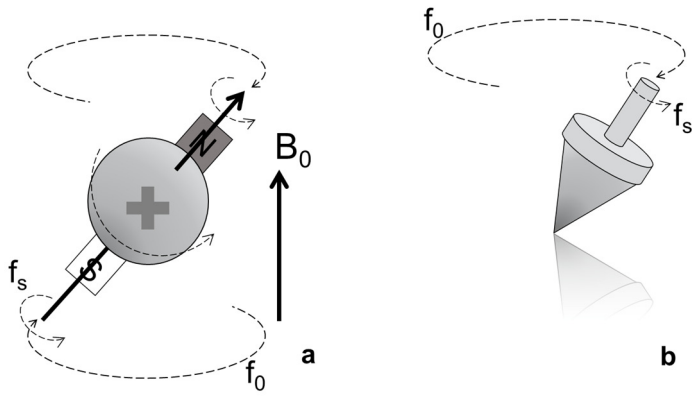

Figure 1.2: In the classical mechanical model, a hydrogen atom may be considered a sphere spinning around its axis with frequency f_s (a). Its electric charge effectively becomes a rotating current which induces a microscopic magnetic field. The nuclear magnetic moments precess around the B_0 field with the Larmor frequency f_0, very similarly to a spinning top precessing around the earth's gravitation field (b).

1.3.1.2. Excitation

In the MRI scanner, an oscillating electromagnetic field, or electromagnetic wave with a frequency equal to the Larmor frequency of hydrogen nuclei is transmitted into the patient using a transmission coil to create detectable magnetization. As the Larmor frequency of hydrogen nuclei is on the same order of radiofrequency (RF) waves, the transmission coil and transmitted field are often referred to as RF transmission coil and RF field, respectively. The matched frequency causes many nuclei to resonate at the RF field, absorb some of its energy, and arrive in an excited state at a higher energy level. As a result, the magnetization is rotated from its equilibrium state, arriving at an angle with respect to the B_0 field, where it precesses with the Larmor frequency around the B_0 field axis.

The mechanism behind this rotation of the magnetization is best understood by considering the nuclei and the magnetization in a so-called rotating frame of reference, i.e. a coordinate system that rotates with the same frequency as the precessing motion of the nuclei (Figure 1.3). The concept of a rotating frame of reference may be understood with the metaphor of a glacier on the earth's surface: as the earth rotates around its axis in 24 hours, so does the

glacier and its speed may be several thousands of kilometers per day. Yet, considered in a coordinate system which is static with respect to the earth's surface, the speed of the glacier is obviously much slower and usually in a different direction.

In the rotating frame of reference, the nuclei as well as the magnetization remain at a static angle with respect to the B_0 field, and the RF wave changes into a static magnetic field, which is commonly referred to as the B_1 field. This B_1 field induces a rotation of the magnetization during the time the RF wave is transmitted, analogously to the precession of nuclei caused by the B_0 field:

$$f_1 = \gamma B_1. \qquad (1.2)$$

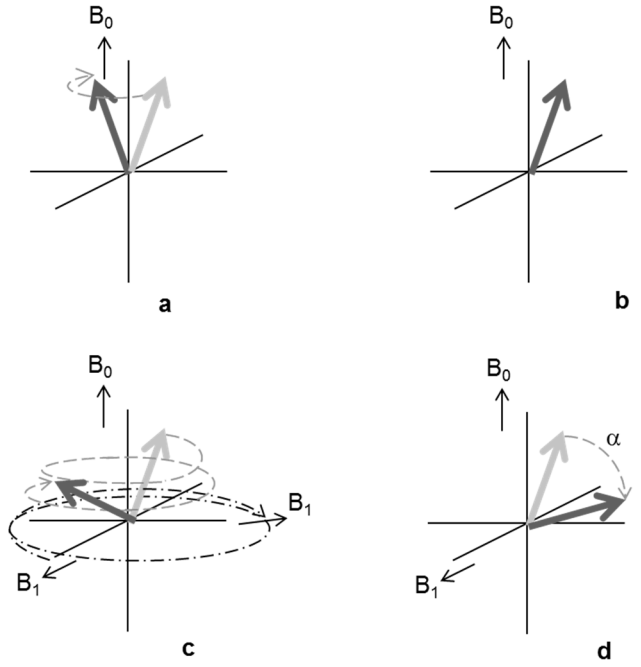

Figure 1.3: Precession of the magnetization around the B_0 field, observed in the static frame of reference (a) and in the rotating frame of reference, where the orientation of the magnetization is static (b).
An RF pulse may be considered a rotating magnetic "B_1" field (c), which is static in the rotating frame of reference (d). The B_1 field causes the magnetization to rotate by the flip angle α.

The induced rotation angle α is called the flip angle or tip angle, which is determined by the pulse amplitude B_1 and the pulse length t_p of the RF wave:

$$\alpha = \int f_1 dt = \int \gamma B_1 dt = \gamma B_1 t_p. \qquad (1.3)$$

Thus, a 90° RF pulse causes the magnetization to flip from alignment with the B_0 field to the transverse plane orthogonal to the B_0 field, where it rotates with the Larmor frequency around the B_0 field axis, remaining static in the rotating frame of reference. The B_0 field axis is commonly referred as the z axis, while the x and y coordinates together span the transverse plane. A shorter RF pulse duration will flip the magnetization by a smaller angle, leading to a transverse magnetization component (M_{xy}) orthogonal to the B_0 field and a longitudinal magnetization component (M_z) parallel to the B_0 field (Figure 1.4).

The precessing transverse magnetization can be measured as it induces a current in an RF receiving coil. The strength of this magnetic resonance (MR) signal depends on the receive coil sensitivity as well as on the magnetization, and with that on the density of hydrogen nuclei as well as on the strength of the applied magnetic field.

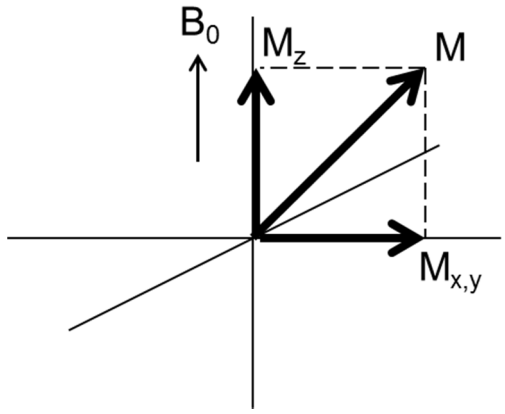

Figure 1.4: The magnetization vector M may be tilted away from the B_0 field vector by an RF pulse. The magnetization vector can be decomposed into a longitudinal component M_z parallel to the B_0 field and a transverse component M_{xy}, orthogonal to the B_0 field.

1.3.1.3. Spatial location of signal using gradients

An MRI scanner is equipped with three gradient coils. Switching on one of these gradient coils induces a magnetic field that varies approximately linearly in one of the three orthogonal spatial dimensions ("gradient field"). This gradient field is superimposed onto the static magnetic field. A linear field gradient leads to a linear variation of the precession frequency of spins. Hence, the precession frequency identifies the location of the spins in the direction of the gradient.

By design, the spatial dimensions of the gradients are in the direction of and orthogonal to the bore of the MRI scanner. However, linear superposition of two or three gradients allows application of gradient fields in any direction. This enables full freedom of orientation of MRI scans, which is a powerful property of MRI.

1.3.1.3.1. Signal selection

During excitation, a selection gradient may be applied in order to limit the region, where the spin precession frequency corresponds to the excitation pulse frequency, and where spins will thus resonate to and be excited by the RF pulse. Figure 1.5 shows a gradient inducing a linearly varying spin precession frequency f_0 in the selection direction *s* which is the through-plane direction. Each *s* position corresponds to a unique f_0. Transmitting an RF pulse with a limited bandwidth (BW) excites only spins in a limited region: a slice with slice thickness STK.

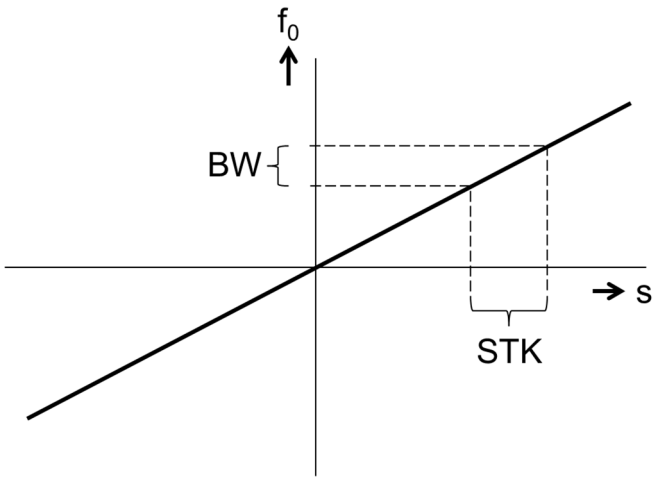

Figure 1.5: Slice selection uses a selection gradient to induce a linearly varying precession frequency (f_0) in the slice selection (s) direction. Applying an RF pulse with a limited frequency bandwidth (BW) excites spins within a slice with limited slice thickness (STK).

1.3.1.3.2. Frequency encoding

After excitation, a gradient may be applied in a direction orthogonal to the selection direction, while MR signal is being acquired. Again, the spin precession frequency varies linearly with the spatial position and with that, the position of the spins generating the MR signal is encoded in the MR signal frequency. This process is called frequency encoding (see e.g. page 9 of [15]). As the acquisition or "read-out" of the MR signal is performed while the frequency encoding gradient is active, this gradient is also known as the read-out gradient G_{READ}. The MR signal is sampled at discretized time intervals t_i, and the phase shift of signal at these time points is given by:

$$\Delta\varphi_{m,i}(\mathrm{m}, t_i) = \gamma \int_0^{t_i} (\mathrm{G_{READ}} \cdot \mathrm{m}) dt. \qquad (1.4)$$

Here, m is the coordinate in the frequency encoding direction (sometimes referred to as the "*measurement* direction").

Applying frequency encoding in the m direction only results in a Cartesian sampling approach. This is the most commonly used sampling approach, though other approaches exist as well.

1.3.1.3.3. Phase encoding

In a Cartesian sampling approach, a single read-out of signal will provide information about the distribution of spins in the frequency encoding direction only. In the orthogonal direction(s), phase encoding may be applied. Phase encoding may be considered a step-wise variant of frequency encoding, and provides very similar information about signal position, though in the orthogonal direction.

While frequency encoding applies a continuously active gradient during read-out, and samples signal at discrete time-points within the acquisition window, phase encoding briefly applies a gradient between excitation and read-out. This introduces an additional phase shift term of spins at position p which is proportional to the area under the curve of the phase encoding gradient G_{PE}:

$$\Delta\varphi_{\mathrm{p},j}(\mathrm{p}) = \gamma \int (\mathrm{G_{PE},}_j \cdot \mathrm{p}) dt. \qquad (1.5)$$

The signal acquisition process including excitation and read-out is repeated with progressively increasing phase encoding gradient strengths, inducing a progressively increasing phase shift $\Delta\varphi_{\mathrm{p},j}$ depending on the position in the direction of the applied phase encoding gradient. The number of times the signal acquisition process needs to be repeated for phase encoding is determined by the desired resolution in the phase encoding direction. For instance, 256 phase encoding steps require 256 acquisition repetitions and in principle lead to an image with 256 voxels in the phase encoding direction.

1.3.1.3.4. Image space and k-space

As the position of image signal in image space is encoded by frequency and phase, image space, or the image domain, is sometimes referred to as the frequency domain. Yet, the MR signal is acquired by measuring a discretized set of samples of the signal over time, in the so-

called time domain, or k-space [16]. Transforming measured signal in the time domain into an image in the image domain is done using a Fourier transform [17].

1.3.1.3.5. Summary of spatial location of signal using gradients

In summary, the spatial location of signal is selected and encoded by varying the magnetic field using gradient coils, which leads to a well-defined variation of the magnetization precession frequency depending on the location. This dependency becomes much less well defined if the main magnetic field is disturbed by a metal object that enters the scanner bore, which will be explained in detail in the next chapter.

1.3.1.4. Refocusing

After excitation, the spin precession frequency variation, caused by the frequency encoding gradient as well as by field inhomogeneities, leads to incoherence of spin phases at different positions. Due to this phase incoherence –or dephasing– the transverse magnetization will decline and signal will decrease rapidly. To restore signal, the spins need to be refocused. Refocusing the spins leads to restoration of signal after some time, which is referred to as an echo. In MR imaging, there are two approaches commonly used to generate an echo.

First, an echo may be generated by applying an additional RF pulse with a flip angle of 180° (Figure 1.6). This approach is called RF echo or spin echo (SE) [18,19]. In a spin echo sequence, excited spins are first dephased by a rewinder gradient G_{REW}. Additional dephasing may occur due to B_0 inhomogeneities (ΔB_0) or the spectral content of the sample. The 180° RF pulse inverts the phases of the spins, causing fast spins to lag and slow spins to lead. Using the same polarity for the read-out gradient G_{READ} will cause the spin phases to refocus, resulting in an echo.

Second, the spin phases may be refocused by using a read-out gradient with opposite polarity with respect to the rewinder gradient (Figure 1.7). In this case, no refocusing RF pulse is required. This approach is referred to as a gradient echo or fast field echo (FFE) technique [20].

An essential difference between SE and FFE is the influence of local B_0 deviations on the signal. For SE, a B_0 deviation leads to a magnetization phase shift of:

$$\Delta\varphi_{\mathrm{B_0,SE}} = \gamma \cdot \Delta \mathrm{B_0}(\vec{\mathrm{r}}) \cdot t_{\mathrm{ref}}, \qquad (\ 1.6\ )$$

where $\vec{\mathrm{r}} = (\mathrm{m}, \mathrm{p}, \mathrm{s})$ is the spatial position, and t_{ref} is the time between excitation and refocusing. This phase term is inverted by the refocusing pulse. Then, an additional phase shift accumulates between refocusing and echo:

$$\Delta\varphi_{\mathrm{B_0,SE}} = \gamma \cdot \Delta \mathrm{B_0}(\vec{\mathrm{r}}) \cdot (\mathrm{TE} - t_{\mathrm{ref}}). \qquad (\ 1.7\ )$$

Here, TE is the echo time, which is the time between the excitation of spins and the echo. The refocusing pulse is applied exactly between excitation and echo, i.e. at TE/2. Therefore, the inverted ΔB_0 phase term before refocusing (Eq. 1.6) cancels the ΔB_0 phase term between refocusing and echo (Eq. 1.7).

For FFE, however, the phase shift if not inverted and the ΔB_0 contribution to the phase shift accumulates from the excitation until the echo, leading to an additional phase term [21,22]:

$$\Delta\varphi_{B_0,\mathrm{FFE}} = \gamma \cdot \Delta B_0(\vec{r}) \cdot \mathrm{TE}. \qquad (1.8)$$

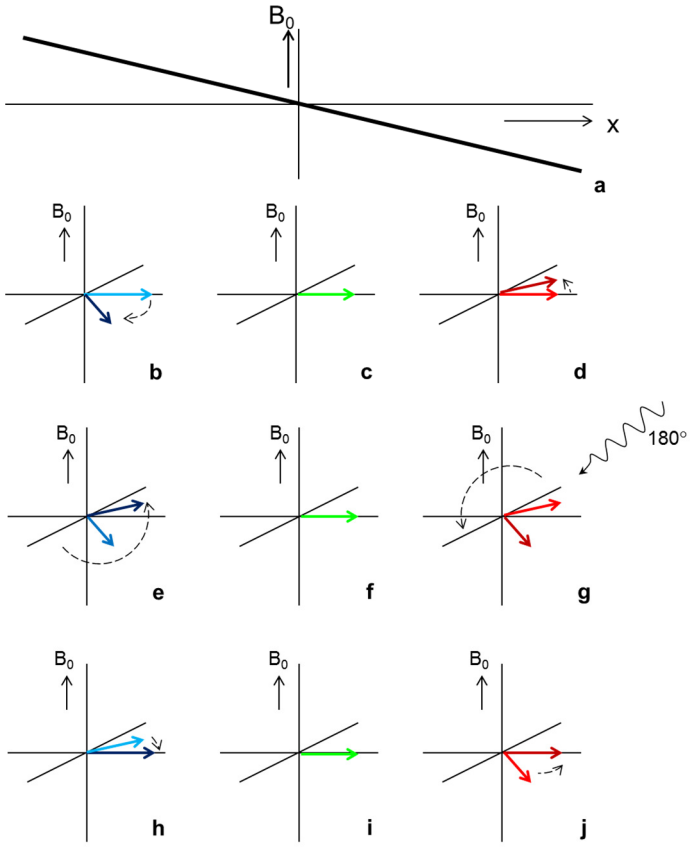

Figure 1.6: In an RF echo or spin echo (SE) sequence, excited spins are first dephased by a rewinder gradient (a), causing the phase of spins to lead (b), lag (d), or remain static (c) in the rotating frame of reference depending on their location. Then, a 180° RF pulse inverts the phase order of the spins (e,f,g): the phases of fast spins now lag (e) and the phases of slow spins lead (g). Now, using the same gradient polarity will cause the spin phases to refocus (h,i,j), resulting in an echo.

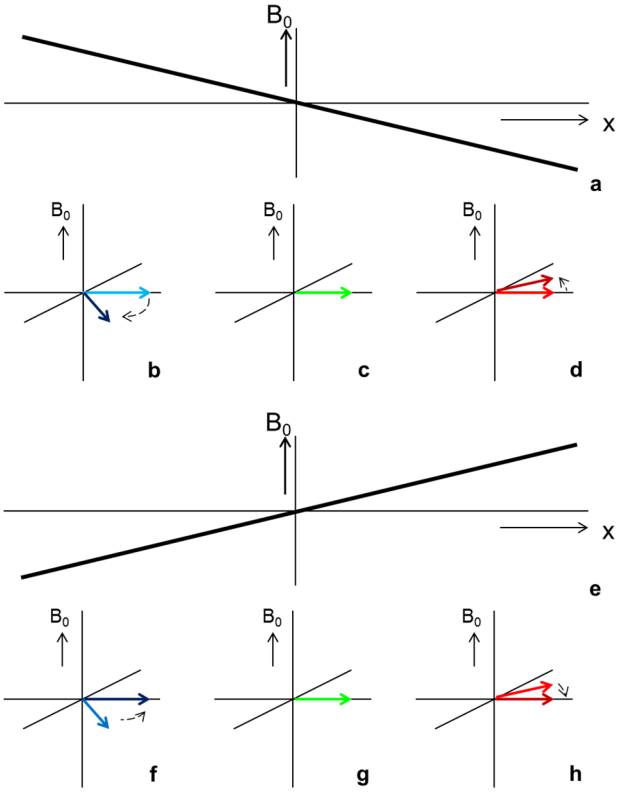

Figure 1.7: In a gradient echo or fast field echo (FFE) sequence, excited spins are first dephased by a rewinder gradient (a), causing the phases of spins to lead (b), lag (d), or remain static (c) in the rotating frame of reference depending on their location. Then, the polarity of the gradient is reversed (e), which also reverses the dephasing process (f,g,h), eventually leading to an echo signal when all spins are rephased.

1.3.1.5. Turbo Spin Echo

In Turbo Spin Echo (TSE), also known as Fast Spin Echo (FSE), an excitation is followed by multiple refocusing pulses to induce multiple echoes [23,24]. In the Carr-Purcell-Meiboom-Gill (CPMG) scheme [25], this refocusing pulse rotates the spins along an axis that is orthogonal to the rotating axis during excitation, to reduce accumulating effects of imperfections in the 180° pulses. The time interval between two echoes of a TSE echo train is referred to as the echo spacing. In TSE, the TE value is commonly assigned to the echo that has the main contribution to the overall signal in the image, which is the sample in the center of k-space. Figure 1.8 presents the sequence in time of applied gradients and RF pulses in SE or TSE, as well as the timespan when RF signal is acquired, the acquisition window.

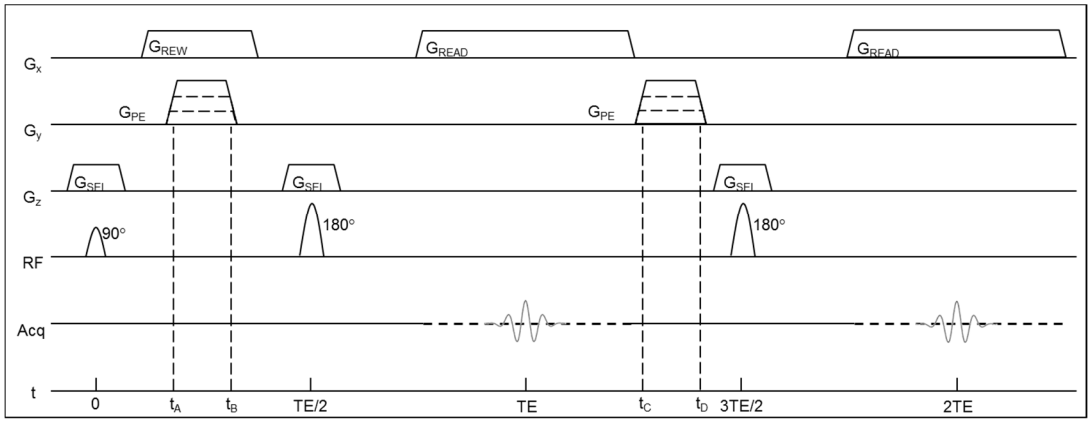

Figure 1.8: TSE pulse diagram illustrating the sequence in time of applied gradients, RF pulses, and signal acquisition window. The 90° excitation pulse and the first 180° refocusing pulse together result in an echo at echo time TE (spin echo sequence). Multiple refocusing pulses may be used to generate multiple spin echoes (turbo spin echo). The dashed line indicates the acquisition window during which signal is sampled.

1.3.1.6. Two- or three-dimensional imaging

MRI may be performed two or three-dimensionally. Signal selection of a relatively thin slice enables imaging of that slice by encoding only the two in-plane dimensions (2D imaging). Adjacent slices may be selected consecutively (multi-slice imaging, Figure 1.9a). Alternatively, in 3D imaging, a larger volume is selected for every excitation and phase encoding is applied in two directions, in-plane and through-plane, orthogonal to the frequency encoding direction (Figure 1.9b). Repeatedly selecting the larger volume causes MR signal of the entire volume to contribute to all signal acquisitions. Hence, 3D imaging generally results in a higher SNR than multi-slice imaging. However, exciting the same volume repetitively requires sufficient waiting time between consecutive read-outs to allow sufficient T1 relaxation (see section 1.3.3) before it can be excited again. In multi-slice imaging, this time may be used more efficiently by interleaving the acquisition of signals from different slices.

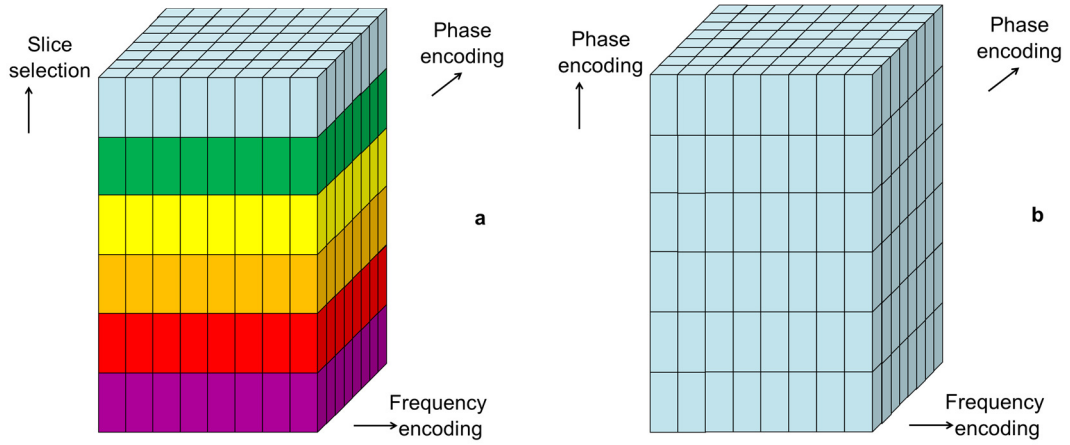

Figure 1.9: Selection of signal using slice selection (a) or volume selection (b). With slice selection, signal is localized using frequency encoding in one in-plane direction and phase encoding in the other. With volume selection, phase encoding is applied in the through-plane direction as well.

Instead of selecting a volume, 3D imaging may also be performed using non-selective RF pulses for excitation and refocusing. In this case, no selection gradient is used, and all spins in the MRI scanner within the range of the RF transmit coil are excited and refocused. Limiting the imaging region in non-selective 3D imaging may be achieved by appropriate positioning and selection of a set of RF receive coils with local sensitivity.

1.3.1.7. Parallel Imaging

Next to frequency encoding and phase encoding, the position of signal may also be encoded using the sensitivity of receive coils. Many receive coils consist of multiple receive channels, each covering a limited spatial area. Depending on the position of the signal, it may be received more easily by one receive channel than by another. Conversely, the received signals in different receive channels may be used to assign the correct signal to the correct position, provided the spatial sensitivity profile of each receive channel is known.

Spatial sensitivity profiles of the receive coils may be obtained using calibration data, either in the form of a few additional signals acquired during the diagnostic scan, or by means of an additional quick low resolution scan, a so-called reference scan. The additional information about the signal position that is obtained using the sensitivity profiles of multiple receive channels can be employed to accelerate the acquisition. This approach is called parallel imaging, exemplified by SENSE [26], SMASH [27], and GRAPPA [28].

1.3.2. Coordinate systems and terminology

In MRI, the x, y, z coordinate system is commonly used to indicate the three main axes of the MRI scanner itself, with z being the coordinate in the direction of the main magnetic field. However, MRI allows full flexibility of scan orientation by using linear combinations of gradients, and thus scans do not necessarily line up with the x, y, z coordinate system. The m,p,s coordinate system is used for the description of the image space, where the m,p and s symbols stand for *measurement*, *phase encoding*, and *slice selection* direction, respectively.

K-space commonly uses the kx,ky,kz coordinate system. Note, that these coordinates do not correspond to the x,y,z coordinate system, but to the m,p,s coordinate system in the image domain.

In general, the patient's body is aligned with the main axes of the MRI scanner. Yet, variations in patient positioning are common, as the patient may lie prone or supine, with his head or with his feet in the positive direction of the main magnetic field. The patient coordinate system is defined using widely adopted medical terminology, as indicated in Figure 1.10.

The orientation of the imaging plane with respect to the patient may either be orthogonally aligned with or oblique to the patient's coordinate system. The three orthogonal imaging planes are referred to as transverse or axial (i.e. orthogonal to the patient's long axis), sagittal and coronal.

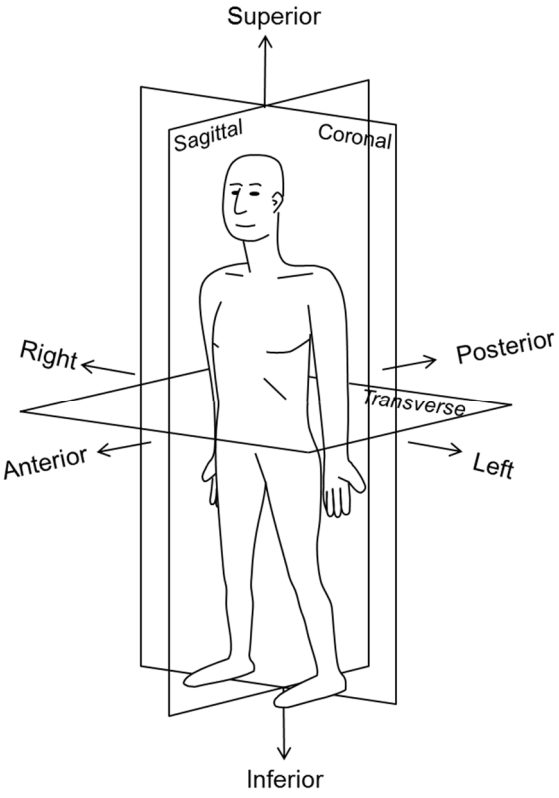

Figure 1.10: Definition of directions and planes used to describe anatomy. These directions span the patient coordinate system. Superior is also known as cranial, inferior as caudal, anterior as ventral, and posterior as dorsal. The transverse plane is also referred to as the axial plane as it is orthogonal to the patient's long axis. Note, that left and right are defined as viewed from the patient.

1.3.3. Relaxation

Over time, excited nuclei will tend to return to their original state, M_{xy} will decay and M_z will be restored. The restoration of M_z is an exponential process with time constant T1 and is called spin-lattice relaxation or T1 relaxation. The MR signal decays as M_{xy} decays. The value of T1 is dependent on the sample itself as well as on the magnetic field strength.

The other mechanism behind MR signal decay is interaction between spins. As spins interact, the phases of some spins will turn slower than the phases of other spins. On a macroscopic scale, this dephasing of spins leads to a decline of the transverse magnetization M_{xy} and

consequently to MR signal decay. Theoretically, for a homogeneous object, this can be described as an exponential process which is referred to as spin-spin relaxation or T2 relaxation, the time constant T2 being much less dependent on the magnetic field strength, but mainly on the material, as well as on temperature.

These relaxation processes are described by:

$$\mathrm{M_z}(t) = \mathrm{M_{z,0}} - \left(\mathrm{M_{z,0}} - \mathrm{M_z}(0)\right) \cdot e^{-t/\mathrm{T1}}, \qquad (1.9)$$

$$\mathrm{M_{xy}}(\mathrm{t}) = \mathrm{M_{xy}}(0) \cdot e^{-t/\mathrm{T2}}. \qquad (1.10)$$

Here, t represents time, $M_{z,0}$ is the longitudinal magnetization in equilibrium before the RF pulse is applied, and $M_z(0)$ and $M_{xy}(0)$ are the longitudinal and transverse magnetizations, respectively, directly after application of the RF pulse.

In FFE, signal decay due to spin dephasing is caused not only by T2 relaxation but also by local B_0 inhomogeneities in the tissue (Eq. 1.8). In regions with strong field variations, this additional ΔB_0 phase term has a significant influence on the signal decay. The combination of the ΔB_0 induced dephasing in FFE and T2 decay is often referred to as T2* decay.

1.3.4. Image contrasts

The contrast between tissues can be controlled by the selection of MR imaging parameters. The time between two consecutive excitations is called the repetition time TR. A longer TR allows more time for T1 relaxation and recovery of M_z, which is then available for the next excitation. A short TR may prevent recovery of M_z and lead to saturation of signal after several excitations. As the T1 is dependent on the tissue, a relatively short TR will lead to varying levels of saturation, and thus to varying MR signal intensity for different tissues. Thus, the image contrast can be weighted with the T1 values of the imaged tissues. This is called a T1 weighted (T1w) contrast. In a T1w image, signal increases with decreasing T1.

Another parameter that influences contrast is the TE. The TE must be sufficiently short to capture MR signal before it has decayed too much due to T2 (or T2*) relaxation. The T2 being dependent on the tissue, a relatively long TE will lead to varying MR signal intensity for different tissues. Thus, with the appropriate TE, the image contrast will be weighted according to the T2 of the imaged tissues. This is called a T2 weighted (T2w) contrast. In a T2w image, signal increases with increasing T2.

Using a long TR and a short TE results in an image contrast that is neither weighted with the T1 nor with the T2 of the tissues. In this case, the contrast is mostly determined by the density of excited hydrogen atoms. This contrast is referred to as proton density weighted (PDw).

Different contrasts complement each other for tissue evaluation and characterization. For example, T2w imaging is commonly preferred for visualization of fluids as they show up brightly in these contrasts. Fat has bright signal as well, both in T2w and in T1w imaging. Hence, in T2w images, it may be difficult to distinguish fat from fluid. MR signal from fat may be suppressed using the fact that fat differs from water in precession frequency and in T1 relaxation time.

Figure 1.11 shows example images using a T1w, a T2w, and a fat suppressed image contrast. Especially in the bladder, the influence of the contrast weighting on the signal intensity of fluid is noticeable. These are axial images of the pelvic region of a volunteer with hip fixation screws. Note the metal artifacts in the left femoral head, depicted on the right side of the image. Also note the lower SNR in the fat suppressed image, which was produced using the STIR technique (section 2.3.6) in this case.

Figure 1.11: Example MR images with T1w (a), T2w (b) and fat suppressed (c) contrasts. Influence of contrast weighting is visible e.g. in the bladder (solid arrows). Hip fixation screws in the left femoral head (right side of the image) cause metal artifacts (dashed arrows).

2. Current Issues with Metal in the MRI scanner

2.1. When metal enters the MRI Scanner

2.1.1. Safety concerns

MR imaging is often the modality of choice to evaluate soft tissues, and as many patients are treated with metal implants, there is a clear need for robust MR imaging near metal. Yet, depending on the implant type and material, there may be risks involved with an MRI examination or even with having the implant near the MRI scanner [29], and for some implants an MRI examination is contraindicated. These risks are related to the static magnetic field, the field gradients and the transmitted RF field.

The static magnetic field may exert forces on the implant, which may include translational and rotational forces, if the implant contains ferromagnetic materials. Forces can also result from eddy currents in the metal when the patient moves the body part that contains the implant in the magnetic field. Typically, in highly conducting materials like copper or aluminum, strong eddy currents may be induced by motion of the implant in the magnetic field. Eddy currents in turn induce a local magnetic field which counteracts the motion with respect to the main magnetic field. Both ferromagnetic attraction and eddy currents need to remain limited to avoid painful and potentially dangerous torque and translational forces between the implant and the patient's body.

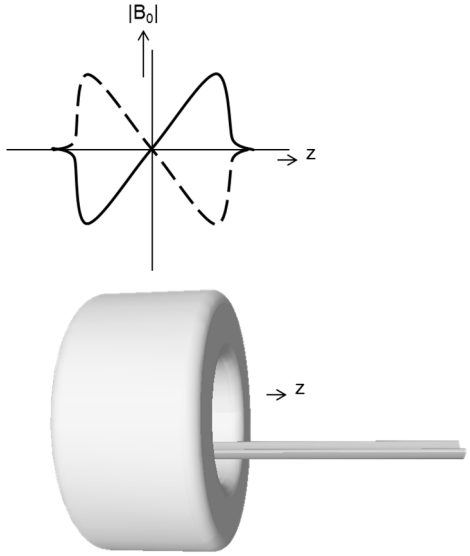

Figure 2.1: Gradient induced magnetic field as a function of the position z. The induced field has its maximum at the edges of the bore of the scanner, while the gradient does not influence the field at all in the iso-center. By switching between positive (solid line) and negative (dashed line) gradient polarity, the variation of the magnetic field also has its maximum at the edges of the bore of the scanner. This is where PNS is felt most.

Switching gradients result in magnetic field variations that depend on the gradient strength, the repetition time and the rate at which the gradient gains strength, the "slew-rate". While the gradient does not contribute to the magnetic field in the iso-center, the field variation is especially strong near the edges of the bore of the MRI scanner (see Figure 2.1), and in these regions, switching gradients may also lead to eddy currents. In tissue, switching gradients may lead to Peripheral Nerve Stimulation (PNS, [30]), which may be noticed by the patient as a feeling of tingling or slight movement of e.g. the skin. If the same eddy currents are

induced in electronic implants, such as pacemaker leads or Deep Brain Stimulation (DBS) electrodes, there may be severe undesired consequences [31].

The RF field disposes energy into the patient. The Specific Absorption Rate (SAR) refers to the amount of energy absorbed by the patient during an MRI scan sequence. A distinction is made between global SAR and whole-body SAR which reflects the energy absorbed by the patient's entire body, and local SAR pertaining to potential local elevation of the energy absorption. Each commercially available MRI scanner is equipped with a SAR model that predicts and specifies the whole-body SAR level in W/kg for any defined scan protocol. These model predictions are based on the energy required to transmit the RF field, on calorimetric phantom studies, and on numerical simulations of Maxwell's equations. For head scans, models are available to predict the local SAR (head SAR). By regulation, limitations apply to the SAR level allowed. For example, whole-body SAR is limited to 2 W/kg in normal mode and 4 W/kg in first level controlled mode, which requires medical supervision of the patient (see section 51.103.2 of [32]).

Generally, global SAR is more easily estimated than local SAR, as the spatial distribution of the energy in the body may be influenced by many factors. Estimating local SAR becomes increasingly difficult near metal implants due to the interaction of the transmitted RF field and the metal prosthesis, which leads to increased local SAR in the tissue near the implant. Numerical simulations may be used to derive the local SAR distribution. Using such simulations, Powell et al. found that, for bilateral hip implants, local SAR levels near metal implants may reach up to 73 W/kg and may exceed recommended limits of 20 W/kg averaged over 6 minutes in extremities when the whole-body SAR is maintained at normal mode (2 W/kg) [33].

The presence of implants that are categorized as MR-unsafe, such as most pacemakers, cochlear implants and most aneurysm clips, is a contraindication to perform an MRI examination. But many other implants are labeled MR-safe or MR-conditional, meaning that for those implants, the patient is allowed to undergo an MR examination within specified conditions for the static magnetic field, the gradient strength and slew-rate applied during the scan sequences, as well as the SAR. For many implants, these conditions have been listed by Shellock et al. [http://www.mrisafety.com]. More initiatives that provide MRI safety information about medical implant devices are available online, e.g. at [http://www.magresource.com].

2.1.2. Magnetic field inhomogeneity and precession frequency variations

For the majority of MRI scan sequences, image quality is strongly dependent on the homogeneity of the static magnetic field. The applied magnetic field H of the scanner itself is optimized for homogeneity ("shimmed") during system installation, with variations on the order of 0.5 ppm (parts per million) up to a distance of 250 mm from the iso-center.

However, when a patient or an object enters the magnet, homogeneity is compromised, as the patient or object becomes magnetized. For ferromagnetic materials, magnetization may persist even in absence of the applied magnetic field. For other materials, the magnetization M is linearly dependent on the applied magnetic field via the relation

$$\mathrm{M} = \chi \mathrm{H}, \qquad (2.1)$$

where χ is the magnetic volume susceptibility of the material [34,35]. The magnetization may have equal or opposed sign to the applied magnetic field for paramagnetic (e.g. air, $\chi = +4 \cdot 10^{-7}$), and diamagnetic materials (e.g. water, $\chi = -8 \cdot 10^{-6}$), respectively [34]. The magnetization M itself contributes to the induced magnetic field B_0, which is given by [34,35]:

$$\mathrm{B}_0 = \mu \mathrm{H} = \mu_0(\mathrm{H} + \mathrm{M}) = \mu_0(1 + \chi)\mathrm{H}, \qquad (2.2)$$

with μ the magnetic permeability of the material and μ_0 the magnetic permeability of vacuum.

As different tissue materials are at different positions within the scanner, the values of M and B_0 will depend on the position as well. The precession frequency f_0 of hydrogen nuclei is dependent on the position as it is directly proportional to the spatially varying induced magnetic field B_0:

$$\mathrm{f}_0(\vec{\mathrm{r}}) = \gamma \mathrm{B}_0(\vec{\mathrm{r}}). \qquad (2.3)$$

Ideally, a linear gradient, e.g. the read-out gradient G_{READ}, induces a linear variation of the magnetic field in the m direction (constant dB_0/dm), which results in a linear variation of the precession frequency f_0 as a function of the position. However, the local variations in B_0 lead to additional precession frequency deviations.

Sudden variations in susceptibility at transitions of adjacent tissues cause relatively small variations of the B_0 field. Therefore, even in homogeneous material, the B_0 homogeneity may still be compromised in regions close to the adjacent material, which is a well-known phenomenon from e.g. cardiac MRI, where cardiac tissue neighbors the air in the lungs.

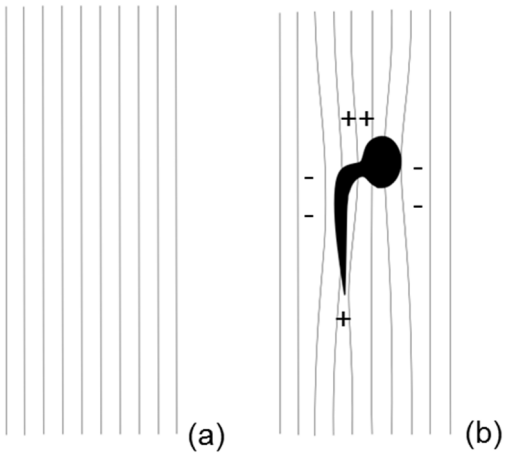

Figure 2.2: B_0 field lines of a homogeneous B_0 field (a) and deflected by a metal implant (b). The magnetization of the implant amplifies the B_0 field in the metal, which is represented by the condensed field lines. The B_0 field strength increases where the field lines enter and leave the implant, i.e. at the two magnetic poles of the magnetized implant, but decreases at the left and right side of the implant, resulting in a dipole character of the induced field.

The majority of metal implants are strongly paramagnetic. Placed in the MRI scanner, the metal causes B_0 inhomogeneities that lead to substantial spatial variations of the spin precession frequency f_0. The metal leads to an increased B_0 field inside the metal, which may be represented by an increased density of magnetic field lines (Figure 2.2). With this deflection, the field lines are condensed where they enter and leave the implant, i.e. at the two magnetic poles at the cranial and caudal ends of the magnetized implant, and dispersed

beside the implant, parallel to the field lines, resulting in a dipole character of the induced field.

Resonance frequency offsets associated with metal implants can range from a few kHz (titanium) to well over 10 kHz (stainless steel, see e.g. Figure 2.12).

2.1.3. Image quality concerns

Especially bulk metal implants, in e.g. hip, knee or spine, may cause significant local inhomogeneities in the main magnetic field, leading to image artifacts in the area around the implant that hamper soft tissue evaluation and severely impair the diagnostic value of the images.

2.1.3.1. T2 dephasing*

As explained in section 1.3.1.4, refocusing is achieved either by inverting the read-out gradient (FFE) or by inverting the phase of the spins using an additional refocusing RF pulse (SE or TSE). While MR signal in an SE or TSE sequence decays due to T2 relaxation, the T2* decay in FFE may be much stronger depending on the local B_0 inhomogeneities of the tissue (section 1.3.3). Near metal, B_0 inhomogeneities are much stronger and T2* decay in FFE is further accelerated. Even for relatively short echo-times on the order of 30 ms and relatively thin slices on the order of 3 mm, intra-voxel T2* dephasing may lead to complete signal loss at susceptibility induced gradient fields as modest as 2 mT/m (Eq. 1.8), while metal may commonly induce gradient fields of 10 mT/m or higher (section 8.4.1).

2.1.3.2. Through-plane distortion

Slice selection (section 1.3.1.3.1), which is used in many MRI sequences, employs an RF pulse of a limited bandwidth BW_{SEL} while a selection gradient G_{SEL} is applied (see Figure 2.4a,b).

With a homogeneous B_0 field and linear gradients, this technique results in a straight slice of excited spins with slice thickness:

$$\mathrm{STK} = \frac{\mathrm{BW_{SEL}}}{\gamma \cdot \mathrm{G_{SEL}}}. \qquad (\ 2.4\ )$$

However, susceptibility induced field inhomogeneities cause spatial frequency variations, leading to a distortion of the excited slice (Figure 2.4c,d).

Signal is selected if it satisfies the excitation condition:

$$|\gamma \cdot \Delta s \cdot \mathrm{G_{SEL}} + \gamma \cdot \Delta \mathrm{B_0}(\vec{r})| < \mathrm{BW_{SEL}}/2, \qquad (\ 2.5\ )$$

where Δs is the offset in the through-plane direction from the intended slice center. From Eq. 2.5, it can be seen that the through-plane distortion of the slice is given by:

$$\Delta s = -\Delta \mathrm{B_0}(\vec{r})/\mathrm{G_{SEL}}. \qquad (\ 2.6\ )$$

2.1.3.3. In-plane distortion

In-plane, the location of the signal is determined by frequency encoding in the m direction and phase encoding in the orthogonal p direction. The read-out gradient G_{READ} applied

during frequency encoding induces a linear frequency variation, causing each position in the gradient direction to correspond to a unique frequency (Eq. 1.4).

Susceptibility induced field variations lead to frequency deviations that disturb the frequency encoding process, and cause displacement of signal in the m direction by a distance Δm:

$$\Delta f_0(\vec{r}) = -\gamma G_{READ} \cdot m + \gamma \Delta B_0(\vec{r}) = \gamma G_{READ}\left(m + \frac{\Delta B_0(\vec{r})}{G_{READ}}\right) \quad (2.7)$$

$$= \gamma G_{READ}(m + \Delta m).$$

The displacement in the read-out direction is then given by:

$$\Delta m = \Delta B_0(\vec{r})/G_{READ}. \quad (2.8)$$

For TSE, the resulting phase shift of signal sampled at a discrete time point t_i is:

$$\Delta\varphi_{m,i}(\vec{r}) = \gamma \int_{TE}^{t_i}\left(G_{READ} \cdot m + \Delta B_0(\vec{r})\right)dt. \quad (2.9)$$

At the echo time TE, the phase shift is zero, due to the applied rewinding gradient G_{REW} before read-out. Note that a linear phase shift in k-space corresponds to a displacement in image space.

Phase encoding is achieved by briefly applying a gradient between excitation and read-out. This phase encoding gradient induces an additional phase shift term of spins at position p which is proportional to the area under the curve of the gradient (see Eq. 1.5). The total phase shift as result of frequency encoding and phase encoding is:

$$\Delta\varphi_{i,j}(\vec{r}) = \Delta\varphi_{p,j}(\vec{r}) + \Delta\varphi_{m,i}(\vec{r})$$

$$= \gamma \int \left(G_{PE,j} \cdot p\right)dt + \gamma \int_{TE}^{t_i}\left(G_{READ} \cdot m + \Delta B_0(\vec{r})\right)dt. \quad (2.10)$$

Note, that the susceptibility induced phase term is proportional to the frequency encoding time point t_i. Therefore, for any t_i, the phase shift increment between two consecutive samples in the p direction is independent of the field deviation:

$$\Delta\varphi_{i,j1}(\vec{r}) - \Delta\varphi_{p,j2}(\vec{r}) = \gamma \int_{t_A}^{t_B}\left(\left(G_{PE,j1} - G_{PE,j2}\right) \cdot p\right)dt. \quad (2.11)$$

Hence, phase encoding is spatially accurate and insensitive to susceptibility effects.

2.1.3.4. Signal intensity errors

Signal displacement [36] leads to geometry distortion and may result in blurring. As some imaged signal is displaced onto other signal, the signal intensity is often disturbed as well, leading to signal pile-up and signal voids [21,37]. Slice profile distortions, including thickness variations and even disjunct regions of excited signal, also lead to geometry distortion and signal intensity variations [21].

In FFE, strong local variations of the resonance frequency may cause intra-voxel dephasing, leading to signal voids.

2.1.3.5. Fat suppression issues

Finally, susceptibility variations may also cause issues with fat suppression [36]. The precession frequencies of hydrogen atoms in fat and in water differ by 3.4 ppm. Spectral fat suppression techniques such as Spectral Presaturation with Inversion Recovery (SPIR, [38]) or SPectral Attenuated Inversion Recovery (SPAIR, [39]) use this difference to selectively saturate the hydrogen signal of fat (Figure 2.3a). However, metal induced f_0 deviations are typically much larger than the 3.4 ppm chemical frequency shift of fat with respect to water. This renders spectral fat suppression techniques unreliable near metal implants (Figure 2.3b).

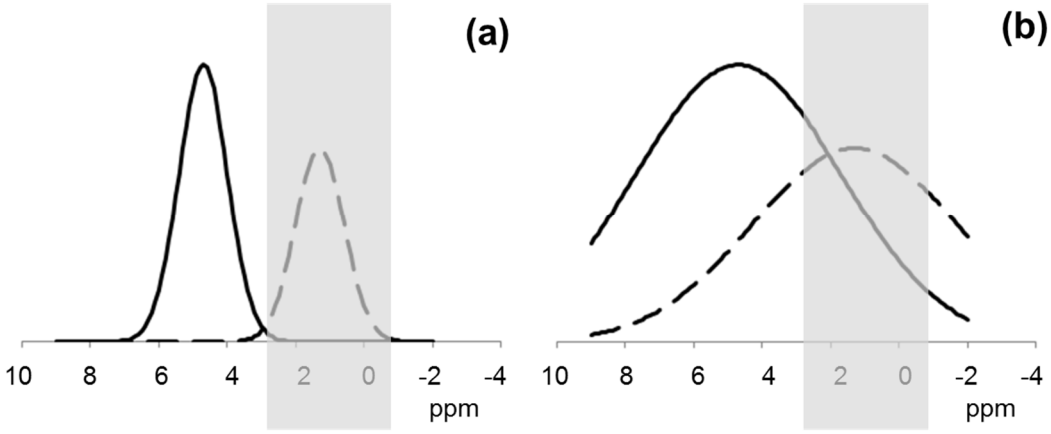

Figure 2.3: Spectral fat suppression (a): hydrogen atoms in fat (dashed line) resonate at a slightly different frequency compared to hydrogen atoms in water (solid line), the chemical frequency shift of fat with respect to water being 3.4 ppm. Fat signal can be suppressed using a presaturation RF pulse with a frequency band that includes fat signal only (grey). Spectral fat suppression fails near metal (b), because the metal induced f_0 deviations are typically much larger than the chemical frequency shift of fat with respect to water. Hence, not all fat signal is suppressed and some water signal is suppressed.

2.2. Clinical impact

The information in the following sections on the clinical impact of metal artifacts is kindly provided by Volker Otten (orthopedics), Kjell-Gunnar Nilsson (orthopedics), Conny Ström (radiology), and Jörgen Strinnholm (radiology) at the Norrlands Universitetssjukhus, Umeå, Sweden and by Stephan Vehmeijer (orthopedics) and Linda van Zeeland (radiology) at the Reinier de Graaf Groep, Delft, the Netherlands. Additional information was obtained from literature.

Compromised image quality has substantial impact on clinical diagnosis. Next to physical examination, diagnostic imaging provides essential input for evaluation of tissue in many cases.

Some complications require accurate imaging of bone tissue. These include bone fractures, osteolysis or loosening of the implant. In these cases, an X-ray or CT will be an adequate imaging solution, which will cost less than MRI.

MRI is especially valuable for the evaluation of soft tissue properties. Indications for which MRI is used include especially pseudotumors, edema, to some extent muscular atrophy, and

also bone oncology. Although for infections, including abscess, either CT or nuclear medicine is often used [40], MRI has been recommended as a valuable modality to evaluate infections in soft tissue [41,42,43].

For many patients, it is often the implant surgery or the metal implant itself that led to the need for tissue evaluation using imaging [44].

When MR image quality is compromised by artifacts due to the presence of a metal implant, it may be difficult or even impossible to evaluate tissue in the vicinity of the implant. In all cases, it is preferred to be able to see as large a region around the implant as possible and as close to the implant as possible. The image quality level required for diagnosis and how close to the implant diagnostic image quality is required depends on the type of disease and on the criteria that are used to decide whether or not to treat the patient or to monitor the disease. The next few sections contain more detailed discussions of a number of indications for which MRI may be useful depending on whether the artifacts due to metal can be maintained within limits.

2.2.1. Pseudotumors

Pseudotumors were discovered recently by coincidence [45,46], and have been associated with wear in metal-on-metal (MOM) implants. Where many hip implants have a metal or ceramic femoral head and a polyethylene liner in the acetabular component (cup), there is no such liner in MOM implants. Instead, the contact surface of both head and acetabular component typically is made of stainless steel or a titanium alloy. Introduced to the orthopedic market over 30 years ago, these MOM implants were first intended for the younger and more physically active patients. More recently, studies have shown [46,47,48] that wear of the contact surface of these implants results in migrating metallic particles. As the particles migrate to the surrounding tissue or the blood, they may cause pseudotumors. Pseudotumors have only been found in the capsule, which is where they seem to start growing from.

Knowledge about pseudotumors is still limited, and different stages of pseudotumors have not yet been defined. Pseudotumors may vary in severity and may be symptomatic or silent [49]. They may cause a wide variety of symptoms including mainly pain and swelling, but also late dislocation or instability [45], and sometimes reduced strength or reduced ranged of motion (ROM). Surgeons indicate that pseudotumors smaller than a centimeter are not considered problematic. When pseudotumors grow to roughly a centimeter in diameter, it becomes important to follow them. Pseudotumors larger than a centimeter are likely to compress other tissue. For these pseudotumors it may be required to revise the implant and insert a non-MOM articulation [49].

For the decision to treat a patient, size is an important but never the only criterion. Depending on the location, compression of other tissue may or may not be problematic, as it may or may not include vital parts, such as the iliac and femoral artery in the pelvic area or the nerves anterior and posterior to the implant. Next to imaging, blood sample values are always taken into account.

A crucial factor for treatment decision is the preference of the patient. For example, at higher age, a patient may be inclined to accept the presence of a pseudotumor and decide that the benefits of surgery are not worth the risks. Some patients keep walking with a pseudotumor of 4 to 5 centimeters in diameter. In case the decision is made to go for surgery, the implant bearing needs to be changed, and the pseudotumor needs to be removed.

MRI is an essential modality to diagnose pseudotumors [49], and the radiologists have found that T2w contrast provides the images that are most useful for this diagnosis. As the pseudotumors result from wear of the implant itself, and reside in the capsule around the implant, MR imaging of pseudotumors is typically compromised by the presence of metal artifacts.

2.2.2. Effusion and bone marrow edema

Each joint is lubricated by fluid called synovial fluid, which is maintained within the joint cavity by the synovial membrane, lining the capsule. Excess synovium may accumulate either within or outside of the joint as a result of trauma or injury. Injury may also lead to accumulation of excess fluid within the bone, which will cause swelling of the bone, referred to as bone marrow edema.

According to the surgeon and the radiologist, MRI is the preferred modality to image effusion, bone marrow edema, or more generally to image fluid. It is important to see the fluid in and around the joint. In practice, for a lesion of about a centimeter in diameter, it must be possible to determine whether that lesion is edema or not, by using a combination of contrast weightings including T2w imaging. Fluid may be present close to a metal implant, and especially bone marrow edema may have been caused by injury during the implant surgery procedure. In these cases, metal artifacts are likely to compromise the image quality at the location of the fluid.

2.2.3. Bone oncology

A small number of patients have a bone tumor close to the implant. To image bone oncology, nuclear medicine is usually the modality of choice. But when tumors expand into soft tissue, MRI is used to evaluate whether the tumor expands in the direction of blood vessels or nerves. Typically, a tumor of two centimeters or larger should be treated, according to the orthopedist. One of the radiologists said that tumors of roughly a centimeter must be visible, which may be difficult in cases where the tumor is close to the metal.

2.2.4. Muscular atrophy

During implant surgery, a muscle insertion may be cut, either intentionally or unintentionally or even unconsciously. In those cases, the muscle will atrophy and fat will start to replace the muscle fibers. For the diagnosis of muscle atrophy, which in many cases is for the shoulder, the radiologists often use CT, and sometimes MRI. For such diagnosis, it must be possible to resolve structures smaller than a centimeter. These structures must be visible down to 1 or 2 centimeters from the implant, although in most cases they are further away.

2.2.5. Osteolysis and loosening

In the first weeks or month after implant surgery, there will be activity of osteoclasts (cells that dissolve bone tissue) and there can be movement of the implant. After that initial period, the implant should become well fixed by bone growing into the outer metal structure. If at a later time osteolysis (i.e. bone resorption) occurs, it is a problem that needs to be fixed.

Osteolysis usually only becomes symptomatic in a later stage when the implant already starts to loosen. The main symptom is pain according to the orthopedists. It is only when the implant is loose, that it needs to be replaced. In most cases it will still be possible to insert a new implant. But the longer osteolysis progresses, the more difficult it becomes to fit a new implant. Instead, whenever possible, it is much better to find and fill the osteolysis well before the implant is loose and symptoms start. Therefore, the earlier the osteolysis is found the better, according to the surgeon, and early diagnosis is needed to decide if there is a risk that the implant will loosen in the near future.

The surgeon compared the influence of osteolysis on the implant stability to the influence of rust on the reliability of a car chassis: both size and location of the osteolysis need to be considered for the treatment decision.

In hip, when osteolysis occurs in cortical bone, and especially around and above the hip cup, it is likely to lead to instability of the implant, and it will be difficult to get a new implant stable. With a large osteolysis in the medial wall there is risk for medial luxation of the cup, a type 3B defect according to the Paprosky classification [50], and these belong to the most difficult defects to deal with in the revision.

The size of the osteolysis is an important, but never the only factor in the decision to recommend a revision or not. The orthopedist estimated that when osteolysis in the hip near the cup is larger than typically 3 to 4 cm^3, it is more likely to lead to loosening of the implant in the future. Yet, in some cases, he could fill 20 cm^3 of osteolysis with bone chips and maintain a fixed cup. Conversely, he found other cases where 2 cm^3 of osteolysis led to implant loosening, and with cemented cups loosening is often seen with only a zone of as little as 2 to 3 mm in the interface between the cup and the bone. Depending on the location of the osteolysis, it may need to be treated immediately at the smallest perceivable size. To diagnose osteolysis in such an early stage, the preference is to see immediately adjacent to the implant to evaluate the bone-implant interface.

Evaluation is done using a combination of multiple modalities that provide complementary information. X-ray provides high resolution, but in 2D only, while 3D imaging is important for sufficient information about the size and location of the osteolysis with respect to the implant. CT shows the border of the osteolysis and is an adequate and cost-efficient imaging solution for both osteolysis and implant loosening. Yet, MRI is able to show fluid. T1w contrast and fat suppressed imaging complement each other. When the implant starts to loosen, it is surrounded by a film of fluid of about 1 or 2 mm thickness. MRI would be able to identify this fluid film and the associated infection, if it were not affected by metal artifacts from the directly adjacent implant.

MRI may become a more valuable modality in the future, depending on the outcome of research investigations related to osteolysis. There may be biomarkers for osteolysis, using PET or SPECT in combination with MRI. The effects of osteolysis on soft tissue and the metabolic changes in the bone have not been fully investigated yet. Trials will need to prove whether pharmaceutical treatment, including tnf-alpha-inhibitors and trastuzumab, will be able to prevent or reverse osteolysis [51,52,53]. When pharmaceutical treatment proves to be effective, MRI will be important for monitoring, and metal artifacts will need to be limited.

2.2.6. Infections

Infections may occur near a metal implant, e.g. as a consequence of implant surgery. Especially for infections in the soft tissue, MRI will be an important imaging modality [41,42,43]. In many of these cases, the impact of metal artifacts on tissue evaluation will be modest as the infection will be observable at a reasonable distance from the implant.

2.3. Currently available measures to reduce metal artifacts

To aid in the diagnosis of the abovementioned conditions, metal artifacts need to be reduced. There are a number of measures available for metal artifact reduction with the current state of the technology. A practical overview is provided by Lee et al. [54].

2.3.1. Limited magnetic field strength

For paramagnetic materials, magnetization M (Eq. 2.1), induced magnetic field deviations ΔB_0 (Eq. 2.2), and resonance frequency deviations Δf_0 (Eq. 2.3) are linearly dependent on the applied static magnetic field H. The effect of the increased magnetization may be compensated partly by the stronger gradient fields and broader RF pulse bandwidths that are commonly used at higher main magnetic field strengths [54], as far as PNS and SAR limitations as well as hardware limitations allow.

The most straightforward approach to reduce the cause of all metal induced artifacts is to use the available scanner with the lowest magnetic field strength that enables sufficient SNR and spatial resolution.

2.3.2. Turbo Spin Echo

FFE suffers from signal dephasing due to local ΔB_0 variations, while TSE is much less sensitive to such dephasing effects (section 2.1.3.1). As the strongest ΔB_0 variations are found close to the metal, TSE enables imaging closer to the implant than FFE. Hence, TSE is commonly used when scanning near metal.

2.3.3. Through-plane distortion

The through-plane distortion (section 2.1.3.2) depends on the ratio between the B_0 field inhomogeneity and the selection gradient strength (Eq. 2.6). By increasing the selection gradient strength, the relative influence of the susceptibility induced frequency deviations reduces compared to the linear frequency variation induced by the gradient (cf. Figure 2.4c,d and Figure 2.4e,f). Practically, the selection gradient may be increased by using thin slices. Alternatively, to maintain the slice thickness, the selection bandwidth may be increased as

well, by shortening the RF pulse duration. This usually leads to increased SAR, as achieving an equal flip angle within a shorter RF pulse duration requires a higher B_1 amplitude.

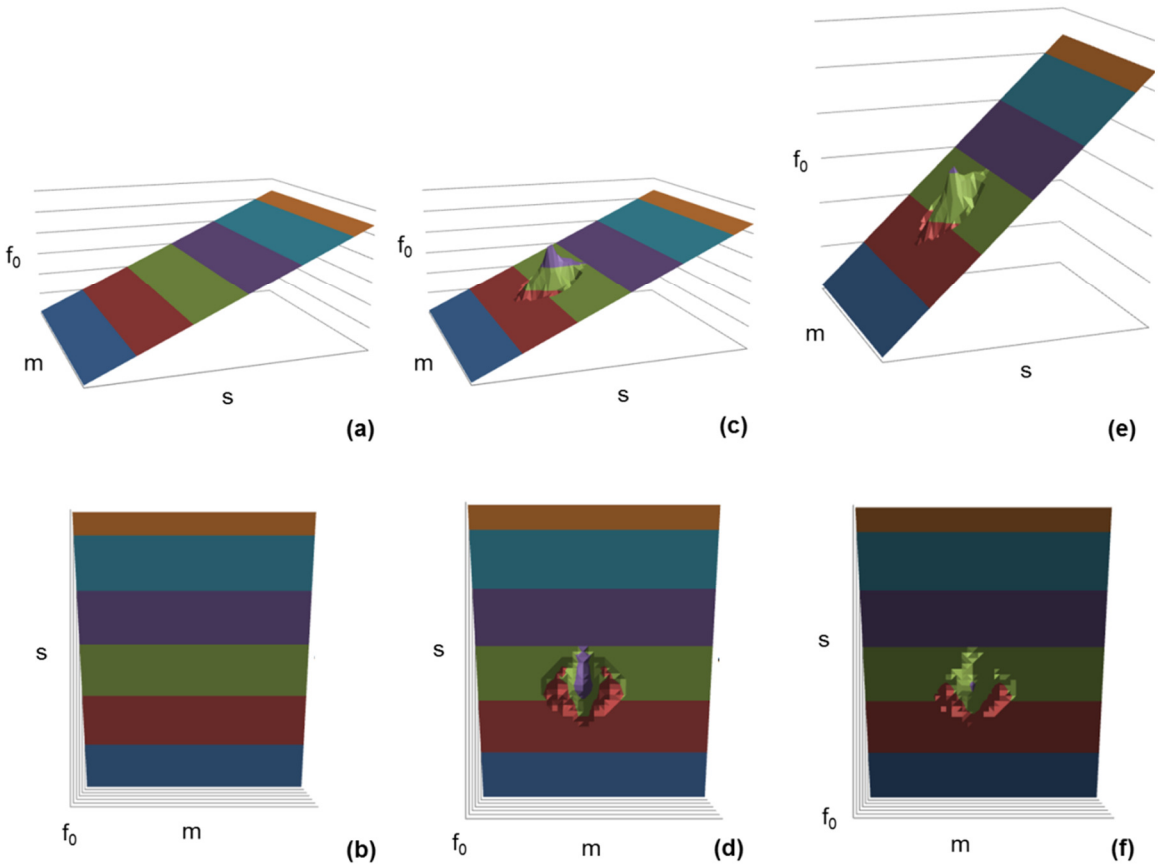

Figure 2.4: Slice selection using a selection gradient. A linear gradient causes spins to precess at linearly increasing frequency f_0 with increasing spatial position s (a). Adjacent RF bands are used to excite and refocus adjacent straight slices (colored bands, b). Susceptibility induced f_0 deviation leads to distortion of the selected slice (red, green, purple in c,d). Increasing the selection gradient strength reduces the relative influence of susceptibility on the resonance frequency f_0 (e,f). In the illustrated case, the RF bandwidth is also increased. Alternatively, at the original RF bandwidth, stronger selection gradients lead to selection of thinner slices.

As an alternative to slice selection, 3D imaging may be performed, by exciting and refocusing a larger volume. In this case, phase encoding is applied in the through-plane direction to resolve the through-plane position of signal. Phase encoding is spatially accurate and insensitive to susceptibility effects (see Eq. 2.11). However, the selection gradient used in 3D imaging is much weaker, as the frequency range covers a larger distance in the through-plane direction (Figure 2.5).

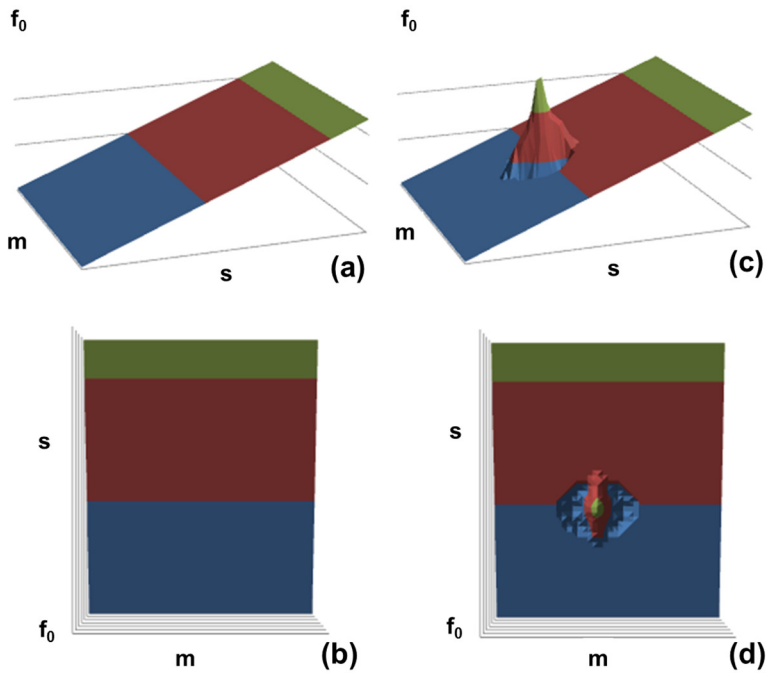

Figure 2.5: 3D volume selection using a selection gradient. A relatively weak linear gradient causes spins to precess at linearly increasing frequency f_0 with increasing spatial position s (a,b). The bandwidth of the RF pulses determines the volume where spins are excited (red area). Outside that volume, spins are not excited (green and blue areas). Susceptibility induced f_0 deviations can be large with respect to the selection gradient and lead to strong distortion of the selected volume (c,d). Hence, signal voids may appear in the volume of interest (green top of the peak and blue areas adjacent to the peak). Or, conversely, off-resonance signal outside the volume of interest may be excited (red part of the peak extending into the blue area).

The weaker selection gradient leads to even stronger distortions of the selected volume, requiring additional phase encoding steps in order to avoid aliasing. In addition, in a substantial part of the volume of interest, signal is not excited, leaving voids in the image (Figure 2.6).

Spatially non-selective 3D imaging applies excitation and refocusing RF pulses without the application of a selection gradient, and may be a useful alternative if the entire anatomy within the sensitivity range of the RF receive coil is imaged. However, near metal implants, spatially non-selective acquisition suffers from substantial signal voids where the susceptibility-induced frequencies exceed the RF bandwidth (Figure 2.7).

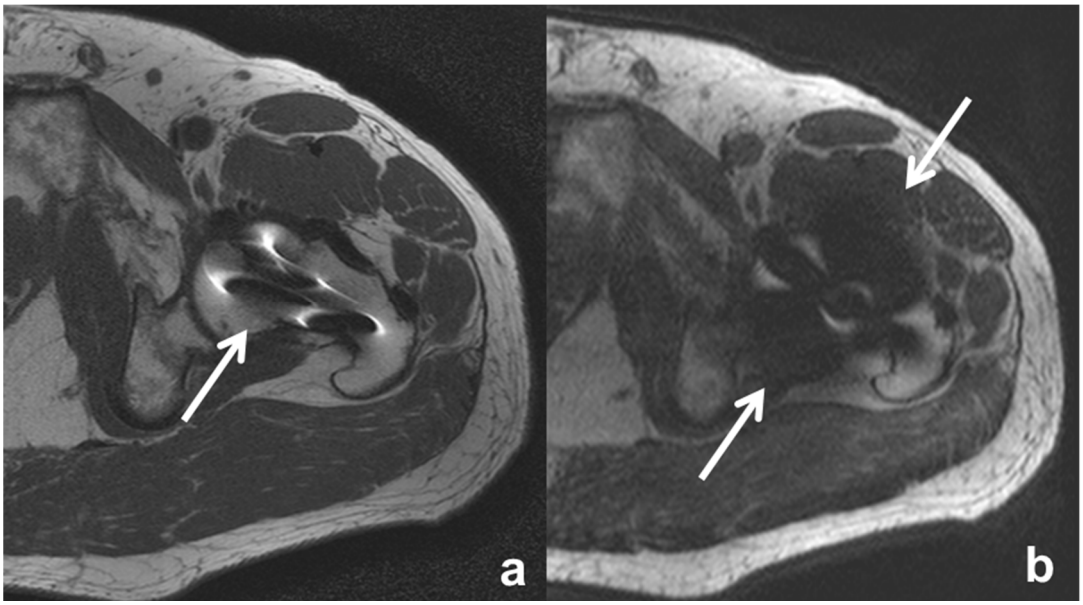

Figure 2.6: Axial images of a volunteer with hip fixation screws (arrows). Images were acquired using 2D TSE (a) and 3D TSE with volume selection (b). 3D imaging suffers from signal voids in a substantial part of the volume of interest, because the weak selection gradient leads to strong distortions of the selected volume due to susceptibility near the metal implants.

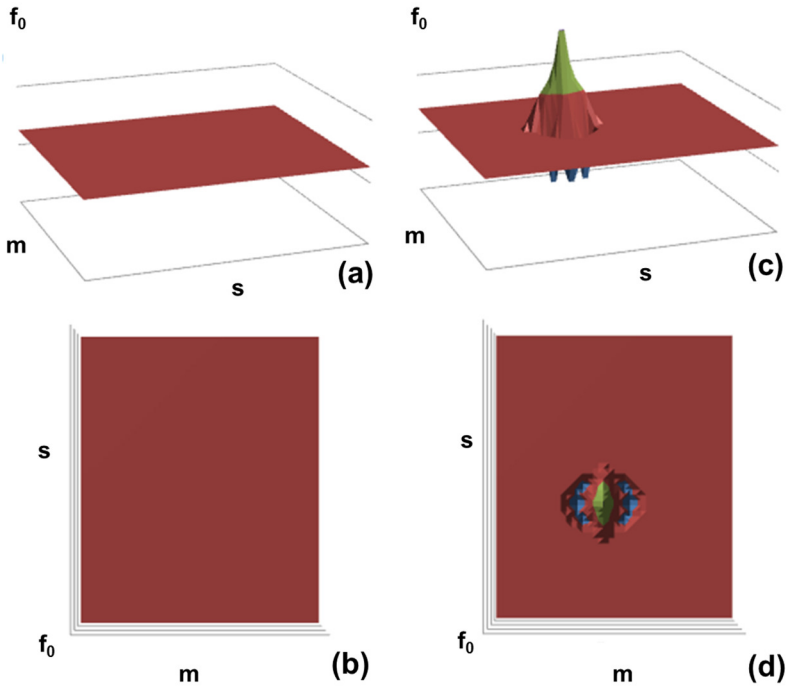

Figure 2.7: Spatially non-selective 3D imaging applies excitation and refocusing RF pulses without using a selection gradient (red areas in a,b). Near metal, the frequency deviations may exceed the RF bandwidth leading to substantial signal voids (green and blue areas in c and d).

2.3.4. Off-resonance suppression

The maximum frequency deviation due to the presence of metal implants depends on the material and the shape of the metal implant, as well as the orientation of the implant with respect to the static magnetic field. With increasing frequency deviation of selected signal, the artifact level increases. However, a commonly applied adaptation of the TSE sequence allows selecting only part of the frequency dispersion, by using different gradient strengths for excitation than for refocusing [55]. Thus, off-resonance signal with a strong frequency deviation is suppressed.

The selection mechanism is illustrated in a so-called s-f_0 diagram showing spatial coverage of excitation and refocusing vertically, and spectral coverage horizontally (Figure 2.8). These s-f_0 diagrams illustrate the distribution of signal content over frequency offset horizontally and in the through-plane phase encoding direction vertically. Selection of signal that complies with the selection condition (Eq. 2.5) is represented as a straight band in an s-f_0 diagram. Using different gradient strengths for excitation than for refocusing results in a limited overlap between the two selection bands (Figure 2.8b).

This technique was initially meant to suppress so-called “ambiguity artifacts” [55], also referred to as “annefacts” or “flames”. These artifacts result from unintendedly selected signal that originates from the regions near the end of the bore of the MRI scanner, where the homogeneity of the applied magnetic field is substantially compromised by design. The technique may similarly be used to limit the spectral coverage when scanning near metal, and will be referred to as Off-Resonance Suppression (ORS).

Typically, for high-bandwidth TSE sequences with off-resonance suppression and with 4-mm slices, excited and refocused signal includes frequency deviations ranging from 5 to 10 kHz.

2.3.5. In-plane distortion

Similar to slice distortion, distortion in the frequency encoding direction may be reduced by applying a strong frequency encoding gradient, which reduces the relative influence of the susceptibility induced frequency deviations (Eq. 2.8). In practice, a strong frequency encoding gradient may be obtained by selecting a limited field of view (FOV) in the frequency encoding direction. Alternatively, if the FOV is maintained, using a stronger frequency encoding gradient increases the total frequency dispersion of spins, and requires a larger read-out bandwidth to acquire all signal from the FOV. Hence, the acquired noise also comprises a wider frequency range, and this reduces the SNR.

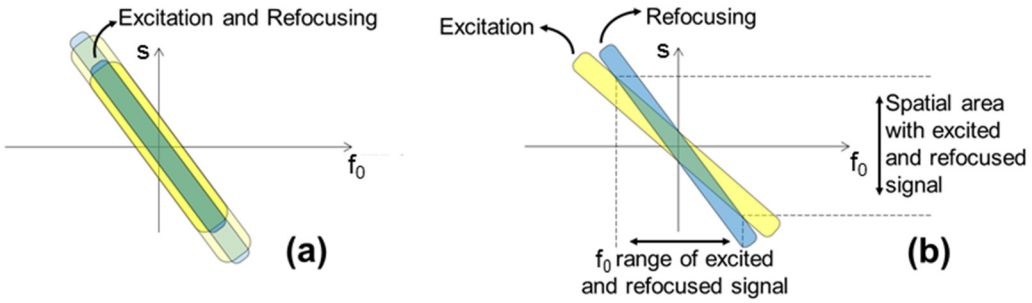

Figure 2.8: s-f_0 diagrams showing spatial (vertical) and spectral (horizontal) coverage of excitation and refocusing. If a TSE sequence uses equal gradients during excitation and refocusing, distant signal with strong f_0 offset is also excited and refocused (a). Using different gradients for excitation (yellow) than for refocusing (blue) is commonly used to suppress so-called ambiguity artifacts originating from distant off-resonance signal. This technique limits the total range of f_0 offsets as well as the maximum distance of selected signal from the intended slice (b).

2.3.6. Fat suppression

In regions with a substantial susceptibility induced distortion of the signal frequency spectrum, spectral fat suppression techniques are unreliable (see 2.1.3.5). A more robust technique uses the difference in T1 relaxation time between fat signal and water signal, which is far less sensitive to factors such as the presence of metal, because T1 can be considered constant for B_0 variations of a few mT. Short Tau Inversion Recovery (STIR, Figure 2.9) first applies a 180° inversion RF pulse. After an appropriate inversion time TI, the longitudinal magnetization of fat is zero.

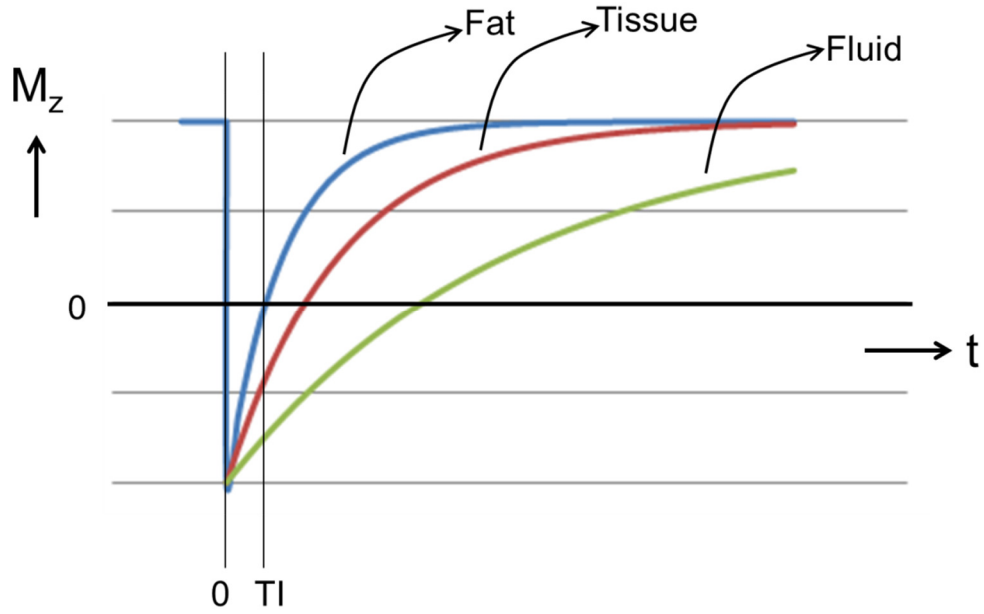

Figure 2.9: Fat suppression using the STIR sequence. Magnetization is inverted at t = 0 using a 180° inversion RF pulse. After an inversion delay TI, the fat magnetization is zero. At this moment, the TSE pulse sequence is commenced, which enables imaging tissue and fluid without fat. SNR is reduced, due to the reduced initial magnetization of tissue and fluid at t = TI.

At this time, the standard TSE pulse sequence is commenced, starting with a 90° excitation RF pulse. As the longitudinal magnetization of fat is zero at this time point, no transverse magnetization of fat results from this excitation pulse. Note, that at this point the magnitude of all other signal is also reduced. Hence, SNR is usually compromised in STIR images (see Figure 1.11c). The additional 180° inversion RF pulse leads to increased SAR.

2.3.7. Impact on SNR, SAR and scan duration

The above described measures to reduce imaging artefacts related to metal have an impact on SNR, SAR and scan duration.

The SNR of the images is reduced by using a limited magnetic field strength, thinner slices, high-bandwidth read-out, off-resonance suppression, and in case fat signal is suppressed, by using STIR. The SNR loss may be compensated by decreasing the resolution and by using averaged repetitions of the acquisition. Shorter echo-spacing will also compensate for the SNR loss. While the high-bandwidth read-out results in short acquisition windows, the shorter echo-spacing allows consecutive acquisition windows to follow each other quickly, thereby (partly) maintaining the time-efficiency of the sequence.

Using TSE with high bandwidth RF pulses and, if applicable, STIR significantly increases SAR. SAR is further increased by using shorter echo-spacing for SNR compensation. As was mentioned before, the SAR is an important aspect to consider in view of safety when scanning patients with metal implants.

Finally, the scan duration is usually prolonged by using TSE instead of FFE and by covering a volume of interest with thinner slices. And especially if averaged repetitions of the entire acquisition are required for sufficient SNR, scan duration is substantially increased.

2.4. Residual artifact

The remaining susceptibility artifacts in high-bandwidth TSE include a variety of effects that can be quite significant, including residual displacement, signal pile-ups and signal voids. It is important to note the difference between displacement and extent of the artifact, as many small displacements of multiple signals throughout the image may together constitute substantial artifacts that cover a much larger region.

2.4.1. Through-plane distortion

Through-plane distortion, often also referred to as slice distortion or “potato-chipping”, may especially cause serious confusion during image reading as it is often difficult to understand the origin of the displaced signal. It translates to through-plane geometric distortion, which also includes thickness variations that lead to signal intensity variations. Moreover, disjunct regions of signal may arise that lead to particularly conspicuous bright edges in the image, due to the sudden thickness changes of the selected slice [21].

Although slice distortion may be minimized by maximizing the selection gradient, residual slice distortion remains. This residual distortion is given by Eq. 2.6. When ORS (see section 2.3.4) is applied, excited and refocused signal may be include frequency deviations of typically 5 to 10 kHz, which corresponds to a ΔB_0 of 0.1 to 0.2 mT. With selection gradients

of typically 7 to 10 mT/m, the slice distortion may be on the order of 20 mm. Without ORS, the slice distortion may be much larger.

2.4.2. In-plane distortion in conventional TSE

During readout, off-resonance signal disturbs the frequency encoding process. The displacement is determined by the maximum field deviation and the read-out gradient (Eq. 2.8). The read-out gradient is usually about 20 mT/m. Using ORS, the field deviation where signal is selected may be up to ΔB_0 = 0.2 mT, which thus corresponds to an in-plane displacement on the order of 10 mm. When ORS is not used, the in-plane displacement may be much larger.

2.4.3. Signal voids due to incomplete spectral coverage in TSE

When using ORS (section 2.3.4), the total spectral coverage in TSE is limited, and signal outside this spectral range is not imaged, which may lead to signal voids. In practice, including frequency deviations up to 5 kHz is sufficient to cover most of the signal near titanium implants. Near stainless steel, the frequency deviation will be so large that signal voids are left as a consequence of the modified slice selection process only.

2.4.4. Signal voids due to insufficient frequency encoding

Any MRI technique that uses frequency encoding suffers from in-plane distortions as soon as the frequency range of the signal is of the order of or larger than the bandwidth per pixel during read-out. In more extreme cases, local field gradients in the frequency encoding direction may exceed and counteract the applied frequency encoding gradient [37]:

$$\frac{\mathrm{dB_0/dm}}{\mathrm{G_{READ}}} \leq -1. \qquad (2.12)$$

Particularly in regions where the local gradient is nearly equal and opposite to the read-out gradient, the read-out gradient is nearly cancelled and all signal is mapped onto a single image position, while leaving signal voids elsewhere [37].

2.5. Scan robustness issues

The wide frequency dispersion encountered near metal may invalidate certain presumptions that were made during the design of the MRI scanner software. Specifically, one of the first preparation measurements performed before an MRI sequence is acquired, the f_0 determination (Figure 2.10), can be substantially impacted by strong frequency deviations. During this preparation measurement, unexpected measurement results may lead to scan aborts, as the f_0-preparation algorithm may conclude that no object is present in the scanner.

Each measurement within the f_0 determination phase starts with a STIR pulse to saturate the fat signal. The first measurement performed is a volume selective measurement (Figure 2.10a). If the peak frequency of this measurement has a limited frequency offset, then this completes the f_0 determination.

If, in the first step, a large frequency deviation is found, the f_0 determination is continued with a slice-selective wide-band retry, for a coarse estimate of the peak frequency (Figure 2.10b).

If the wide-band retry succeeds, the resulting coarse estimate of the peak frequency is used as reference and the initial volume selective measurement is repeated (Figure 2.10c). If this final measurement still results in a peak frequency with a significant offset, the user is notified about this large frequency offset.

If the f_0 measurement fails to find a reliable peak frequency during the second or third measurement, the scan is aborted. Whether a peak frequency is considered reliable depends on its SNR. A low SNR resonance peak is considered a sign that no object is present in the scanner. The noise is determined in a different part of the same measured spectrum, under the assumption, that the signal is limited to a narrow band in the spectrum near the resonance peak. This presumption may not hold when a metal object is present in the MRI scanner. Depending on the frequency dispersion induced by the metal, this may cause the f_0 measurement to fail and the scan to abort.

If a limited amount of metal is present in the scanner, the peaks in the frequency responses will typically become broader and weaker. This is illustrated by f_0 measurement results with a 10-mm diameter stainless steel rod placed in doped water and positioned vertically in the scanner bore (Figure 2.11). If the stainless steel rod is replaced with a 30-mm specimen, the frequency response becomes even more broad and weak (Figure 2.12). After that, the frequency response resulting from the wide band retry shows signal throughout the entire measured band. The wide frequency dispersion of spins induced by the metal is misinterpreted as background noise, and the SNR of the resonance peak is considered too low, resulting in a scan abort.

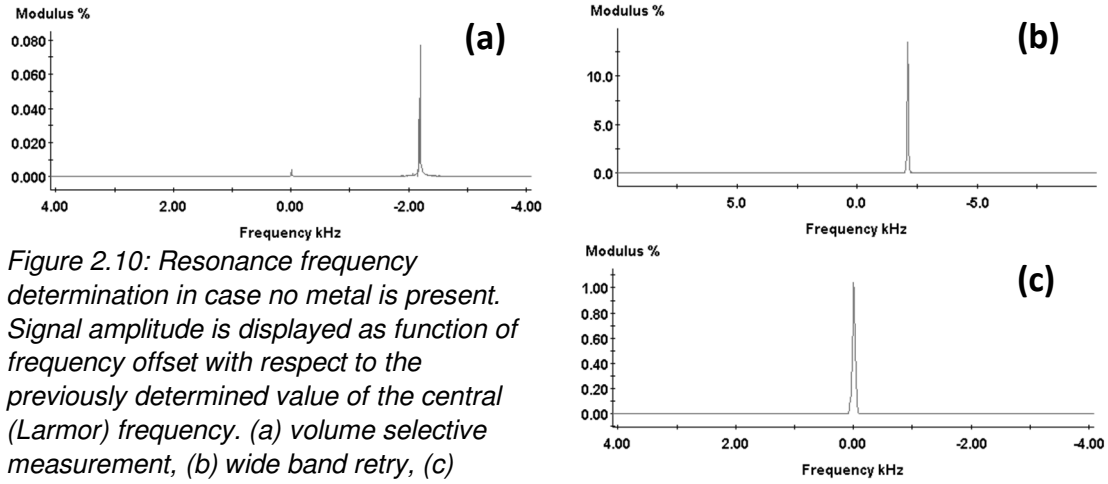

Figure 2.10: Resonance frequency determination in case no metal is present. Signal amplitude is displayed as function of frequency offset with respect to the previously determined value of the central (Larmor) frequency. (a) volume selective measurement, (b) wide band retry, (c) repeated volume selective measurement with adjusted central frequency.

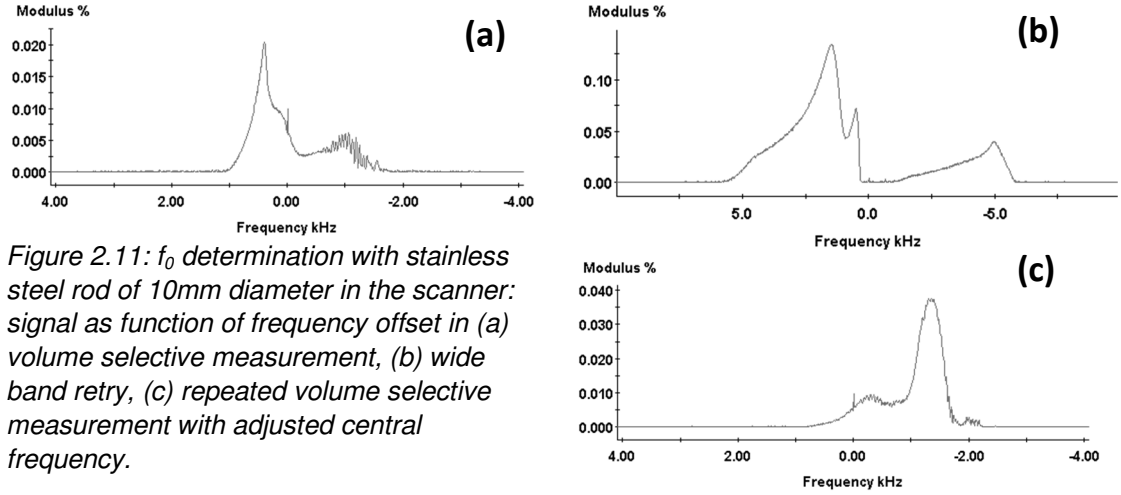

Figure 2.11: f_0 determination with stainless steel rod of 10mm diameter in the scanner: signal as function of frequency offset in (a) volume selective measurement, (b) wide band retry, (c) repeated volume selective measurement with adjusted central frequency.

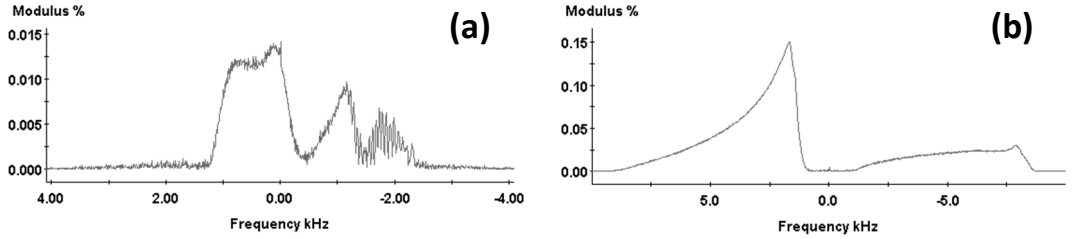

Figure 2.12: f_0 determination with stainless steel rod of 30mm diameter in the scanner: signal as function of frequency offset in (a) volume selective measurement, (b) wide band retry.

3. Advanced Techniques for Metal Implant Artifact Reduction

The conventional techniques described in the previous chapter to reduce metal induced artifacts have been available on commercial scanners for many years. Depending on the size, shape and material of especially bulk implants, the residual artifacts associated with these techniques are often too large to allow tissue evaluation near the metal. Especially in view of the soft tissue complications associated with metal implants, the interest for more advanced metal artifact reduction techniques has considerably increased recently [36,56]. Some of these techniques were first published over twenty years ago [57], while others were developed more recently [58,59,60]. This chapter gives an overview of a number of the more advanced techniques, the mechanism behind these techniques and their benefits and drawbacks.

3.1. View Angle Tilting

In conventional TSE imaging, the through-plane distortion (Eq. 2.6) and the displacement of signal in the frequency encoding direction (Eq. 2.8) are both proportional to the local main field deviation ΔB_0. Therefore, there is a fixed angle, at which the excited signal is projected onto the imaging plane (Figure 3.1a). This projection angle can be compensated by tilting the view angle of the voxels [57]. View angle tilting (VAT) is achieved by reapplying the selection gradient during read-out. This gradient is then called the VAT gradient G_{VAT} and is applied simultaneously with the frequency encoding gradient G_{READ}. The view-angle β is determined by the ratio of these two gradients:

$$\beta = \tan^{-1}(G_{VAT}/G_{READ}). \qquad (3.1)$$

VAT does not resolve the slice distortion, but uses the slice distortion to correct for the in-plane distortion (Figure 3.1b). The intensity artifacts remain present, but they appear at the correct in-plane position and are typically reduced. As such, the artifacts do not hide other signal which is often more relevant. VAT is a time-efficient technique: the scan duration is equal for a VAT acquisition and conventional TSE.

On-resonance signal is largely insensitive to the applied VAT gradient, except for some blurring [58]. As the voxels are imaged under a tilted angle, their shape becomes an oblique prism, and the extent of the voxel in the read-out direction exceeds the distance between the voxels (Figure 3.2). The resolution in the read-out direction is therefore determined not only by the distance between voxels but also by the view angle and the slice thickness.

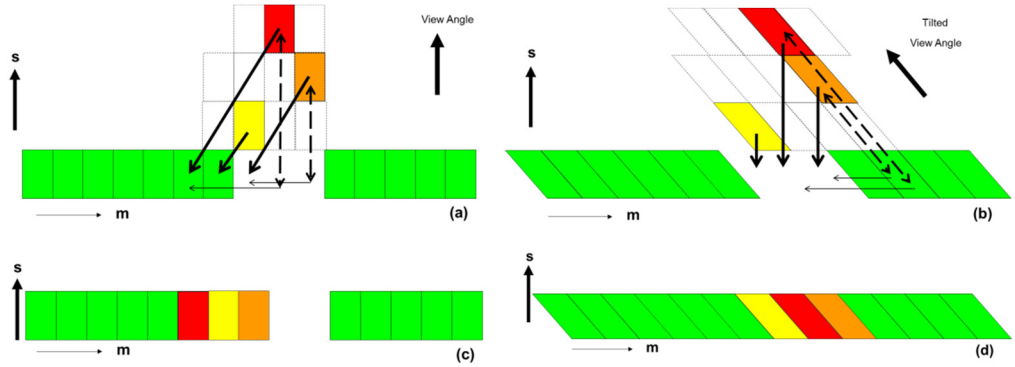

Figure 3.1: Through-plane and in-plane distortion in conventional TSE imaging (a,c) and in VAT imaging (b,d). When the slice (green voxels) is selected using a selection gradient, off-resonance signal at a distance is also selected (slice distortions, yellow, orange, red). Both the distortion in the through-plane direction (s, dashed arrow) and the displacement of signal in the frequency encoding direction (m, thin arrow) are proportional to the frequency deviation (red for large, yellow for small Δf_0). Hence, there is a fixed angle at which off-resonance signal is projected onto the image plane (thick arrow). The projection angle can be compensated by titling the view angle of the voxels (b,d). View angle tilting uses the existing slice distortion to correct for the in-plane distortion.

More accurately, the voxel response is compromised by a convolution with the slice selection profile, which may even be much wider than the slice thickness. For a given RF bandwidth, an RF pulse with a shorter duration results in a slice profile with wider tail and side-lobes and this effect introduces additional blurring in the read-out direction. This convolution in image space with the slice selection profile has been described by Butts et al. as a modulation in k-space with the Fourier transform of the slice profile, which becomes prominent if the RF pulse duration is short compared to the read-out duration [62].

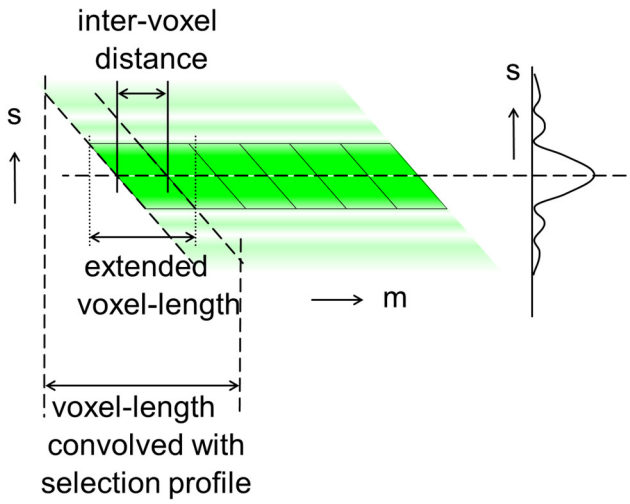

Figure 3.2: Tilted voxels imaged with VAT and viewed in the m,s-plane (left). By tilting the view angle, the voxel-length is extended in the read-out direction (dotted vertical lines), and exceeds the distance between voxels (solid vertical lines), which leads to blurring. The extended voxel-length is dependent on the view angle and the slice thickness (solid horizontal lines). Additionally, the voxel response is convolved (green to white fading regions) with the slice selection profile (right) [62], which results in additional blurring in the read-out direction.

3.1.1. Slice profile restoration by frequency mapping

VAT does nothing to correct for slice selection distortions, which translate to through-plane geometric distortion that can cause severe confusion during image reading. Slice distortion may also include thickness variations that lead to signal intensity variations and even selection of disjunct regions [21].

Recently, Morin et al. proposed an extension of the VAT technique to restore the slice profile by frequency mapping [63]. In this approach, the VAT acquisition is repeated fourfold with varying time offsets between the k-space center and the spin echo position. From these four acquisitions, the ΔB_0 induced phase shift of the k-space data is derived, that needs to be corrected. Correcting the phase shift in k-space corresponds to correcting the displacement in image space.

This technique corrects not only for in-plane but partly also for through-plane distortion. However, thickness variations of selected slices remain uncorrected. At the current state of this technique, the corrected images suffer from an SNR penalty.

3.2. Multi-Spectral Imaging

Correction of both in-plane and through-plane distortion including selection thickness variations is achieved by Multi-Spectral Imaging (MSI) techniques. In these techniques, correct through-plane geometry is maintained by applying through-plane phase encoding, which is spatially accurate. MSI techniques involve an additional iteration during acquisition, and are therefore associated with prolonged scan duration compared to conventional TSE.

3.2.1. Slice-Encoding for Metal Artifact Correction (SEMAC)

SEMAC [58] is based on a multi-slice TSE acquisition. It uses VAT for in-plane correction. The through-plane distortion is corrected by applying an additional through-plane phase encoding. As such, each slice profile is measured using a sub-volume centered on the intended slice position (Figure 3.3a). Consecutive sub-volumes partly overlap and are shifted by the distance between consecutive slices (Figure 3.3b). Image sections from different sub-volumes are then combined into images that contain signal from multiple slice selections. Multiple combined images result in a corrected image volume (Figure 3.3c).

The number of through-plane phase encoding steps needs to be sufficient to cover the extent of the slice distortion, in order to avoid through-plane back-folding artifacts.

In regions with extreme field variations, the individual slice selections and their transitions may be visible in the combined images and lead to a residual signal fluctuation artifact, sometimes referred to as *pile-up artifact* [64] or *ripple artifact* [58,37]. As with any frequency encoding technique, residual displacement of off-resonance signal remains in the frequency encoding direction, as a consequence of the finite selection bandwidth. The in-plane distortion correction using VAT may lead to blurring in the read-out direction if the RF pulse duration is short compared to the read-out duration [62].

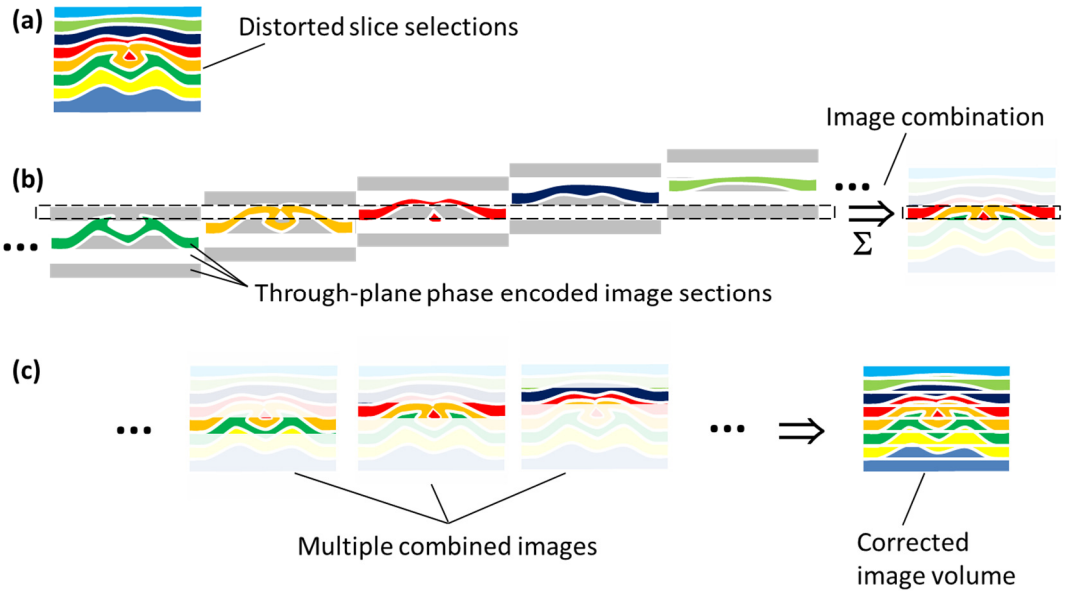

Figure 3.3: Slice Encoding for Metal Artifact Correction (SEMAC) is based on a multi-slice TSE acquisition (a), using VAT to correct for in-plane distortion. The slice selection distortions are resolved using additional through-plane phase encoding for each slice (b). Image sections from overlapping sub-volumes are combined into a single image containing signal from multiple slice selections. Multiple combined images then constitute a corrected image volume (c).

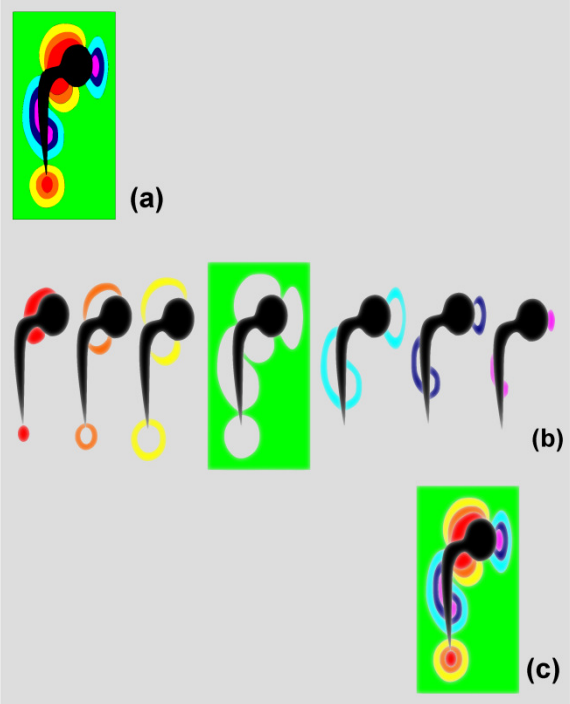

Figure 3.4: Signal frequency dispersion near implant (a) and acquisition of signal using Multi-Acquisition Variable-Resonance Image Combination (MAVRIC) (b). MAVRIC is based on a 3D spatially non-selective TSE acquisition, which acquires a limited bandwidth of the entire frequency dispersion. The 3D TSE acquisition is repeated with variable central RF frequencies during transmission and signal reception. The resulting 3D sub-volumes at equal position represent varying parts of the signal spectrum (b). The sub-volumes are combined into a single 3D volume representing the entire signal spectrum (c).

3.2.2. Multi-Acquisition with Variable-Resonance Image Combination (MAVRIC)

MAVRIC [59] is based on a spatially non-selective 3D TSE acquisition that selects signal within the frequency range determined by the bandwidths of the RF selection pulses. The

acquisition is repeated with variable central RF frequencies during transmission and signal reception, resulting in multiple 3D sub-volumes at equal position representing the individual signal frequency bands (Figure 3.4). The 3D sub-volumes are combined into a single 3D volume that represents the entire frequency dispersion of signal. The frequency bands of adjacent sub-volumes or *spectral bins* overlap to ensure a smooth transition between the spectral bins.

Spatially accurate phase encoding is applied in two directions, in-plane and through-plane. In-plane, there may be residual signal displacement in the frequency encoding direction [37]. As MAVRIC uses overlapping frequency bands, these displacements may also lead to blurring [65]. Using spatially non-selective RF pulses, MAVRIC may require phase encoding of a large volume, depending on the sensitivity of the RF coil used, and the size of the imaged anatomy. Phase encoding of a smaller volume may result in through-plane back-folding artifacts.

3.2.3. Hybrid MSI techniques

More recently, properties of SEMAC and MAVRIC have been combined into hybrid MSI techniques, such as VS-3D-MSI [60], which is at the basis of MAVRIC-SL used in later publications [37], and MSVAT-SPACE [66]. In particular, the selectivity principle of SEMAC is combined with the smooth overlap between adjacent selections used in MAVRIC.

In spite of this smooth overlap, transitions between adjacent selections may still be visible in regions with extreme B_0 variations. These transitions may be emphasized by signal displacement, which may reduce the overlap in the frequency encoding direction [37]. Conversely, these signal displacements may also lead to excessive overlap between adjacent selections which results in blurring. Blurring may also result from the usage of VAT in these techniques.

VS-3D-MSI is much less sensitive to through-plane back-folding than SEMAC and MAVRIC, as demonstrated by the s-f_0 diagrams in Figure 3.5 (s-f_0 diagrams were introduced in section 2.3.4). In SEMAC, through-plane back-folding occurs where the slice distortion exceeds the phase-encoded extent of the sub-volume (Figure 3.5a) due to unexpectedly strong frequency deviations. MAVRIC suffers from back-folding if the spatial extent of the selected signal is larger than anticipated.

In VS-3D-MSI, neither very remote on-resonance signal nor nearby signal with very strong f_0 deviation is selected. To date, reports of through-plane back-folding artifacts in VS-3D-MSI have not been published. Theoretically, through-plane back-folding may only occur due to signal that is both remote and off-resonance. In clinical practice, such signal may originate from an additional implant at some distance from the imaged implant, e.g. in the contralateral hip or in a distant vertebra in spine imaging. Alternatively, if an implant is only partly covered by the scan –e.g. when a hip or a spine with a large longitudinally oriented implant is imaged in the axial plane–, the remainder of the implant may cause through-plane back-folding.

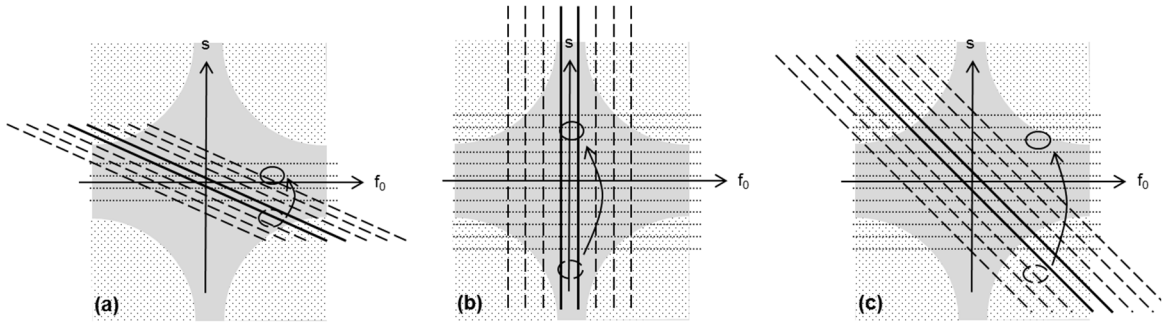

Figure 3.5: s-f_0 diagrams of SEMAC (a), MAVRIC (b) and hybrid techniques such as VS-3D-MSI (c). Sufficient through-plane phase encoding steps (dotted horizontal lines) are required to avoid through-plane back-folding artifacts (circles). Signal (shaded regions) may reside at substantial distance from the implant in the s direction where the f_0 deviation is limited, or nearer the implant with substantial f_0 deviation. In SEMAC, selected signal (solid and dashed lines) may result in back-folding of unexpectedly strong frequency deviations that lead to larger slice distortions than the phase encoded sub-volume. In MAVRIC, a larger anatomy or a larger receive coil sensitivity region than anticipated may lead to through-plane back-folding. VS-3D-MSI selects neither very remote on-resonance signal nor nearby signal with strong f_0 deviation. Therefore, the risk for through-plane back-folding is substantially reduced, and may result only from signal that is both outside the imaged volume and outside the anticipated frequency content (dotted regions).

3.2.4. Image combination algorithms

All MSI techniques result in sub-images that need to be combined into diagnostic images. SEMAC initially used linear complex summation while carefully adjusting the RF phases and/or receive phases [58]. The linear complex summation was later extended with an approach to denoise the data, based on singular value decomposition (SVD) and selection of data that represent meaningful signals [67]. In the initial publication, SEMAC sub-images were acquired with a boxcar selection profile [58], and combining them using this extended linear complex summation approach provided images with better homogeneity than was achieved using sum-of-squares, although sum-of-squares resulted in higher SNR [67].

MAVRIC sub-images were acquired using Gaussian-shaped profiles, and the combination of MAVRIC sub-images used a sum-of-squares algorithm from the initial publication onwards [59], for optimal homogeneity and SNR. Sub-images acquired using the hybrid technique have a mutual spectral overlap similar to those acquired using MAVRIC, and are also combined using sum-of-squares [60], to result in optimal homogeneity.

One inherent property of sum-of-squares image combination is that all phase information is lost. Though this may be a drawback of the algorithm when phase information is clinically relevant, e.g. in phase contrast imaging, the advantage is that any potential phase errors in the uncombined images will not lead to local dephasing artifacts or SNR loss (global dephasing) in the combined image.

In SEMAC, there is only partial spatial overlap between sub-volumes (Figure 3.3). And especially the most peripheral of the combined images have incomplete spectral coverage, as they are constituted of only a few sub-images that contain image information for that slice-location.

3.2.5. Residual artifact reduction

MSI techniques, as any other MRI technique that uses frequency encoding, suffer from signal displacements in the frequency encoding direction [37]. The signal displacements in the individual MSI sub-images may lead to blurring in the combined image. Signal displacements may also cause signal pile-up at slightly varying locations for the different MSI sub-images, which leads to signal fluctuations in the combined image (*ripple artifact*) [58,37]. Koch et al. proposed to generate a B_0-map from MAVRIC sub-images, and to use this B_0-map to compensate for these signal displacements using processing [64]. This processing technique shows a promising reduction of the signal displacement artifacts. Full correction using processing is impossible. An example limitation is that loss of resolution due to signal displacements, which occurs for extreme static local field gradients near metal, is not corrected by relocating the signal in processing. The B_0-map is best derived from the same data that will be corrected, in order to avoid differences due to patient motion between the B_0-map and the data to be corrected. Yet, this inherently implies that the B_0-map is compromised by the very same signal displacements that need to be corrected. For derivation of a B_0-map from MSI sub-images, the most suitable MSI acquisition technique is MAVRIC [64], where –contrary to SEMAC or hybrid techniques– sub-images correlate directly with a limited frequency band.

3.3. Other advanced techniques

3.3.1. Ultra-short echo-time techniques

Ultra-short echo-time (UTE) techniques use the free induction decay (FID) signal directly after RF excitation instead of refocusing the signal later to form an echo [68]. Echo-times as short as 50 µs are feasible, leaving little time for spin dephasing due to local field deviations, which is a beneficial property for imaging near metal.

UTE has been applied to improve image quality near metal implants of limited size [69,70,71]. A comparison between UTE and MSI for imaging near bulk metal implants has not yet been published.

As no time for phase encoding is available, UTE usually applies a 2D radial or 3D radial (*koosh-ball*) k-space trajectory, with frequency encoding in multiple directions. This leads to blurring and nearer the metal to signal displacement and pile-up. Between excitation and read-out, there is little to no time for T2 or T2* decay of the tissue signal. This allows evaluation of tissues with short T2, e.g. tendons and solid-state materials such as prosthesis cement, but leaves little contrast between the tissues, though RF prepulses may be used to introduce tissue contrast in UTE imaging [72,73].

3.3.2. Single-Point Imaging

A very rigorous way to deal with frequency encoding issues near metal is to completely eliminate the frequency encoding from the imaging sequence. Single-Point Imaging (SPI) acquires one sample at a fixed phase encoding time after excitation [74,75]. Localization of signal is achieved by phase encoding in all spatial directions. Ramos-Cabrer et al. presented the application of SPI for imaging near metal, which resulted in images completely free of

distortions caused by susceptibility effects [76]. Additionally, the absence of frequency encoding enables signal acquisition at very short echo-times, which may aid the visualization of tendons and potentially even solid-state materials. However, the use of phase encoding in all three directions severely increases the scan duration to more than an hour [76], and more investigations are needed to accelerate SPI substantially, before it may be useful in clinical practice.

3.3.3. Balanced steady state free precessing and phase cycling

Hoff et al. presented a reduction of susceptibility induced signal displacement [77,78] using an approach based on balanced steady state free precessing (b-SSFP) with phase cycling to suppress the banding artifacts associated with b-SSFP. The images using this approach show promising geometric accuracy. As T2* decay is only partially refocused in b-FFE [79], the technique does suffer from residual signal loss due to intra-voxel dephasing of spins. By repeating the acquisition with variable gradient shim settings and combining the images thus acquired [80], these signal voids may be reduced at the cost of substantially increased scan-time.

3.3.4. Image processing using gradient reversal acquisition

Image processing techniques to correct for susceptibility induced image distortions after acquisition have been a widely investigated topic especially for echo-planar imaging (EPI), where the signal displacements are much larger and may hinder tissue evaluation even without the presence of metal. Initially proposed as the “rectification” method for spin echo by Chang and Fitzpatrick [81], the gradient reversal approach utilizes two acquisitions with opposing polarity of the gradient in the direction of the susceptibility induced signal displacement. In either acquisition, the signal displacement is equal but in the opposite direction. The amount of signal integrated along the direction of the signal displacement remains equal for the two acquisitions, both for the entire images and more locally. This property may be used to correlate signals between both images. The distortion in both images may then be calculated, and the images may be corrected.

Correlating matching signals between both images is feasible as long as signals are stretched or compressed. However, when extreme local static gradients exceed the encoding gradient, excessive signal displacement leads to folding of some signal past other signal, and signal matching will fail.

The technique has been applied with success to image near metallic aneurysm clips [82]. But the approach may be less appropriate near bulk metal implants, where extreme local static gradients that approach or exceed the encoding gradient are commonly encountered.

4. Solution Requirements

4.1. Main clinical requirement

For usefulness and reliability of MRI in diagnosis, consistent and robust diagnostic image quality is essential. Image quality may be compromised by several external factors, including susceptibility effects induced by metal, as explained in section 2.1. Often, the implant surgery or the implant itself may be the cause of the soft tissue complications that need to be evaluated using MRI. And with aging population and many patients that are treated with metal implants, the need for diagnostic imaging near metal increases.

This work describes a prototype with the purpose to evaluate to what extent advanced acquisition techniques help to meet this need. The main clinical requirement of the prototype is therefore defined as:

Robust diagnostic MR image quality of soft tissue near metal implants.

4.2. Stakeholders and their focus

Robust diagnostic MR image quality of soft tissue near metal implants has multiple stakeholders, each with their own focus and interest.

Firstly, for the *patient*, it is obviously essential to receive accurate treatment if and to the extent possible. But preventing wrong or unnecessary treatment is similarly important, since any treatment involves risk. During the MRI examination itself, it is important to the patient that the MR sequences be safe in all aspects, including energy disposition (Specific Absorption Rate or SAR). The examination should be as comfortable as possible, which again sets limits to SAR, but also to nerve stimulation (Peripheral Nerve Stimulation or PNS), acoustic noise and scan duration.

For *radiologists*, robust diagnostic image quality without artifacts is essential to enable reliable soft tissue evaluation near the metal implant. For robust image quality without motion artifacts, scan duration needs to stay within comfortable limits for the patient to remain still. While the radiologist needs to have access to quality image information for the entire volume of interest, it is also important that no images with incomplete information are presented to the radiologist, to avoid confusion or frustration about useless images. In some parts of the world, legislation may even require the radiologist to review all presented image material, which puts an additional emphasis on the requirement that only images with complete and useful information are available.

The *MRI technologists* need to be able to comfortably operate the MRI scanner and its software. This includes sufficient ease of use to control any adaptations to MRI sequences, reconstructions or processing steps required to provide diagnostic image quality near metal. Reliability of both hardware and software is vital, and there must be no failures, crashes and scan aborts.

The *referring physician*, often the orthopedist, combines different sources of information for the diagnosis and for the decision on whether and how to treat or monitor the patient. Within the collection of available information, imaging is usually an important element. Reliable MR imaging of soft tissue may be crucial for the treatment decision, and may be required at moderate to short distance from the implant, as elaborated in section 4.3.1.

The improved treatment decision process may reduce the number of wrong or unnecessary treatments. While in first instance this reduction obviously benefits the *patient* physically, there is also a reputational as well as a financial benefit to the *hospital* in reducing the number of unnecessary treatments or required corrective treatments.

Next to the clinical professionals, the abovementioned cost reduction by avoiding wrong or unnecessary treatment is an important and immediate benefit for *health insurance* as well. More indirectly, if an accurate diagnosis leads to early treatment when the patient needs it, the patient may revalidate and return to the labor market quickly, which may translate into substantial further reduction of insurance cost. And reduction in health cost should eventually be beneficial to the entire *society* that pays insurance premium. In general, accurate healthcare contributes to a healthy and independent population.

With over a million joint replacements for hip and knee in the US only in 2010 [http://www.cdc.gov/nchs/fastats/inpatient-surgery.htm] and as musculoskeletal examinations are being performed on roughly half or more of all MRI scanners, the possibility to deliver technology for diagnostic MR imaging near metal is an important opportunity for the *healthcare industry*. To assess the value of this opportunity, the healthcare company needs a fully functional prototype to investigate whether and to what extent the clinical need can be met, as well as the assurance that this functionality will be a valuable market offering and thus provide the basis for a valid business case. Finally clear design and implementation recommendations are needed to enable the development department to build a usable and adequate product that meets the requirements.

Stakeholder		Focus
Patient		Accurate treatment
		Avoid wrong or unnecessary treatment
		Safety (SAR)
		Comfort (SAR/PNS/Acoustic noise/scan-time)
Clinical Professionals	Radiologists	Reliable soft tissue evaluation near implant
		Usability: only useful images
	MR technologists	Usability: ease of use, software stability, scan stability
	Referring physician	Treatment decision
	Hospital	Reputation & cost reduction: avoid wrong or unnecessary treatment
Health Insurance		Cost reduction: avoid wrong or unnecessary treatment
		Cost reduction: accurate treatment → healthy employee
Society		Cost reduction: avoid wrong or unnecessary treatment
		Healthy employee
		Healthy and independent population
Healthcare Industry		Valuable market offering
		Fully functional prototype
		Design & implementation instructions

Table 4.1: Stakeholders and their focus

4.3. Clinical requirements

As with any technology, for the functionality to be used, it must adequately address the needs of the user and the issues that the user is confronted with. It must fit the way of working of the MR technologist and the radiologist, and it must meet the purpose for which the functionality is meant. Therefore, it is important to start defining the requirements from the user's perspective. Especially the interests of the patient, of the clinical professionals and to some extent of healthcare industry (Table 4.1, second column) are essential considerations in defining these clinical requirements.

4.3.1. Artifact correction

For robust diagnostic MR image quality of soft tissue near metal implants, foremost, the artifacts associated with metal implants in MRI need to be removed as much as possible by appropriate correction techniques. This *correction* includes the correct position of signal, both in-plane and through-plane, as well as correct signal intensity and homogeneity. Better

artifact correction translates into a smaller distance from the implant where the image still has diagnostic quality.

As discussed in section 2.2, it is preferred to be able to see as close to the implant as possible. But the distance from the implant where diagnostic image quality is required depends on the disease of the patient examined. And for many indications, other modalities than MRI are more commonly used. Indications for which MRI is especially used include pseudotumors, edema, to some extent muscular atrophy and bone oncology. In the future, the value of utilizing MRI for osteolysis may increase.

The following sections describe the distance from the implant where diagnostic imaging is required for each of these diseases. The information about these distances is kindly provided by Stephan Vehmeijer (orthopedics) and Linda van Zeeland (radiology) at the Reinier de Graaf Groep, Delft, the Netherlands.

4.3.1.1. Pseudotumors

For pseudotumors (section 2.2.1), as for most diseases, size is an important but never the only criterion for the decision to treat a patient. Nonetheless, pseudotumors smaller than a centimeter are usually not problematic. And monitoring typically becomes important for pseudotumors of about a centimeter in diameter or larger. As the pseudotumor may be very close to the implant, diagnosis of a centimeter wide pseudotumor requires diagnostic imaging at about half a centimeter distance from the implant.

4.3.1.2. Effusion and Bone Marrow Edema

Fluid must be visible both in and around the joint. Especially bone marrow edema may be close to the implant, as the implant surgery itself could have caused the injury the led to the edema (section 2.2.2). In practice, it must be possible to determine whether a lesion of roughly one centimeter in diameter is edema or not, which requires diagnostic imaging at half a centimeter from the implant.

4.3.1.3. Bone oncology

Though bone oncology treatment typically is done only for tumors of two centimeters or wider, tumors of one centimeter must be visible. Bone tumors may be close the metal implant, and again diagnostic imaging at half a centimeter distance from the implant is required, to be able to image these small tumors near the implant (section 2.2.3).

4.3.1.4. Muscular atrophy

In many cases, muscular atrophy occurs at larger distance from the implant (section 2.2.4). Even so, structures associated with atrophy, such as fatty degeneration, must be visible at one or two centimeters distance from the implant.

4.3.1.5. Osteolysis and loosening

For osteolysis (section 2.2.5), the diagnosis is usually made on the combination of X-ray and CT, as these modalities are adequate and cost-effective and can currently image closer to the implant than MRI. However, MRI shows soft tissue contrast, and may play an important role in the future depending on the outcome of research investigations on soft tissue effects of

osteolysis and implant loosening. When pharmaceutical treatment proves to be effective, MRI will be important for monitoring.

Implant loosening may occur due to osteolysis of a zone of only 2 to 3 mm in the interface. Using MRI for diagnosis of these cases would require diagnostic image quality at 1 or 2 mm distance from the implant.

4.3.2. Applicability

The functionality needs to be *applicable* in the anatomical regions examined using MRI where patients most commonly carry implants. In first instance, the focus is mainly on hip, spine and knee, but application areas may extend to other orthopedic regions like shoulder and ankle, and eventually perhaps heart, brain, and abdomen.

Spatial resolution must be sufficient. The required resolution depends on the type of MRI examination. Especially for pseudotumors and osteolysis, high resolution is required, down to roughly a millimeter per pixel. For most clinical applications, a resolution of 1×1 mm in-plane and 4 mm through-plane is usually appropriate. Exceptions are more recent and advanced applications, such as high-resolution cartilage imaging, for which sub-millimeter resolution may be required. In many cases, cartilage is imaged in a region without metal implants, but in other cases, there may be implants nearby, such as ligament fixation screws, or unicompartmental knee arthroplasty. For the latter, high resolution metal artifact reduction techniques would enable assessment of the cartilage close to the metal. But these applications are considered exceptional and will therefore not be included in the intended use of the functionality.

The standard contrast weightings are to be available, including PDw, T1w, T2w, and fat suppressed PDw. For diagnosis of pseudotumors as well as fluid collections, the T2w and fat suppressed PDw contrasts are especially important, as these provide clear visibility of fluid and distinction between fluid and fatty tissue. For osteolysis, T1w and fat suppressed PDw contrasts complement each other.

4.3.3. Speed

Acquisition *speed* is important for the radiology department schedule as well as for the patients and consequently for image quality. Patients will only be able to remain still for a limited amount of time, and each acquisition needs to finish within that time to make sure that the image is free of motion artifacts. Typically, many patients seem to have difficulty remaining still after about ten minutes, and this is therefore considered the maximum scan duration per acquisition, while scan durations substantially shorter than ten minutes are preferred.

4.3.4. Usability

In first instance, proper usability of the functionality means that the scanner interface is easy to use by the MRI technologists. Another crucial aspect of usability is that the acquisitions run robustly without scan aborts, firstly because repeating the lengthy acquisition is not always possible and never desirable, and secondly to avoid frustration that could ultimately

lead to the functionality not being used anymore altogether. Finally, usability requires that only useful images be presented to the radiologist.

Aspect	**Requirement**
Artifact correction	Correct through-plane position of signal
	Correct in-plane position of signal
	Homogeneity / correct signal intensity
	Diagnostic image quality at: • 1 or 2 cm from the implant for muscular atrophy • 1 or 2 mm from the implant for osteolysis • 5 mm from the implant for pseudotumors, edema, effusion, and bone oncology
Applicability	Standard weightings available: T2w, STIR, T1w, PDw
	Sufficient resolution: 1×1 mm in-plane, 4 mm through-plane
	Applicable in hip, spine, knee
Speed	Acquisition ≤ 10 minutes
Usability	No scan aborts
	Only useful images

Table 4.2: Solution requirements from a user's perspective

5. Off-Resonance Suppression for Multi-Spectral Imaging near Metallic Implants*

5.1. Introduction

MR imaging is often the modality of choice to evaluate soft tissues, and with many patients treated with metal implants, there is a clear need for robust MR imaging near metal. Although certain implants are a contraindication for MR examination, many others are labeled MR safe or MR conditional, and for those the patient may in principle be allowed to undergo an MR examination. Resonance frequency offsets associated with metal implants can range from a few kHz (titanium) to well over 10 kHz (stainless steel). Associated image artifacts hamper soft tissue evaluation close to the implant. Displacement of signal in the readout direction [36] leads to in-plane geometric distortion, signal pile-up and signal voids. Slice selection distortion, sometimes referred to as "potato-chipping", translates to through-plane geometric distortion, which includes thickness variations that lead to signal intensity variations. Moreover, disjunct regions of signal may even arise that lead to particularly conspicuous bright edges in the image, due to the sudden thickness changes of the selected slice [21]. 3D imaging may seem advantageous, because it uses through-plane phase encoding which resolves distortion in slice direction. However, the slab selection gradients used are much weaker, which leads to even stronger distortions of the selected volume, requiring additional phase encoding steps in order to avoid aliasing. In addition, in a substantial part of the volume of interest, signal is not excited, leaving voids in the image. 3D imaging using spatially non-selective excitation suffers from signal voids where frequencies exceed the RF bandwidth. Any frequency encoding based technique is susceptible to read-out distortions [37].

For slice selection based techniques, View Angle Tilting (VAT, [57]) has been proposed as a time-efficient technique to correct for in-plane distortions in the frequency encoding direction. More recently, Multi-Spectral Imaging (MSI) techniques, instantiated by Slice Encoding for Metal Artifact Reduction (SEMAC) [58], Multi-Acquisition with Variable-Resonance Image Combination (MAVRIC) [59], and hybrid techniques such as Volume Selective 3D Multi-Spectral Imaging (VS-3D-MSI) [60] and MSVAT-SPACE [66], were introduced to correct for metal induced susceptibility artifacts at the cost of a significant

---

* Published as:
den Harder JC, Blume UA, van Yperen GH, Bos C. Off-resonance suppression for multispectral MR imaging near metallic implants. *Magn Reson Med 2014. doi: 10.1002/mrm.25126.*

and based on Patent Application:
den Harder JM, Bos C, Blume UA, inventors; Koninklijke Philips Electronics N.V., applicant. Restriction of the imaging region for MRI in an inhomogeneous magnetic field. European Patent Application EP2500742. September 19, 2012.

scan-time increase. These MSI techniques are based on Carr-Purcell-Meiboom-Gill (CPMG) spin echo train sequences. SEMAC extends a multi-slice spin-echo measurement with additional through-plane phase encoding to resolve slice selection distortion, and includes VAT to resolve in-plane distortion. A combination algorithm, for example sum-of-squares, is then used to combine sub-images with the same physical position that contain signal from different slice selections. MAVRIC repeats a spatially non-selective 3D acquisition with variable central RF frequencies during transmission and reception, and combines the resulting sub-images from different spectral bins into one image, after correcting the readout displacement for the known, and limited, frequency band of the excitation. As a spatially non-selective technique, MAVRIC may require many phase encoding steps to cover the entire region that contains signal, depending on the anatomy size and the sensitivity profile of the receive coil used. If signal is received from outside the phase encoded FOV, it will cause back-folding in through-plane direction.

SEMAC is selective in through-plane direction: the use of selection gradients ensures that signal within a given limited frequency range is only selected if it resides in a limited spatial area. Yet if stronger frequency deviations than anticipated are present outside the prescribed phase-encoded volume, it may result in back-folding artifacts.

In the present work, Off-Resonance Suppression (ORS) is presented as a technique that limits the spatial extent and/or the spectral range of selected signal, in a way that is predictably and purely determined by sequence parameters. The technique is applicable to VAT imaging, and can be used to provide well-defined spatial-spectral selectivity for SEMAC. The same concept can also be applied in the form of Outer-Region Suppression (also abbreviated to ORS) to provide well-defined spatial selectivity for MAVRIC. The feasibility of the technique is evaluated in phantom and volunteer experiments.

5.2. Theory

5.2.1. Off-Resonance Signal Distortion

In 2D Spin Echo (SE) and Turbo Spin Echo (TSE) imaging, during slice selection, spins are excited and refocused if they match the selection condition:

$$|\gamma \cdot \Delta s \cdot G_{SEL} + \gamma \cdot \Delta B_0(\vec{r})| < BW_{SEL}/2. \qquad (5.1)$$

Here Δs is the offset in slice direction from the intended slice center, and $\Delta B_0(\vec{r})$ is the field deviation at position $\vec{r}$ = (m,p,s). G_{SEL} is the selection gradient and BW_{SEL} is the bandwidth of the RF-pulse, which translates into G_{EX} and BW_{EX} for excitation and G_{REF} and BW_{REF} for refocusing. Spins with a B_0-offset that are distant from the intended slice position may match the selection condition, whereas off-resonance spins at the intended slice position may not, which leads to distortion of the selected slices. Slice distortions may also include thickness variations, where the field deviation reinforces or counteracts the selection gradient. In areas with strong field deviations, even disjunct regions of selected signal may occur [21].

From Eq. 5.1, it can be derived that in the center of the selection band, the slice distortion is given by:

$$\Delta s = -\Delta B_0(\vec{r})/G_{SEL}. \quad (5.2)$$

During readout, off-resonance signal is incorrectly frequency encoded, and is displaced by:

$$\Delta m = \Delta B_0(\vec{r})/G_{READ}. \quad (5.3)$$

Here, G_{READ} is the readout gradient. Since both slice distortion and displacement in readout direction are directly proportional to the B_0-offset, there is a fixed ratio between Δm and Δs. This ratio defines a projection angle θ describing the projection of off-resonance signal onto the imaging plane:

$$\theta = \tan^{-1}(\Delta m/\Delta s) = -\tan^{-1}(G_{SEL}/G_{READ}). \quad (5.4)$$

View Angle Tilting (VAT) aims to counteract the displacements in readout direction (Eq. 5.3) by applying the slice selection gradient during readout [57]. The tilted view angle β compensates the distortion angle θ and is defined by the ratio of the two simultaneously applied gradients:

$$\beta = \tan^{-1}(G_{VAT}/G_{READ}). \quad (5.5)$$

VAT has been associated with blurring. Kolind et al. [61] proposed to use a high read-out bandwidth to minimize this blurring by minimizing the tilt angle. Replaying the selection gradient causes a signal modulation in k-space that also leads to blurring, and solutions for this effect have been proposed and investigated by Butts et al. [62].

5.2.2. Off-Resonance Suppression

So far, in VAT imaging, the excitation gradient G_{EX} has always been chosen equal to the refocusing gradient G_{REF} [57,62]. In this case, the refocused slice may include signal with a strong frequency offset that originates from areas at a significant distance from the intended slice position (Figure 5.1a). VAT does nothing to correct the slice distortion artifacts. In order to achieve Off-Resonance Suppression [83] in VAT imaging, we intentionally choose different values for G_{EX} and G_{REF} (Figure 5.1b), thus limiting the spatial offset range for which excitation and refocusing overlap. In TSE acquisitions, this same technique is used to avoid interference from peripheral signals that could lead to ambiguity artifacts [55]. In case $G_{EX} > G_{REF}$, as illustrated, signal that is both excited and refocused tapers off with increasing frequency offset Δf_0. Equating the slice selection conditions for the lower frequency boundary of excitation and the upper frequency boundary of refocusing, defines a cutoff frequency $\Delta f_{0,max}$:

$$-\gamma G_{EX}\Delta s_{max} - \frac{BW_{EX}}{2} = -\gamma G_{REF}\Delta s_{max} + \frac{BW_{EX}}{2} \equiv \Delta f_{0,max} = \gamma \Delta B_{0,max}. \quad (5.6)$$

Here, Δs_{max} is the maximum distance from the intended slice center, where excitation and refocusing overlap, and signal is created. Solving Eq. 5.6 for Δs_{max} gives:

$$\Delta s_{max} = \frac{1}{2\gamma}\left(\frac{BW_{EX} + BW_{REF}}{|G_{EX} - G_{REF}|}\right). \quad (5.7)$$

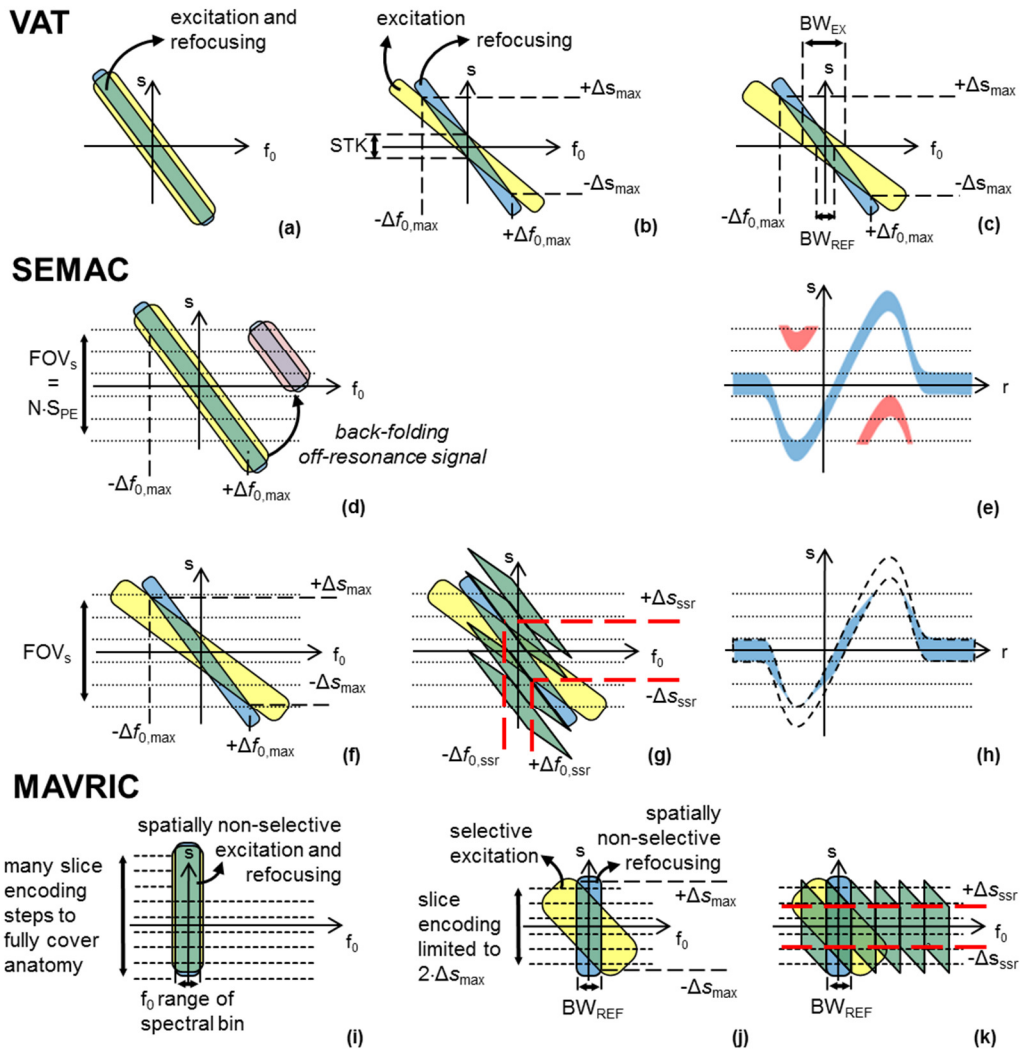

Figure 5.1: Conventional VAT uses equal gradients (a), whereas VAT with ORS uses different gradients for excitation (yellow) and refocusing (blue) (b). Pulse bandwidths determine the slice thickness (STK) for excitation and refocusing. With increased STK for either one, the slice profile is constant for a limited range of f_0 offsets (c).
SEMAC uses equal selection gradients (d). With strong frequency offsets, slice distortions may extend outside the phase encoded area FOV_s, resulting in back-folding (red) (e). ORS-SEMAC uses different gradients for excitation and refocusing (f). Depending on selection pulse bandwidths, the slice profile for limited f_0 offsets remains constant, leading to a smooth spatial response after image combination (g). Signal tapers off for increasing f_0 offset and is suppressed for strong slice distortions that would otherwise cause back-folding (h).
MAVRIC uses non-selective excitation and refocusing, and may require many slice encoding steps to fully cover the selected signal (i). ORS-MAVRIC uses a gradient during excitation, leading to a confined spatial extent of the spectral bin (j). The volume where the combination of multiple spectral bins leads to a smooth spectral response is dependent on gradient strengths and pulse bandwidths (k).

Inserting this expression for Δs_{max} in Eq. 5.6 gives us the cutoff frequency for any value of G_{EX} and G_{REF}:

$$\Delta f_{0,max} = \frac{1}{2}\left(\frac{BW_{EX}}{G_{EX}} + \frac{BW_{REF}}{G_{REF}}\right)\left(\left|\frac{1}{G_{EX}} - \frac{1}{G_{REF}}\right|\right)^{-1}. \qquad (5.8)$$

If we assume that the intended slice thickness STK is equal for excitation and refocusing, the expression for the cutoff frequency deviation simplifies to:

$$\Delta f_{0,max} = \gamma \cdot STK \left(\left| \frac{1}{G_{EX}} - \frac{1}{G_{REF}} \right| \right)^{-1}. \quad (5.9)$$

With unequal slice thickness for excitation and refocusing, there will be a small range of frequency offsets, where the smaller of the two slice thicknesses sets the limits on the response in the z-direction, and where, as a consequence, the thickness of the selected signal remains constant (Figure 5.1c). Typically, RF bandwidths are more easily increased for excitation in view of SAR limitations, but only to a limited extent depending on hardware capabilities.

5.2.3. Off-Resonance Suppression for Multi-Spectral Imaging

SEMAC [58] extends View Angle Tilting with additional through-plane phase encoding to resolve slice distortions up to:

$$|\Delta s| < \frac{N \cdot S_{PE}}{2} = FOV_z/2, \quad (5.10)$$

where N is the number of through-plane phase encoding steps, which can be defined during scan prescription, and S_{PE} the phase encoded image thickness (Figure 5.1d). SEMAC is selective in the z-direction [60] because the selection gradient limits the spatial area from which signal with a given frequency deviation may originate. Yet, if spins with larger frequency offset than anticipated are present and the slice distortion consequently exceeds the prescribed volume, signal is aliased in the through-plane direction (Figure 5.1e).

In ORS-SEMAC, similar to the application of ORS to VAT, off-resonance signal is suppressed by intentionally choosing different values for G_{EX} and G_{REF} [84]. This augments SEMAC with well-defined spatial-spectral selectivity, which is completely determined by sequence parameters and independent of the total frequency range induced by the implant. The distance of selected signal to the intended slice center is limited (Figure 5.1f) and given by Eq. 5.7. With Eq. 5.10, the condition to avoid back-folding is:

$$N > \frac{BW_{EX} + BW_{REF}}{\gamma \cdot S_{PE} |G_{EX} - G_{REF}|}. \quad (5.11)$$

The choice of RF pulse bandwidths and gradient strengths determines the range of field offsets for which the slice profile remains constant and homogeneous image combination is ensured. A smooth spatial response is obtained for field deviations up to $\Delta f_{0,ssr}$ and slice distortions up to Δs_{ssr} from the intended slice center (Figure 5.1g,h):

$$\Delta f_{0,ssr} = \frac{1}{2} \left(\frac{BW_{EX}}{G_{EX}} - \frac{BW_{REF}}{G_{REF}} \right) \left(\frac{1}{G_{EX}} - \frac{1}{G_{REF}} \right)^{-1}, \quad (5.12)$$

$$\Delta s_{ssr} = \frac{1}{2\gamma} \left(\frac{BW_{EX} - BW_{REF}}{G_{EX} - G_{REF}} \right). \quad (5.13)$$

For stronger frequency offsets and consequently larger slice distortions, the signal of individual selected slices tapers off. Firstly, this leads to lower signal intensity and gradually

compromises homogeneous image combination in these regions. Secondly, the tapering reduces the efficiency C to cover the spatial-spectral range of interest, which we may define as the area in s-f_0 space that is covered per unit time. The reduction in efficiency is given by:

$$\frac{\mathrm{C_{MSI}} - \mathrm{C_{ORS-MSI}}}{\mathrm{C_{MSI}}} = \frac{1}{2}\left(1 - \frac{\Delta s_{\mathrm{ssr}}}{\Delta s_{\mathrm{max}}}\right) = \frac{1}{2}\left(1 - \frac{|\mathrm{BW_{EX}} - \mathrm{BW_{REF}}|}{(\mathrm{BW_{EX}} + \mathrm{BW_{REF}})}\right). \quad (5.14)$$

The impact of the reduction of spatial-spectral coverage on the total signal in the final image depends on the actual spectral distribution of magnetization present. For example, signal is reduced significantly in case there is substantial off-resonance magnetization beyond Δs_{ssr}, but there is no signal reduction if all magnetization has a frequency between $-\Delta f_{0,\mathrm{ssr}}$ and $+\Delta f_{0,\mathrm{ssr}}$.

MAVRIC [59] is based on a spatially non-selective 3D acquisition. Depending on anatomy size and sensitivity of the RF coil used, many phase encoding steps may be required to fully cover the anatomy and avoid slice wrap (Figure 5.1i).

If we apply the same concept of Off-Resonance Suppression to MAVRIC and use a gradient during excitation, it is not the off-resonance signal but rather the signal from the peripheral regions that is suppressed (Figure 5.1j). In this way, Outer-Region Suppressed MAVRIC (ORS-MAVRIC) [85] adds spatial selectivity to MAVRIC. The gradient G_{EX} during an excitation pulse with bandwidth BW_{EX} in combination with non-selective refocusing pulses with bandwidth BW_{REF} results in selection of signal with maximum volume thickness equal to twice the maximum distance Δs_{max} from the volume center:

$$\Delta \mathrm{s_{max}} = \frac{\mathrm{BW_{EX}} + \mathrm{BW_{REF}}}{2\gamma \cdot |\mathrm{G_{EX}}|}. \quad (5.15)$$

In this case, the width of a single spectral bin remains limited by BW_{REF}, and within the selected volume, a smooth spectral response is obtained up to a distance Δs_{ssr} from the volume center (Figure 5.1k):

$$\Delta \mathrm{s_{ssr}} = \frac{\mathrm{BW_{EX}} - \mathrm{BW_{REF}}}{2\gamma \cdot |\mathrm{G_{EX}}|}. \quad (5.16)$$

For slices in the volume periphery, the spectral bins narrow and incomplete spectral coverage leads to signal loss and eventually inhomogeneous image combination. For a homogeneous spectral distribution of signal within the volume of interest up to $\pm\Delta s_{max}$, the total signal reduction by bin narrowing is given by Eq. 5.14.

Variations of ORS-MAVRIC are possible, where a gradient is applied during refocusing pulses or even during both excitation and refocusing pulses, with the gradients having different strength and/or opposite polarity. The region for which homogeneous image combination is obtained depends on gradient strengths and polarities and on RF pulse bandwidths (Figure 5.1j,k). Similar to ORS-SEMAC, the use of different gradients during excitation and refocusing in ORS-MAVRIC limits the spectral response to the intended spectral bin and provides well-defined spatial selectivity. As a consequence, the number of slice encodes needed is completely determined by sequence parameters and independent of the total frequency range induced by the implant, the anatomy size or the receive coil sensitivity profile. Similar

to MAVRIC, ORS-MAVRIC does not require VAT, which may cause blurring in the readout direction.

Interleaved acquisition of slices or spectral bins is possible, provided sufficient distance is kept between spectral bins to avoid saturation of signal in the adjacent bins. The conditions to avoid saturation of signal are explained in Figure 5.2. Selected regions are areas in s-f_0 space where excitation and refocusing of a spatial-spectral bin overlap. Spins within selected regions contribute to the image signal. Bin-to-bin interaction may occur in several ways, where excitation or refocusing of one bin overlaps with excitation or refocusing of another bin within the same package or concatenation. As all excitations use the same excitation gradient, the excitation bands remain mutually parallel in s-f_0 space. As long as adjacent excitation bands within the same package don't overlap, which can be achieved by dividing the acquisition into multiple packages, there is no interaction between excitations of different bins. Likewise, we can prevent overlap between refocusing bands within one package. The required spectral distance between bins within a package is determined by the maximum of both RF pulse bandwidths, taking a substantial margin into account for side-lobes and tails of the RF pulse profile. Scanning multiple packages may reduce scan-time efficiency for some contrasts and increase the risk that image quality is impacted by bulk motion.

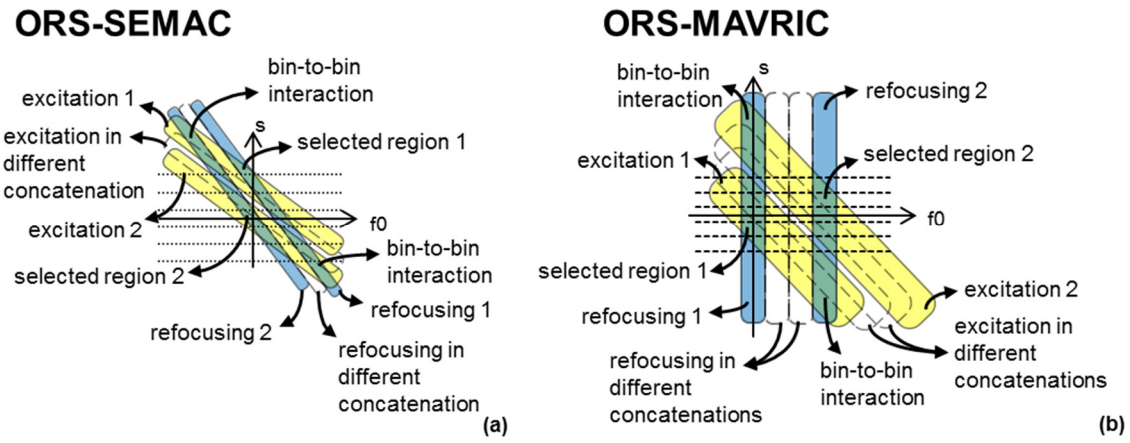

Figure 5.2: Selected regions and bin-to-bin interactions in ORS-SEMAC (a) and ORS-MAVRIC (b): selected regions are areas in s-f_0 space, where excitation (yellow) and refocusing (blue) of the same spectral bin –or echo train– overlap, and spins contribute to the image signal. Bin-to-bin interaction occurs in regions, where excitation of one bin overlaps with refocusing of another bin within the same concatenation or package. Yet, all excitation bands remain parallel in s-f_0 space, as they experience the same excitation gradient strength. Likewise, refocusing bands also remain parallel. Saturation of signal by bin-to-bin interaction occurs only if a selected region overlaps with excitation or refocusing of another bin within the same package. Therefore, as long as - within a single package- there is neither mutual overlap of excitation bands nor mutual overlap of refocusing bands, bin-to-bin interaction does not affect the selected regions. By taking the maximum of both RF pulses as minimal spectral distance between the bins, it is ensured, that all bin-to-bin interaction is outside the selected regions, and saturation will not affect them.

Finally, there are areas where excitation of one bin overlaps with refocusing of another bin. In these areas, magnetization is excited that has been affected by the refocusing pulses of other bins. However, this magnetization is not refocused during the current echo-train, and

does not contribute to the signal. In ORS-MAVRIC and ORS-SEMAC, there are no regions where refocusing overlaps with both excitation of the same spectral bin (selected region) and excitation of the adjacent spectral bin (bin-to-bin interaction), provided the minimal required spectral distance is maintained. So as long as the bin-to-bin interaction does not occur within a selected region, saturation is avoided.

5.3. Methods

VAT (with and without ORS), SEMAC, MAVRIC, ORS-SEMAC and ORS-MAVRIC were implemented on a 1.5T clinical MRI scanner and applied in phantom and volunteer experiments. Phantom setups included an Allopro titanium alloy (TiAlNb) hip replacement sample (Sulzer, Switzerland) and an Exeter stainless steel hip implant stem (Stryker, NJ, USA). To verify geometric imaging accuracy, each hip implant was placed on rectangular plastic Ampmodu Mod IV connectors (Tyco Electronics, PA, USA) in Gd-doped water. For smooth overlap between spectral bins, truncated and heavily windowed sinc pulses with Gaussian-like profiles were used for all RF selection pulses in all acquisitions [60]. Pulse bandwidths are specified as Full Width at Half Maximum (FWHM) in this work.

5.3.1. View Angle Tilting and Off-Resonance Suppression

Phantom experiments were performed on the titanium and stainless steel hip replacement samples. An 8-channel RF-coil was used to acquire coronal T1w datasets (TR = 570 ms / TE = 16 ms) with eighteen slices of 2-mm slice thickness, 0.5×0.9 mm in-plane resolution, and 220×170 mm FOV. Imaging time was 3'16". Image sets were acquired without VAT and with VAT at a view angle of 33°. In VAT imaging, ORS was first disabled, then enabled with $\Delta f_{0,max}$ = 4.2 kHz for weak ORS, using an RF bandwidth of 1.62 kHz and 1.25 kHz for excitation and refocusing, respectively. Finally, RF pulse bandwidths of 1.94 kHz and 0.77 kHz were used for strong ORS, with $\Delta f_{0,max}$ = 1.2 kHz. The readout bandwidth was 811 Hz/mm for all scans (the unit Hz/mm is used in this work for easy comparison of the read-out bandwidths between scans with different pixel-sizes). Through-plane distortion was measured from multi-planar reformats, directly below the implant in the rectangular plastic connectors, which were known to be straight.

Next, an otherwise healthy volunteer with stainless steel hip fixation screws was imaged without VAT, with VAT and with the combination of VAT and weak ORS. Here, an in-plane resolution of 0.7×1.0 mm was used.

5.3.2. ORS-SEMAC

The stainless steel hip replacement sample was used in phantom experiments where we acquired coronal T1w datasets (TR = 575 ms / TE = 24 ms) with 24 slices, 3-mm slice thickness, 0.8×0.8 mm in-plane resolution, and 221×173 mm FOV. ORS was disabled, as in standard SEMAC imaging, or enabled with $\Delta f_{0,max}$ = 5 kHz. In both cases, the read-out bandwidth was 888 Hz/mm. Signal was selected using RF bandwidths BW_{EX} = 2.03 kHz and BW_{REF} = 1.14 kHz. Similar to all other acquisitions described in this work, Gaussian-like RF pulse profiles were used, which is different from the boxcar profiles used originally in SEMAC [58]. Gaussian-like profiles provide a smoother overlap between adjacent slices [60].

However, this adaptation imposes stricter requirements on the slice interleaving scheme, and may be more susceptible to slice aliasing resulting from the side-lobes and tails of the RF pulses. Odd and even slices were measured in two separate packages, following the scheme 1, 5, 9, 13, … 3, 7, 11, … within each package. Nine slice phase encoding steps were used (Eq. 5.11) leading to an imaging time of 5'31". A standard TSE image with a read-out bandwidth of 811 Hz/mm was acquired for reference.

Furthermore, an otherwise healthy volunteer with ankle fixation plate and screws was scanned using an intermediate weighted SEMAC acquisition (TR = 2.4 s / TE = 30 ms) with 26 slices, 3-mm slice thickness, 0.6×0.75 mm in-plane resolution, and 173×216 mm FOV. The sequence was run without ORS and with ORS enabled at $\Delta f_{0,max}$ = 5 kHz. The read-out bandwidth was 897 Hz/mm in both cases. Selection pulse bandwidths were BW_{EX} = 2.03 kHz for excitation and BW_{REF} = 1.14 kHz for refocusing. Odd and even slices were measured in two packages, using the same slice order as described above for the phantom study.

5.3.3. ORS-MAVRIC

Again using the stainless steel hip implant, axial T1w images (TR = 525 ms / TE = 30 ms) were acquired with 27 slice encodes, 2.8-mm slice thickness, 160×80 mm FOV. An ORS-MAVRIC dataset was acquired in 3'13", with 31 spectral bins, each shifted by 830 Hz, using selection pulse bandwidths BW_{EX} = 3.29 kHz and BW_{REF} = 1.09 kHz. The scan was acquired in 4 packages of 8 spectral bins each. The in-plane resolution was 1.1×1.1 mm and the read-out bandwidth was 886 Hz/mm. With otherwise the same settings and bandwidths, non-selective MAVRIC images of the same volume were acquired for comparison as well as non-selective MAVRIC images of the entire object using 73 slice encodes in 8'37". To verify that interleaving the spectral bins did not cause saturation of signal in adjacent bins, the ORS-MAVRIC acquisition was repeated without interleaving, using 31 packages of a single spectral bin each.

Finally, an otherwise healthy volunteer with fixation screws in the femoral neck was imaged using non-selective MAVRIC and using ORS-MAVRIC. For both sequences, an axial view was acquired with 27 slice encodes and 200 mm×240 mm FOV, using 13 spectral bins, an echo train length of 33, an echo spacing of 5 ms, elliptical k-space filling, half-scan factor 0.7 and SENSE factor 2 for acceleration. The spectral bins in these acquisitions were not interleaved, but measured in separate packages. Scan-time was 4'12". In addition, a bilateral coronal view with 240 mm×420 mm FOV, SENSE factor 2.5 and otherwise the same scan settings was acquired in 5'39", using original MAVRIC as well as ORS-MAVRIC. A spin-echo based SENSE calibration scan with high bandwidth RF pulses was used to avoid T2* dephasing and minimize distortion. For reference, a multi-slice axial TSE acquisition, with 16 slices of 2.8 mm, was made with a read-out bandwidth of 891 Hz/mm.

5.4. Results

5.4.1. View Angle Tilting and Off-Resonance Suppression

Images acquired without VAT showed in-plane geometric distortion that improved when VAT was used (Figure 5.3). In VAT imaging, ORS with $\Delta f_{0,max}$ = 4.2 kHz clearly reduced bright

signals that were seen in standard VAT imaging (Figure 5.3c,g). With the titanium implant these could be completely suppressed. However, for the stronger setting of ORS with $\Delta f_{0,max}$ = 1.2 kHz, noticeable signal loss was observed (Figure 5.3d). The signal attenuation is attributed to the fact that the area in s-f_0 space where signal was selected tapered off as the frequency offset of the spins approached the cut-off frequency. For the stainless steel implant, ORS revealed structures initially obscured by off-resonance signals. Some signal loss was seen at $\Delta f_{0,max}$ = 4.2 kHz (Figure 5.3g), whereas $\Delta f_{0,max}$ = 1.2 kHz was clearly too narrow and caused large regions without signal (Figure 5.3h). Through-plane distortion was not resolved by VAT. The maximum through-plane distortion was found to be 7 mm for the titanium implant, and 30 mm for the stainless steel implant (reformats not shown).

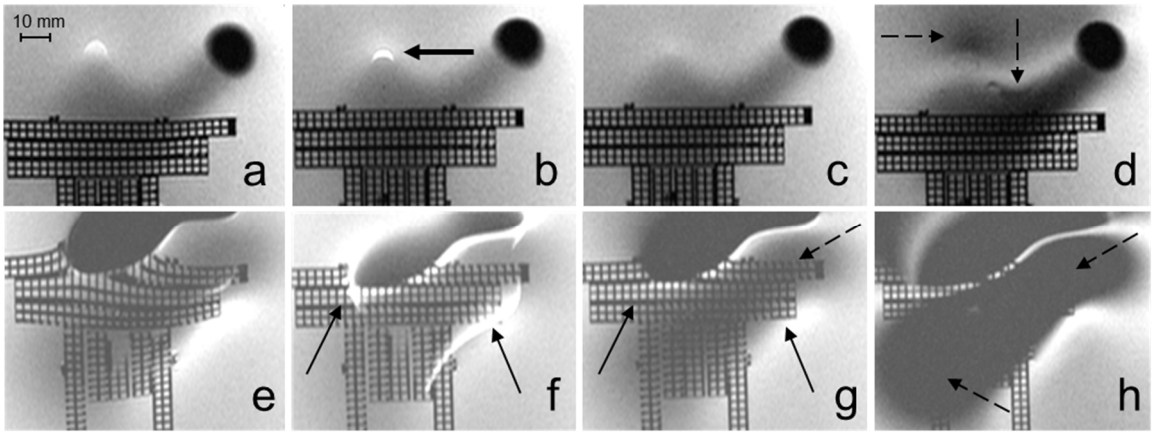

Figure 5.3: Images of titanium (top row) and stainless steel (bottom row) hip implants. High-bandwidth TSE without VAT (a,e), VAT without ORS (b,f), VAT with weak ORS (c,g) VAT with strong ORS (d,h). In-plane geometry was improved by VAT, as demonstrated by the connector strip phantom. ORS removed excessive bright signal (thick arrow) and revealed structures initially obscured by off-resonance signals (thin arrows), but also caused attenuation of useful signal (dashed arrows).

In the volunteer, VAT reduced geometrical distortion and bright signal overlaying the cartilage edge (Figure 5.4). Applying VAT with ORS further helped to suppress the unwanted bright streaks that were due to slice thickness variations in the femoral head.

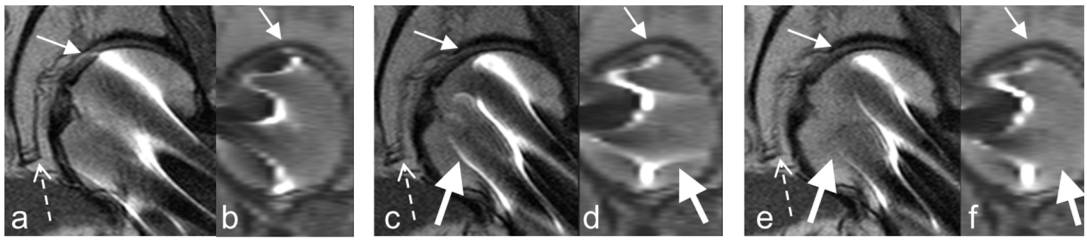

Figure 5.4: Details of coronal image of a hip with fixation screws, with sagittal reformats. Conventional high-bandwidth TSE without VAT (a,b), VAT without ORS (c,d) and VAT with ORS (e,f). The cartilage edge was overlaid by artifact in conventional TSE, but not so when using VAT (thin arrows). VAT caused blurring in some through-plane structures (dashed arrows). ORS helped to suppress unwanted streaks in the femoral head (thick arrows).

5.4.2. ORS-SEMAC

The strong in-plane distortion shown in standard TSE (Figure 5.5a) was nicely corrected by SEMAC (Figure 5.5b), as was apparent from the straight phantom structures. Although through-plane distortion was resolved to a large extent, off-resonance signal from near the implant showed brightly in regions with phantom fluid only (Figure 5.5b,d), and signal from the phantom structure was aliased to other slices 27 mm more anteriorly (Figure 5.5c,h). ORS-SEMAC reduced aliasing in slice direction (Figure 5.5e,f,g,i). Using standard SEMAC, resolving the complete frequency band of ±12 kHz would have required 19 slice phase encoding steps, thus doubling the required scan-time. The strong field deviations close to the stainless steel implant caused discontinuities between slices, which resulted in signal fluctuations (Figure 5.5c). In the ORS-SEMAC image combination, these discontinuities became more pronounced (Figure 5.5f), as a manifestation of narrowing overlap of excitation and refocusing. In ORS-SEMAC, attenuation of signal was observed where the frequency offset of the signal approached the cut-off frequency (Figure 5.5e,f).

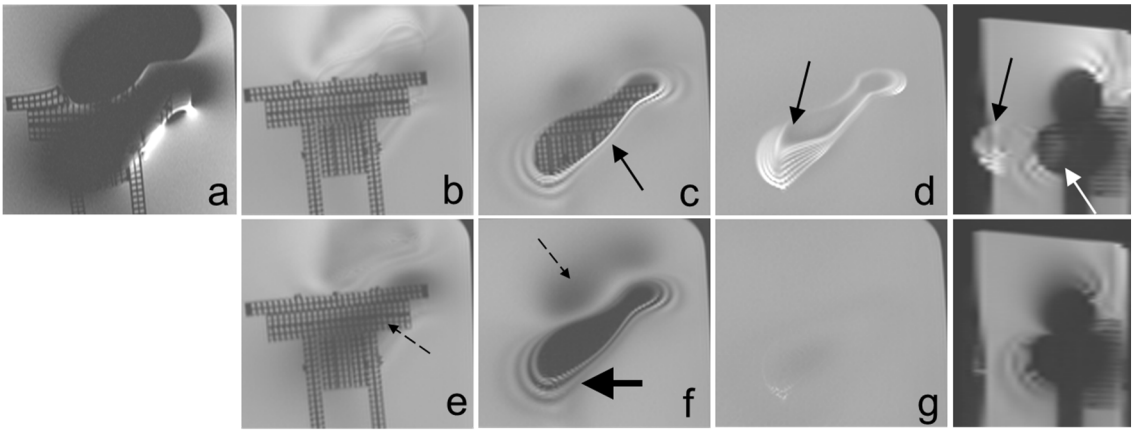

Figure 5.5: Images of a stainless steel hip implant. High-bandwidth TSE (a), original SEMAC (b,c,d), ORS-SEMAC (e,f,g) and reformats of original SEMAC (h) and ORS-SEMAC (i). Geometric distortion was corrected by SEMAC, as can be seen from the connector strips. Signal that was back-folded in through-plane direction in original SEMAC (c,d) was almost completely suppressed in ORS-SEMAC (f,g) (thin arrows). In regions with strong field deviations, close to the implant, signal was attenuated (e,f, dashed arrows), slice profiles became narrower, and the visibility of individual slices and their transitions became more pronounced (f, thick arrow) than in original SEMAC.

In the volunteer, frequency content was measured to exceed ±10 kHz (data not shown). In original SEMAC, several cases of back-folded off-resonance signal were seen. For example, signal adjacent to a fixation screw in the tibia was displaced to the level of another fixation screw at again 27 mm distance (Figure 5.6a,b,c). This signal was suppressed by using ORS-SEMAC, though some suppression of signal from the bone marrow was also observed locally (Figure 5.6d,e,f).

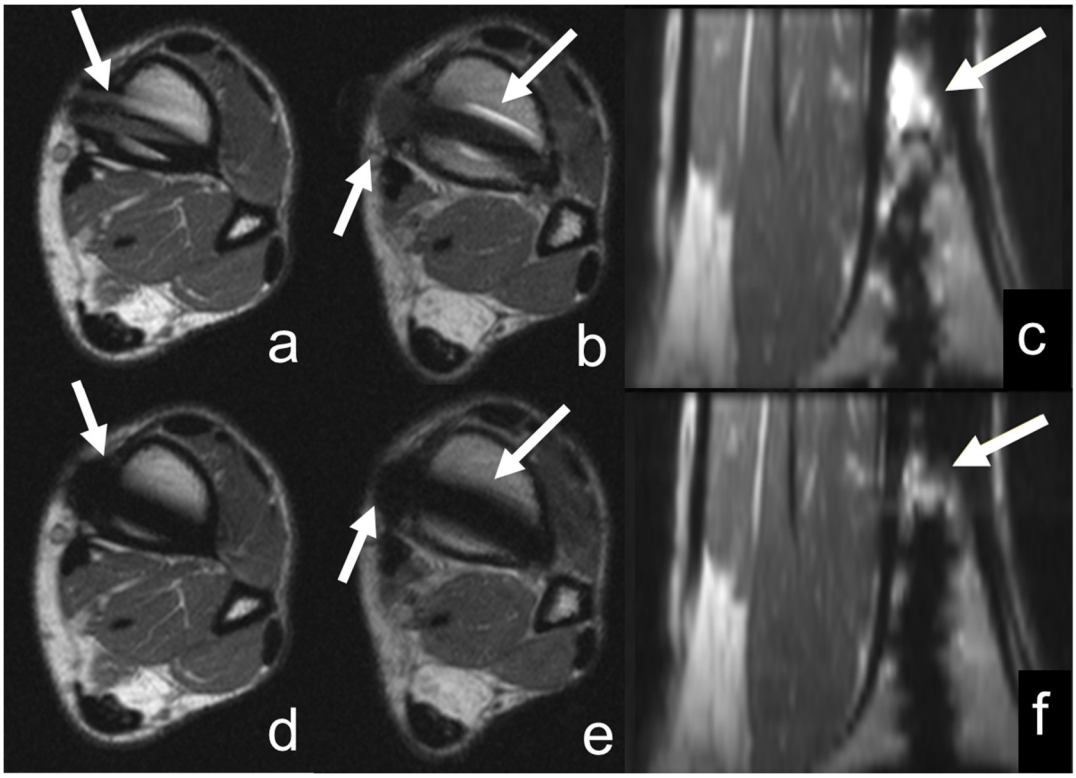

Figure 5.6: Ankle with fixation plate and screws. Axial SEMAC (a,b), ORS-SEMAC (d,e) and corresponding sagittal reformats (c,f). Back-folded off-resonance signal was suppressed in ORS-SEMAC by using ORS, though at the cost of local signal reduction in the bone (arrows).

5.4.3. ORS-MAVRIC

In the phantom experiments, ORS-MAVRIC was similarly effective at reducing metal artifact as the standard MAVRIC sequence (Figure 5.7). Yet, the coverage and corresponding scan duration were substantially reduced (cf. Figure 5.7a,d, and Figure 5.7c,f). Using standard MAVRIC, reducing the coverage resulted in severe slice wrap artifacts that were absent in the ORS-MAVRIC images (cf. Figure 5.7b,e and Figure 5.7c,f). Both MAVRIC and ORS-MAVRIC showed intensity variation artifacts, which potentially resulted from B1 effects close to the stainless steel implant, and from effects of extreme local field gradients [37]. We found no noticeable differences between the ORS-MAVRIC acquisition without spectral bin interleaving (Figure 5.8a,c) and the interleaved acquisition (Figure 5.8b,d).

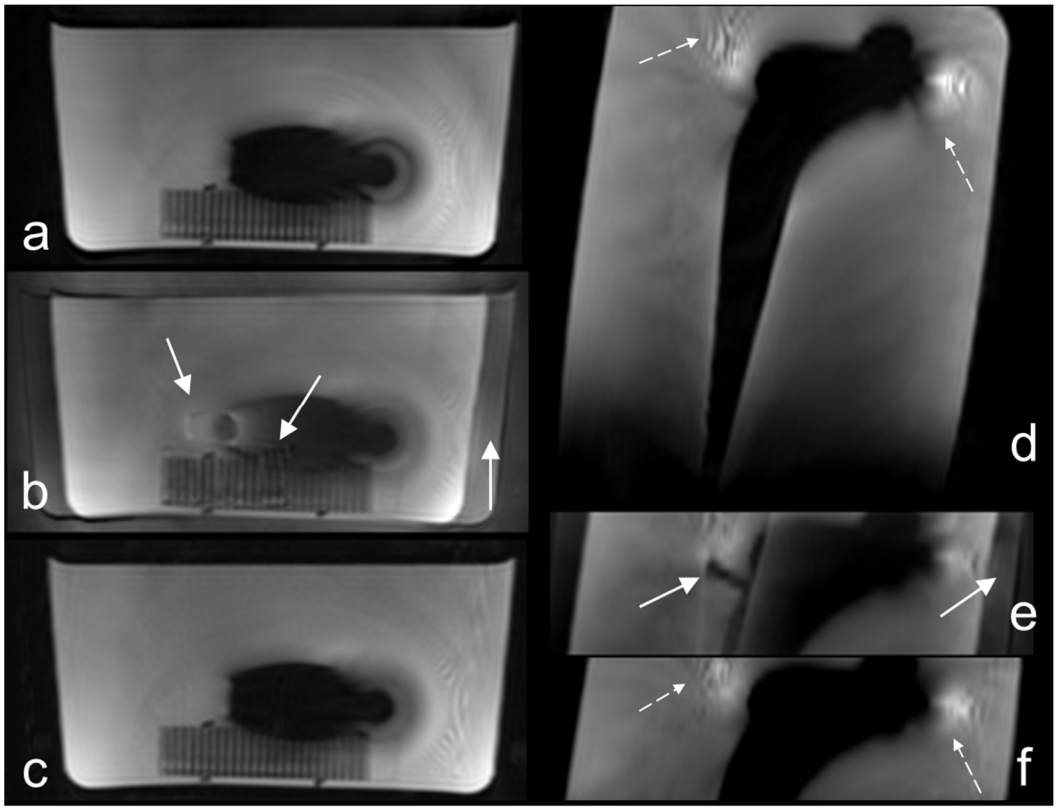

Figure 5.7: Axial scans (left) and coronal reformats (right) of a stainless steel hip implant. MAVRIC with full coverage (a,d), MAVRIC with limited coverage (b,e), ORS-MAVRIC (c,f). MAVRIC (a,d) and ORS-MAVRIC (c,f) were similarly effective at reducing metal artifact. ORS-MAVRIC allowed acquisition with a substantially reduced coverage, and correspondingly shorter scan-time. Using standard MAVRIC, the same reduced coverage led to severe slice wrap (b,e, arrows). The intensity variation artifacts, visible in both MAVRIC and ORS-MAVRIC, potentially resulted from B1 effects close to the stainless steel implant and from effects of extreme local field gradients [37] (dashed arrows).

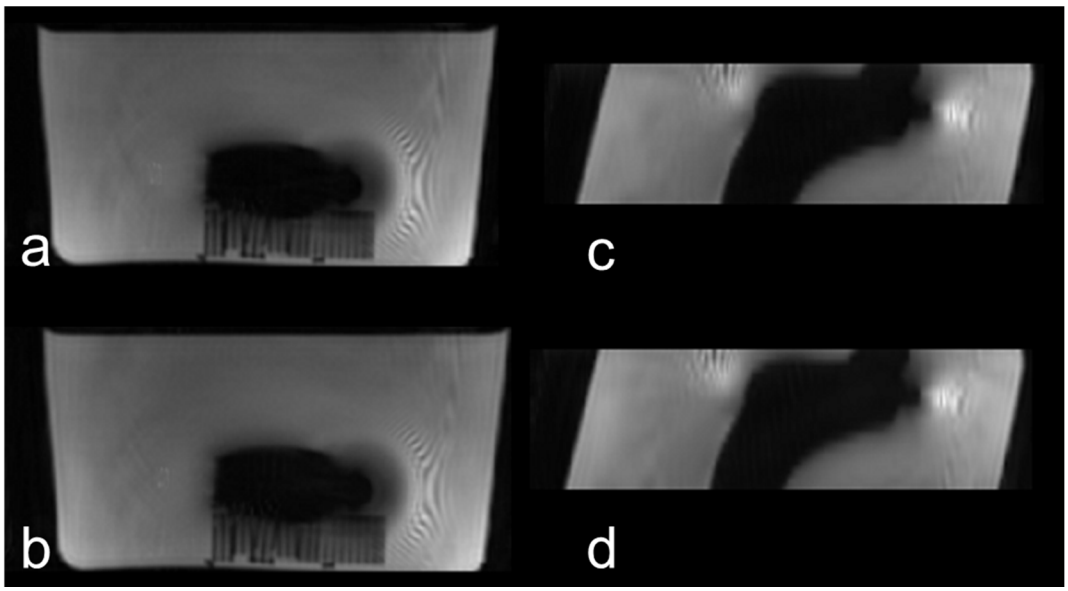

Figure 5.8: Axial scans and coronal reformats of a stainless steel hip implant using ORS-MAVRIC without spectral bin interleaving (a, reformat c) and ORS-MAVRIC with spectral bin interleaving (b, reformat d). No noticeable differences were found between the two acquisition schemes.

The in-vivo images of the hip show that the strong in-plane distortions and signal pile-up in standard TSE (Figure 5.9a,d) were corrected by non-selective MAVRIC (Figure 5.9b,e) and ORS-MAVRIC (Figure 5.9c,f). However, the axial non-selective MAVRIC was substantially compromised by back-folded signal from the leg (Figure 5.9b,e) which was absent in the ORS-MAVRIC images (Figure 5.9c,f). In the bilateral hip acquisition, ORS-MAVRIC showed bone tissue information close to the implants, without back-folding artifacts (Figure 5.9h), while the same acquisition using standard MAVRIC resulted in severe through-plane back-folding artifacts (Figure 5.9g).

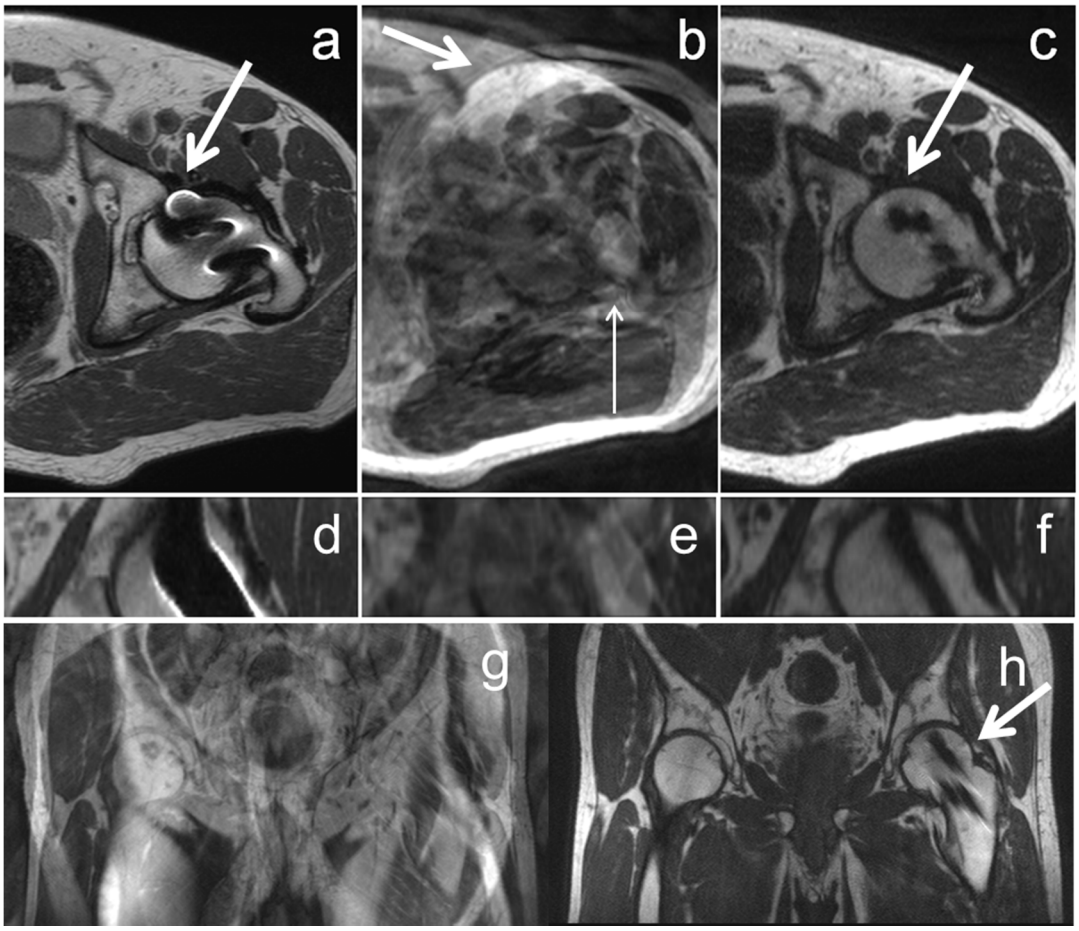

Figure 5.9: Axial scans (top row) and coronal oblique reformats (center row) of a hip with fixation screws, acquired with conventional TSE (a,d), MAVRIC (b,e), and ORS-MAVRIC (c,f). In conventional TSE, geometric distortion caused signal voids and bright signal streaks near the fixation screws (a, arrow), which was corrected by ORS-MAVRIC (c, arrow), providing anatomic information much closer to the implants. Original MAVRIC suffered from aliased signal from the leg, recognizable by the subcutaneous fat (b, arrow) and the femur (b, thin arrow). A non-angulated bilateral coronal T1w acquisition of the hips using MAVRIC (g) showed severe through-plane back-folding whereas the same acquisition using ORS-MAVRIC showed bone tissue information close to the implants, without back-folding artifacts (h).

5.5. Discussion

In this chapter, Off-Resonance Suppression was demonstrated to provide well-defined spatial and spectral selectivity of MRI signal, which facilitates reduction of artifacts in areas

with strong main field variations. The presented technique can be applied to improve imaging near metal implants.

As reported by the AAOS, 327,000 total hip replacement procedures and 676,000 total knee replacements were carried out in 2009 in the US only [http://www.cdc.gov/nchs/fastats/insurg.htm]. Especially for metal-on-metal hip implants, evaluation of soft tissue in the vicinity of the metal implant is important for signaling complications such as pseudotumors [46], which may lead to revision of the implant. Additional applications of metal artifact reduction include imaging of the neural foramina and delineation of implants in the spine [12] as well as imaging of the bone-component interface in the knee [86].

Susceptibility effects related to metal implants in MRI may cause artifacts that seriously hamper diagnosis. In routine practice today, these metal artifacts may be limited by using high-bandwidth TSE sequences [54], but significant artifacts remain.

The combination of VAT and ORS can be used for implants that cause moderate field disturbances, to reduce the extent of metal artifacts at high resolution without time penalty, while using thin slices and high readout bandwidth to minimize blurring [61,62]. The ORS cutoff frequency $\Delta f_{0,max}$ provides a trade-off between artifact suppression and inclusion of useful off-resonance signal. MSI techniques especially hold potential for implants that lead to a broad frequency range, e.g. stainless steel. The range of main field variations depends strongly on the material and size of the implant, and is often unknown at the start of an MR examination. The acquisition of an additional distortion scout has been proposed by Hargreaves et al [87] as an approach to determine the full signal spectrum. ORS-MSI techniques confine selected signal to a well-defined spatial area and spectral coverage, purely determined by sequence parameters. Thus, ORS-MSI provides a tunable trade-off between scan-time and signal proximity to the implant, and avoids through-plane back-folding.

In ORS-SEMAC, suppression of distant off-resonance signal may compromise homogeneity and lead to signal voids. To some extent, suppression of local off-resonance signal also occurs, due to incomplete spectral coverage. But these signal losses may well be less confusing than superposition of signal from another slice location.

ORS-MAVRIC allows acquisition of a limited encoded volume, independent on the size of the anatomy or the sensitivity of the receive RF coil used. In a recent paper by Hayter et al., non-selective MAVRIC of the hip was evaluated using acquisitions of up to 11 minutes [88], indicating that ORS-MAVRIC can indeed reduce the required time for acquisition, and can be particularly useful for evaluating large anatomies such as the hip and the spine in clinically feasible imaging times. Especially the possibility to perform examinations in the axial orientation may be valuable: although MAVRIC is based on 3D acquisition, it is hardly ever acquired using isotropic voxels, limiting the possibilities for multi-planar reformatting.

As opposed to VS-3D-MSI, ORS-MAVRIC doesn’t require VAT, and thus may reduce blurring in the read-out direction. It has not yet been demonstrated, however, that the use of VAT

imposes limitations on the resolution in VS-3D-MSI, and more investigations are needed to determine if a selective MSI technique without VAT has additional benefits.

So far, multi-spectral acquisitions have been limited in resolution, partly by restrictions on scan-times to what is clinically acceptable. Therefore, it can be expected that clinical examinations will consist of a combination of a number of conventional high-bandwidth TSE acquisitions and one or two multi-spectral scans. ORS-MSI enables scan-time reductions similar to those achieved using parallel imaging [89]. Further acceleration of ORS-MSI is possible by applying parallel imaging [26,27,28] and/or compressed sensing [90]. ORS-MAVRIC can be accelerated by using interleaved acquisition of the spectral bins, taking into account the required bin spacing to avoid signal suppression by cross-talk. When SNR allows, scan-time reduction can be traded for improvement of in-plane image resolution.

There are limitations to the techniques and the study presented in this chapter. The study presented here focuses on demonstration of the feasibility of the proposed techniques. Clinical applicability of the ORS-MSI techniques proposed here needs to be proven in future patient studies, of which early results have recently become available [10].

With respect to the technical limitations, we observe that significant scan-time reductions are achievable where SNR allows, but maintaining a sufficient amount of phase encoding steps is vital to avoid issues such as ringing artifacts which may be especially confusing in through-plane direction. While the proposed techniques reduce B_0 induced artifacts, B1 issues are not addressed. As with original MSI, residual pile-up artifacts in read-out direction and signal loss [91] remain in ORS-MSI where strong local gradients compromise the frequency encoding process. In ORS-MSI, the efficiency to cover the spatial-spectral range of interest is reduced. Hence, for strong slice distortions in ORS-SEMAC, signal of the individual selected slices tapers off, and homogeneity of combined images is further compromised, as off-resonance signal may or may not be selected, depending on its position. Especially close to the implant, this may lead to more pronounced signal fluctuation due to discontinuities between selected slices. In the experiments described here, these discontinuities may also have been impacted by the Gaussian-like RF profile used for SEMAC and ORS-SEMAC. In ORS-MAVRIC, such compromised homogeneity occurs in the peripheral region of the selected volume and the implementation can be modified to only produce the images with optimal bin combination. This modification clearly affects scan-time efficiency, and for the cases shown in this work, 17 out of 27 acquired slices (63%) were used to produce actual images. This reduction in scan-time efficiency is not applicable to VS-3D-MSI, where homogeneity is not compromised by signal tapering off. However, ORS-MAVRIC enables selection of a region that may be smaller than the implant, and allows arbitrary orientation of the selected region.

In conclusion, spectral and spatial selection in multi-spectral imaging can contribute to imaging near metal in clinically feasible times. It provides freedom of slice positioning and orientation, as well as a trade-off mechanism between coverage and acquisition time, while predictably avoiding back-folding artifacts, independently of anatomy size, receive coil sensitivity profile, or induced frequency range.

6. Ripple Artifact Reduction using Slice Overlap in SEMAC*

6.1. Introduction

MRI is often the preferred modality to evaluate soft tissue, and with many patients carrying metal implants, there is a clear need for distortion-free MRI near metal. Susceptibility effects related to the presence of metal include geometric distortions, signal pile-ups and signal voids [36]. Multi-Spectral Imaging (MSI) techniques have been shown to significantly reduce susceptibility artifacts. Slice Encoding for Metal Artifact Correction (SEMAC) [58] extends a multi-slice spin-echo measurement with additional through-plane phase encoding to resolve slice distortion, and includes View Angle Tilting (VAT) [57] to resolve distortion in the frequency encoding direction. VAT has been associated with blurring, especially when the read-out duration exceeds the excitation duration [62]. Multi-Acquisition with Variable-Resonance Image Combination (MAVRIC) [59] repeats a spatially non-selective 3D acquisition with variable central RF frequency during transmission and reception, and combines the resulting sub-images from different spectral bins into one image. Hybrid techniques, like Volume Selective 3D Multi-Spectral Imaging (VS-3D-MSI) [60] and MSVAT-SPACE [66] use a volume selection gradient to provide 3D MSI with spatial selectivity. From the initial publications onwards [59,60], MAVRIC and VS-3D-MSI have used a strong overlap between spectral bins to ensure homogeneous image combination.

Residual intensity fluctuations in MSI, referred to as *pile-up artifact* [64], or *ripple artifact* [58,37], have been attributed to limitations of the frequency encoding process [64]. A systematic analysis of the effects of susceptibility gradients in the frequency encoding direction was recently published by Koch et al. [37]. For SEMAC, an additional effect of discontinuities between selected slices has been suggested [92].

In this chapter, we present an investigation of the ripple artifact in SEMAC and analyze the effect of the combination of in- and through-plane field gradients. Because SEMAC uses gradient selection of slices on the order of the through-plane resolution, special attention is given to resolution effects, which were studied in two-dimensional time domain simulations. As a potential solution, we then propose slice overlap, in analogy to spectral bin overlap in

---

* Published as:
den Harder JC, Blume UA, van Yperen GH, Bos C. Ripple Artifact Reduction Using Slice Overlap in Slice Encoding for Metal Artifact Correction. Magn Reson Med 2014. doi: 10.1002/mrm.25127.

and based on Patent Application:
Jurrissen MPJ, den Harder JM, Blume UA, de Weerdt E, van IJperen GH, inventors; Koninklijke Philips Electronics N.V., applicant. Metal resistant MR imaging. International Patent Application WO2014115043. July 31, 2014.

MAVRIC, to reduce the ripple artifact in SEMAC. Its efficacy was evaluated in simulations and validated in phantom experiments.

6.2. Theory

Ideally, SEMAC would completely resolve in-plane distortions by using VAT, and slice distortions by through-plane phase encoding. However, susceptibility induced field gradients compromise the frequency encoding process [64] as is illustrated for SEMAC in Figure 6.1: in regions where B_0 varies in-plane, slice selections traverse the image sections (Figure 6.1a). Still, adjacent selections remain spectrally and spatially contiguous, which would lead to homogeneous imaging results. The selection of multiple adjacent slices remains contiguous, even if B_0 varies through-plane (Figure 6.1c), and slice profiles are stretched or compressed in the slice direction.

By frequency encoding with VAT, magnetization from a physical position (m,s) is mapped to an imaged position (m',s), where m' is given by:

$$m' = m + \frac{\Delta B_0(m,s) + (s - s_{ISC})G_{VAT}}{G_{READ}}, \qquad (6.1)$$

with G_{READ} the read-out gradient, $\Delta B_0(m,s)$ the main field deviation, and G_{VAT} the VAT gradient, which is usually equal to the selection gradient G_{SEL}. Here, s_{ISC} is the intended slice center position, which also determines the demodulation frequency during signal reception. Signal is displaced in the frequency encoding direction due to resonance frequency deviation of the spins. At the slice center, the VAT gradient completely compensates this displacement, but at the slice boundaries a residual displacement remains, resulting in shear distortion of the voxels (Figure 6.1b,d).

If B_0 only varies through-plane ($dB_0/dm = 0$, $dB_0/ds \neq 0$), all slices remain parallel to the imaging sections and leave no in-plane intensity fluctuations. Where B_0 varies in the read-out direction ($dB_0/dm \neq 0$), however, signal displacements in the read-out direction lead to voxel shear which compresses or dilates imaged slice profiles in the m',s-frame (Figure 6.1b).

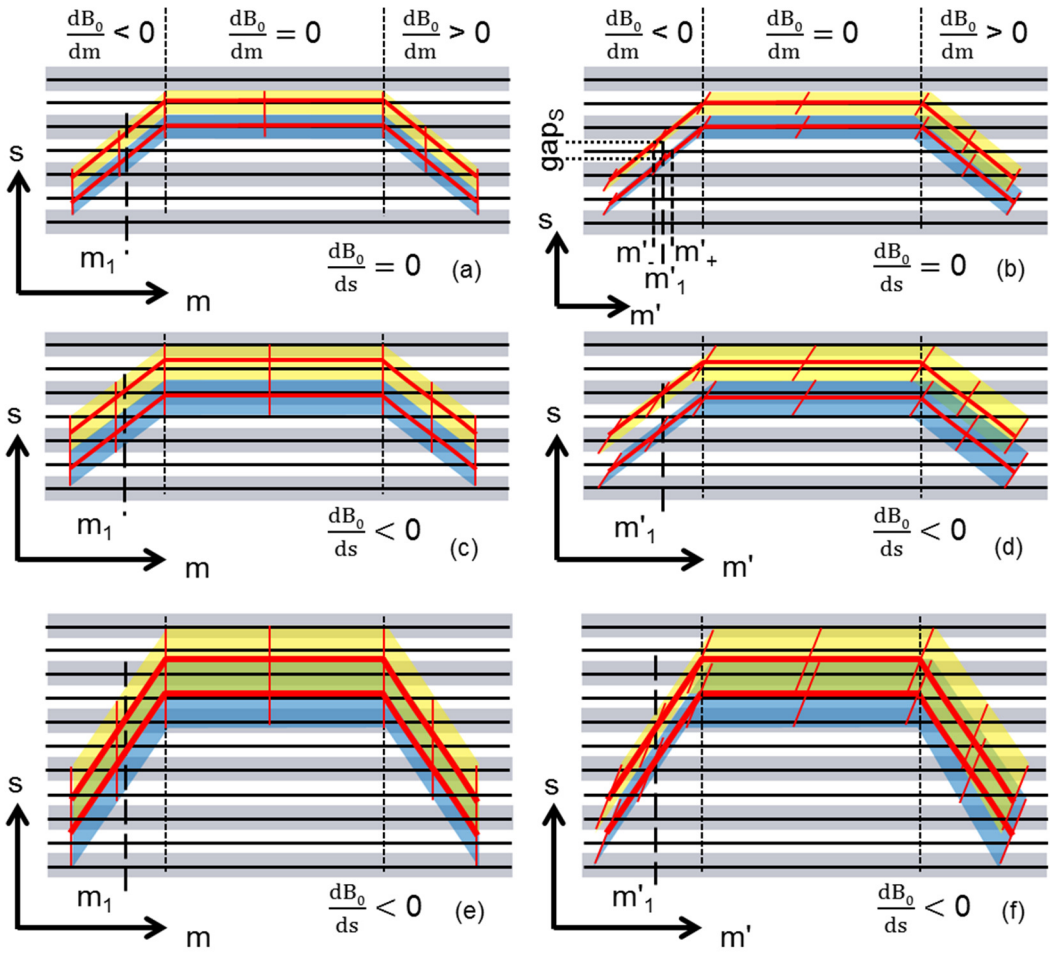

Figure 6.1: Geometrical description of SEMAC experiment showing two adjacent slice selections (yellow/blue). Thick red lines indicate slice selection centers, thin red lines indicate positions of constant m. Sections are indicated by grey and white bars with black centerlines.
Selected slices are shown for the case that B_0 varies only in read-out, m (a), or both in read-out and slice, s direction (c). Slices are transformed into their imaged equivalents in the m',s frame (b,d). B_0 deviations cause displacement of signal in the frequency encoding direction, Eq. 6.1. VAT compensates for these displacements accurately in the slice center, but leaves residual displacements at the slice boundaries (m'_+, m'_-).
In case B_0 varies in the m direction, regions without signal (gaps) become apparent between compressed slices in the m',s frame (b). Yet, as $dB_0/ds = 0$, the distance between slice centers remains equal to the section thickness. Therefore, a slice may distort out of a section, e.g. at m'_1, yet the adjacent slice will simultaneously distort into the same section, such that a nearly constant signal is obtained within that section, originating either from a single slice, or from the lower part of the upper slice plus the upper part of the lower slice, which adds up to the same amount of signal.
It is only when B_0 varies both in the m and s direction, that the distance between imaged slice centers in the through-plane direction is wider than the section thickness, and the slice transition can be resolved (d). Several of these transitions between selected slices lead to a signal variation that is perceived as the ripple artifact.
Slice overlap, in the demonstrated example created by using a decreased selection gradient strength (e), avoids these regions without signal in the m',s frame (f).

In this frame, regions without signal appear between the compressed slice profiles. The size of a gap in the read-out direction is:

$$\begin{aligned} \mathrm{gap_m} &\equiv \mathrm{m'_+} - \mathrm{m'_-} \\ &= \frac{\Delta B_0(m,s) + \frac{STK_{EFF}}{2}\cdot G_{VAT}}{G_{READ}} - \frac{\Delta B_0(m,s) - \frac{STK_{EFF}}{2}\cdot G_{VAT}}{G_{READ}} \\ &= STK_{EFF}\cdot\frac{G_{VAT}}{G_{READ}} = STK_{EFF}\cdot\frac{G_{SEL}}{G_{READ}}, \end{aligned} \qquad (6.2)$$

with m'_+ and m'_- the signal displacement at the upper and lower boundary of a slice, respectively, and STK_{EFF} the effective slice selection thickness. In SEMAC, the nominal selection thickness STK_N usually equals the section thickness. In regions where $dB_0/ds \neq 0$, STK_{EFF} differs from STK_N and is given by:

$$STK_{EFF} = \frac{BW_{SEL}}{\gamma\left(dB_0/ds + G_{SEL}\right)} = STK_N\cdot\frac{G_{SEL}}{\left(dB_0/ds + G_{SEL}\right)}, \qquad (6.3)$$

with BW_{SEL} the selection bandwidth and γ the gyromagnetic ratio. In SEMAC, which uses closely aligned adjacent selections [58], STK_{EFF} also equals the distance between slice centers. During slice selection with the gradient G_{SEL} active, ΔB_0 is constant at the selection boundary. Therefore:

$$\Delta B_0(m+dm, s+ds) - \Delta B_0(m,s) = \left(\frac{dB_0}{dm}\right)dm + \left(\frac{dB_0}{ds} + G_{SEL}\right)ds = 0, \qquad (6.4)$$

or:

$$\frac{ds}{dm} = -\frac{\left(dB_0/dm\right)}{\left(dB_0/ds + G_{SEL}\right)}. \qquad (6.5)$$

The gap in the through-plane direction is proportional to gap_m:

$$\begin{aligned} \mathrm{gap_s} &= \mathrm{gap_m}\cdot\frac{ds}{dm} = -STK_{EFF}\cdot\frac{G_{SEL}}{G_{READ}}\cdot\frac{\left(dB_0/dm\right)}{\left(dB_0/ds + G_{SEL}\right)} \\ &= -STK_N\cdot\frac{\left(dB_0/dm\right)}{G_{READ}}\cdot\left(\frac{G_{SEL}}{dB_0/ds + G_{SEL}}\right)^2. \end{aligned} \qquad (6.6)$$

It never exceeds the distance between adjacent slice centers, because VAT fully corrects signal displacements there:

$$\mathrm{gap_s} \leq \mathrm{STK_{EFF}} = \mathrm{STK_N} \cdot \left(\frac{\mathrm{G_{SEL}}}{\mathrm{dB_0}/_{\mathrm{ds}} + \mathrm{G_{SEL}}} \right). \qquad (\ 6.7\ )$$

The value of $\mathrm{gap_s}$ is negative in case adjacent selections overlap. $\mathrm{STK_{EFF}}$ is independent of $\mathrm{dB_0/dm}$. If $\mathrm{dB_0/ds} = 0$, $\mathrm{STK_{EFF}}$ equals the section thickness. In this case, a slice may distort out of a section, e.g. at m_1, yet the adjacent slice will simultaneously distort into the same section, such that a nearly constant signal is obtained, originating from either a single or two adjacent slices. It is only when $\mathrm{dB_0/ds} < 0$, and $\mathrm{dB_0/dm} < 0$, that the distance between slice centers will exceed the section thickness and $\mathrm{gap_s}$ can be resolved in the through-plane direction, e.g. at m'_1 (Figure 6.1d) where it will be visible as a substantial intensity decrease [93]. Multiple neighboring intensity variations then constitute a ripple artifact.

6.2.1. Selection profile and image combination

The extent to which signal intensity variations at slice transitions become visible in the combined image depends on the selection profile and the combination method. For box-car slice profiles, as originally proposed for SEMAC, linear complex summation has been reported to provide better homogeneity, but lower SNR, than sum-of-squares [67]. Other slice profiles can be used, as long as a good match is maintained between slice profile and image combination. For example, if sum-of-squares is used, homogeneous image combination requires that $\sum_n \mathrm{F}(\omega_n)^2 \propto 1$, where $\mathrm{F}(\omega_n)$ is the spectral response of the n-th selection.

As was shown by Koch et al., strongly overlapping Gaussian selection profiles lead to a reduction of intensity artifacts in 3D MSI compared to closely aligned box-car profiles, when a sum-of-squares combination is performed [60]. In SEMAC, widening the slice profile while maintaining the original slice interval leads to increased slice overlap (Figure 6.1e,f), which may be beneficial to reduce intensity fluctuations, in analogy to the bin overlap strategy used in MAVRIC [59] and VS-3D-MSI [60]. Widening of the selection profile is achieved either by using higher bandwidth RF pulses, or similarly, as illustrated in Figure 6.1, by decreasing the selection gradient strength and maintaining the selection pulse bandwidth. Higher bandwidth pulses lead to increased SAR. Weaker selection gradients lead to increased slice distortion, requiring more phase encoding steps. The section resolution in the through-plane direction is left unchanged in both cases.

Changes to the selection profile may contribute to intensity fluctuations. These profile changes may be unintended, e.g. slice profile erosion in fast spin echo sequences, or a consequence of adaptations to SEMAC such as Off-Resonance Suppression (ORS) [83,84]. With ORS, the selection profile is intentionally narrowed as a function of slice distortion, by using different gradient amplitudes for excitation and refocusing, in order to avoid back-folding artifacts from strong slice distortions.

6.3. Methods

6.3.1. Simulations

Time domain MRI simulations were run based on Eq. 6.1. A two-dimensional digital phantom was constructed with three regions, where B_0 varied linearly in the read-out direction, with dB_0/dm = -6 mT/m, dB_0/dm = 0 and dB_0/dm = 6 mT/m, respectively. The linear B_0 variation in slice direction was set separately for each simulation. In the center of each region, a 3 mm wide space without signal was defined. The spatially accurate in-plane phase encoding direction was not considered during these simulations. Using G_{SEL} = 10 mT/m, 5 slices were selected with intended centers at 4-mm intervals. The Gaussian selection profiles with a Full Width at Half Maximum (FWHM) of 5.5 mm overlapped at approximately $1/\sqrt{2}$ of the maximum intensity. SEMAC imaging was simulated on a 0.1-mm grid, with 25 phase encodings in slice direction and 4-mm section thickness. In-plane, simulations had a 128-mm FOV, 1-mm resolution and G_{READ} = 20 mT/m. After Fourier transform, images were combined using sum-of-squares. A set of simulations was run to study different aspects of the interplay between local gradients, slice width and section resolution.

1. Simulations were performed for through-plane gradient strength dB_0/ds in the range of -4 mT/m to 4 mT/m at 1 mT/m increments, to estimate the B_0 variation required for the ripple artifact to become visible.
2. Thinner sections of 2 mm were simulated for dB_0/ds = 0, to assess the influence of the section thickness in spatially resolving the gaps between selections, gap_s, and potentially making the ripple artifact appear.
3. Using simulations with a wider bandwidth, the Gaussian selection profile was increased to 11.1-mm FWHM, to study the effect of profile width on the ripple artifact.
4. Finally, slice overlap was simulated with a weaker selection gradient of G_{SEL} = 5 mT/m, which in combination with the original bandwidth led to a profile of 11.1-mm FWHM. To cover the increased slice distortion, 50 through-plane phase encoding steps were used.

6.3.2. Phantom experiments

A coaxial cylinder positioned perpendicularly to the B_0 field has been shown to provide a powerful model to analyze susceptibility effects [94,22]. With the cylinder positioned along the y-axis, and B_0 along z, the magnetic field in a plane perpendicular to the cylinder in the area outside the cylinder is given by [34]:

$$B_e(x,z) = B_0\left[1 - \chi_e/6 + \left(\frac{\chi_e - \chi_i}{2}\right) R_i{}^2 \frac{(x^2 - z^2)}{(x^2 + z^2)^2}\right], \qquad (6.8)$$

where R_i is the cylinder radius and χ_i and χ_e represent the susceptibility of the cylinder and its environment. As the magnetic field is independent of the y coordinate, an imaging plane orthogonal to the cylinder contains in-plane field gradients only. Angulating the imaging plane by e.g. 45° introduces through-plane field gradients of similar strength as the in-plane field gradients.

A stainless steel rod of 10-mm diameter was positioned vertically in Gd-doped water. A resolution phantom, consisting of AMPMODU Mod IV rectangular plastic connectors, was attached to the rod at an angle of 45°, to enable verification of geometric imaging accuracy. SEMAC was implemented on a 1.5T clinical scanner. Using an 8-channel RF-coil, scans were made in the coronal plane orthogonal to the rod and at an angulation of 45°, parallel to the resolution phantom. The angulated acquisition was performed once with positive and once with negative read-out gradient polarity.

Images were acquired with and without ORS, to investigate the effects of selection profile changes. With ORS, the selection gradient was 8.8 mT/m during excitation and 7.3 mT/m during refocusing. The RF pulse bandwidth was 2.0 kHz during excitation and 1.25 kHz during refocusing, using truncated and windowed sinc pulses with Gaussian-like profiles, resulting in 4-mm slices. With these settings, the ORS cut-off frequency was 8.7 kHz, which covered most of the spectrum near stainless steel. The slice distortion was resolved using 13 through-plane phase encoding steps [84]. 27 slices of 160×200 mm were acquired in 7'43".

Next, to investigate the effect of slice overlap, another angulated acquisition was run with weaker selection gradients of 4.4 mT/m during excitation and 3.7 mT/m during refocusing, using the same RF pulses and bandwidths as before. For this acquisition, 25 through-plane phase encoding steps were used to resolve the increased slice distortion, resulting in a scan-time of 14'51".

In all scans, the read-out gradient was 20.7 mT/m, with a bandwidth of 880 Hz/pixel, in-plane resolution 1×1 mm, TR = 475 ms and TE = 15 ms. Sum-of-squares image combination was used for all acquisitions.

Finally, to study the ripple artifact near a metal object used in clinical practice, a stainless steel Exeter hip implant stem (Stryker, Mahwah, NJ, USA) was scanned coronally using SEMAC, with similar acquisition settings as used for the stainless steel rod. With an in-plane SENSE [26] factor of 1.8, scan-time was 4'53". The scan was repeated with the same RF bandwidths but with weaker selection gradients, resulting in overlapping selections. In this acquisition, additionally, a through-plane SENSE factor of 1.4 was used, resulting in a scan-time of 6'45". Images were combined using sum-of-squares as well as linear complex summation. A spin-echo based SENSE calibration scan with high bandwidth RF pulses was used to avoid T2* dephasing and minimize distortion.

6.4. Results

6.4.1. Simulations

For all slice selections, compression or dilation was observed where the sign of dB_0/dm was opposite or equal to the sign of G_{READ}, respectively (individual selections not shown). When dB_0/ds and G_{SEL} had equal sign (Figure 6.2a), or in absence of through-plane B_0 variation (Figure 6.2b), the distance between selections was too small to lead to visible intensity fluctuations. The ripple artifact was only apparent when through-plane B_0 variation led to selection intervals substantially larger than the section thickness, in these simulations

starting at roughly -2 mT/m (Figure 6.2c). For dB_0/ds = -3 mT/m, the ripple was well established (Figure 6.2d). This corresponds to a gap_s of roughly 50% to 60% of STK_N (Eq. 6.6).

Acquiring sections substantially thinner than the slice selection also led to ripple artifact (Figure 6.2f). The edges of the phantom's spaces were jagged as a manifestation of signal displacements.

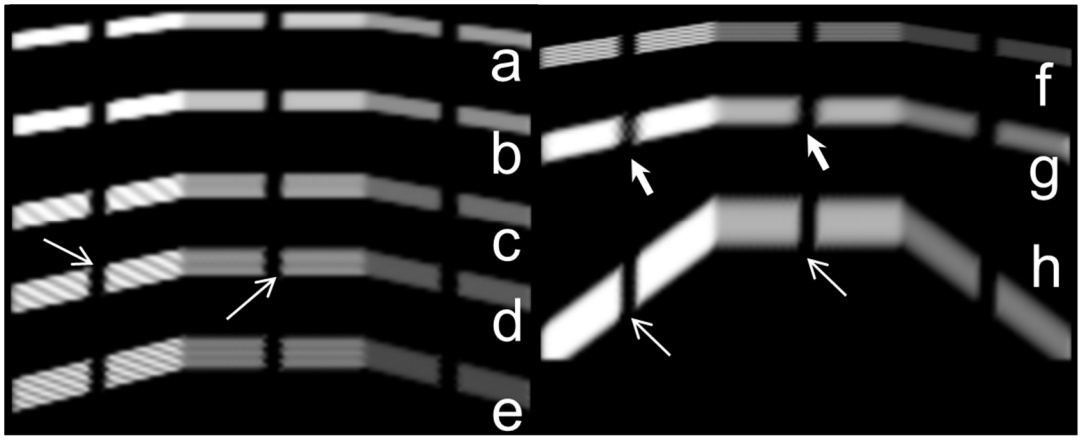

Figure 6.2: Simulations of sum-of-squares combination of 5 slice selections at 4-mm intervals acquired with 4-mm sections. Each simulation consists of three regions, with dB_0/dm = -6 mT/m (left), 0 mT/m (center), and +6 mT/m (right). The otherwise homogeneous digital phantom contains three 3-mm wide spaces without signal, centered in the abovementioned three B_0 regions. The simulations demonstrate the effect of the local gradient strength in through-plane direction, dB_0/ds = +2 mT/m (a), 0 mT/m (b), -2 mT/m (c), -3 mT/m (d) and -4 mT/m (e). If the selection gradient reinforces the through-plane B_0 variation (a), the distance between selections is too small compared to the section thickness to result in visible intensity fluctuations. Without through-plane B_0 variation, the ripple artifact is not observed either (b), unless thinner sections of 2 mm are acquired, which is substantially thinner than the slice profiles (f). With 4-mm sections, and a read-out gradient of 20 mT/m, the ripple was well established at dB_0/ds = -3 mT/m (d). The jagged edges of the spaces (d, thin arrows) are related to the remaining signal displacements in the frequency encoding direction with VAT.
Again using 4-mm sections and dB_0/ds = -3 mT/m, slice overlap was simulated using doubled RF pulse bandwidth while maintaining the same selection gradient (g), and using the original RF pulse with a weaker selection gradient (h). Using twice the RF pulse bandwidth removed the ripple artifact, but impaired the in-plane resolution as is apparent from the edges of the spaces (g, thick arrows). When the original RF pulse was used with a weaker selection gradient, the ripple artifact also disappeared. In this case, the weaker VAT gradient led to reduced blurring, and a smaller frequency range per selection was maintained. As a consequence, the edge definition of the spaces was improved (h, thin arrows).

In summary, the simulations confirmed that only where B_0 varies both in-plane and through-plane, the discontinuities between slices become large enough to be resolved and result in the ripple artifact, as proposed in our analysis (Figure 6.1).

In the simulation with overlapping double bandwidth RF pulses (Figure 6.2g), the ripple artifact was absent. But the larger frequency range per selection led to increased signal displacement in the frequency encoding direction and increased blur near the phantom's spaces. Applying the original RF pulse with a weaker selection gradient also led to overlapping selections and absence of the ripple artifact. Slice distortion increased

significantly, but the reduced VAT gradient led to reduced blurring [62]. In addition, maintaining a smaller frequency range per selection limited residual displacements in the frequency encoding direction and improved resolution as is visible at the edges of the phantom's spaces (Figure 6.2h).

6.4.2. Phantom experiments

The ripple artifact was absent in the coronal SEMAC images of the stainless steel rod (Figure 6.3a) and only appeared in the angulated acquisition with both in-plane and through-plane field variations (Figure 6.3b). The ripple artifact was distinctly different on either side of the rod and, by inverting the read-out gradient, the appearances of the ripple artifact could be mirrored (Figure 6.3c). Note, that also in the phase encoding direction, even without ORS, signal fluctuations occurred (Figure 6.3d).

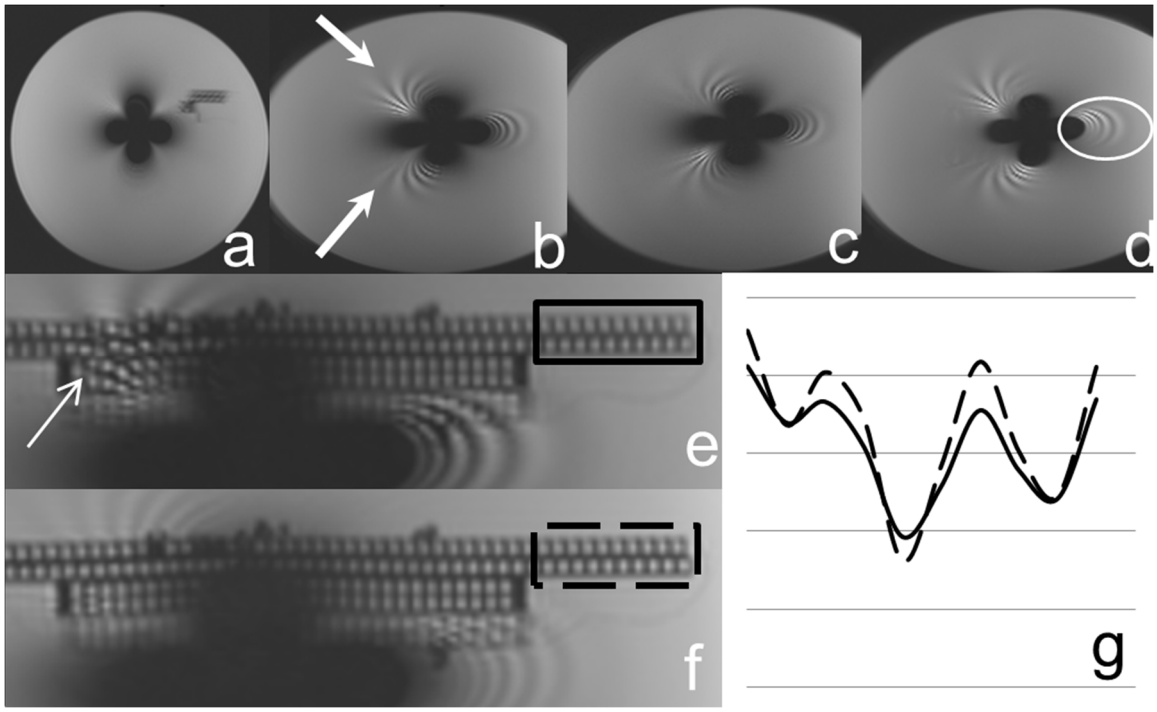

Figure 6.3: SEMAC acquisitions of stainless steel rod positioned vertically in Gd doped water. The read-out direction is from top to bottom. In the coronal scan orthogonal to the rod (a), the ripple artifact is not observed. In the 45° angulated scan, the ripple artifact is present and has a different appearance on either side of the rod (b, thick arrows), where slice selections are compressed and dilated, respectively. Inverting the read-out gradient sign interchanges the appearances of the ripple artifact on either side of the metal (c). In the acquisition without ORS, the ripple artifact remains present in the same regions, though the appearance changes (d). Note that signal fluctuations occur also in the phase encoding direction (left-right, ellipse). The distortions and signal fluctuations disturb the image of the resolution phantom (thin arrow) that was aligned with the imaging plane (e). Slice overlap suppresses the ripple artifact (f). Underlying structure is unveiled and resolution is improved. An averaged signal profile –averaged in the phase encoding direction (left-right)– of the resolution phantom (g) further illustrates the resolution improvement in the frequency encoding direction (top-bottom) obtained with slice overlap (dashed line) vs. the standard SEMAC acquisition (solid line).

The SEMAC images of the resolution phantom evidenced geometric distortion and intensity variations (Figure 6.3e). Slice overlap by selection gradient reduction substantially reduced

the ripple artifact, unveiling the regular structure of the phantom (Figure 6.3f). The resolution improvement (Figure 6.3g) may be attributed to a weaker VAT gradient [62].

In conventional SEMAC images of the hip implant sample, distortions and signal fluctuations of the ripple artifact notably compromised image information (Figure 6.4a,b). Slice overlap substantially reduced the ripple artifact (Figure 6.4e,f). Using linear complex summation for image combination did influence the artifact's appearance (Figure 6.4c,d,g,h), indicating that this combination algorithm was a closer match for the selection profile used than sum-of-squares [67]. However, the improvement was less significant than the improvement achieved using slice overlap. In this case, linear complex summation compromised SNR, because all selections contributed equally to the combined image, with the majority containing only noise [67].

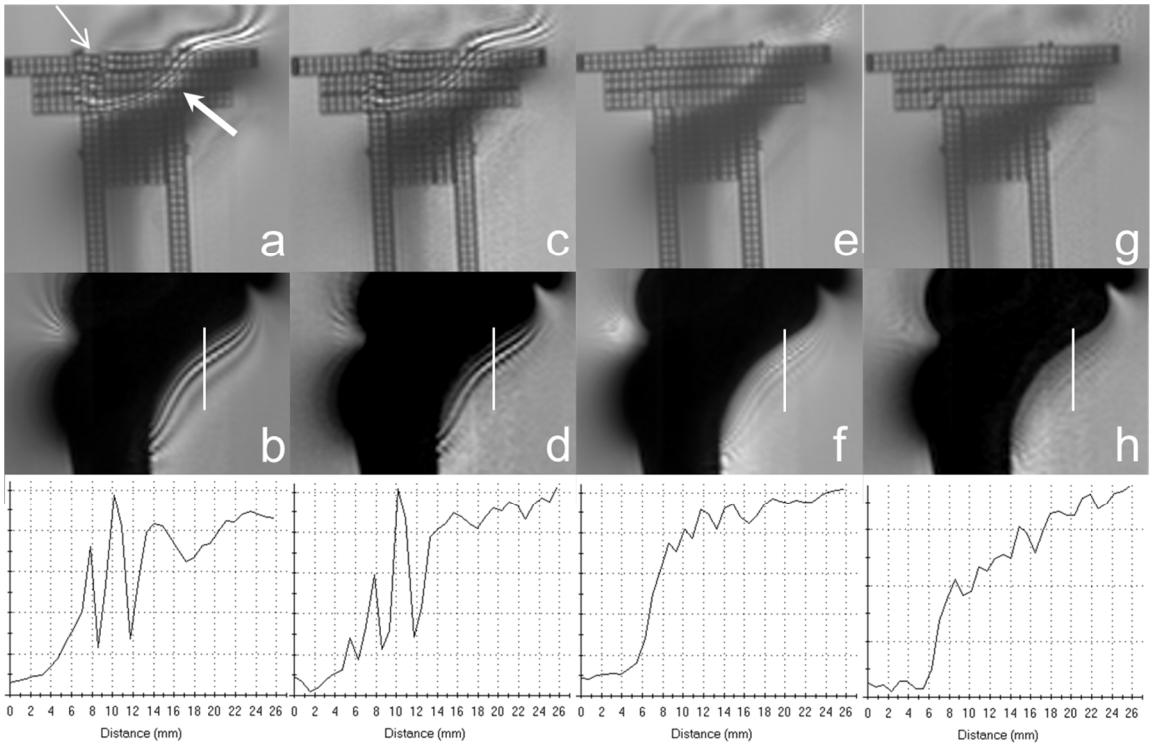

Figure 6.4: Images of stainless steel hip implant sample, acquired with conventional SEMAC (a,b,c,d) and SEMAC with slice overlap (e,f,g,h). Images were combined with sum-of-squares (a,b,e,f) and linear complex summation (c,d,g,h). In conventional SEMAC, the ripple artifact (a, b) leads to distortion (thin arrow), and image information is compromised by severe signal fluctuations (thick arrow). Slice overlap significantly reduces the artifact, unveiling the underlying structure (e) and improving homogeneity (f). The signal profiles below indicate that linear complex summation instead of sum-of-squares to combine slice selections (c,d,g,h) gives a slight further reduction of the ripple artifact and improvement of the overall homogeneity, however at the cost of the signal-to-noise ratio.

6.5. Discussion

The ripple artifact is an important limitation of current MSI techniques used to reduce metal artifacts [58,37], in particular SEMAC that uses gradient selection of slices on the order of the through-plane resolution. In this work, an analysis is presented of the cause of the ripple artifact: compression of slice selections by frequency encoding may lead to hyper-intense

regions and hypo-intense slice transitions and it is shown that these transitions are only spatially resolved, where the main field varies both in-plane and through-plane. Time domain simulations and phantom experiments confirmed this analysis. Phantom experiments showed intensity fluctuations in the phase encoding direction as well, which may be attributed to slice profile erosion with increasing refocusing pulse number.

Signal displacement during read-out may be compensated for in processing by using a B_0-map generated from MAVRIC sub-images, as proposed by Koch et al. [64]. This technique shows a promising reduction of the ripple artifact. Although it corrects for the part of the ripple artifact caused by signal displacement, the signal fluctuation caused by selection profile variations is not corrected. As with any processing technique, resolution loss caused by signal displacement or VAT blurring is not easily corrected.

Alternatively, as shown by the presented analysis and experiments, the ripple artifact may be substantially reduced by widening the selection profile so as to create overlap between slices. Slice overlap can be achieved by applying higher bandwidth RF pulses while maintaining the same selection gradient, though this increases SAR. Decreasing the selection gradient while maintaining the RF bandwidth will also lead to slice overlap. The associated increased slice distortion requires more through-plane phase encoding steps, which increases scan-time. However, by maintaining a smaller selection bandwidth, the frequency range per section interval decreases, which improves the accuracy of the frequency encoding process. With decreased selection gradient strength, G_{VAT} also decreases proportionally, which reduces blurring as a consequence of signal modulation effects in k-space [62].

Depending on the relation between coil geometry and scan geometry, the larger slice-encoding dimension may in some cases facilitate parallel imaging [58,60] in the through-plane direction to compensate for the increased scan-time. In the experiments presented here, no artifacts were found from applying through-plane SENSE. Further acceleration is possible by taking into account the sparsity of the SEMAC data, using compressed sensing approaches [58,59].

The study presented here is limited to simulations and phantom experiments. Future studies will need to prove the clinical applicability of this work.

In conclusion, the presented analysis and simulations help to understand the ripple artifact. The simulations and experiments show that, at a scan-time penalty, the presented slice overlap strategy allows for improved resolution and substantially reduces the ripple artifact, thereby improving the quality of soft tissue imaging near metal implants.

7. Prototype

7.1. Technical requirements

With the clinical requirements inventoried (section 4.3, Table 4.2), the required functionality can be defined in more technical detail. At this stage a distinction is made between technical requirements of the functionality of the prototype and product requirements, because the prototype and the product serve different purposes. While the prototype is meant to investigate the value of and the need for the different features, the final product is meant to provide the best offering in terms of price and value. Though many requirements apply to both prototype and product, the value of some features in the product may be very clear without having to investigate them using a prototype. Conversely, for features of which the value is investigated using a prototype, it may be decided to keep or drop the requirement for the product, depending on the results of this investigation and other considerations like cost or duration of product development. As the prototype is a tool for investigation, suboptimal usability may to some extent be acceptable, whereas the usability of the product needs to be fully optimized. Prototype specific technical requirements are discussed in section 7.2.

7.1.1. Artifact correction

Correction of metal artifacts, including geometric distortion and signal intensity deviations (section 2.4), is needed to provide diagnostic image quality. The required accuracy of image geometry and intensity depends on the clinical application. For most complications that relate to metal implants, conventional scanning techniques do not provide sufficient image quality sufficiently close to the implant (see section 4.3.1): diagnostic image quality as close as half a centimeter from the implant is required for many clinical applications, including pseudotumors, effusion, bone marrow edema, and bone oncology. Muscular atrophy imposes slightly milder requirements on the scanning technique. For osteolysis and implant loosening, diagnostic image quality much closer to the implant is required, as close as 1 or 2 mm from the implant.

Quantitative clinical requirements have not been defined for the homogeneity and correctness of signal intensity or for the correctness of the position of signal. Signal intensity variations may be caused by many more factors than only metal artifacts. Quantitatively determining the level of homogeneity required for diagnosis is complicated. The technical requirement used for the prototype is to obtain a level of homogeneity comparable to the homogeneity in a remote region where image quality is not significantly influenced by the metal. The technical requirement used for the correctness of the position of signal is that displacements may not exceed the imaging resolution.

The size of the metal artifact is strongly dependent on the material, shape and orientation of the implant. An overview of approximate magnetic susceptibilities of commonly used materials in metal implants is given in table 7.1. Yet, for most metallic implants, imaging at a distance from metal implants of roughly half a centimeter requires advanced scanning

techniques like SPI or MSI. b-SFFP with phase cycling is considered an interesting alternative, yet the remaining signal voids near the metal implants make this technique less effective to image near metal than SPI or MSI. SPI at its current technological state requires too long scan-times to be used in clinical practice. Therefore, MSI is chosen as the most appropriate technique for improved image quality near metal.

MSI is instantiated by SEMAC and MAVRIC, each with its own characteristics. To allow comparison of SEMAC and MAVRIC, both techniques must be available in the prototype. Especially in SEMAC, the residual ripple artifact may extend to a substantial distance from the implant, depending on the implant material and scan orientation. This ripple artifact may severely complicate visualization of soft tissue, and therefore increases the distance from the implant where tissue evaluation is feasible. Therefore, the possibility to use slice overlap to reduce the ripple artifact (chapter 6) is an important requirement, at least for the prototype, which allows judging whether this feature is to be included in the final product. VS-3D-MSI, which combines properties of SEMAC and MAVRIC, is not included (see section 7.1.3).

Material	Approximate susceptibility (ppm)	Source
Titanium	182	[34]
Cobalt-chromium	900	[95]
Cobalt-chromium-molybdenum	1370	[96]
Stainless steel (non-magnetic, austenitic)	3520-6700	[34]

Table 7.1: Approximate magnetic susceptibilities of commonly used materials for metal implants.

MSI techniques produce sub-images that need to be combined. The homogeneity of the resulting images requires good match between the selection profiles, the spacing between spatial-spectral bins and the image combination algorithm.

Slice profile restoration by frequency mapping to improve the geometric correctness of VAT images ([63], section 3.1.1) may fill the gap between VAT and MSI, as it requires intermediate scan-times and provides partial correction including in-plane and through-plane repositioning of signal. However, this quite recent technique does not correct for slice thickness variations, is still substantially slower than VAT and the image quality seems to be compromised by reduced SNR. The technique requires a B_0-map. The quality of the B_0-map derived from multiple VAT images has not yet been optimized. If an improvement of the quality of the B_0-map proves to require that the B_0-map be derived from multiple sub-images of a MAVRIC sequence, the point of introducing a faster technique than MAVRIC would be defeated.

7.1.2. Applicability

Preset MSI scan sequence definitions are helpful if not indispensable for a good start to use the functionality. These sequence definitions need to be appropriate for the intended clinical applications. Therefore, they must include the conventionally used contrast weightings PDw,

T1w, T2w and fat suppressed PDw (section 4.3.2). Robust fat suppression in areas with strong B_0 inhomogeneity requires STIR.

Different ExamCards need to be provided for different anatomic areas, including the knee, the hip, and the spine, which often contain metal implants. For each anatomy, the ExamCard needs to contain scan sequences with common orientations, appropriate coverage and using the appropriate RF-coil.

The preset sequences are to be defined at the appropriate resolution. For most clinical applications 1×1 mm in-plane and 4 mm through-plane is sufficient (section 4.3.2).

7.1.3. Speed

To be clinically usable, a scan sequence is to remain shorter than ten minutes (section 4.3.3). As mentioned, current SPI techniques are too slow to meet this condition. But also MSI techniques are known for their substantial scan-time increase, and require additional measures to allow sufficient coverage and resolution within an acceptable scan-time.

Spatial-spectral selectivity using ORS-SEMAC and ORS-MAVRIC is required to use scan-time efficiently, without spending time on image information outside the spatial-spectral range of interest.

VS-3D-MSI also provides selectivity, but requires that all of the metal is included within the selected volume. Acquiring a VS-3D-MSI scan with a coverage smaller than the implant (intended or unintended) may lead to back-folding of off-resonance signal outside the volume of interest. In principle, ORS could be applied to VS-3D-MSI as well. This would result in a variant of ORS-MSI, which similarly to ORS-MAVRIC acquires a 3D volume, but requires VAT to correct for displacements in the frequency encoding direction. For the prototype, it is decided not to include the hybrid VS-3D-MSI technique, but rather to explore the differences between the slice selective MSI variant (SEMAC and ORS-SEMAC) and the intrinsic 3D technique without VAT (MAVRIC and ORS-MAVRIC).

The MSI techniques must be compatible with parallel imaging (SENSE) and half-scan, also known as partial matrix or partial Fourier, for further acceleration. SENSE uses an additional reference scan as calibration of the coil sensitivity. This reference scan is usually based on a gradient echo (FFE) sequence, which results in signal voids due to de-phasing, especially close to the metal. A signal void in the reference scan results in SENSE unfolding errors in the diagnostic scan. To avoid these unfolding errors, a TSE reference scan with strong gradients for excitation and refocusing is required. The maximum allowable scan-time of the reference scan is one minute. A longer scan-time than one minute for a scan that does not produce visible images would annoy the MR operator. Using a TSE reference scan must not take any of the user's attention and the choice of the type of reference scan must be completely transparent to the user. The correct reference scan must automatically be selected and inserted in the list of sequences to be scanned.

Even if combined with acceleration techniques, MSI sequences require substantially increased scan-times, and an examination consisting only of multiple MSI sequences would take too much time for practical use. Therefore, faster techniques that reduce metal

artifacts must also be available. These include conventional high-bandwidth TSE as well as VAT.

7.1.4. Usability

For fast and easy use of the functionality, ExamCards that contain appropriate sequences for scanning near metal are provided with the prototype. As the time available for a patient examination only allows for a few accelerated MSI sequences, these ExamCards also need to include the faster high-bandwidth TSE sequences with or without VAT. During evaluation of the functionality using the prototype, high-bandwidth TSE sequences without VAT can be used to compare the MSI techniques against the current state of the art scanning techniques. A TSE survey is to be included in the ExamCards as well. The TSE reference scan must be included in the ExamCards, or preferably, the TSE reference scan is even inserted automatically. Robust scanning without scan aborts is essential, and this includes the scan preparation phases. The scanner may issue warnings to the user that preparation phase results indicate the presence of unusual materials such as metal, as long as these warnings do not lead to scan aborts.

MSI techniques produce intermediate images that need to be combined before evaluation. The appropriate image combination algorithm must automatically start to combine the MSI sub-images. The sub-images are not useful for tissue evaluation and must therefore not be presented to the radiologist and must not cause confusion to the MR operator.

The spectral bins of a MAVRIC acquisition all contain the same spatial volume. Therefore, each image is combined of sub-images from all spectral bins and all combined images contain the full signal spectrum. In ORS-MAVRIC, the spectral coverage of individual spectral bins taper off and homogeneity is compromised in the peripheral regions of the volume of interest, as explained in chapter 5. Only images with acceptable homogeneity are to be produced.

In SEMAC, image combination produces mainly images with complete spectral coverage, but also images with partial spectral coverage, some of which do not contain the on-resonance information (Figure 7.1). Nevertheless, images with partial spectral coverage may still be valuable for tissue evaluation. However, images without the on-resonance information are considered too incomplete, and should not be presented to the radiologist. The same applies to ORS-SEMAC as well.

The number of slice selections N_S and the SEMAC factor SF determine the total number of combined images that can be produced, N_{total}, the number of combined images containing full spectral coverage, N_{full}, and the number of images that contain on-resonance signal, $N_{on\text{-}res}$:

$$N_{total} = N_s + SF - 1, \quad (7.1)$$

$$N_{full} = N_s - SF + 1, \quad (7.2)$$

$$N_{on-res} = N_s. \quad (7.3)$$

7.2. Prototype specific technical requirements

As the prototype is meant to evaluate the functionality as well as its usability, the requirements for the prototype are grossly set by the clinical requirements (section 4.3) and the technical requirements (section 7.1) for the product. Yet, evaluation of the functionality can be performed with a subset of all features, as the value of some aspects of the required functionality is clear without the need for evaluation. And not all eventually required features need to be available in the prototype already, as long as the workflow during evaluation is acceptable.

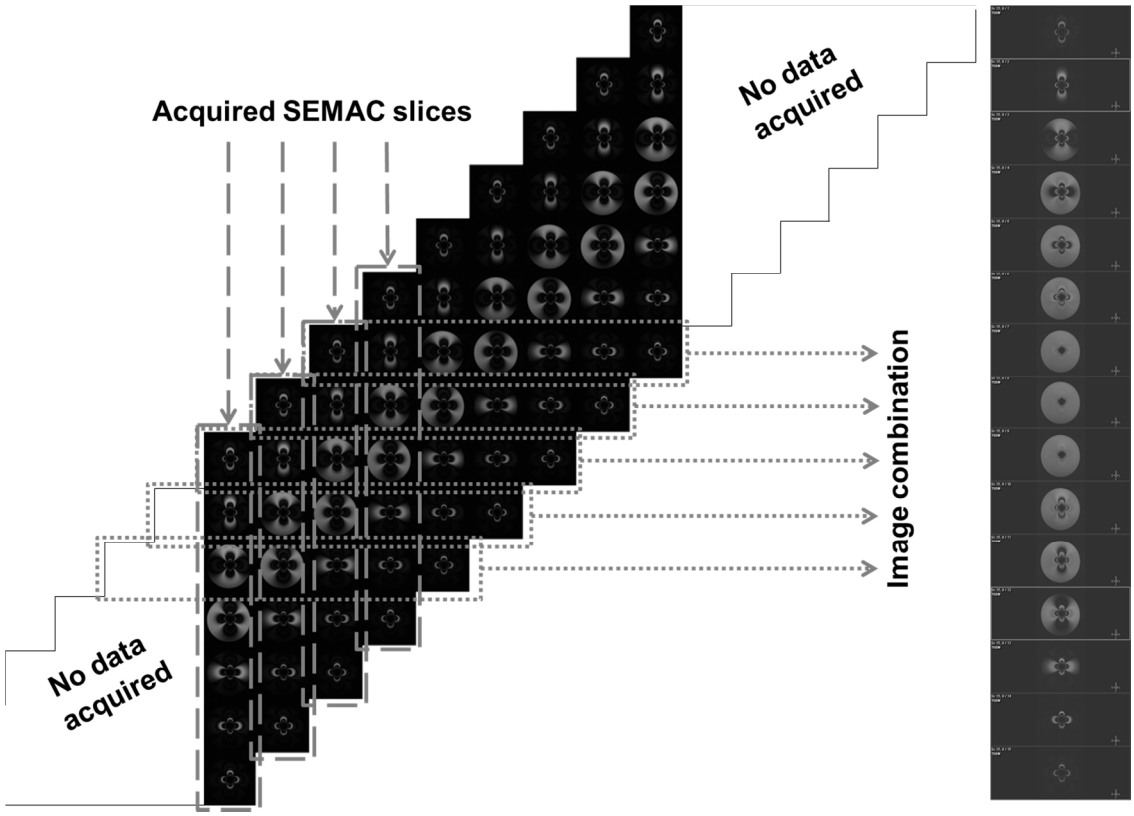

Figure 7.1: Example of SEMAC sub-images and image combination. Nine acquired slices (dashed vertical boxes) of a coronal SEMAC acquisition with SEMAC factor 7 of a phantom setup with 10-mm stainless steel rod positioned vertically in Gd-doped water. Images of different slices but at the same physical position are combined (dotted horizontal boxes) into a single image containing the entire signal spectrum (right column). Near the edge of the acquired volume, not all off-resonance images are acquired, and the 3 slices at either end of the acquired volume even lack the central on-resonance image.

Evaluation of the prototype's functionality must be possible on existing Philips MRI scanners that are available in hospitals. Therefore, the prototype is provided as a software extension or "patch", based on MRI product software that was released not too long before the availability of the prototype, e.g. R2.6.3 or R3.2.1. This MRI software basis is referred to in this chapter as the *scanner release software*.

As the prototype will be used for investigation purposes in a clinical environment, it must be possible to quickly activate and deactivate the prototype on a regular basis, to allow clinical use of the scanner without the prototype and investigational use with the prototype

activated. To avoid mistakes, all activation actions are to be started with a single button, and likewise for deactivation.

In the prototype, automated and transparent selection and insertion of the TSE SENSE reference scan into the list of sequences to be scanned is not vital. Instead, it will be sufficient to provide the TSE SENSE reference scan as a preset sequence together with the preset MSI sequences. However, this reference scan must be included in the ExamCards, and usage of the SENSE reference scan must be intuitive and unhampered, meaning that it must be possible to select the entire ExamCard including the TSE SENSE reference scan.

During evaluation, the production of superfluous or sub-images is considered acceptable. Moreover, sub-images may in some cases during evaluation be useful to study the frequency distribution of signal. And during evaluation, peripheral SEMAC images may help to validate whether the presence of on-resonance signal in an image is the appropriate criterion to keep or dispose the image. It must be clear to the MR operator though, which images are meant for diagnosis and which ones are sub-images.

Ideally, all preparation phases are robust against the presence of wide frequency dispersions. The f_0 determination is the only preparation phase which may abort in some cases with extreme f_0 inhomogeneity. Yet, for evaluation of the prototype, and especially for evaluation of the MSI techniques, the f_0 determination itself is not very important. In fact, MSI is based on the notion, that many frequencies need to be scanned, and that f_0 deviates strongly depending on the position of the signal with respect to the metal.

The f_0 determination is used for the positioning of the slice. The scans used near metal are based on a TSE pulse sequence and apply strong selection gradients on the order of 10 mT/m, which corresponds to 0.4 kHz/mm. Omitting an f_0 determination and instead using the f_0 value determined during the examination of a previous patient may lead to deviations on the order of roughly 100 Hz or smaller, leading to a maximum deviation of 0.25 mm for the slice position. Such a deviation is considered acceptable, compared to the slice thickness of 2 to 4 mm, and especially compared to the slice distortion near metal in conventional multi-slice TSE, which may be on the order of 30 mm for stainless steel (see section 5.4.1).

Even in case metal is present in the scanner, the f_0 determination often succeeds. Therefore, for the prototype, it is considered acceptable to provide the user with a short instruction to temporarily switch off the f_0 determination when confronted with a scan abort.

7.3. Design

7.3.1. Pulse profile and spectral bin spacing

SEMAC originally uses closely aligned boxcar pulse profiles to excite and refocus signal. MAVRIC, in contrast, uses strongly overlapping Gaussian profiles to allow a smooth transition between adjacent spectral bins. As described in section 6.2.1, the approach to use overlapping Gaussian profiles may be used for SEMAC as well, and can help reduce the artifacts resulting from discontinuities between slices, that may be aggravated by small signal displacements. The prototype therefore uses windowed sinc RF pulses with Gaussian-like profile for excitation and refocusing, both in SEMAC and in MAVRIC.

Aspect	Requirement	Prototype	Product
Artifact correction	MSI: SEMAC & MAVRIC	Required	Required
	Possibility to reduce ripple artifact	Required	t.b.d.
	Match between pulse profile, spectral bin spacing and sub-image combination for homogeneity.	Required	Required
Applicability	ExamCard with appropriate preset scan sequences	Required	Required
	TSE survey	Required	Required
	Contrasts: PDw, T1w, T2w, STIR	Required	Required
	1×1 mm in-plane, 4 mm through-plane resolution	Required	Required
	Appropriate RF-coils, FOV and orientations for anatomies: hip, spine, knee	Required	Required
Speed	ORS-SEMAC & ORS-MAVRIC	Required	Required
	TSE & VAT	Required	Required
	Compatibility with parallel imaging	Required	Required
	TSE SENSE reference scan	Required	Required
	TSE SENSE reference scan ≤ 1 minute	Required	Required
	Automatic insertion of TSE SENSE reference scan	Not required	Required
	TSE SENSE reference scan included in ExamCard	Required	Not required
	Compatibility with partial matrix	Required	Required
Usability	No scan aborts	Required	Required
	Robust f_0 preparation phase	Dropped	Required
	Automatic image combination	Required	Required
	Only combined images (no sub-images)	Dropped	Required
	Only images with acceptable homogeneity and containing on-resonance signal	Dropped	Required
	Quick single-button prototype activation/deactivation	Required	n.a.

Table 7.2: Technical requirements for prototype and product.

A different gradient for excitation than for refocusing is used to enable ORS for VAT or SEMAC. The same technique is applied for the suppression of ambiguity artifacts. This is available already in the scanner release software and may therefore be used for ORS as well.

Based on a multi-slice sequence, SEMAC and ORS-SEMAC select consecutive slices by applying RF pulses with consecutive frequency bands. Therefore, in SEMAC and ORS-SEMAC, a selected slice corresponds to a spatial-spectral bin. The spacing between slices, which is the spectral bin spacing, equals the through-plane distance between image centers. In MAVRIC and ORS-MAVRIC, the spectral bin spacing is not linked to the through-plane distance between image centers. Hence, MAVRIC and ORS-MAVRIC allow much more freedom to optimize the spectral bin spacing for image homogeneity given the bandwidth of the spectral bins and the image combination method.

For example, if a sum-of-squares algorithm is used, otherwise known as an L_2 algorithm, optimal image homogeneity is obtained when the condition $\sum_n \mathrm{F}(\omega_n)^2 \propto 1$ is met, where $\mathrm{F}(\omega_n)$ is the spectral response of the n-th selection. For a linear addition or L_1 algorithm, this condition changes to $\sum_n \mathrm{F}(\omega_n) \propto 1$. More generally, for an L_x algorithm, the condition is $\sum_n \mathrm{F}(\omega_n)^x \propto 1$.

These conditions are reflected in the optimal spectral bin spacing, as shown by a few simple simulations. A windowed sinc RF pulse with Gaussian-like profile and a single side-lobe on each side of the main lobe was used in these examples (Figure 7.2a). Three profiles with equal bandwidths were used at increasing frequency offsets (Figure 7.2b). The mutual overlap between the profiles was varied by changing the frequency spacing (Figure 7.2b-d). The signal from the three profiles was combined using different combination algorithms, including linear addition (L_1, Figure 7.2e-g), sum-of-squares (L_2, Figure 7.2h-j), and Maximum Intensity Projection (MIP, L_∞, Figure 7.2k-m). These simulations demonstrate that signal homogeneity in the combined image depends on the combination method, the spectral bin spacing and the selection profile. Note that the selection profile may differ from the profile of a single RF pulse in a TSE sequence, as signal is selected using multiple RF pulses.

If the spectral bin spacing is decreased, the overlap between adjacent bins increases, and a bin may even overlap with more than just the directly adjacent two bins. To avoid saturation of signal or “cross-talk”, overlapping bins must be acquired in different packages, separated in time, to allow relaxation of the signal. Whether two bins overlap is determined by the maximum of all pulses used in the sequence including excitation and refocusing (section 5.2.3) but also potential pre-pulses such as inversion for fat suppression.

To avoid saturation of signal in SEMAC or ORS-SEMAC, similar conditions apply as to conventional multi-slice or multi-slab TSE. In fact, SEMAC and ORS-SEMAC can be considered conventional multi-slice TSE without and with ambiguity artifact suppression [55], respectively, but with additional through-plane phase encoding (see also section 5.2.3). To maintain an appropriate distance between slices within a single package, odd and even slices were measured in two separate packages, following the scheme 1, 5, 9, 13, … 3, 7, 11, … within each package. This scheme is already available in the existing design of the scanner release software, as it is used for conventional multi-slice TSE acquisitions.

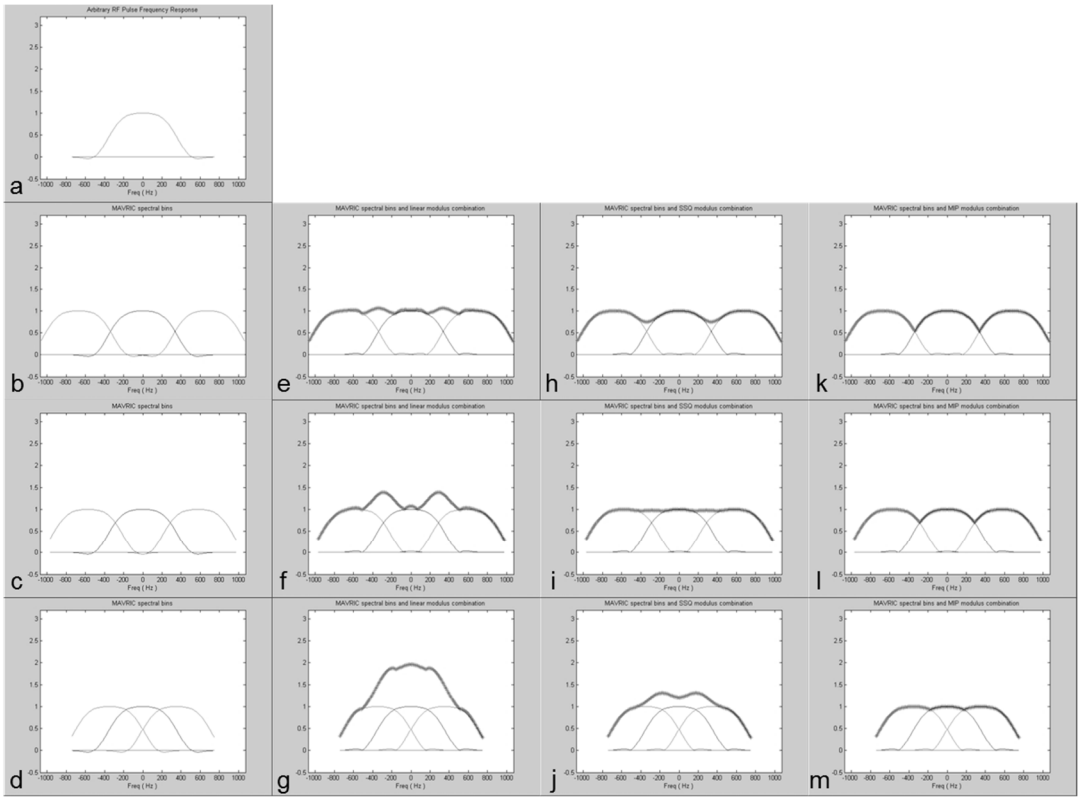

Figure 7.2: Simulation of windowed sinc pulse with Gaussian-like profile (a), three such profiles at increasing frequency offsets with different spacings between the spectral bins (b,c,d), and the result after signal combination using a linear summation (L_1, e-g), sum-of-squares (L_2, h-j), or MIP algorithm (L_∞, k-m). Different rows demonstrate the results for different spacings between the spectral bins. Signal homogeneity after combination depends on the profile used, the spectral bin spacing and the combination algorithm.

For MAVRIC and ORS-MAVRIC, an *acceptable nearness* of spectral bins within a single package is defined in the prototype, which is determined by the maximum FWHM bandwidth of excitation and refocusing pulse, multiplied by a preset factor to take into account the required margin for side-lobes and tails of the pulse profile.

For the MSI sequences, truncated and windowed sinc pulses with Gaussian-like profiles are used, to maintain reasonable RF pulse durations and to provide a smooth overlap between neighboring spectral bins. As a TSE echo train consists of one excitation and many refocusing pulses, the RF bandwidth of the refocusing pulse contributes most to SAR. Therefore, when using ORS for VAT or SEMAC, the stronger of the two gradients and the wider of the two bandwidths is applied during excitation.

ORS-MAVRIC is implemented with a gradient during excitation and without gradient during refocusing. The gradient and bandwidth during excitation correspond roughly to the size of the volume of interest for on-resonance signal. The actually selected volume is slightly larger due to the parallelogram shaped selected regions in s-f_0 space (see Figure 5.1) and the volume used to produce images is chosen slightly smaller, to maintain sufficient image homogeneity (see section 5.5).

For robust fat suppression near metal, STIR is the preferred method. In the scanner release software, the inversion pulse in a conventional 3D TSE sequence is designed to cover at least the same volume as the excitation and refocusing pulses. But the inversion pulse bandwidth is not optimized to match the excitation and refocusing bandwidths. In fact, the inversion pulse uses a much narrower bandwidth. Although this strategy works fine for imaging on-resonance signal, the narrower bandwidth causes incomplete inversion of signal with wider frequency dispersion. Therefore, in MAVRIC and ORS-MAVRIC, the inversion pulse bandwidth is multiplied with a configurable factor compared to the inversion pulse bandwidth of a conventional 3D TSE sequence.

If STIR is used in SEMAC, stricter conditions apply to the inversion pulse. Here, it is not only the inversion pulse bandwidth that should be matched with excitation and refocusing, but the same gradient strength must be used as well to ensure that the slice distortion during inversion is the same as that during excitation and refocusing. For example, an inversion gradient that is much weaker than the excitation gradient (Figure 7.3a) will lead to a stronger distortion of the inverted slice compared to the excited slice (Figure 7.3b). This mismatch will result in incomplete inversion of the excited slice and potential cross-talk with the adjacent slices. Using equal gradient strengths for inversion as for excitation and refocusing (Figure 7.3c) leads to complete inversion of the slice (Figure 7.3d). For ORS-SEMAC, the gradient and pulse bandwidth during inversion are matched to the gradient and pulse bandwidth during refocusing.

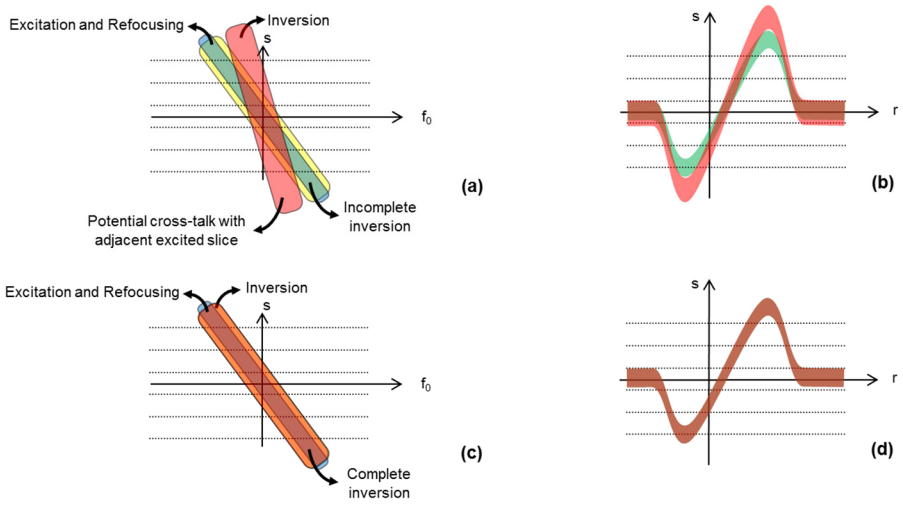

Figure 7.3: STIR in SEMAC: using a weaker gradient during inversion (red) than during excitation (yellow) and refocusing (blue), leads to incomplete inversion (a,b) and potential cross-talk with adjacent slices. Equal gradients for all pulses (c,d) lead to complete inversion of the slice.

7.3.2. Image Combination and Selection

Different combination algorithms are prescribed in the literature. For MAVRIC, sum-of-squares image combination provides homogeneous combination and high SNR [59]. In the original paper, SEMAC used linear complex summation, which fits well with the closely

aligned boxcar profiles [58,67]. SVD has been proposed to reduce the noise level in these combined images [67].

As the prototype uses overlapping Gaussian-like profiles rather than boxcar profiles, a sum-of-squares algorithm is likely more appropriate for both MAVRIC and SEMAC. However, to enable further comparison and evaluation of different methods, four combination algorithms are made available:

- Linear modulus summation: $\mathrm{I} = \sum_n |\mathrm{I}_n|$
- Sum of squares: $\mathrm{I} = \sqrt{\sum_n \mathrm{I}_n{}^2}$
- MIP: $\mathrm{I} = \max(\mathrm{I}_n)$
- Linear complex summation: $\mathrm{I} = \sum_n \mathrm{I}_n$

Here, I_n is the (complex) intensity of a voxel in a sub-image n and I is the voxel intensity in the combined image. In MAVRIC, the spectral bin spacing can be adapted to the algorithm that is chosen, but in SEMAC, the spectral bin spacing is less flexible. Therefore, a comparison was made between algorithms applied on SEMAC data. SEMAC data was acquired of a 10-mm diameter stainless steel rod centered in a cylinder-shaped phantom that was filled with Gd-doped water. The linear modulus summation (Figure 7.4a) and the MIP algorithm (Figure 7.4c) result in suboptimal homogeneity of combined images. Sum-of-squares (Figure 7.4b) leads to improved homogeneity. The combined image using linear complex summation (Figure 7.4d) shows the best homogeneity, but at decreased SNR compared to sum-of-squares, as expected [67].

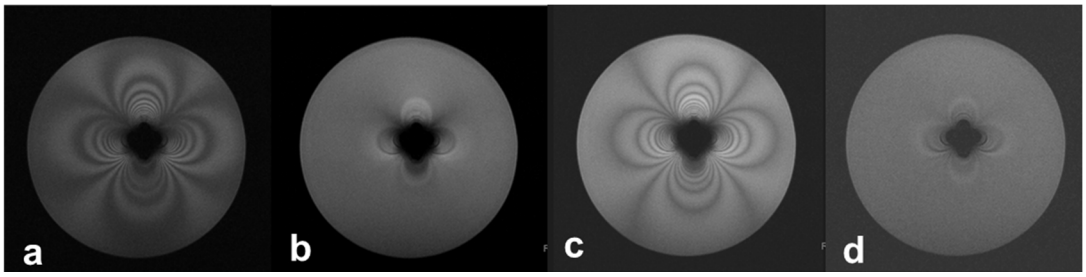

Figure 7.4: Coronal SEMAC scan of a phantom setup with 10-mm stainless steel rod positioned vertically in Gd-doped water. Of the same acquisition, images were produced using different combination algorithms: linear modulus summation (a), sum-of-squares (b), MIP (c) and linear complex summation (d). Linear modulus summation and MIP clearly compromise homogeneity and show the distribution of the spectral bins, reflecting the dipole B0 field. Linear complex summation provides the best homogeneity, but at reduced SNR compared to sum-of-squares.

Linear complex summation may be very valuable for SEMAC, especially in combination with noise reduction using SVD. However, the availability of complex data for combination requires reliable phase information of the signal. And this information may not always be available, e.g. when acceleration techniques such as half-scan are used, which may be one of the many measures that can be taken to keep the SEMAC acquisition within clinically feasible scan-times. Therefore, the default combination algorithm for SEMAC is sum-of-squares.

Also for MAVRIC, the default combination algorithm is sum-of-squares, as this fits best with the MAVRIC profiles used, robustly results in high SNR and is compatible with half-scan acquisitions.

When running an MSI acquisition, the prototype produces a DICOM image series with sub-images. Although sub-images are not considered useful for tissue evaluation, keeping the sub-images for comparison between different combination algorithms may be very useful, as this allows applying the algorithms to the sub-images of the very same acquired data.

The image combination algorithms are made available as part of the prototype in the form of an image processing tool, based on the Philips Research Image Development Environment (PRIDE) framework. The PRIDE framework first takes the DICOM image series containing the sub-images as input and converts these to a documented research image format (.XML/.REC). Then, the processing tool, installed as a separate executable program, is run to combine the sub-images and output the combined images in the same research image format. Finally, the combined images are reconverted to DICOM and stored in the patient database of the scanner.

This setup enables running the image combination tool multiple times on the same acquisition data while using different algorithms. The separate executable program may optionally be replaced by an alternate, custom-made image combination program containing yet more alternative algorithms (Figure 7.5).

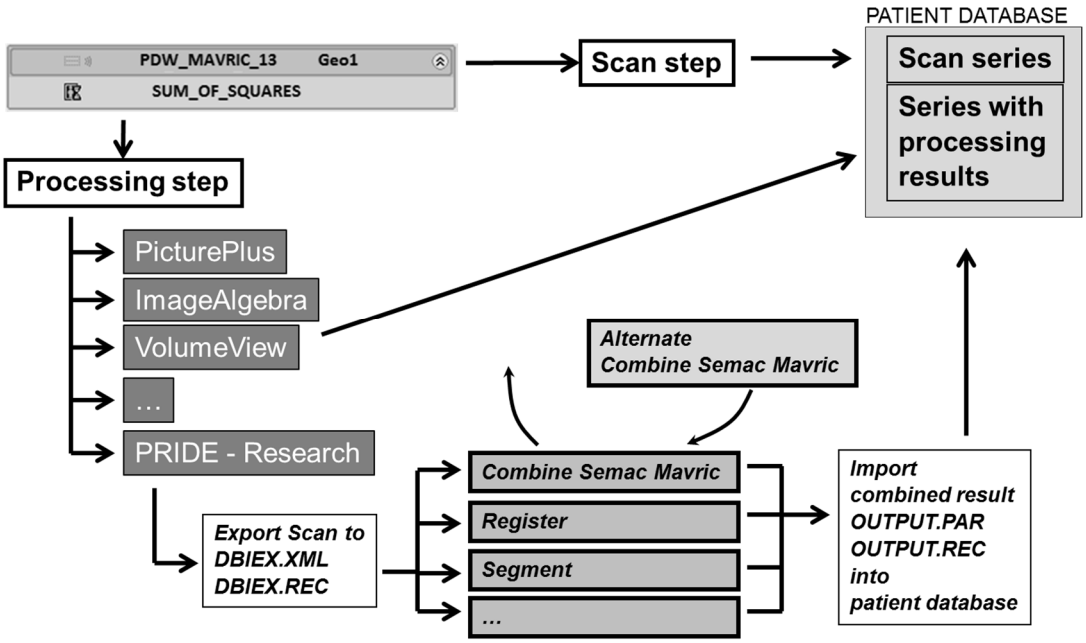

Figure 7.5: The scan step and the processing step are presented together in the UI (top left). The scan step produces sub-images, which are combined into diagnostic images by the processing step. The PRIDE framework provides an entry for a research tool (bottom) as an integrated processing step, similar to other processing packages like PicturePlus (left). PRIDE is very suitable for using and testing image combination algorithms. It allows running different image combination algorithms on the same acquired data, it stores the data in the patient database (top right), which allows the use of e.g. the conventional image comparison tools on the scanner, and it is possible to plug in a custom-made tool with an alternate combination algorithm.

The PRIDE framework will show the image combination run as a separate entry (referred to as processing step) in the scan execution list directly following the MSI acquisition entry (scan step). Storing the executed scans as an ExamCard includes the processing step. Reloading the same ExamCard for a different patient automatically starts the processing tool and selects the same combination algorithm that was used before.

7.3.3. Supported configurations

For imaging near metal, a low to moderate field strength is preferable. However, in some hospitals a 3T scanner may be a more accessible option than a 1.5T scanner or even the only option available for scanning patients with implants. Therefore, supporting all field strengths is important, especially during evaluation of the functionality using the prototype.

In first instance, the functionality is aimed at bulk implant material in the spine, the hip and the knee. Nonetheless, the prototype allows the evaluation of the functionality for any other application area as well.

7.4. User Interface

7.4.1. Acquisition parameters

The UI needs to provide a high level of flexibility to allow evaluation of different aspects of the functionality. The prototype includes additional acquisition parameters to switch and tune the advanced acquisition techniques.

For a good balance between flexibility and ease-of-use, a limited set of parameters is added and these are made available only if the combination with other more general acquisition parameters is useful. For example, VAT and MSI techniques are only made available if the *scan technique* is set to *TSE* (see Table 7.4).

Each parameter is assigned a sensible default value. For instance, the advanced scanning techniques are switched off by default and the default SEMAC factor covers the frequency content of signal selected with the default ORS factor, which is defined as the ratio of excitation and refocusing gradients.

Some parameters are implemented as *control scan parameters.* Unlike acquisition parameters, which are part of a scan sequence, a control scan parameter is defined at the system level and has a value which applies to all scan sequences, until it is changed explicitly by the user. An example is the configurable factor by which the refocusing pulse bandwidth is divided to obtain a suitable inversion pulse for homogeneous inversion in MAVRIC and ORS-MAVRIC. This factor is implemented as a control scan parameter called *IR 3D enc. inv. ratio.*

The ORS factor is defined as the ratio of excitation gradient and refocusing gradient. This ratio is accessible already in the scanner release software for suppression of ambiguity artifacts and can be manipulated using the control scan parameter *RFE selection gradient ratios*. For VAT and SEMAC, the value of the ORS factor is set to 1.2.

The ratio of excitation and refocusing gradient has no meaning for ORS-MAVRIC, as the refocusing gradient is zero. MAVRIC and ORS-MAVRIC are switched by a single UI parameter called “MAVRIC”, which may have the value No, Non-selective, or Selective.

Some UI parameters are mainly for the purpose of determining the most appropriate value, and are not expected to be maintained in the final product. An example of such a parameter is the frequency shift between adjacent bins within MAVRIC and ORS-MAVRIC. There is interdependence between the spectral bin spacing, the FWHM bandwidth of the spectral bins, and the image combination method, which is to be selected out of four available combination methods, as described in section 7.3.1. The FWHM may be influenced by slice profile erosion, depending on the number of refocusing pulses of the scan sequence. This effect has not yet been studied fully. The possibility must be provided to adapt the spectral bin spacing when needed.

To verify that bin interleaving does not lead to saturation due to cross-talk in MAVRIC or ORS-MAVRIC, the prototype must allow a comparison of interleaved and non-interleaved bin acquisition. Therefore, the UI includes a parameter for MAVRIC and ORS-MAVRIC acquisitions called “number of packages”, which can be set to minimum (closest bin interleaving without saturation) and maximum (no bin interleaving).

VAT reapplies the selection gradient during readout. ORS uses different gradients during excitation and refocusing, which results in a slight ambiguity in the definition of the selection gradient strength and of the VAT gradient, in case VAT with ORS or ORS-SEMAC is used. In the prototype the VAT gradient may therefore be chosen equal to the excitation gradient, the refocusing gradient strength, the mean of both gradients or the inversed mean of both gradients $\left(\frac{2}{{}^{1}/_{G_{EX}}+{}^{1}/_{G_{REF}}} = \frac{2 \cdot G_{EX} \cdot G_{REF}}{G_{EX}+G_{REF}}\right)$. These four options are provided to determine which one gives the best results.

Table 7.4 presents an overview of parameters related to metal artifact reduction, the value options, default values and dependencies on other parameters.

7.4.2. Image combination

Starting the PRIDE framework opens a window with a basic user interface with two entries that allow the user to select the research tool and its arguments. The image combination tool is called “Combine Semac Mavric” and takes a single argument of a single character to select the combination algorithm (Figure 7.7).

The tool creates an output series that contains the combined data. The name of the output series is a copy of the name of the input series, prefixed with the abbreviation of the selected algorithm (see Table 7.3).

Argument	Algorithm	Prefixed output series name
0	Maximum Intensity Projection	MIP_<input series name>
1	Linear Modulus Summation	LIN_<input series name>
2	Sum of Squares	SSQ_<input series name>
C	Linear Complex Summation	CPX_<input series name>

Table 7.3: Algorithm selection and prefix for output series name

Figure 7.6: The user interface of the PRIDE framework has two entries: one for selection of the processing tool (top) and one for passing arguments (bottom).

7.5. Implementation and tuning of default parameter values

7.5.1. Through-plane phase encoding

Both MAVRIC and SEMAC entail a through-plane phase encoding. In SEMAC, the selected volume is equal to or on the order of the phase encoded slice thickness, which is much smaller than the entire encoded volume, and also much smaller than the through-plane dimension of a selected volume in MAVRIC. Yet, as through-plane phase encoding is used in both MAVRIC and SEMAC, they can both be considered 3D techniques.

In the scanner release software, all required structures and loops for through-plane phase encoding are available for standard 3D techniques. Therefore, MAVRIC and SEMAC are also implemented as 3D techniques. This implementation is not only the most appropriate, but also the least invasive to the existing scanner release software, and therefore the least error-prone. The MAVRIC and SEMAC options are enabled only if the user has selected 3D scan mode.

7.5.2. SENSE reference scan

In the existing scanner release software, reference scans are available as fixed protocols, and the user is not allowed to adapt the parameters of these reference scans. Reference scan protocols with deviating parameters are even automatically replaced by conventional FFE reference scans. Obviously, when scanning near metal, the use of the TSE reference scan must be allowed and the automatic replacement disabled.

In the prototype, the default value of the existing control scan parameter *SENSE ref. scan UI* is changed to *full* which allows the use and adaptation of any SENSE reference scan protocol, and prevents SENSE reference scan to be replaced by an FFE SENSE reference scan.

7.5.3. Spectral bins and packaging in MAVRIC and ORS-MAVRIC

7.5.3.1. Spectral bin spacing

To determine the optimal bin spacing for typical ORS-MAVRIC acquisition settings, a simple phantom setup was made with a homogeneously filled water bottle and a shim-gradient switched on at 1 mT/m in the AP direction, orthogonal to the bottle's main axis, leading to a varying B_0-field in this direction. This phantom setup was imaged at 1.5T using a multi-channel head RF-coil. ORS-MAVRIC acquisitions were made with different spectral bin spacings (Figure 7.7). Spectral bins were not interleaved in these acquisitions.

Especially for ORS-MAVRIC, using different bandwidths for excitation and refocusing is helpful to maintain a constant spectral coverage for a range of off-center positions (Eq. 5.16). In view of SAR limitations, the bandwidth of the excitation RF pulse is increased and the refocusing RF bandwidth is maintained. The RF pulse bandwidths per spectral bin were 3.3 kHz for excitation and 1.1 kHz for refocusing at a B1 amplitude of 20 µT. These RF pulse bandwidth settings may be considered quite common for MAVRIC and ORS-MAVRIC acquisitions at 1.5T. They are independent on other acquisition settings like FOV or resolution, and may be used as long as implant specific SAR limitations allow. For these settings, 830 Hz spectral bin spacing resulted in combined images with the best homogeneity at 1.5T. Hence, 830 Hz is adopted as the default value for Δf_0, the f_0 shift parameter.

7.5.3.2. Acceptable nearness

The same phantom setup was used to determine the acceptable nearness of spectral bins measured within a single package of an ORS-MAVRIC acquisition. Again, the RF pulse bandwidths per spectral bin were 3.3 kHz for excitation and 1.1 kHz for refocusing, and the default spectral bin spacing of 830 Hz was used. Images were acquired using different settings for the distance between spectral bins within a single package, ranging from 3 to 6 times the spectral bin spacing. While 4×830 Hz or higher resulted in very similar image homogeneity, a distance of 3×830 Hz caused cross-talk between bins and homogeneity was clearly more affected (Figure 7.8). Hence, we can derive that the acceptable nearness is 4×830 Hz = 3.3 kHz, which equals the excitation bandwidth.

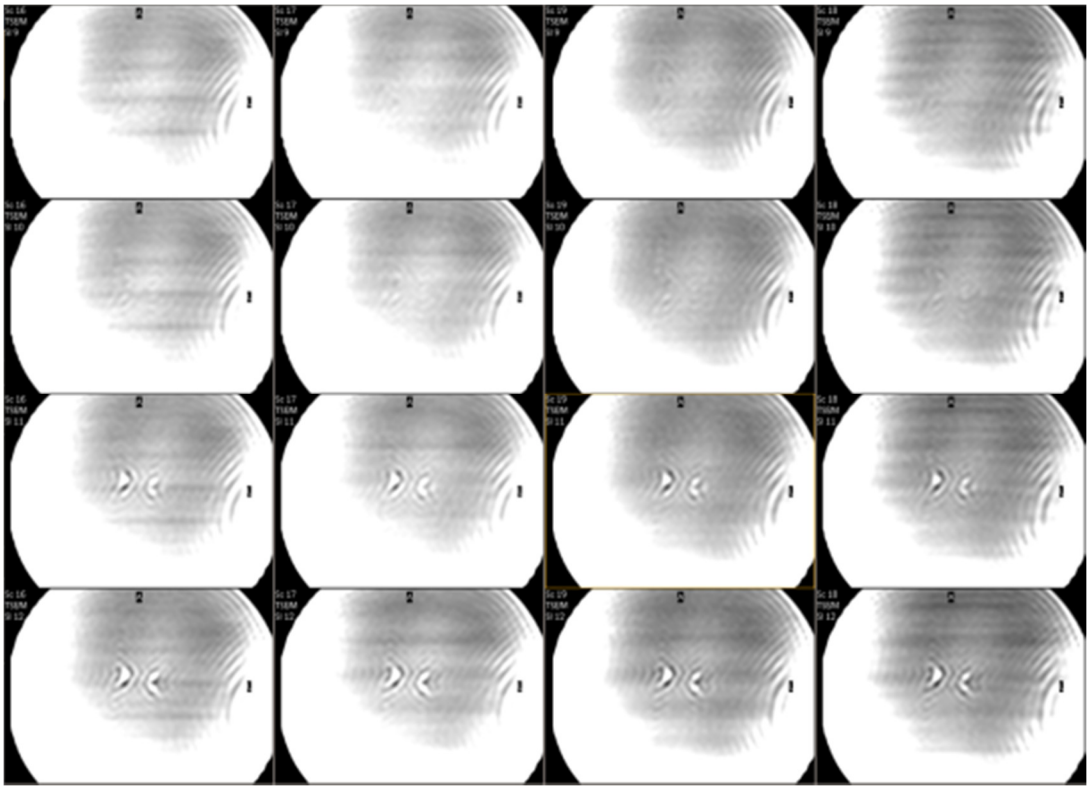

Figure 7.7: ORS-MAVRIC acquisitions of a homogeneously filled water bottle in an applied gradient field of 1 mT/m in the AP direction (vertical), scanned with different spectral bin spacings of –from left to right– 770 Hz, 800 Hz, 830 Hz and 860 Hz. For the RF pulse bandwidths used in this acquisition, 830 Hz spacing resulted in the best homogeneity.

As mentioned in section 7.3.1, the acceptable nearness is determined by the maximum FWHM bandwidth of excitation and refocusing pulse bandwidth, multiplied by a factor to account for side-lobes and tails of the RF pulses. This factor is implemented as a control scan parameter *Min. rel. freq. distance of Mavric bins* in the prototype and its value is set to 1.0 based on this phantom experiment.

7.5.3.3. Acquisition order of spectral bins

After determining the number of packages, the distribution of the spectral bins over packages can be defined. To minimize the risk of cross-talk, the spectral distance between bins that reside within one package is maximized. All bins between two consecutive bins of the same package must each be assigned to a uniquely different package, to ensure the same maximized bin spacing for all packages. Therefore, the distance between bins within a package, expressed in number of bins, equals the number of packages in the scan (Figure 7.9).

A special point of attention is the first bin measured. Reconstruction scales pixel values to 12-bits integer values for storage according to the DICOM standard. This enables values ranging from 0 to 4095. This range is to be exploited well, as too small a range of pixel values would result in discretization noise, and too large a range of pixel values will not fit in the 12 bits prescribed by the DICOM standard.

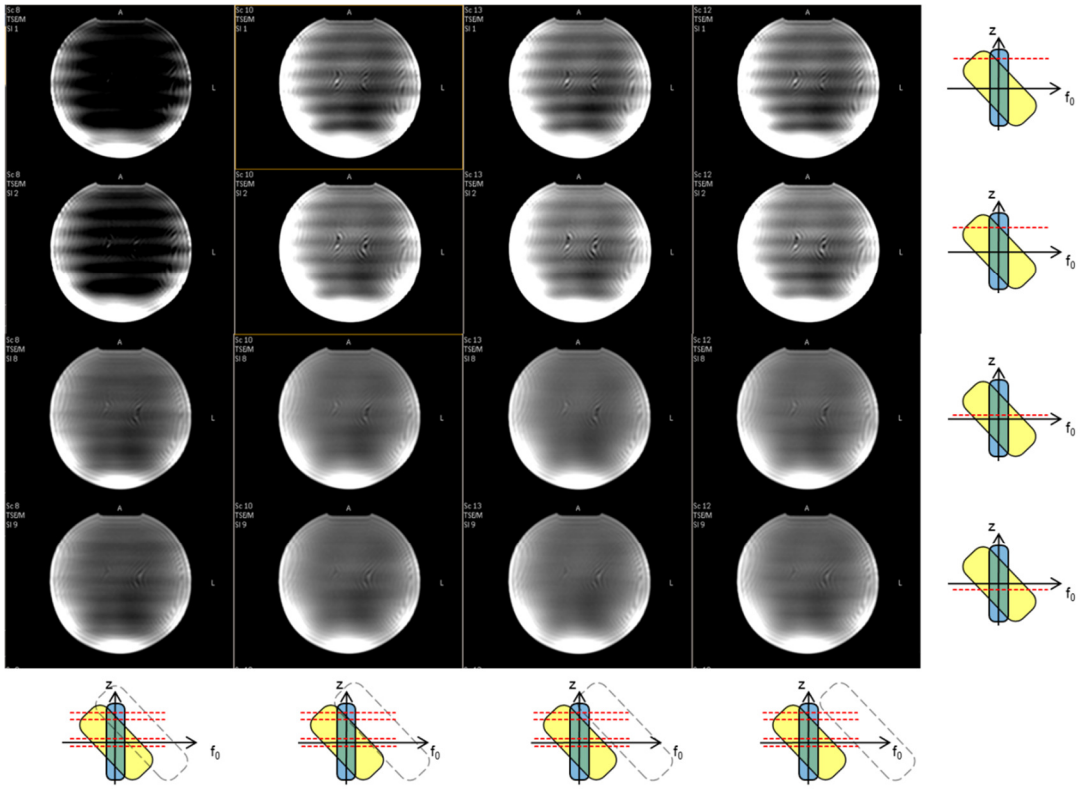

Figure 7.8: ORS-MAVRIC acquisitions of homogeneously filled water bottle in an applied gradient field of 1 mT/m in the AP direction (vertical), scanned with a spectral bin spacing of 830 Hz. The spectral bins were interleaved keeping a minimal distance between bins within one package of –from left to right– 3, 4, 5, and 6 times the spectral bin spacing. Slices shown are from the peripheral part (top two rows) and the central part (bottom two rows) of the selected volume.
In the right column, the through-plane position of the slices is indicated by the red dotted lines in s-f_0 diagrams that are analogous to the s-f_0 diagram shown in Figure 5.1j. The diagrams in the bottom row show that the risk of cross-talk with the excitation pulse (dotted diagonal bar) of another spectral bin depends on the bin spacing and on the slice position (see also Figure 5.2b).
The images show that 4×830 Hz distance between bins (second column) was acceptably near, and increasing the distance between bins (third and right column) did not lead to better homogeneity. A distance of 3×830 Hz within a single package (left column) clearly resulted in reduced homogeneity and loss of signal due to cross-talk between spectral bins.

Reconstruction always determines the scaling factor and intercept at the start of the acquisition, which allows storing all reconstructed image in DICOM immediately as soon as it can be made available for early viewing. All subsequent images are scaled with the same scaling factor and intercept. The reconstruction software may use the first reconstructed image, to verify and -if needed- adjust the maximum signal level expected during the scan for optimal scaling, just before this first image is stored in DICOM.

In the prototype implementation of MAVRIC and ORS-MAVRIC this first reconstructed image is in fact a sub-image from a single spectral bin. Depending on the frequency offset of a spectral bin, and the frequency dispersion of the signal present in the scanned object, a sub-image may contain very little signal, and reconstruction may underestimate the maximum signal level to be expected during the scan. This may lead to “clipping” of higher signal levels

later on, as the signal surpasses the maximum value of 4095. To avoid clipping, the first sub-image acquired must be from the on-resonance bin. So, the on-resonance bin is to be acquired first and must be part of the first package. All other packages may be acquired in order of frequency offset.

As in the example shown in Figure 7.9, the number of bins may not be a multiple of the number of packages, and some packages –e.g. the package that contains bins at the strongest off-resonance frequencies– may contain one bin more than others.

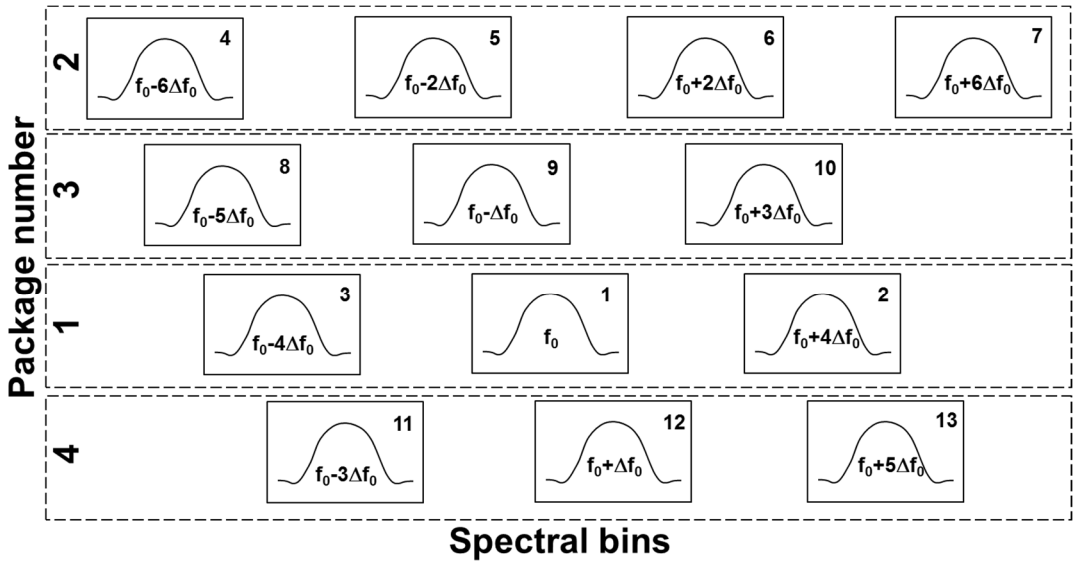

Figure 7.9: Distribution of spectral bins over packages in MAVRIC or ORS-MAVRIC acquisition: the separation between spectral bins that belong to a single package equals the number of packages: in the shown example this separation is $4 \cdot \Delta f_0$.
The package acquired first (third row) is the one containing the center bin. Within the first package, the center bin is acquired first to ensure on-resonance signal in the first image for correct scaling. Subsequent packages are acquired in order of bin frequency.
In the example shown here, the second package (top row) contains one bin more than the other packages, including the first package.

The following algorithm determines the overall acquisition order of spectral bins after distributing them over packages, taking into account that the first sub-image must be on-resonance and the distance between bins within a package must equal the number of packages.

```
center_bin = round_up( number_of_bins / 2 )
bin_index = 1

for each package ranging from 1 to number_of_packages {
    // The first package must contain the center bin
    if ( package == 1 ) {
        start_bin = center_bin
    }
    else if ( package <= center_bin MOD number_of_packages ) {
        // Next, fill the packages
        // starting from the package containing the lowest frequency bin
        // up until the package preceding the package containing the center bin
        start_bin = package - 1
    }
    else {
        // Finally, fill the remaining packages
        // starting from the package beyond the package containing the center bin
        start_bin = package
    }

    // Place all bins with positive frequency offset in order
    for each bin_offset ranging from start_bin to number_of_bins
            with steps of number_of_packages {
        acquisition_order[ bin_index ] = bin_offset
        increment bin_index
    }
    // Then, continue from the lower frequency side of the spectrum
    for each bin_offset ranging from (start_bin MOD number_of_packages)
            to number_of_bins with steps of number_of_packages {
        acquisition_order[ bin_index ] = bin_offset
        increment bin_index
    }
}

// The number of larger packages equals the number of bins left over
// after distributing as many bins as possible evenly over packages:
min_bins_per_package = round_down( number_of_bins / number_of_packages )
max_bins_per_package = round_up( number_of_bins / number_of_packages )
number_of_larger_packages = number_of_bins - min_bins_per_package * number_of_packages
for each package ranging from 1 until number_of_packages {
    if ( package <= number_of_larger_packages ) {
        number_of_bins_per_package[ package ] = max_bins_per_package
    }
    else {
        number_of_bins_per_package[ package ] = min_bins_per_package
    }
}

// All larger packages are now at the start,
// so the first small package is number_of_larger_packages+1
// But the center_bin is not in package number (center_bin MOD packages):
// instead this package was moved to the start.
if (center_bin MOD packages > number_of_larger_packages) {
    // the package containing the center_bin is a smaller package
    number_of_bins_per_package[ 1 ] = min_bins_per_package
    number_of_bins_per_package[ number_of_larger_packages+1 ] = max_bins_per_package
}
```

In this algorithm the MOD operator is used, which is defined as the residual value after performing an integer division of the first argument through the second argument.

7.5.4. Spectral bins and packaging in SEMAC and ORS-SEMAC

In SEMAC and ORS-SEMAC, the spectral bin spacing equals the spacing between slices and saturation between slices within a single package is avoided by using a fixed slice interleaving scheme (section 7.3.1). Hence, there is no need for tuning or using configuration parameters such as *acceptable nearness*.

The acquisition order is much less critical in SEMAC and ORS-SEMAC than in MAVRIC, as the center slice of each SEMAC sub-volume contains on-resonance signal. In the scanner release software, the center image of any 3D volume is reconstructed first, to ensure early availability of useful anatomical information from the center of the volume. Similarly, for SEMAC and ORS-SEMAC, the center sub-image of a 3D sub-volume is reconstructed first.

7.5.5. Image selection

ORS-MAVRIC images may have compromised homogeneity, especially in the peripheral region of the selected volume, and an optional modification of the implementation is to only produce images with optimal bin combination, around the center of the volume (see section 5.5). In the scanner release software, a parameter called “slice oversample factor” is available which acquires additional through-plane phase encodes on top of the requested and produced number of images. This parameter is quite appropriate for ORS-MAVRIC to produce only the images around the center of the acquired volume.

As explained in section 7.1.4, SEMAC images in the peripheral region increasingly lack spectral content, as the selected sub-volumes are not completely aligned (Figure 7.1). In the prototype, all images are made available, even if the essential on-resonance signal lacks, to validate whether the availability of on-resonance signal in the image is the appropriate criterion to determine its value.

7.5.6. Sub-image geometry

In the scanner release software, the attribute *location* is a unique identifier for each excited volume. In a conventional 3D acquisition, which may consist of multiple adjacent 3D volume selections, or slabs, each volume selection is identified as a *location*. For conventional multi-slice acquisitions, a *location* refers to a slice selection. An MSI acquisition consists of multiple sub-volumes. Each sub-volume corresponds to a selected slice with through-plane phase encoding for SEMAC or ORS-SEMAC, and to a spectral bin for MAVRIC or ORS-MAVRIC. MSI sub-volumes are also identified using the *location* attribute.

In conventional 3D multi-slab acquisitions, multiple slabs are positioned consecutively, and the geometric position of subsequent *locations* shifts by the size of the slab. In SEMAC and ORS-SEMAC, sub-volumes largely overlap, and the geometric position shifts by the thickness of an image. In MAVRIC and ORS-MAVRIC, all sub-volumes fully overlap and are at the same physical position. The geometric definition of a *location* is used for both the position of acquired signal, which is determined by the RF frequency offset and the gradients used during selection, as well as for reconstruction to determine and store the geometric position of each sub-image.

Acquisition Parameter	Parameter description	Value options	Default value	Condition for parameter availability
VAT	View Angle Tilting	Yes, No	No	Scan technique = (Turbo) Spin Echo
ORS	Off-Resonance Suppression	Yes, No	No	Scan technique = (Turbo) Spin Echo VAT = Yes
gradient strength	Strength of VAT gradient	Excitation, Refocus, Mean, Inversed-mean	Excitation	Scan technique = (Turbo) Spin Echo VAT = Yes ORS = Yes
SEMAC	SEMAC or ORS-SEMAC	Yes, No	No	Scan Mode = 3D Scan technique = (Turbo) Spin Echo VAT = Yes
encoding factor	Number of through-plane phase encoding steps	1-20	11	Scan Mode = 3D Scan technique = (Turbo) Spin Echo VAT = Yes SEMAC = Yes
MAVRIC	MAVRIC (Non-selective) or ORS-MAVRIC (Selective)	No, Selective, Non-selective	No	Scan mode = 3D Scan technique = (Turbo) Spin Echo
MAVRIC factor	Number of spectral bins	1-64	11	Scan mode = 3D Scan technique = (Turbo) Spin Echo MAVRIC != No
f0 shift (Hz)	Spectral bin spacing	0-10000	830	Scan mode = 3D Scan technique = (Turbo) Spin Echo MAVRIC != No MAVRIC factor > 1
number of packages	Option to put each spectral bin in a separate package	minimum, maximum	minimum	Scan mode = 3D Scan technique = (Turbo) Spin Echo MAVRIC != No

Control Scan Parameter	Parameter description	Value options	Default Value
RFE selection gradient ratios	ORS factor: ratio of excitation and refocusing gradient	0.1 – 10.0	1.2
SENSE ref. scan UI	Freedom to use and adapt SENSE reference scan protocols	default, extended, full	full
Min. rel. freq. distance of Mavric bins	Factor to account for side-lobes and tails of the RF pulse to avoid cross-talk	0.1 – 10.0	1.0
IR 3D enc. inv. ratio	Ratio between refocusing pulse bandwidth and inversion pulse bandwidth	1.0 – 5.0	2.0

Table 7.4: Acquisition parameters and control scan parameters in prototype

The prototype uses the reconstruction setup of the scanner release software to produce MSI sub-images, which are seen by the reconstruction software as normal images. The data for MSI sub-images is provided by the acquisition software to the reconstruction software in the same way as is done for diagnostic images in conventional scan sequences.

Subsequently, in the image processing tool, the combination of MSI sub-images into diagnostic images is done using the geometric information to identify sub-images from different sub-volumes that have identical position and therefore are to be combined.

7.5.7. Prototype activation and deactivation

For quick, easy, and robust activation and deactivation, the prototype comes with Perl scripts that are used more often for prototypes on the Philips MRI scanner. The activation script first terminates all processes on the MRI scanner. Then, the binary files of the scanner release software, that have been adapted in the prototype, are first renamed and then replaced by the prototype version of the same files. Additional files are copied to their appropriate location. Finally, the scanner processes are restarted. The deactivation script also first terminates the scanner processes, then it restores the original binary files of the scanner release software, and finally it restarts the scanner processes.

For safety, activation is only possible when the prototype is deactivated and vice versa. Both activation and deactivation script are available as a single click option at the start menu of the scanner's operating system. These menu options are made available automatically during first installation of the prototype software.

7.6. Prototype software and documentation

The prototype described in this chapter has been built and its source code, binary installation files and all relevant documentation are archived as the *MetAll* prototype at Philips Healthcare, Best, the Netherlands, in the *ClearCase* software archive, *acd* stream, versioned object base (VOB) *predevelopment*.

8. Verification and Validation of Artifact Reduction

8.1. Introduction

The prototype with MSI and ORS-MSI functionality, as described in chapter 7, was installed on a Philips 1.5T Achieva MRI scanner and used for technical verification and validation of the metal artifact reduction.

Phantom experiments were used to verify the achieved artifact reduction by comparison with the artifact reduction that is expected from theory. The thus verified aspects were through-plane distortion, in-plane distortion, the extent of the area with signal fluctuations and signal voids due to incomplete spectral coverage.

Additional phantom experiments were performed to validate whether the achieved artifact reduction met the clinical need (section 4.3.1) to provide diagnostic image quality sufficiently close to the metal implant.

8.2. Expected artifact reduction

As described in chapter 2, a variety of susceptibility effects may arise as a result of the presence of metal in the MRI scanner. MSI and ORS-MSI aim at substantially reducing many of these effects. Residual artifacts remain. This section gives an estimation of the upper limit of the extent of the residual artifacts as expected from theory and literature.

8.2.1. Through-plane distortion in MSI and ORS-MSI

In SEMAC and ORS-SEMAC, slice distortion is resolved by applying additional through-plane phase encoding, the accuracy of which is determined by the phase encoded image thickness S_{PE}. As 3D acquisition techniques, MAVRIC and ORS-MAVRIC use through-plane phase encoding as well. The sensitivity in the through-plane direction of a voxel in a 3D acquisition technique is much wider than the phase encoded image thickness [97]. Yet, signal is best represented by the voxel that resides closest to that signal, which in practice is maximally half the image thickness away. Hence, for both techniques, the remaining through-plane distortion from the center position of the image is limited to:

$$\Delta s_{max} = \frac{S_{PE}}{2}. \qquad (8.1)$$

8.2.2. In-plane distortion in SEMAC & ORS-SEMAC

SEMAC uses VAT for correction of in-plane distortion. VAT is associated with blurring as it leads to an extended voxel-length in the read-out direction (see section 3.1). The VAT induced geometric inaccuracy of imaged signal is determined by the view angle (Eq. 3.1) and is proportional to the off-center position of the signal in the through-plane direction, which has a maximum of half the through-plane phase encoded image thickness S_{PE} (Eq. 8.1):

$$\Delta m_{max} = \Delta s_{max} \cdot \tan(\beta) = \frac{S_{PE}}{2} \cdot \frac{G_{VAT}}{G_{READ}}. \qquad (8.2)$$

Here, G_{VAT} is the VAT gradient, which can be chosen in between or equal to one of the selection gradients. By using a maximum read-out bandwidth G_{READ} [61], and essentially reducing the tilt of the voxels, blurring is minimized.

8.2.3. In-plane distortion in MAVRIC & ORS-MAVRIC

In MAVRIC, the frequency range of selected signal is limited to the bandwidth of the spectral bin, as determined by the spatially non-selective pulse, which is usually the refocusing pulse. With both the transmission and reception RF frequency set to the center of the spectral bin, the disturbance of the frequency encoding process by off-resonance signal leads to a maximum displacement of:

$$\Delta m_{max} = \frac{BW_{REF}}{2\gamma \cdot G_{READ}}. \qquad (8.3)$$

8.2.4. Signal fluctuations and ripple artifact

Different mechanisms may lead to signal fluctuations. Slice distortions in conventional TSE include thicker or thinner slice selections where local field gradients (dB_0/ds) counteract or add to the applied selection gradient, respectively. These slice thickness variations lead to difficult to predict signal variations because they depend on the metal induced local field deviations and gradients, and with that on the material, size, shape, and orientation of the metal implant. The through-plane phase encoding of SEMAC resolves the slice thickness variations, resulting in homogeneous image intensity. MAVRIC uses slab selection significantly larger than the phase encoded image thickness, and therefore does not suffer from inhomogeneities due to selection thickness variation.

In SEMAC and ORS-SEMAC, another mechanism may cause signal fluctuations in regions with both in-plane and through-plane local field gradients ($dB_0/dm \neq 0$ and $dB_0/ds \neq 0$) (see chapter 6).

Although the in-plane distortion itself is limited to Eq. 8.2, the extent of the area that includes resulting signal fluctuations is much larger. Diagnostic value of the image can be compromised significantly by the ripple artifact. The actual extent of the ripple artifact is difficult to predict as it depends on the distribution of metal induced main field deviations and gradients. But it is possible to qualitatively compare the extent of the ripple artifact in SEMAC with the artifact extent in conventional TSE, as explained below.

In SEMAC, the ripple artifact may appear where slices traverse the image plane, i.e. where the slice distortion exceeds the phase encoded image thickness:

$$\Delta s > S_{PE}. \qquad (8.4)$$

Eq. 8.4 is not the only criterion for the visibility of the ripple artifact. Other criteria include the sign of the local field gradient dB_0/dm compared to the read-out gradient, and the sign of dB_0/ds compared to the selection gradient (chapter 6).

Similarly, for conventional high-bandwidth TSE, the distortion of the selected slice is appreciable where it is on the order of or larger than the slice thickness:

$$\Delta s \gtrsim \mathrm{STK}. \qquad (8.5)$$

In the physical region where this condition is met, off-resonance signal is selected. In the image, the distorted region may extend further due to potentially substantial in-plane distortion of this off-resonance signal (Eq. 5.3).

Typically, the image thickness S_{PE} used in SEMAC corresponds to the slice thickness STK used in conventional high-bandwidth TSE, as both are determined by the desired through-plane resolution. This suggests that for typical acquisition parameters, Eq. 8.4 and Eq. 8.5 express similar conditions, and the artifacts have similar size in SEMAC and high-bandwidth TSE. Depending on the field gradients, the ripple artifact in SEMAC may also be substantially smaller than the distorted area in high-bandwidth TSE (chapter 6).

In ORS-SEMAC, the ripple artifact is more pronounced than in SEMAC, but the area affected by the ripple artifact is very similar as in principle the same conditions apply for the appearance of the ripple artifact.

In MAVRIC, signal fluctuations may also arise as a consequence of signal displacement due to disturbance of the frequency encoding process. As shown by Koch et al. in [37], significant signal increase may be observed if local susceptibility gradients reach roughly 60% of the read-out gradient strength, with opposing sign:

$$\frac{\mathrm{dB_0/dm}}{\mathrm{G_{READ}}} \leq -0.6. \qquad (8.6)$$

In areas where signal frequencies vary more than the bandwidth of a single spectral bin of the MAVRIC acquisition, signal pile-up in multiple spectral bins results in signal fluctuation.

Generally, the condition given in Eq. 8.6 is only met in areas considerably nearer to the implant than where Eq. 8.4 is met in SEMAC acquisitions. Therefore, the artifact area is likely significantly smaller in MAVRIC than in SEMAC. With a strongly overlapping frequency response of adjacent spectral bins, MAVRIC is also less sensitive than SEMAC to signal intensity variations due to the disturbance of the frequency encoding process in these areas.

8.2.5. Signal voids due to incomplete spectral coverage in ORS-MSI

The selectivity of ORS-MSI allows for tunable trade-off between scan-time and spectral coverage in ORS-MAVRIC by the number of spectral bins and in ORS-SEMAC by the selection gradients (Eq. 5.9).

In principle, in conventional TSE, it is also possible to tune the selection gradient ratio in order to improve spectral coverage, but consequently increased slice distortion would not be resolved. Therefore, increasing the spectral coverage in conventional TSE would only add to the metal artifact. The originally proposed SEMAC uses equal selection gradients. In principle, this results in unlimited spectral coverage, where strongly off-resonance signal leads to back-folding due to the limited SEMAC factor.

8.3. Methods

This section describes the phantom experiments to verify the estimations provided in section 8.2 of the extent of the residual artifact and to validate whether the achieved artifact reduction met the clinical need.

8.3.1. Verification using stainless steel rod

Using the prototype with SEMAC, ORS-SEMAC, MAVRIC and ORS-MAVRIC functionality, phantom experiments were performed to verify the amount of signal displacement and the artifact extent. A stainless steel rod of 10 mm diameter was placed vertically in a container with water and Gadolinium. A plastic Ampmodu Mod IV connector (Tyco Electronics, PA, USA) with 1×1-mm holes was used as resolution grid and was attached horizontally to the rod, with the holes parallel to the rod.

A conventional multi-slice TSE scan was made orthogonal to the rod in the coronal plane, with the read-out direction parallel to the main magnetic field. The in-plane resolution was 1×1 mm, and the slice thickness 4 mm. Then, an ORS-SEMAC acquisition was made with the same geometry and the same resolution. A spectral range of 17.4 kHz centered on the Larmor frequency was covered by applying a SEMAC factor of 13. An ORS-MAVRIC scan was also acquired, again with the same geometry and resolution. With 19 spectral bins at a frequency shift of 830 Hz per bin, the total spectral coverage was 15.8 kHz. Sub-images of the ORS-SEMAC and ORS-MAVRIC acquisitions were combined using a sum-of-squares algorithm. The combined images of the three acquisitions were processed with a minimum intensity projection of the acquired volume along the main magnetic field axis and along the direction of the rod to show through-plane and in-plane distortion, respectively.

Next, for verification of the extent of the ripple artifact, the conventional multi-slice TSE and the ORS-SEMAC acquisitions were repeated with an angulation of 45° around the axis of the main magnetic field. In the non-angulated coronal plane orthogonal to the rod, only in-plane field gradients are present due to symmetry. The 45° angulation introduces through-plane field gradients of similar strength as in-plane field gradients, and sets suitable conditions for the ripple artifact to appear (see chapter 6).

Finally, a non-angulated coronal ORS-SEMAC scan was acquired, but with an increased selected spectral range of 26.1 kHz, which was covered by a SEMAC factor of 21. And similarly, additional ORS-MAVRIC scans were acquired with 31 spectral bins for a spectral range of 25.7 kHz, and with 55 spectral bins for a spectral range of 45.7 kHz. This last acquisition was used to derive a B_0 map.

Parallel imaging can be used to speed up these acquisitions but this was disabled in all sequences. Selection gradients and RF bandwidths used during excitation and refocusing in all above acquisitions are listed in Table 8.1. In all scans, the read-out gradient was 20.7 mT/m, leading to a bandwidth of 880 Hz/mm.

Acquisition	G_{EX} (mT/m)	G_{REF} (mT/m)	BW_{EX} (kHz)	BW_{REF} (kHz)	Spectral coverage (kHz)	Scan-time
Conventional TSE	6.12	7.34	1.13	1.47	14.1	1'28"
ORS-SEMAC, factor 13	8.81	7.34	1.98	1.25	17.4	6'30"
ORS-MAVRIC, 19 bins	0.80	0	3.29	1.09	15.8	8'42"
ORS-SEMAC, factor 21	8.26	7.34	1.85	1.25	26.1	10'30"
ORS-MAVRIC, 31 bins	0.80	0	3.29	1.09	25.7	13'55"
ORS-MAVRIC, 55 bins	0.80	0	3.29	1.09	45.7	12'36"

Table 8.1: Experimental parameters for acquisitions using stainless steel rod phantom setup.

8.3.2. Validation using hip implant samples

To validate the capability of the functional prototype to meet the clinical requirements (section 4.3), measurements were performed on two phantom setups using hip implant samples placed on Ampmodu Mod IV connectors in Gd doped water. One phantom setup included an Allopro titanium alloy hip implant (Sulzer, Switzerland), the other an Exeter stainless steel hip implant stem (Stryker, NJ, USA).

Scans were made on the same 1.5T MRI scanner as during the verification. For each implant, the scans included a conventional multi-slice TSE protocol, an ORS-SEMAC protocol and ORS-MAVRIC protocols. All acquisitions were made in the coronal plane, using a read-out gradient of 20.7 mT/m leading to a read-out bandwidth of 873 Hz/mm. The in-plane resolution was 1×1 mm and the slice thickness 4 mm. The FOV was 212×140 mm. Other scan parameters are listed in Table 8.2.

Since it is based on a 3D TSE acquisition with reduced refocusing flip angles, ORS-MAVRIC is sensitive to so-called FID artifacts: signal resulting from the FID of a refocusing pulse. These signals are not properly phase encoded and may appear at completely different positions in the image than the signal source they originate from. FID artifacts may especially be found when scanning large volumes of fluid such as the phantom setup used in these experiments. The ORS-MAVRIC protocols were therefore repeated with two averaged measurements (Number of Signals Averaged – NSA), where the phase of the RF pulse was inverted in the second measurement to cancel the FID signals in both measurements.

Near the stainless steel implant, the spectral coverage of the signal was incomplete. Hence, an additional ORS-MAVRIC scan with 55 spectral bins was acquired for increased spectral coverage.

Acquisition	G_{EX} (mT/m)	G_{REF} (mT/m)	BW_{EX} (kHz)	BW_{REF} (kHz)	Spectral coverage (kHz)	TR/TE (ms)	NSA	Scan-time
Titanium alloy hip implant sample								
Conventional TSE	6.12	7.34	1.13	1.47	14.1	400 16	2	1’24”
ORS-SEMAC factor 13	8.81	7.34	1.98	1.25	17.4	500 15	1	3’54”
ORS-MAVRIC 19 bins	0.80	0	3.29	1.09	15.8	450 32	1	4’03”
ORS-MAVRIC 19 bins	0.80	0	3.29	1.09	15.8	450 32	2	8’06”
Stainless steel hip implant sample								
Conventional TSE	6.12	7.34	1.13	1.47	14.1	400 16	2	1’24”
ORS-SEMAC factor 19	8.26	7.34	1.85	1.25	26.1	500 15	1	8’33”
ORS-MAVRIC 19 bins	0.80	0	3.29	1.09	15.8	450 32	2	7’48”
ORS-MAVRIC 55 bins	0.80	0	3.29	1.09	39.0	450 32	2	21’50”

Table 8.2: Experimental parameters for acquisitions using hip implant sample phantoms.

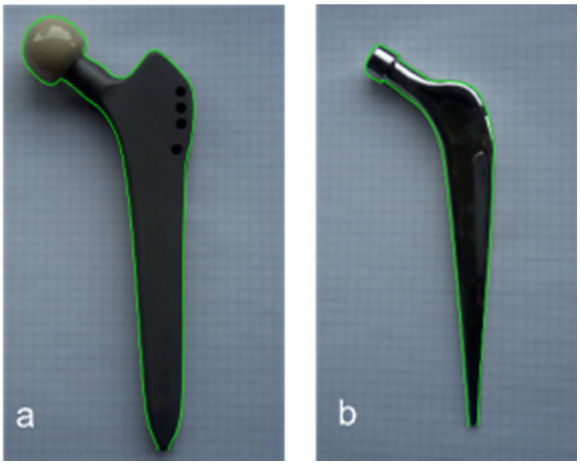

Figure 8.1: Photographs of titanium alloy (a) and stainless steel (b) hip implant samples on a background of graph ruled paper with a 5×5 mm grid, with contour drawn around the implant (green).

A photograph was taken of each hip implant sample on a background of graph ruled paper with a 5×5 mm grid (Figure 8.1). The photographs were resized to match the MR images. A contour was drawn on the photograph around the implant and was matched with the position of the implant in the acquired images. The extent of the artifacts surrounding the implant, defined as the maximum distance from the implant, was then estimated using the overlaid contour and an overlaid 10×10-mm grid.

8.4. Results

8.4.1. Verification using stainless steel rod

8.4.1.1. Through-plane distortion

In conventional TSE, signal was visible close to the rod up to a frequency deviation of 6 to 7 kHz. This frequency deviation was deduced from visual correlation with the ORS-MAVRIC acquisition by counting grid holes in the uncombined images and from the derived B_0 map (Figure 8.2). This frequency deviation was near the cut-off frequency of 7 kHz as predicted by Eq. 5.8 (see also the spectral coverage listed in Table 8.1). Minimum intensity projection along the main magnetic field axis showed a through-plane distortion of the grid of 22±2 mm (Figure 8.3a), where a frequency deviation of 6.5±0.4 kHz was found which corresponds to a slice distortion of 23±3 mm. At the cut-off frequency of 7 kHz, the distortion would proportionally be 25±2 mm, which nicely corresponds to the predicted maximum through-plane displacement of 25.0 mm by Eq. 5.7.

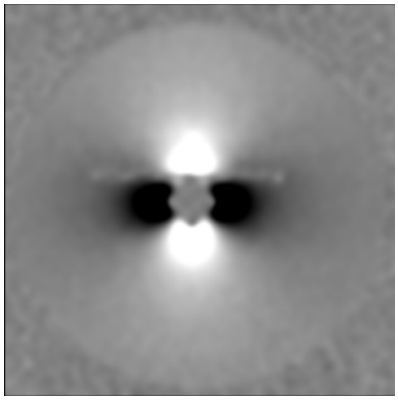

Figure 8.2: B_0 map derived from ORS-MAVRIC acquisition with 55 bins at a frequency shift of 830 Hz/bin.

In the minimum intensity projections of both ORS-SEMAC (Figure 8.3b) and ORS-MAVRIC (Figure 8.3c), no through-plane distortions larger than 2 mm were visible, which confirms a spatial accuracy of half the slice thickness (Eq. 8.1).

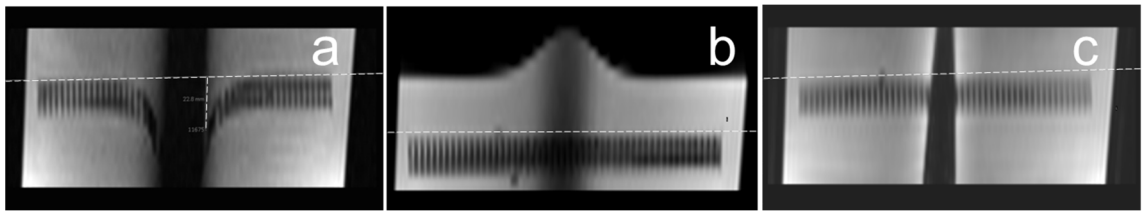

Figure 8.3: Minimum intensity projection along the main magnetic field axis, showing through-plane distortion in conventional TSE (a), ORS-SEMAC (b) and ORS-MAVRIC (c).

8.4.1.2. In-plane distortion

The minimum intensity projection of the conventional TSE along the direction of the rod showed displacement of signal in the frequency encoding direction by 7.5±1 mm at a frequency deviation of 6.5±0.4 kHz (Figure 8.4a). This implies a distortion of 8.1±1.5 mm at

the cut-off frequency of 7 kHz, which corresponds to the predicted maximum in-plane displacement of 7 mm (Eq. 2.6).

The same minimum intensity projections for ORS-SEMAC showed a maximum in-plane displacement of roughly 1 mm (Figure 8.4b). The difference with the expected maximum in-plane displacement based on theory (0.7 mm, Eq. 8.2) is well below the resolution of the acquisition. Similarly, for ORS-MAVRIC, an in-plane displacement of roughly 0.5 mm was observed (Figure 8.4c), where the model predicted 0.6 mm (Eq. 8.3), which is both well below the acquired resolution.

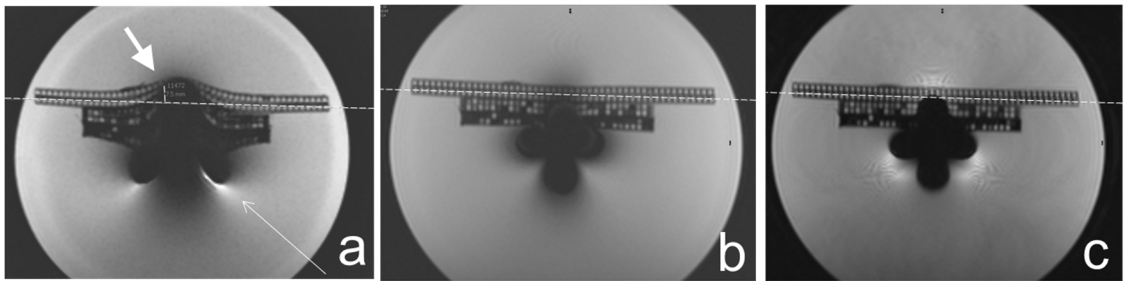

Figure 8.4: Minimum intensity projection along the direction of the rod. The resolution grid has a straight geometry. A line parallel to the grid shows the in-plane distortion near the metal, in conventional TSE (orthogonal line near thick arrow, a), in ORS-SEMAC (b) and in ORS-MAVRIC (c). Note the signal intensity variation due to signal displacement in the conventional TSE (thin arrow), which is substantially reduced in ORS-SEMAC and ORS-MAVRIC.

8.4.1.3. Signal fluctuations and ripple artifact

The ripple artifact was absent in the ORS-SEMAC acquired orthogonally to the rod, but was clearly observed in the angulated ORS-SEMAC scan (Figure 8.5). The extent of the artifact was compared to the distorted area in the conventional TSE scan acquired under the same angulation. Due to the slice distortion in conventional TSE, there is no single slice that completely matches the ORS-SEMAC image for comparison. The comparison was made based on the slices where the position of the artifact areas matched most closely. At this slice position, the extent of the ripple artifact in ORS-SEMAC was similar to the extent of the distorted area in conventional TSE (Figure 8.5a), up to 39 mm distance from the rod center. Note, that for conventional TSE, the extent of the distorted area was on the same order in the non-angulated scan (Figure 8.4a).

In the ORS-MAVRIC scans, signal fluctuations were observed as well. The extent of the artifact area was considerably smaller, up to 25 mm distance from the rod center, reducing the artifact area roughly by a factor 2 to 3. The local susceptibility gradient in the artifact area was determined by measuring the distance between signal peaks that correspond to the centers of spectral bins spaced at 830 Hz (white line in Figure 8.5c), and was found to be 12 mT/m which is 60% of the read-out gradient of 20 mT/m used (Eq. 8.6). The relative signal intensity varied much less in ORS-MAVRIC than in ORS-SEMAC, as shown in the intensity profiles of Figure 8.5b and c.

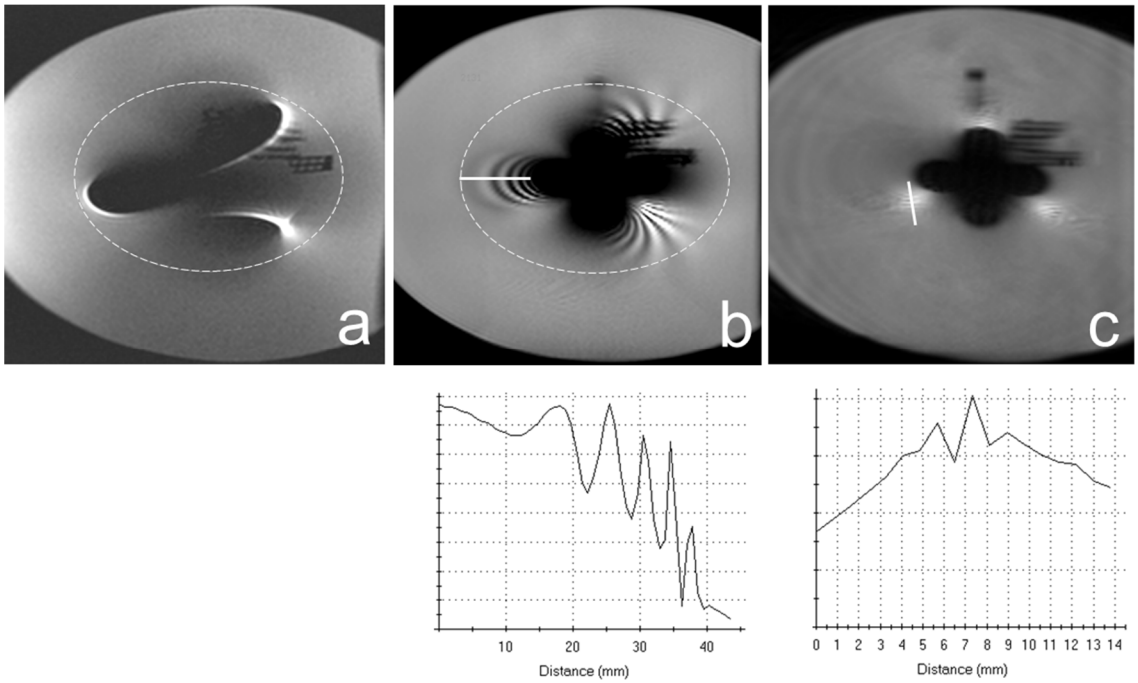

Figure 8.5: Conventional TSE (a), ORS-SEMAC (b) and ORS-MAVRIC (c) acquired under 45° angulation to the stainless steel rod. The dashed contour indicates similar extent of the distortion area in conventional TSE (a) and the extent of the ripple artifact in ORS-SEMAC (b). The signal fluctuation in ORS-MAVRIC has considerably smaller extent as well as smaller relative signal intensity variation than in ORS-SEMAC.

8.4.1.4. Signal voids due to incomplete spectral coverage

ORS-SEMAC with SEMAC factor 13 and ORS-MAVRIC with 19 spectral bins showed similar extent of the signal void (Figure 8.6a,b), which corresponds to the similar spectral coverage for these two acquisitions listed in Table 8.1. In conventional TSE, the extent of the signal void was larger due to in-plane distortion (Figure 8.4a). In both the ORS-SEMAC with SEMAC factor 21 and the ORS-MAVRIC with 31 spectral bins, the spectral coverage was around 26 kHz (Table 8.1), leading to similarly reduced signal voids (roughly 15 mm instead of roughly 20 mm) and a similar amount of additional unveiled signal in both sequences (Figure 8.6c,d). Note, that both ORS-SEMAC and ORS-MAVRIC provide a trade-off mechanism between scan-time and spectral coverage.

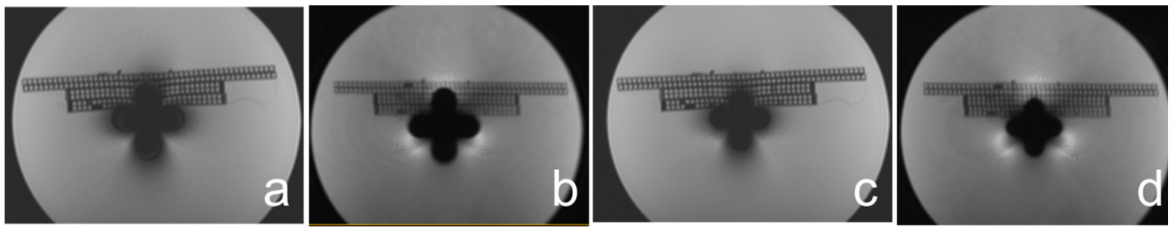

Figure 8.6: ORS-SEMAC with SEMAC factor 13, spectral coverage 17.4 kHz (a), ORS-MAVRIC with 19 bins, spectral coverage 15.8 kHz (b), ORS-SEMAC, factor 21, 26.1 kHz (c), and ORS-MAVRIC, 31 bins, 25.7 kHz (d).

8.4.2. Validation using hip implant samples

Figure 8.7 shows the MRI images of the titanium hip implant with overlaid contour and grid. The conventional TSE images (Figure 8.7a,b) were hyper-intense next to the implant stem,

and showed through-plane distortion especially around the femoral neck. Signal voids and signal pile-ups extended up to roughly a centimeter from the implant, as estimated using the 10×10-mm grid.

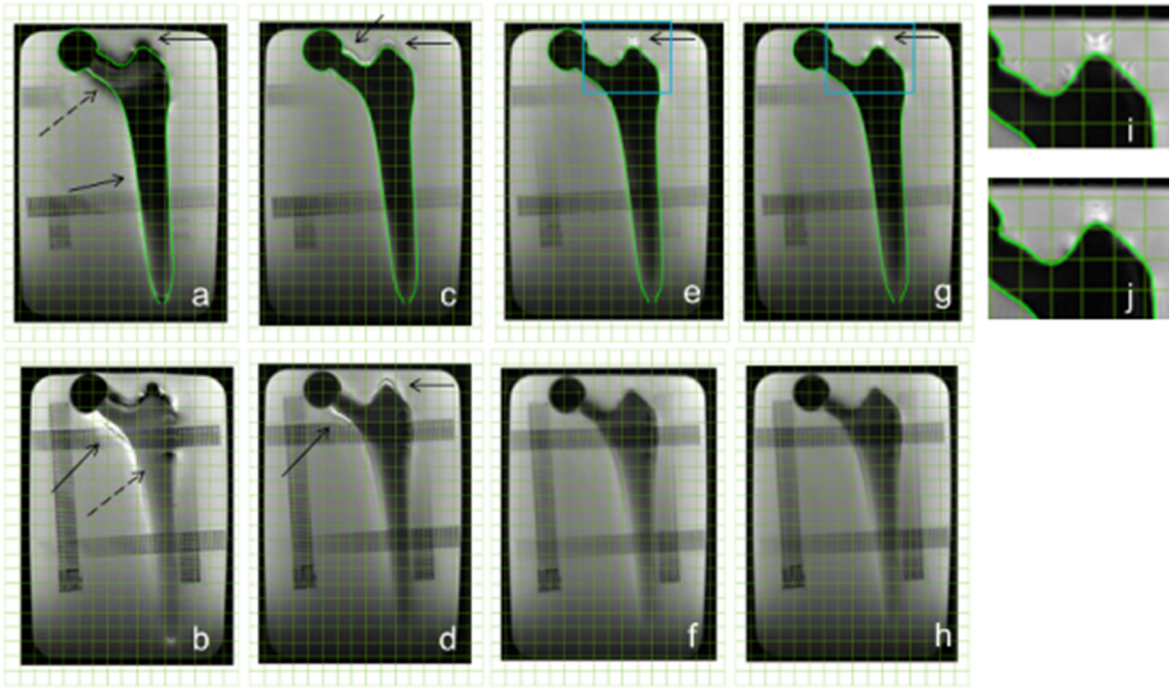

Figure 8.7: Titanium alloy hip implant sample: conventional TSE (mid-slice shown in a, adjacent slice in b), ORS-SEMAC (c,d), ORS-MAVRIC with 1 NSA (e,f, zoomed area in i) and with 2 NSA (g,h, zoomed area in j). In the conventional TSE image, through-plane distortion (dashed arrows) is visible especially inside the implant (b) where signal should be absent. Solid arrows indicate other residual in-plane artifacts: signal voids (a), signal pile-up (b), ripple-artifact (c,d), FID artifacts (e) and bin compression (e,g).

The ORS-SEMAC images (Figure 8.7c,d) showed reduced artifact, and especially reduced through-plane distortion and better homogeneity along the hip stem, resulting in a clear delineation of the hip stem. The ripple artifact was clearly visible up to roughly half a centimeter from the implant.

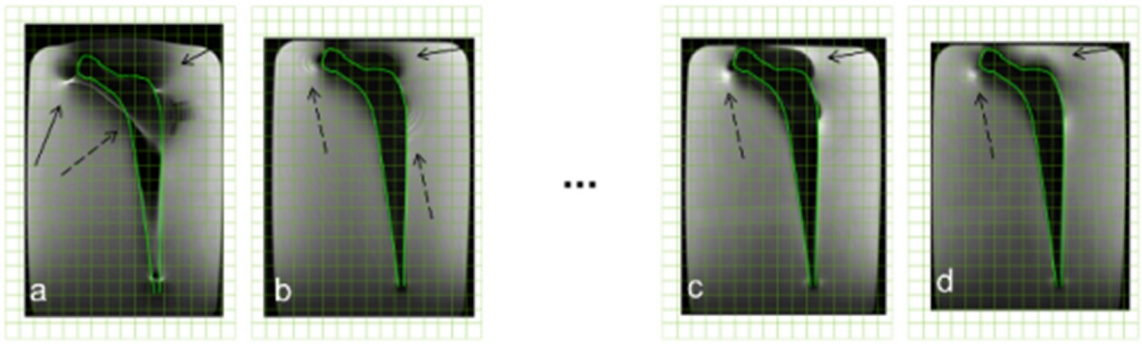

Figure 8.8: Stainless steel hip implant sample: conventional TSE (a), ORS-SEMAC (b), ORS-MAVRIC with 2 NSA and 19 spectral bins (c) and with 55 spectral bins (d). Arrows indicate residual artifacts: signal voids and signal pile-up (solid arrows), through-plane distortion (dashed arrow, a), ripple-artifact (dashed arrows, b), bin compression (dashed arrows, c,d). No single-NSA ORS-MAVRIC image is shown (dots).

ORS-MAVRIC (Figure 8.7e,f) further reduced the artifacts near the implant. Residual signal fluctuations were visible at the cranial side of the implant (zoomed area in Figure 8.7i). These signal fluctuations were reduced when the ORS-MAVRIC acquisition was performed with two measurements (NSA=2, Figure 8.7g,h), which confirmed that these fluctuations were at least partly caused by FID signal induced by the refocusing pulses. Yet, some residual signal intensity error remained (zoomed area in Figure 8.7j) extending up to roughly half a centimeter from the implant, which may be attributed to compression of signal in the frequency encoding direction [37].

Figure 8.8 shows the MR images of the stainless steel implant. Conventional TSE images (Figure 8.8a) showed signal pile-ups and large signal voids (solid arrows) as well as through-plane distortion (dashed arrows).

Using ORS-SEMAC (Figure 8.8b), showed better delineation of the hip stem and the signal pile-ups disappeared. But signal voids, though reduced, were still visible up to more than a centimeter from the implant in some regions (solid arrows), as was the ripple artifact (dashed arrows).

ORS-MAVRIC (Figure 8.8c) using NSA = 2 (single-NSA ORS-MAVRIC image not shown) also suffered from signal voids of more than a centimeter measured from the implant (solid arrows). Hyper-intense regions (dashed arrows) resulting from signal compression in the frequency encoding direction [37] were generally smaller than the signal voids but were also visible up to more than a centimeter from the implant. Increasing the number of spectral bins to 55 (Figure 8.8d) further reduced the signal voids to roughly half a centimeter from the implant, but residual signal intensity error remained at larger distance. The scan duration of more than 20 minutes for this acquisition would have been unacceptable in clinical routine and would require acceleration by combining the multispectral technique with parallel imaging and/or compressed sensing [58,59,60].

8.5. Conclusion & Discussion

The functionality of the prototype was verified using a stainless steel rod phantom. The residual artifacts in terms of in-plane distortion, through-plane distortion, extent of the area with signal fluctuations and spectral coverage corresponded to what was expected from theory. The measured in-plane and through-plane distortions confirmed the estimations based on theory of the signal displacement as well as of the ability of ORS-SEMAC and ORS-MAVRIC to resolve these displacements significantly up to or close to the resolution of the acquisition.

Both in-plane and through-plane distortions caused signal variations, that were substantially reduced simultaneously with the resolution of the displacements by ORS-SEMAC and ORS-MAVRIC (Figure 8.4).

Even though individual residual signal displacements were relatively small, the verification also confirmed that in ORS-SEMAC the extent of the remaining ripple artifact –that consists of multiple displaced signals (section 6.2)– is typically similar to or smaller than the extent of the distorted area in conventional TSE. In ORS-SEMAC, it would have been possible to reduce

the ripple artifact by using slice overlap (chapter 6), but this functionality was not yet available at the time the prototype was developed.

In ORS-MAVRIC, the artifact area and the relative signal intensity variations were considerably smaller than in ORS-SEMAC. In ORS-MAVRIC, additional signal fluctuation may be observed near the edge of the selected volume, where signal tapers off (Figure 5.1j). This effect is largely compensated by only reconstructing images with acceptable homogeneity near the center of the volume (section 7.5.5).

A spectral coverage of 15 kHz centered around the Larmor frequency is often sufficient [56]. ORS-SEMAC and ORS-MAVRIC allowed additional signal with stronger off-resonance frequency to be imaged (Table 8.1), providing a trade-off between scan-time and spectral coverage. ORS-SEMAC and ORS-MAVRIC acquisitions with equally tuned spectral coverage had equal ability to image off-resonance signal.

Signal voids may occasionally occur, where strong local field gradients completely counteract the frequency encoding gradient, but this was not observed in the phantom experiments with the stainless steel rod.

The validation using the hip implant samples showed that conventional TSE imaging near the titanium hip implant led to limited artifact and this could be reduced using ORS-SEMAC or ORS-MAVRIC to a level that would allow diagnosis of many indications listed in the clinical requirements (see section 4.3.1). ORS-SEMAC and ORS-MAVRIC provided correction of through-plane distortion and reduced the original artifact to less than or roughly equal to half a centimeter distance from the titanium implant. Diagnostic image quality at this distance could enable diagnosis of pseudotumors, effusion, edema, bone tumors, and muscular atrophy (section 4.3.1).

Near the stainless steel implant, residual artifacts remained over a centimeter from the implant, especially in the regions cranial from the femoral neck section. In those regions, diagnosis of most of these diseases would be hampered. It was shown that the artifact level could be further reduced in ORS-MAVRIC by acquiring a larger spectral coverage, but residual artifact remained at more than half a centimeter distance from the implant. Imaging near bulk stainless steel implants, such as the hip implant studied here, is expected to be the most challenging. Many other implants, smaller in size or made of different materials, may cause less artifact and allow sufficient artifact reduction in clinically feasible scan-times.

For both hip implants, ORS-SEMAC and ORS-MAVRIC provided improved delineation of the implant stem. Around most of the hip stem, image quality was restored at 1 or 2 mm distance from the implant. Diagnostic image quality at 1 or 2 mm distance from the implant could enable diagnosis of osteolysis (section 4.3.1.5).

The accuracy of the validation described here had limitations. The validation was performed only for two bulk metal implants. There was no exact criterion as to what signal level deviation was to be considered artifact. Instead, the artifact extent was determined by visual inspection. The contour was suitable to estimate artifact extent only in the mid-slice, whereas artifacts were clearly visible in adjacent slices as well. The contour was not suitable

to estimate the extent of the through-plane artifacts. A more accurate and much more elaborate method has been described by Kolind et al. [61], who measured artifact energy in VAT imaging by comparing images of an implant to images of a 3D wax model of that implant. The 3D wax model enabled assessment of the through-plane distortion in the VAT images. That method has not been used in the work described here, as only minimal residual through-plane distortion was found in ORS-SEMAC and ORS-MAVRIC (Figure 8.3b,c), as was expected based on theory.

The performed validation gives a rough impression, of how much artifact reduction is achieved and how much remains, as well as how this compares to the clinical need. Therefore, the validation method used here is considered adequate to assess the usefulness of the prototype in clinical practice.

The residual artifacts near the stainless steel hip implant are generally related to frequency encoding [37]. By choosing a different frequency encoding direction, the largest artifacts are expected to appear at different locations with respect to the implant. Frequency encoding and all its related artifacts may be completely eliminated by using SPI acquisition techniques (section 3.3.2, [74,75,76]). However, at the current state-of-the-art, these techniques are still associated with severely increased scan duration, making them as of yet impractical for clinical use.

9. Recommendations, Outlook and Conclusion

9.1. Required and achieved artifact reduction.

The extent of the artifacts induced by a metal implant depends strongly on the implant, its material, size, shape, and orientation with respect to the main magnetic field. Hence, whether the achieved artifact reduction using ORS-MSI is sufficient for tissue evaluation near the implant depends on the implant (section 8.4.2) and the required artifact limit to enable diagnosis of a disease (section 4.3.1). Table 9.1 gives an overview of the efficacy of the metal artifact reduction by using ORS-MSI to meet these requirements and to correct the position, homogeneity and intensity of signal at the required distance for the implants used during validation (section 8.4.2) and for diseases that are commonly diagnosed using MRI (section 2.2). Validations were performed at the required resolution and within the required scan duration listed in Table 4.2 (see Table 8.2). Although not shown in this work, similar scan protocols can be defined for all required contrast weightings T1w, T2w, STIR and PDw, using either ORS-SEMAC or ORS-MAVRIC.

Disease	**Artifact limit after metal artifact reduction by ORS-MSI**				
	Required distance from implant	**Titanium hip implant**		**Stainless Steel hip implant**	
		Cranial	**Caudal**	**Cranial**	**Caudal**
Pseudotumor	5 mm	+	++	--	++
Effusion and bone marrow edema	5 mm	+	++	--	++
Bone oncology	5 mm	+	++	--	++
Muscular atrophy	10 or 20 mm	++	++	+	++
Osteolysis and loosening	1 or 2 mm	-	+	-	+
Infections	larger distance	++	++	++	++

Table 9.1: Efficacy of metal artifact reduction techniques ORS-SEMAC and ORS-MAVRIC to meet the clinical requirement for diseases near metal that are commonly diagnosed using MRI. At and above the required distance from the implant (second column), the requirements for signal homogeneity and intensity and correct position of signal is met (+) or amply met (++) for some cases, but not met (-) or not nearly met (--) for others.

There is an enormous variety of implants. Especially near smaller implants such as fixation screws (section 5.4.3), or near titanium bulk implants (section 8.4.2), the artifact reduction

with ORS-MSI is sufficient to allow diagnostic imaging for most diseases commonly diagnosed using MRI. For stainless steel bulk implants the achieved artifact reduction only partly meets these clinical requirements (Table 9.1). Yet, even for those more difficult cases, the artifact reduction with ORS-MSI is sufficient in some regions near the implant –e.g. near the hip stem– to meet the requirements for diagnosis of all mentioned diseases. In all our experiments, metal artifacts were never increased by the use of ORS-MSI.

ORS-MSI enables tissue visualization within clinically feasible scan-times in regions more near to metal implants than is possible with conventional scanning techniques. It meets the clinical requirement fully for some implants and partly for others (see Table 9.1), and is in general more adequate than other currently available scan techniques.

Further clinical evaluation of the ORS-MSI functionality is needed to prove the impact of the ability to evaluate tissue closer to the metal in clinical practice. Initial clinical evaluation results have become available recently. These first results show that, near fixation screws in the spine, ORS-SEMAC enables significantly improved periprosthetic visualizations of the pedicle, vertebral body, dural sac and neural foramina, compared with conventional scanning techniques [12,98]. Improved diagnostic accuracy is also demonstrated near hip implants as ORS-SEMAC improves visualization of fluid collections, pseudotumors and osteolysis [10,11]. Based on the technical verification and validation (chapter 8), ORS-MAVRIC may be expected to provide similar or even further improved artifact reduction. These early results are encouraging enough to recommend proceeding with product development of the functionality.

9.2. Recommendations for product development

This section contains recommendations for product development of the technology regarding correction, applicability, usability, and speed, in conformity with the technical requirements (section 7.1).

9.2.1. Correction

9.2.1.1. Scan techniques

Both ORS-SEMAC and ORS-MAVRIC are expected to provide similar substantial artifact reductions. Both techniques enable imaging of a region that covers part or all of the implant, depending on the user's preference.

Each technique has its own characteristics and benefits. ORS-MAVRIC enables imaging near metal without the use of VAT, which causes blurring in the frequency encoding direction (see Figure 5.4 and [61,62]). In ORS-MAVRIC, residual artifacts occur at different locations and tend to be smaller than in ORS-SEMAC. Yet, the residual ripple artifact in ORS-SEMAC can be reduced by using slice overlap. As a 3D technique, ORS-MAVRIC allows the use of acceleration techniques such as parallel imaging or potentially even partial matrix acquisition in two phase encoding directions, whereas in ORS-SEMAC, these acceleration techniques are not appropriate in the through-plane direction due to the limited number of phase encoding steps.

Based on a multi-slice acquisition, ORS-SEMAC uses RF pulse profiles that are better optimized for interleaving than those used in ORS-MAVRIC. The wide excitation bandwidth (Table 8.1) used in ORS-MAVRIC imposes strict limitations on the acceptable nearness of spectral bins within a single package. With a much narrower excitation bandwidth, ORS-SEMAC slices acquired within one package require much less spacing (cf. Figure 5.2a and Figure 5.2b). Additionally, for many implants such as fixation screws or bulk titanium implants, the required number of spectral bins in ORS-MAVRIC (typically on the order of 13 or less) is usually smaller than the number of slices in ORS-SEMAC (typically on the order of 24). Thus, interleaving slices in ORS-SEMAC is more efficient than interleaving spectral bins in ORS-MAVRIC. This property makes ORS-SEMAC especially suitable for T2w acquisitions and for efficiently using the long TR in T2w acquisitions. Enabling slice overlap in ORS-SEMAC increases the required spacing between slices of one package, and may reduce the efficiency of ORS-SEMAC for T2w acquisitions.

With each technique featuring its own benefits, it is recommended to include both techniques in the product. As an example, experiences with the different parallel imaging approaches SENSE [26] and GRAPPA [28] have shown that each technique has its strengths and benefits. Similarly, as the MSI technology has not been widely used yet, it can be expected that new insights provide additional arguments for the availability of both potentially complementary techniques.

It is recommended to have ORS enabled per default, to avoid the risk of unexpected and confusing through-plane aliasing. The option to disable ORS should be available but may not be needed routinely and may be provided as a control scan parameter, to avoid accidental mistakes (see Table 9.2).

Hybrid techniques, such as MSVAT-SPACE [66] and VS-3D-MSI [60], combine properties of MAVRIC and SEMAC. The selectivity of these techniques enables acquisition of a limited region that includes the implant. However, back-folding may still occur depending on the scan orientation, if a region smaller than the implant is selected or if another implant is present in the patient (see section 3.2.3). The selectivity mechanism of ORS-MAVRIC and ORS-SEMAC allows full planning flexibility in these respects, without the risk of back-folding. Hence, providing a hybrid technique next to ORS-MAVRIC and ORS-SEMAC is not recommended.

9.2.1.2. Pulse profile, spectral bin spacing and acceptable nearness

Homogeneity requires that a good match is maintained between the selection pulse profile, the spectral bin spacing and the image combination algorithm (see section 9.2.1.3).The truncated and windowed sinc RF pulses with Gaussian-like profiles that were used for the prototype provided optimal homogeneity in the combined diagnostic images with relatively low sensitivity to signal displacements in the frequency encoding direction ([60], sections 6.2.1 and 7.3.1). The same pulses are therefore recommended to use in the product as well.

For the spacing between spectral bins in ORS-MAVRIC, 830 Hz was found to be an appropriate value for the acquisitions made during verification (section 7.5.3). In these acquisitions, the RF pulse bandwidths per spectral bin were commonly 3.3 kHz for excitation

and 1.1 kHz for refocusing at 1.5 T. Spectral response profiles resulting from a CPMG pulse train depend on the number of refocusing pulses and are often considered roughly comparable to the profile of the refocusing pulse. A suitable value for the spectral bin spacing at any main field strength and for any pulse bandwidth is obtained by defining the spectral bin spacing as a fraction of the refocusing pulse. Based on the experiments, the recommended default value for this fraction is 830 Hz / 1.1 kHz = 0.75.

The acceptable nearness of spectral bins measured within a single package of an ORS-MAVRIC acquisition was determined for the prototype (section 7.5.3.2). For product development, the same approach and value is recommended, to ensure that excitation pulses and refocusing pulses of neighboring spectral bins within a single package do not overlap. If additional pulses are used, such as an inversion pulse for STIR, it is essential that these preparation pulses do not overlap either. As such preparation pulses may be associated with much larger bandwidths and tails, an acceptable nearness is to be defined for all preparation pulses to be used with ORS-MSI as well.

In ORS-SEMAC, with or without STIR, saturation of neighboring spectral bins is avoided by complying with the same conditions as apply to conventional multi-slice or multi-slab TSE (section 7.3.1).

9.2.1.3. Image Combination and Selection

The experiments showed that the image quality in terms of SNR and homogeneity depends on the combination algorithm used for combining the sub-images. Homogeneity was substantially compromised if a MIP algorithm or linear modulus summation was used. Using sum-of-squares led to superior SNR compared with linear complex summation, but the latter resulted in a slightly improved homogeneity ([67], section 7.3.2), specifically near transitions between spectral bins. However, linear complex summation requires reliable phase information of the signal, which may not always be available. For instance, if acceleration techniques such as half-scan are used, and available phase information is unreliable, linear complex summation may lead to dephasing between overlapping adjacent spectral bins causing loss of SNR and homogeneity. Therefore, it is recommended that sub-images are always combined with sum-of-squares for robust, reliable, and especially consistent SNR. Sum-of-squares generally results in a reasonable homogeneity. Residual inhomogeneity near spectral bin transitions such as the ripple artifact may be addressed by using slice overlap. Linear complex summation may be provided via a control scan parameter as an additional option for research purposes.

As opposed to the prototype, sub-images are not considered useful for the product. Instead, the image combination should be performed in the reconstruction software, which then stores the combined diagnostic images directly into the image database.

Images from the periphery of an ORS-SEMAC acquisition contain off-resonance signal only, and are not considered useful. Instead, it is recommended that the number of combined images produced by reconstruction software is equal to the number of slices requested in the acquisition parameters. This does not only avoid confusion about the number of

obtained images, but also ensures, that every produced image contains on-resonance signal and is likely useful for diagnosis.

To ensure that at least one ORS-SEMAC image –in the center of the volume of interest– has full spectral coverage, it is recommended that the number of user requested slice selections is enforced to be equal to or larger than the SEMAC factor (Eq. 7.2).

9.2.1.4. Slice Overlap

Slice overlap may be used to reduce the ripple artifact in ORS-SEMAC and improve image quality near the metal implant as well as to improve resolution, though at the cost of an additional increase in the already substantial scan-time. As this trade-off between scan-time, resolution and artifact level is not easily settled for all applications, the choice whether or not to use slice overlap should be available to the user. Therefore, it is recommended to make slice overlap available as a binary option acquisition parameter.

9.2.2. Applicability

Preset scan sequence definitions with the appropriate contrasts and resolution, as described in section 7.1.2, need to be made available together with the product.

Early evaluation results of the ORS-MSI functionality shows that the achieved artifact reduction is clinically relevant on both 1.5T [10,11] and 3.0T [12]. At lower field strengths (such as a 1.0T open MRI scanner), metal implants induce smaller artifacts, which makes these scanners especially suitable for imaging near metal implants. Therefore, implementation of the product for all clinically available field strengths is recommended.

9.2.3. Usability

9.2.3.1. User interface and acquisition parameters

While the aim of the prototype was to provide maximum flexibility for experiments on the different aspects of the novel acquisition techniques, the aim of the product is to enable robust and consistent application of these techniques in clinical practice, requiring simplicity in the user interface and ease-of-use of the acquisition parameters.

Ease-of-use is achieved first by providing a single switch which enables or disables the metal artifact reduction techniques. This switch may be implemented as an acquisition parameter “Metal Artifact Reduction”. By default, all techniques are disabled (parameter value “No”). The user may choose to enable MARS (Metal Artifact Reduction Sequence), ORS-SEMAC or ORS-MAVRIC in the acquisition protocol. The MARS option enables TSE with VAT and a high-bandwidth read-out.

If ORS-SEMAC or ORS-MAVRIC is selected, an additional parameter “Correction” is provided with a few preset value options that correspond to the spectral coverage of the scan needed for e.g. small stainless steel implants (weak, e.g. 11 kHz coverage), bulk titanium implants (medium, e.g. 16 kHz) and bulk stainless steel implants (strong, e.g. 25 kHz), respectively. If ORS-SEMAC is selected, a binary option acquisition parameter “Slice Overlap” is made available as well.

Setting the “Metal Artifact Reduction” parameter to anything else than “No” puts the scanner in imaging-near-metal-mode. In this mode, the user is first warned that specific safety regulations apply for scanning in the presence of metal implants. Second, special measures are taken for robustness against scan aborts, as elaborated in section 9.2.3.3. And third, the combinations with techniques that are incompatible with metal artifact reduction, such as spectral fat suppression techniques, are disabled. Specifically for ORS-SEMAC, the number of through-plane phase encoding (kz) steps is relatively small. Therefore, the possibility to change the filling of ky-kz space, using parameters such as the k-space shutter, is disabled to avoid discretization artifacts. Here, ky represents the in-plane phase encoding dimension.

In the prototype, the SEMAC factor and the ORS factor were available as independent parameters, even though they may both be derived from the cut-off frequency using the well-defined relation given in Eq. 5.9. For the product, it is recommended to derive both factors automatically from the cut-off frequency determined by the acquisition parameter “Correction”.

While the VAT gradient must equal the selection gradient, the definition of the selection gradient becomes ambiguous when ORS is enabled and the excitation gradient differs from the refocusing gradient. The prototype acquisition parameter “VAT gradient strength” allowed investigation of the influence of small variations of the VAT gradient from excitation to refocusing gradient strength. Though this investigation has not yet been performed, the image quality using the default value of this parameter (excitation) appeared to be sufficiently encouraging to decide for product development. Therefore, for the product, it is recommended to maintain the VAT gradient at the excitation gradient strength. The acquisition parameter “VAT gradient strength” may be removed or replaced by a control scan parameter for future investigations.

Table 9.2 presents an overview of parameters related to metal artifact reduction, the value options, default values and dependencies on other parameters, as recommended for the product.

9.2.3.2. ExamCards and preset sequences

As mentioned in section 7.1.4, ExamCards are indispensable for ease-of-use of the functionality. These ExamCards need to include preset sequences for the hip and pelvis, the knee and the spine, and provide T1w, T2w, PDw and STIR PDw contrasts, based on ORS-MSI techniques, as well as the faster MARS sequences, and a TSE survey.

9.2.3.3. Robustness

In the scanner release software, the f_0 preparation often succeeds in spite of the presence of metal. However, in some cases the f_0 measurement may result in a warning to the user if a large frequency deviation is found. Extreme resonance frequency dispersions that are too wide to determine a single f_0 peak value may even lead to a scan abort as the software concludes that no object is present in the scanner (section 2.5).

While for the prototype it is accepted that sporadically a scan may abort due to a failing f_0 preparation measurement (section 7.2), the product needs a robust f_0 preparation. The existing f_0 preparation determines signal and noise from a single spectrum measurement. Instead, the noise determination should be secluded from the signal determination.

Acquisition Parameter	**Value options**	**Default value**	**Condition for parameter availability**
Metal Artifact Reduction	No, MARS, ORS-SEMAC, ORS-MAVRIC	No	Scan technique = (Turbo) Spin Echo
Correction	Weak, Medium, Strong	Medium	Scan technique = (Turbo) Spin Echo Metal Artifact Reduction = ORS-SEMAC or ORS-MAVRIC
Slice Overlap	No, Yes	No	Scan technique = (Turbo) Spin Echo Metal Artifact Reduction = ORS-SEMAC
Control Scan Parameter	**Value options**	**Default Value**	
Mavric bin spacing fraction	0.1 – 10.0	0.75	
Min. rel. freq. distance of Mavric bins	0.1 – 10.0	1.0	
Min. rel. freq. distance of IR Mavric bins	0.1 – 10.0	2.0	
IR 3D enc. inv. ratio	1.0 – 5.0	2.0	
ORS	Yes, No	Yes	
VAT gradient strength	Excitation, Refocus, Mean, Inversed-mean	Excitation	
MSI combination algorithm	Sum of squares, Linear complex summation, MIP, Linear modulus summation	Sum of squares	

Table 9.2: Acquisition parameters and control scan parameters recommended for the product

If nonetheless –in spite of the secluded noise determination– the presence of metal would corrupt the spectrum measurement severely enough to lead to a failed f_0 preparation, this should not result in a scan abort. Instead, in imaging-near-metal-mode, a failed f_0 preparation should result in using the f_0 value stored during the previous examination. This

f_0 value should be sufficiently accurate, also in view of the fact that in the presence of bulk metal, there is no single f_0 value. The scanner should leave the choice to the user whether or not he wants to abort the scan, with an appropriate warning, informing the user about the potential causes of the failed f_0 preparation:

1. there may be nothing in the bore
2. slices may be misplaced

Several B_0 shimming techniques are available on the scanner to ensure maximally achievable B_0 homogeneity by compensating local gradients with an opposing static term of the scanner gradient. In the presence of metal, B_0 shimming is considered useless, as the B_0 variations near metal are so capricious that they can never be compensated using linear shim gradients. B_0 shimming may even lead to further degradation of the B_0 homogeneity, as the shimming technique may try to compensate strong local gradients in a small region with a shim gradient that is too strong for the larger volume of interest. Instead, switching off all shim gradients leads to more robust B_0 homogeneity. Therefore, it is recommended, that in imaging-near-metal-mode, B_0 shimming is automatically switched off.

9.2.4. Speed

Parallel imaging and partial matrix scanning have been applied successfully for ORS-MSI techniques throughout the evaluations. To maintain clinically feasible scan-times, parallel imaging will be an important acceleration technique to be used in all ORS-MSI sequences of the product implementation as well. This requires the use of a TSE reference scan whenever an ORS-MSI technique is selected. In conformity with the existing automatic insertion of FFE reference scans, the TSE reference scan needs to be inserted automatically in the scan execution list as well.

For further acceleration, the product needs to support the combination of ORS-MSI techniques with any other acceleration technique such as partial matrix scanning and –when available– compressed sensing.

9.3. Next steps

9.3.1. Frequency encoding limitations

Although ORS-MSI techniques provide substantial artifact reduction near metal implants, residual artifacts remain due to displacements in the frequency encoding direction [37]. As discussed in chapter 6, these displacements can be substantially reduced by using slice overlap. Further compensation of these displacements may be gained in processing by using a B_0-map generated from MAVRIC sub-images [64]. This processing technique also reduces blurring due to displacement in opposing directions of signal from overlapping adjacent bins [37]. The processing approach has its limitations especially for correcting resolution loss (section 6.5).

Another approach to reduce displacement in the frequency encoding direction may be to reduce the bandwidth of the RF pulses used for excitation and refocusing, thereby reducing the frequency dispersion of signal to be encoded in a single spectral bin. Effectively, this

approach increases the spectral resolution. Scan-time is increased as this approach requires that additional spectral bins are measured to cover the total frequency dispersion of spins near the metal implant.

More rigorously, SPI [74,75,76] may be used to completely eliminate all frequency encoding issues. SPI does not use any frequency encoding, but uses phase encoding in all spatial directions instead. Unrivaled artifact reduction is achieved with SPI, but at the cost of scan-times that are too long for clinical use at the current state of the art. Multiple studies that are currently being performed focus on accelerating SPI towards clinical usefulness [99,100,101,102] or reducing the scan-time of SPI by combination with MSI [103].

9.3.2. More speed

Even without the additional measures to address residual displacements in the frequency encoding direction, the scan-time of MSI and ORS-MSI techniques is a limiting factor, especially for cases such as bulk stainless steel implants, which require coverage of a large frequency range. Next to parallel imaging and partial matrix scanning, MSI and ORS-MSI techniques may be further accelerated using techniques such as compressed sensing [58,59], adaptive SEMAC which varies the number of through-plane phase encodes per slice depending on the slice distortion [87], and k-space subsampling [104]. RF pulse shapes may be optimized or truncated for shorter echo-spacing, taking into account that the SAR needs to remain limited or if possible reduced when scanning near metal.

9.3.3. B_1 effects

MSI techniques focus on reduction of metal artifact caused by B_0 inhomogeneity. However, especially at field strengths of 3T and higher, the B_1 field homogeneity is often also impacted by metal implants, as shown by Graf et al. [105]. Although the finite element simulations in that investigation clarify the cause of the B_1 field inhomogeneity, an alternate RF pulse scheme for improved robustness of the B_1 homogeneity has not yet been proposed.

A different B_1 effect is the FID artifact that is caused by FID signal induced by refocusing pulses in a CPMG train (see section 8.4.2). Repeating the measurement with an inverted RF pulse phase is an effective but costly approach to cancel the FID signals. As a compromise, the measurement may be repeated for the center of k-space only, which may lead to cancellation of the more prominent part of the FID signal at the cost of a limited scan-time increase.

9.3.4. Other applications

This work has focused mainly on the reduction of artifacts induced by orthopedic implants. But the need for diagnostic imaging near metal is not unique to orthopedics. Likewise, metal artifact reduction may be useful also for neurology, as imaging of the neural foramina is improved near orthopedic spine implants [12]. And there may be other metallic implants in the skull or even in the mandibula that reduce the quality of MR imaging of the brain, and thus require metal artifact reduction. In cardiovascular imaging the artifact reduction techniques may help to restore image quality near stents, aneurysm clips or valve implants. The value of MSI techniques to reduce metal artifacts for improved visualization of

brachytherapy devices was demonstrated by Warner et al. in [106], and MSI may benefit other intervention techniques similarly.

A different application of MAVRIC is to enable detection of microscopic field disturbers, such as iron disposition in the liver, as such disposition induces signal off-resonance that appears in the off-resonance sub-images [107]. In this case, the main aim of the MSI technique is not artifact reduction, but rather the enhanced visibility of the artifact induced by the material by imaging the off-resonance signal separately.

Finally, there may be applications for metal artifact reduction apart from the clinical setting, such as phantom, in-vitro or ex-vivo studies, where the artifact reduction provided by the MSI techniques can be used to its full extent, as scan-times are much less critical.

9.3.5. Clinical evaluation

Clinical evaluation of the functionality is in progress, and early results demonstrate enough clinical benefit to recommend product development at this stage. Further clinical evaluation of the functionality –using either the prototype or the product– will likely help to set the priority on either addressing residual metal artifacts or scan-time reduction.

9.4. Conclusion

In this thesis, the design of a prototype for artifact reduction near metal was described. The prototype was built, its functionality verified and it was validated that the clinical needs can be met by the achieved artifact reduction for many implants. ORS-MSI has been proposed for metal implant artifact reduction within clinically feasible scan-times. In addition, the ripple artifact has been investigated and slice overlap has been proposed for reduction of the residual ripple artifact in ORS-SEMAC. The ORS-MSI technology provides a flexible trade-off between scan-time and metal artifact reduction. Even in cases for which the clinical requirements are only partially met, the substantial artifact reduction is still beneficial for improved evaluation of soft tissue near the metal. In conclusion, the evaluated functionality, soon to be available as commercial product, provides an important improvement in metal implant artifact reduction in MRI and enables tissue evaluation and diagnosis in clinically feasible scan-times closer to the metal implant than any other technique currently available.

A. References

1. Bloch F. Nuclear Induction. Phys Rev 1946;70:460-473.
2. Mansfield P. Proton magnetic resonance relaxation in solids by transient methods. PhD thesis, Queen Mary College, University of London, 1962.
3. Lauterbur, PC. Image formation by induced local interactions: examples employing nuclear magnetic resonance. Nature 1973;242.5394:190-191.
4. Damadian R. Apparatus and Method for Detecting Cancer In Tissue. US Patent US3789832. February 5, 1974.
5. Tofts P, Tofts PS. Quantitative MRI of the Brain: Measuring Changes Caused by Disease. John Wiley & Sons 2005; ISBN 9780470869499.
6. Filippi M, De Stefano N. MR Imaging in White Matter Diseases of the Brain and Spinal Cord. Springer 2005; ISBN 9783540402305.
7. Helms C, Major NM. Musculoskeletal MRI. Saunders 2008; ISBN 9781416055341.
8. Buthiau D, Khayat D. CT and MRI in Oncology. Springer 1998; ISBN 9783540627500.
9. Bogaert J, Dymarkowski S, Taylor AM. Clinical Cardiac MRI. Springer 2012; ISBN 9783642230349.
10. Ström C, Strinnholm J, Otten V, Hauksson J, Bruvold M, Blume U, den Harder C, Bos C. Evaluation of Slice Encoding for Metal Artifact Correction in Patients with Recalled Orthopedic Hip Implants. In Proceedings of the 20th Annual Meeting of ISMRM, Melbourne, Australia, 2012. p.3333.
11. Ström C, Strinnholm J, Crnalic S, Bruvold M, Blume U, den Harder C, Bos C. Evaluation of T2-weighted Slice Encoding for Metal Artifact Correction in Patients with Recalled Orthopedic Hip Implants. In Proceedings of the 21st Annual Meeting of ISMRM, Salt Lake City, UT, USA, 2013. p.3486.
12. Lee YH, Lim D, Kim E, Kim S, Song H-T, Suh J-S. Usefulness of slice encoding for metal artifact correction (SEMAC) for reducing metallic artifacts in 3-T MRI. Magn Reson Imag. 2013 Jun;31(5):703-706.
13. Mansfield P, Morris PG. NMR Imaging in Biomedicine. Academic Press, New York 1982; ISBN 9780120255627.
14. Haacke EM, Brown RW. Magnetic Resonance Imaging Physics: Physical Principles and Sequence Design. Springer Verlag 1998; ISBN 9780387946948.
15. Vlaardingerbroek MT, den Boer JA. Magnetic Resonance Imaging. Springer 1996; ISBN 9783540600800.
16. Ljunggren S. A simple graphical representation of fourier-based imaging methods. J Magn Reson 1983;54:338-343.
17. Bracewell RN. The Fourier Transform and Its Applications (3rd ed.). McGraw-Hill 2000; ISBN 9780071160438.
18. Hahn EL. Spin Echoes. Phys Rev 1950;20(4):580-594.
19. Carr H. Free Precession Techniques in Nuclear Magnetic Resonance. PhD thesis, Harvard University, Cambridge, MA, 1952.

20. Hutchison JMS, Sutherland RJ, Mallard JR. NMR imaging: image recovery under magnetic fields with large non-uniformities. J Phys E: Sci Instrum 1978;11:217-221.
21. Bakker CJG, Bhagwandien R, Moerland MA, Ramos LMP. Simulation of susceptibility artifacts in 2D and 3D Fourier transform spin-echo and gradient-echo magnetic resonance imaging. Magn Reson Imag 1993;11:539–548.
22. Bakker CJG, Bhagwandien R, Moerland MA, Fuderer M. Susceptibility Artifacts in 2DFT Spin-Echo and Gradient-Echo Imaging: the Cylinder Model Revisited. Magn Reson Imag 1993;11:539-548.
23. Carr HY, Purcell EM. Effects of Diffusion on Free Precession in Nuclear Magnetic Resonance Experiments. Phys Rev 1954; 94(3):630-638.
24. Hennig J, Nauerth A, Friedburg H. RARE imaging: a fast imaging method for clinical MRI. Magn Reson Med 1986;3:823-833.
25. Meiboom S, Gill D. Modified Spin-Echo Method for Measuring Nuclear Relaxation Times. Rev Sci Instrum 1958;29(8):688-691.
26. Pruessmann KP, Weiger M, Scheidegger MB, Boesiger P. SENSE: sensitivity encoding for fast MRI. Magn Reson Med 1999;42:952–962.
27. Sodickson DK, Manning WJ. Simultaneous acquisition of spatial harmonics (SMASH): fast imaging with radiofrequency coil arrays. Magn Reson Med 1997;38:591–603.
28. Griswold MA, Jakob PM, Heidemann RM, et al. Generalized autocalibrating partially parallel acquisitions (GRAPPA). Magn Reson Med 2002;47:1202–1210.
29. Shellock FG, Crues JV. MRI Bioeffects Safety and Patient Management. Biomedical Research Publishing Company 2013; ISBN 9780989163200.
30. Liu F, Zhao H, Crozier S. On the induced electric field gradients in the human body for magnetic stimulation by gradient coils in MRI. IEEE Trans Biomed Eng. 2003;50(7):804-815.
31. Oluigbo CO, Rezai AR. Magnetic resonance imaging safety of deep brain stimulator devices. Handb Clin Neurol. 2013;116:73-6. doi: 10.1016/B978-0-444-53497-2.00007-3.
32. International Electrotechnical Commission. Medical electrical equipment. Part 2-33: Particular requirements for the safety of magnetic resonance equipment for medical diagnosis. IEC 60601-2-33. Geneva:IEC, 2002.
33. Powell J, Papadaki A, Hand J, Hart A, McRobbie D. Numerical Simulation of SAR Induced Around Co-Cr-Mo Hip Prostheses In Situ Exposed to RF Fields Associated with 1.5 and 3 T MRI Body Coils. Magn Reson Med 2012;68:960-968.
34. Schenck JF. Role of Magnetic Susceptibility in MRI. Med Phys 1996;23(6):815-850.
35. Bhagwandien R1, van Ee R, Beersma R, Bakker CJ, Moerland MA, Lagendijk JJ. Numerical analysis of the magnetic field for arbitrary magnetic susceptibility distributions in 2D. Magn Reson Imag 1992;10(2):299-313.
36. Hargreaves BA, Worters PW, Butts KM, Pauly JM, Koch KM, Gold GE. Metal-Induced Artifacts in MRI. Am J Roentgenol 2011;197:547–555.
37. Koch KM, King KF, Carl M, Hargreaves BA. Imaging Near Metal: The Impact of Extreme Static Local Field Gradients on Frequency Encoding Processes. Magn Reson Med 2014;71:2024-2034.

38. Haase A, Frahm J, Hänicke W, Matthaei D. ^{1}H NMR chemical shift selective (CHESS) imaging. Phys Med Biol 1985;30:341-344.
39. de Becker J, Rozijn T, Visser F, Jones A, Beekman WH. Silicone Only Breast MRI using a Inversion Recovery TSE sequence with a B1-independent Spectral Selective Water Suppression Prepulse (SPAIR). In Proceedings of the 13th Annual Meeting of ISMRM, Miami, FL, USA, 2005. p.1858.
40. Sciuk J. Scintigraphic techniques for the diagnosis of infectious disease of the musculoskeletal system. Semin Musculoskelet Radiol 2004;8(3):205-213.
41. Ma LD, Frassica FJ, Bluemke DA, Fishman EK. CT and MRI evaluation of musculoskeletal infection. Crit Rev Diagn Imaging 1997;38(6):535-568.
42. Turecki MB, Taljanovic MS, Stubbs AY, Graham AR, Holden DA, Hunter TB, Rogers LF. Imaging of musculoskeletal soft tissue infections. Skeletal Radiol 2010 Oct;39(10):957-971.
43. Yu JS, Habib P. MR imaging of urgent inflammatory and infectious conditions affecting the soft tissues of the musculoskeletal system. Emerg Radiol 2009 Jul;16(4):267-276.
44. Hayter CL, Koff MF, Potter HG. Magnetic resonance imaging of the postoperative hip. J Magn Reson Imag 2012;35:1013-1025.
45. Pandit H, Glyn-Jones S, McLardy-Smith P, Gundle R, Whitwell D, Gibbons CLM, Ostlere S Athanasou N, Gill HS, Murray DW. Pseudotumours associated with metal-on-metal hip resurfacings. J Bone Joint Surg (Br) 2008;90-B(7):847-851.
46. Glyn-Jones S, Pandit H, Kwon Y-M, Doll H, Gill HS, Murray DW. Risk factors for inflammatory pseudotumour formation following hip resurfacing. J Bone Joint Surg [Br] 2009;91-B:1566-1574.
47. Macpherson, GJ and Breusch, SJ, Metal-on-metal hip resurfacing: a critical review. Arch Orthop Trauma Surg, 2011;131(1):101-110.
48. Korovessis P, Petsinis G, Repanti M, Repantis T. Metallosis after contemporary metal-on-metal total hip arthroplasty. Five to nine-year follow-up. J Bone Joint Surg Am. 2006 Jun;88(6):1183-1191.
49. van der Weegen W, Sijbesma T, Hoekstra HJ, Brakel K, Pilot P, Nelissen RGHH. Treatment of pseudotumors after metal-on-metal hip resurfacing based on magnetic resonance imaging, metal ion levels and symptoms. J Arthroplasty 2014;29:416-421.
50. Paprosky WG, Burnett RS. Assessment and classification of bone stock deficiency in revision total hip arthroplasty. Am J Orthop (Belle Mead NJ). 2002 Aug;31(8):459-464.
51. Jin S, Park JY, Hong JM, Kim TH, Shin HI, Park EK, Kim SY. Inhibitory effect of (-)-epigallocatechin gallate on titanium particle-induced TNF-α release and in vivo osteolysis. Exp Mol Med. 2011 Jul 30;43(7):411-418.
52. Dong L, Huang Z, Cai X, Xiang J, Zhu YA, Wang R, Chen J, Zhang J. Localized delivery of antisense oligonucleotides by cationic hydrogel suppresses TNF-α expression and endotoxin-induced osteolysis. Pharm Res. 2011 Jun;28(6):1349-1356.

53. Schwarz EM, Looney RJ, O'Keefe RJ. Anti-TNF-alpha therapy as a clinical intervention for periprosthetic osteolysis. Arthritis Res. 2000;2(3):165-168.
54. Lee M-J, Kim S, Lee S-A, Song H-T, Huh Y-M, Kim D-H, Han SH, Suh J-S. Overcoming Artifacts from Metallic Orthopedic Implants at High-Field-Strength MR Imaging and Multidetector CT. RadioGraphics 2007;27(3):791-804.
55. Heubes P, inventor; Siemens Aktiengesellschaft, assignee. Magnetic Resonance Tomography Method and Apparatus with Suppression of Ambiguity Artifacts in Spin Echo Images. US Patent US20050017719. January 27, 2005.
56. Koch KM, Hargreaves BA, Butts Pauly K, Chen W, Gold GE, King KF. Magnetic Resonance Imaging Near Metal Implants. J Magn Reson Imag 2010;32:773-787.
57. Cho Z, Kim DJ, Kim YK. Total inhomogeneity correction including chemical shifts and susceptibility by view angle tilting. Med Phys 1988;15:7–11.
58. Lu W, Pauly KM, Gold GE, Pauly JM, Hargreaves BA. SEMAC: Slice Encoding for Metal Artifact Correction in MRI. Magn Reson Med 2009;62:66–76.
59. Koch KM, Lorbiecki JE, Hinks RS, King KF. A Multispectral Three-Dimensional Acquisition Technique for Imaging Near Metal Implants. Magn Reson Med 2009;61:381–390.
60. Koch KM, Brau AC, Chen W, Gold GE, Hargreaves BA, Koff M, McKinnon GC, Potter HG, King KF. Imaging Near Metal with a MAVRIC-SEMAC Hybrid. Magn Reson Med 2011;65:71–82.
61. Kolind SH, MacKay AL, Munk PL, Xiang QS. Quantitative Evaluation of Metal Artifact Reduction Techniques. J Magn Reson Imag 2004;20:487–495.
62. Butts K, Pauly JM, Gold GE. Reduction of Blurring in View Angle Tilting MRI. Magn Reson Med 2005;53:418–424.
63. Morin VP, Müller GM, Månsson S. Restoration of large slice profile distortions near metallic implants by frequency mapping. In Proceedings of the 21st Annual Meeting of ISMRM, Salt Lake City, UT, USA, 2013. p.2565.
64. Koch KM, Koff MA, Potter HG. Jacobian-Based Correction of 3D-MSI Images Near Implanted Metal Devices. In Proceedings of the 19th Annual Meeting of ISMRM, Montréal, Québec, Canada, 2011. p.3173.
65. Koch KM, Worters P, Hargreaves BA. Local Gradient Effects on Spectral Binning of 3D Multi-Spectral Images Near Metal Implants. In Proceedings of the 20th Annual Meeting of ISMRM, Melbourne, Australia, 2012. p.2435.
66. Li G, Nittka M, Paul D, Lauer L. MSVAT-SPACE for fast metal implants imaging. In Proceedings of the 19th Annual Meeting of ISMRM, Montréal, Québec, Canada, 2011. p.3171.
67. Lu W, Pauly KB, Gold GE, Pauly JM, Hargreaves BA. Slice Encoding for Metal Artifact Correction With Noise Reduction. Magn Reson Med 2011;65:1352-1357.
68. Robson MD, Gatehouse PD, Bydder M, Bydder GM. Magnetic resonance: an introduction to ultrashort TE (UTE) imaging. J Comput Assist Tomogr 2003;27(6):825-846.

69. Gönner F, Heid O, Remonda L, Nicoli G, Baumgartner RW, Godoy N, Schroth G. MR angiography with ultrashort echo time in cerebral aneurysms treated with Guglielmi detachable coils. Am J Neuroradiol 1998;19(7):1324-8.
70. Gönner F, Lövblad KO, Heid O, Remonda L, Guzman R, Barth A, Schroth G. Magnetic resonance angiography with ultrashort echo times reduces the artefact of aneurysm clips. Neuroradiology 2002;44(9):755-758.
71. Rahmer J, Börnert P, Dries S. Assessment of anterior cruciate ligament reconstruction using 3D ultrashort echo-time MR imaging. J Magn Reson Imag 2009;29:443-448.
72. Rahmer J, Blume U, Börnert P. Selective 3D ultrashort TE imaging: comparison of "dual-echo" acquisition and magnetization preparation for improving short-T2 contrast. MAGMA. 2007 Apr;20(2):83-92.
73. Du J, Ma G, Li S, Carl M, Szeverenyi NM, VandenBerg S, Corey-Bloom J, Bydder GM. Ultrashort echo time (UTE) magnetic resonance imaging of the short T2 components in white matter of the brain using a clinical 3T scanner. Neuroimage. 2014 Feb 15;87:32-41.
74. Chudek JA, Hunter G. Stray field (STRAFI) and single point (SPI) magnetic resonance imaging. Annu Rep NMR Spectrosc 2002;45:151.
75. Balcom BJ, MacGregor RP, Beyea SD, Green DP, Armstrong RL, Bremner TW. Single-point ramped imaging with T1 enhancement (SPRITE). J Magn Reson A 1996;123:131–134.
76. Ramos-Cabrer P, van Duynhoven JP, Van der Toorn A, Nicolay K. MRI of hip prostheses using single-point methods: in vitro studies towards the artifact-free imaging of individuals with metal implants. Magn Reson Imag 2004;22(8):1097-103.
77. Hoff MN, Green JD, Xiang Q-S. Imaging Near Metals with Phase Cycled SSFP. In Proceedings of the 18th Annual Meeting of ISMRM, Stockholm, Sweden, 2010. p.3081.
78. Hoff MN, Xiang Q-S. Correcting bSSFP Distortion near Metals with Geometric Solution Phase. In Proceedings of the 21st Annual Meeting of ISMRM, Salt Lake City, UT, USA, 2013. p.2563.
79. Scheffler K, Hennig J. Is TrueFISP a Gradient-Echo or a Spin-Echo Sequence? Magn Reson Med 2005;49:395-397.
80. Hoff MN, Xiang Q-S. Recovering bSSFP Signal Loss near Metals with Shimming. In Proceedings of the 21st Annual Meeting of ISMRM, Salt Lake City, UT, USA, 2013. p.2564.
81. Chang H, Fitzpatrick JM. A technique for accurate magnetic resonance imaging in the presence of field inhomogeneities. IEEE Trans Med Imaging 1992;11:319–329.
82. Skare S, Andersson J. Correction of MR image distortions induced by metallic objects using a 3D cubic B-spline basis set: application to stereotactic surgical planning. Magn Reson Med 2005;54:169–181.
83. Bos C, den Harder CJ, van Yperen G. MR Imaging near orthopedic implants with artifact reduction using View-Angle Tilting and Off-Resonance Suppression. In

Proceedings of the 18th Annual Meeting of ISMRM, Stockholm, Sweden, 2010. p.129.

84. den Harder CJ, Blume UA, Bos C. MR Imaging near orthopedic implants using Slice-Encoding for Metal Artifact Correction and Off-Resonance Suppression. In Proceedings of the 19th Annual Meeting of ISMRM, Montréal, Québec, Canada, 2011. p.3170.
85. den Harder CJ, Blume UA, Bos C. MR Imaging near metallic implants using Selective Multi-Acquisition with Variable Resonances Image Combination. In Proceedings of the 20th Annual Meeting of ISMRM, Melbourne, Australia, 2012. p.2432.
86. Heyse TJ, Chong LR, Davis J, Boettner F, Haas SB, Potter HG. MRI analysis of the component-bone interface after TKA. Knee. 2012 Aug;19(4):290-294.
87. Hargreaves BA, Gold GE, Pauly JM, Pauly KB. Adaptive Slice Encoding for Metal Artifact Correction. In Proceedings of the 18th Annual Meeting of ISMRM, Stockholm, Sweden, 2010. p.3083.
88. Hayter CL, Koff MF, Shah P, Koch KM, Miller TT, Potter HG. MRI After Arthroplasty: Comparison of MAVRIC and Conventional Fast Spin-Echo Techniques. Am J Roentgenol 2011;197:W405–W411.
89. Hargreaves BA, Chen W, Lu W, Alley MT, Gold GE, Brau ACS, Pauly JM, Butts Pauly KM. Accelerated Slice Encoding for Metal Artifact Correction. J Magn Reson Imag 2010;31(4):987–996.
90. Koch KM, King KF. Combined Parallel Imaging and Compressed Sensing on 3D Multi-Spectral Imaging Near Metal Implants. In Proceedings of the 19th Annual Meeting of ISMRM, Montréal, Québec, Canada, 2011. p.3172.
91. Koch KM, King KF, Chen W, Gold G, Hargreaves BA. Frequency Encoding in the Presence of Extreme Static Field Gradients. In Proceedings of the 19th Annual Meeting of ISMRM, Montréal, Québec, Canada, 2011. p.293.
92. Hargreaves BA, Lu W, Chen W, Gold GE, Brau AC, Pauly JM, Butts Pauly K. Accelerated Slice-Encoding for Metal Artifact Correction. In Proceedings of the 17th Annual Meeting of ISMRM, Honolulu, Hawai'i, USA, 2009. p.258.
93. den Harder CJ, Blume UA, van IJperen G, Bos C. On the relation of the ripple artifact in Multi-Spectral Imaging and susceptibility induced field gradients. In Proceedings of the 21st Annual Meeting of ISMRM, Salt Lake City, UT, USA, 2013. p. 2562.
94. Chu SCK, Xu Y, Balschi JA, Springer CS. Bulk magnetic susceptibility shifts in NMR studies of compartmentalized samples: Use of paramagnetic agents. Magn Reson Med 1990;13:239-262.
95. Koch KM, Hinks RS. Empirical and computed perturbations induced by metallic implants. In Proceedings of the 16th Annual Meeting ISMRM, Toronto, Ontario, Canada, 2008. p.1180.
96. Bartusek K, Dokoupil Z, Gescheidtova E. Magnetic field mapping around metal implants using an asymmetric spin-echo MRI sequence. Measure Sci Technol 2006;17:3293–3300.

97. Parker DL, Du YP, Davis WL. The Voxel Sensitivity Function in Fourier Transform Imaging: Applications to Magnetic Resonance Angiography. Magn Reson Med 1995;33(2):156-162.
98. Lee YH, Lim D, Kim E, Kim S, Song HT, Suh JS. Feasibility of fat-saturated T2-weighted magnetic resonance imaging with slice encoding for metal artifact correction (SEMAC) at 3T. Magn Reson Imaging 2014. doi: 10.1016/j.mri.2014.04.009.
99. Koch K, McKinnon G. On the Feasibility of Overcoming Frequency Encoding Limitations Near Metal Implants with Broadband Single-Point Imaging on Clinical MR Systems. In Proceedings of the 22nd Annual Meeting of ISMRM, Milan, Italy, 2014. p.1679.
100. van Gorp JS, Bakker CJG, Zijlstra F, Smink J, Bouwman JG, Seevinck PR. Geometrically undistorted imaging of orthopedic implants using compressed sensing accelerated phase encoded imaging. In Proceedings of the 22nd Annual Meeting of ISMRM, Milan, Italy, 2014. p.1680.
101. Rea M, Boullier X, Young I, McRobbie D. Phase Encoded Acquisition with Compressed sEnsing. In Proceedings of the 22nd Annual Meeting of ISMRM, Milan, Italy, 2014. p.1509.
102. Artz N, Smith M, Reeder S. Multiband RF Excitation for Accelerating Magnetic Resonance Imaging in the Presence of Metal. In Proceedings of the 22nd Annual Meeting of ISMRM, Milan, Italy, 2014. p.650.
103. van Gorp JS, Bakker CJG, Seevinck PR. A hybrid multi-spectral approach for near metal imaging: combining the best of phase and frequency encoding. In Proceedings of the 22nd Annual Meeting of ISMRM, Milan, Italy, 2014. p.1681.
104. Sveinsson B, Worters PW, Gold GE, Hargreaves BA. Fast Imaging of Metallic Implants by Data Subsampling. In Proceedings of the 21st Annual Meeting of ISMRM, Salt Lake City, UT, USA, 2013. p.557.
105. Graf H, Lauer UA, Berger A, Schick F. RF artifacts caused by metallic implants or instruments which get more prominent at 3 T: an in vitro study. Magn Reson Imag 2005;23(3):493-499.
106. Warner L, Blume U, Kotys-Traughber M. MR imaging techniques with reduced metal artifact for improved brachytherapy device visualization. In Proceedings of the 54th Annual Meeting of AAPM, Vancouver, British Columbia, Canada, 2011. p.15490.
107. van de Maat GH, Blume UA, den Harder CJ, Bos C, Bakker CJ. Macroscopic meets microscopic: the use of Multi Acquisition Variable Resonance Image Combination (MAVRIC) for detection of microscopic objects by means of off-resonance excitation. In Proceedings of the 19th Annual Meeting of ISMRM, Montréal, Québec, Canada, 2011. p.4522.
108. Post, SG. Altruism, Happiness, and Health: It's Good to Be Good. Int J Behav Med 2005; 12(2):66–77.

B. Summary

Metal Implant Artifact Reduction in Magnetic Resonance Imaging

With its proven diagnostic value for many clinical applications, Magnetic Resonance Imaging (MRI) is often the imaging modality of choice to evaluate soft tissue of patients. An increasing number of patients are treated with metal implants, and there is a need to evaluate soft tissue near these metal implants, often in view of complications caused by the implant or the implant surgery. Surgeons and radiologists indicate that for many diseases, tissue evaluation is needed as close as half a centimeter distance from the implant (section 4.3.1). For a number of metal implants, an MRI examination is unsafe and for that reason contraindicated. For others, it may be safe for the patient to undergo an MR examination, provided all safety conditions are respected. Even if safe, metal implants influence the magnetic field, cause “artifacts” (features that do not represent reality) in the image and compromise the image quality, which complicates or sometimes even prevents diagnosis using these images.

The purpose of the investigations and the technological design described here has been to reduce the artifacts in the image and to restore the image quality in order to enable a correct diagnosis. First the physical principles of MRI and the mechanism behind metal induced artifacts are explained. Then, the techniques are described that reduce metal artifacts. These include recently developed existing techniques as well as the new techniques used for the first time in this research.

Physical principles of MRI

The main component of an MRI scanner (Figure 1.1a) is a strong magnet. The magnet polarizes among others the nuclei of hydrogen atoms in the patient’s tissue. In the magnetic field, the hydrogen nuclei behave as spinning tops (Figure 1.2): each nucleus rotates around its axis (“spin”) but also the axis itself rotates around the direction of the magnetic field, like the axis of a spinning top rotates around the direction of the gravity field (“precession”). The precession frequency is directly proportional to the magnetic field strength and is called the “Larmor frequency”. For clinical MRI scanners, the Larmor frequency is in the radiofrequency (RF) range (around 64 MHz for a 1.5 Tesla scanner).

A momentary electromagnetic wave with the right frequency (“RF pulse”) is transmitted into the patient using a transmission coil. The hydrogen nuclei resonate at this frequency, absorb the electromagnetic energy and thus arrive at a higher energy state, called an “excited” state. This process is called excitation (Figure 1.3).

Over time, the tissue transmits the absorbed energy in the form of a new electromagnetic wave, which can be detected with a receive coil. This is the MR signal, which contains the information for constituting an image of the patient’s tissue.

The MR signal decays rapidly as –in a classical mechanics description– the phases of different nuclei become incoherent. This means that the axes of the nuclei turn in all directions and they start to counteract each other. When a second RF pulse is transmitted into the patient, a so-called refocusing pulse, the coherence of the nuclei is restored, making all nuclei

precess synchronously again after a short time, which amplifies their joint MR signal (Figure 1.6). This is referred to as an “RF-echo” or a “spin-echo”.

Roughly speaking, there are two approaches that can be used to obtain information about the spatial position of the MR signal: by frequency or by phase. Both approaches build on the phenomenon that the precession frequency of hydrogen nuclei is proportional to the magnetic field strength. If the field strength varies locally, the precession frequency follows the field strength.

The approach based on frequency is as follows. A gradient coil is used to introduce a linear increase of the magnetic field strength in one direction. This then leads to a linearly increasing precession frequency in the same direction. Hence, the spatial position of each hydrogen nucleus is directly related to its frequency. By carefully tuning the RF pulses within a limited frequency band, only the nuclei with those same frequencies are excited, which thus reside in a limited spatial region (Figure 1.5). This is how nuclei are selected in a relatively thin slice (“slice selection”, Figure 1.9a) or a larger volume (“volume selection”, Figure 1.9b).

During the time that the patient’s tissue transmits MR signal, a gradient is applied in one of the directions within the imaging plane. The linear increase of the magnetic field strength leads to a linearly increasing precession frequency in this new direction, and consequently to a linearly increasing frequency of the MR signal. Thus, the spatial origin of the transmitted MR signal is encoded in its frequency. This process is called frequency encoding.

Frequency encoding is usually applied in one direction only. In the other in-plane direction, phase encoding is used. Here, a gradient is switched on only briefly in that direction, causing some nuclei to momentarily precess slightly faster or slightly slower than others. In other words, the gradient field nudges the axes of the nuclei, causing the phase of some nuclei to lead, and the phase of others to lag, depending on their spatial position. Hence, the spatial position of the nuclei in this direction is encoded in their phase shift. Repeating the measurement process with varying gradient strengths leads to weaker and stronger phase shifts of the nuclei. This phase encoding process provides similar information about the spatial origin of MR signal, as may be obtained using frequency encoding. In essence, phase encoding can be considered a discretized or step-wise variant of frequency encoding. However, phase encoding is a slow process, depending on the required resolution: in principle, the measurement needs to be repeated as often as the required number of lines in the image.

In multi-slice imaging (Figure 1.9a), thin slices are selected, and phase encoding is applied in one in-plane direction only, orthogonal to the frequency encoding direction. In 3D imaging (Figure 1.9b), a large volume is selected, and phase encoding is applied not only in-plane, but also in the through-plane direction.

Image artifacts due to metal implants

Especially frequency encoding and the selection of the tissue that produces a signal due to the RF pulse rely strongly on the Larmor frequency. For a reliable Larmor frequency of all nuclei within the MRI scanner, it is essential that the magnetic field is extremely

homogeneous in the entire bore. However, when a patient with a metal implant enters the MRI scanner, the magnetic field is locally deflected through the implant (Figure 2.2), and the field homogeneity is significantly compromised. The resulting spatial variation of the magnetic field causes substantial deviations in the precession frequency of the nuclei. As this frequency is used for localization of signal, the frequency deviations lead to misplacement of the signal in the image, specifically in the frequency encoding direction. In 2D imaging, additionally, the metal induced frequency deviations lead to distortion of the otherwise straight slice selection profile (Figure 2.4). These distortions in turn cause other artifacts in the image, including bright and dark areas. Phase encoding, however, is insensitive to field variations and hence spatially accurate even near metal.

Existing techniques to reduce metal artifacts

A number of commonly available techniques can be used to keep metal artifacts within limits (section 2.3). However, residual artifacts remain and these are often too large to enable evaluation of tissue at half a centimeter distance from the implant. In recent years, more advanced techniques to address metal artifacts have been developed (chapter 3). These include Multi-Spectral Imaging (MSI) techniques. MSI techniques substantially reduce metal artifacts, though at the cost of increased scan-time. Examples of MSI techniques are SEMAC (Slice-Encoding for Metal Artifact Correction) and MAVRIC (Multi-Acquisition with Variable-Resonance Image Combination). SEMAC is based on a multi-slice signal acquisition, and resolves slice distortion with a few additional phase encoding steps in the through-plane direction (Figure 3.3). MAVRIC is based on a 3D acquisition with a limited frequency content, and repeats this acquisition for a number of adjacent frequency bands, so-called “spectral bins”, to cover the full frequency spectrum of interest (Figure 3.4). Hence, in both MSI techniques a conventional acquisition is repeated multiple times to collect sufficient information about the location and the frequency of MR signals, which results in an increased scan-time.

The number of through-plane phase encoding steps in MSI techniques is dependent on the material and size of the implant and the spatial sensitivity profile of the receive coil. Too many phase encoding steps lead to excessive scan-time increase, but too few phase encoding steps do not cover the MR signal fully, causing the MR signal to show up at a wrong position in the image, or even in the wrong image (“aliasing artifacts”, Figure 3.5).

Innovations in MSI

Chapter 5 presents a new adaptation of MSI techniques, called Off-Resonance Suppression (ORS, Figure 5.1). In the original MSI techniques, the excitation pulse and the subsequent refocusing pulses are aligned and both pulse types affect the same hydrogen nuclei. Using ORS, however, the two pulse types differ and overlap only partly. Hence, a limited set of nuclei experience both the excitation pulse and the refocusing pulses and contribute to the MR signal. Nuclei with strong frequency deviations at a large distance from the intended imaging region experience only one of both pulse types and do not contribute to the MR signal.

This alteration of the selection process enables a controllable limit to the MR signal, and thus to the required number of phase encoding steps to fully cover the MR signal. ORS thus

enables a trade-off between scan-time and the extent of the MR signal without the risk of aliasing artifacts. ORS may be applied to different MSI techniques including SEMAC (ORS-SEMAC) and MAVRIC (ORS-MAVRIC). Examples are shown in phantom and volunteer experiments (Figure 5.5, Figure 5.6, Figure 5.7, Figure 5.9).

A SEMAC image may contain signal from multiple slice selections. Hence, in SEMAC images, a residual artifact may occur, as transitions between adjacent slice selections become visible, resulting in intensity fluctuations, referred to as the *ripple artifact*. In chapter 6, an analysis of the mechanism behind this ripple artifact is presented. The visibility of the transitions between slices is emphasized by the displacements of signal in the frequency encoding direction (Figure 6.1). Using wider overlapping slice selections ensures smoother transitions between the slice selections, and substantially reduces the ripple artifact (Figure 6.3, Figure 6.4). Both the analysis of the mechanism behind the ripple artifact and the approach to reduce the artifact were verified using MRI simulations and phantom experiments.

Prototype

To evaluate whether MSI techniques augmented with ORS (ORS-MSI) can satisfactorily address metal artifacts, a software prototype with the MSI and ORS functionality was built (chapter 7). This prototype is based on software that runs on a clinical Philips MRI scanner, to allow installation of the prototype on Philips MRI scanners in hospitals. Clinical requirements provided by orthopedists and radiologists (chapter 4) and technical requirements (chapter 7) set the standards for the prototype, to enable evaluation of different aspects of the functionality, including correction, applicability, speed and usability.

Phantom experiments were used to verify that the prototype's functionality results in the correction of geometric distortions and signal intensity deviations that may be expected based on theory. A validation study whether the achieved artifact reduction meets the clinical need showed that a good visualization as close as half a centimeter from a titanium hip implant is possible (Figure 8.7). Near a stainless steel hip implant sample the clinical need was not met (Figure 8.8): the artifact size varied per location, and was substantially smaller than half a centimeter near the hip stem but larger than a centimeter near the head of the implant sample. Nonetheless, the artifact was considerably reduced using the prototype's functionality compared to conventional scanning techniques. Artifacts near bulk stainless steel implants may be expected to be the most challenging to reduce. Many other implants, smaller in size or made of different materials, will cause smaller artifacts and for those, ORS-MSI allows sufficient artifact reduction in clinically feasible scan-times. In all experiments, metal artifacts were never increased by the use of ORS-MSI.

The described methods for verification and validation of the technological design include simulations and phantom and volunteer experiments. Evaluation of the functionality on patients in clinical practice is needed to further show the clinical benefit of the techniques. The clinical evaluation is in progress. Early results demonstrate enough clinical benefit to recommend product development of the new functionality. With that, the proposed ORS-MSI functionality for artifact reduction near metal implants will soon become available as commercial product and will enable evaluation and diagnosis of tissue in clinically feasible scan-times nearer metal implants than any other currently available technique.

C. Samenvatting

Reductie van Artefacten door Metalen Implantaten in MRI

Vanwege de bewezen diagnostische waarde voor veel klinische toepassingen gaat vaak de voorkeur uit naar *Magnetic Resonance Imaging* (MRI) als beeldvormende modaliteit om zacht weefsel van patiënten te onderzoeken. Een toenemend aantal patiënten is behandeld met metalen implantaten en er is een behoefte om zacht weefsel in de buurt van deze metalen implantaten te evalueren, vaak vanwege complicaties veroorzaakt door het implantaat of de chirurgische ingreep. Chirurgen en radiologen geven aan dat voor veel ziektes het weefsel tot op een halve centimeter van het implantaat geëvalueerd moet kunnen worden (paragraaf 4.3.1). Voor een aantal metalen implantaten is een MRI onderzoek onveilig en dus gecontra-indiceerd. Voor andere implantaten kan het voor de patiënt veilig zijn om een MR onderzoek te ondergaan, mits alle veiligheidsvoorwaarden in acht worden genomen. Zelfs al is het veilig, metalen implantaten beïnvloeden het magnetische veld, veroorzaken „artefacten" (kenmerken in het beeld die niet met de werkelijkheid overeenkomen) en verminderen daarmee de beeldkwaliteit, hetgeen diagnose met behulp van deze beelden bemoeilijkt en soms zelfs onmogelijk maakt.

Het doel van het hier beschreven onderzoek en proefontwerp was om de artefacten in het beeld te reduceren en de beeldkwaliteit te herstellen opdat een correcte diagnose mogelijk wordt. Eerst worden de fysische principes van MRI en het mechanisme achter metaalartefacten uitgelegd. Vervolgens worden de technieken beschreven om metaalartefacten te reduceren. Hiertoe behoren zowel recent ontwikkelde bestaande technieken als ook de nieuwe technieken die voor het eerst zijn gebruikt in dit onderzoek.

Fysische principes van MRI

Het voornaamste onderdeel van een MRI-scanner (Figuur 1.1a) is een sterke magneet. De magneet polariseert onder meer de kernen van waterstofatomen in het weefsel van de patiënt. In het magnetische veld gedragen de waterstofkernen zich als tolletjes (Figuur 1.2): elke kern roteert om zijn as („spin") maar ook de as zelf roteert rondom de richting van het magnetische veld, zoals de as van een tol roteert rondom de richting van het zwaartekrachtsveld („precessie") . De precessiefrequentie is recht evenredig met de magnetische veldsterkte en wordt de „Larmor frequentie" genoemd. Voor klinische MRI-scanners ligt de Larmor frequentie in het radiofrequentie (RF) gebied (ca. 64 MHz voor een 1,5 Tesla scanner).

Een kortstondige elektromagnetische golf met de juiste frequentie („RF-puls") wordt de patiënt in gezonden met behulp van een zendspoel. De waterstofkernen resoneren op deze frequentie, absorberen de elektromagnetische energie en belanden zo in een hogere energietoestand, ofwel een „aangeslagen" of „geëxciteerde" toestand. Dit proces heet excitatie (Figuur 1.3).

Na verloop van tijd zendt het weefsel de geabsorbeerde energie weer uit in de vorm van een elektromagnetische golf, die met een ontvangstspoel kan worden gedetecteerd. Dit is het

MR-signaal, dat de informatie bevat waarmee een beeld van het weefsel van de patiënt kan worden gevormd.

Het MR-signaal vervalt snel doordat –in de klassieke mechanica beschrijving– de fasen van verschillende kernen incoherent worden. Dat betekent dat de assen van de kernen in alle richtingen draaien en ze elkaar gaan tegenwerken. Wanneer nu een tweede RF-puls de patiënt in wordt gezonden, een zogenaamde refocuseringspuls, herstelt de coherentie van de kernen zich weer, waardoor alle kernen na een korte tijd weer synchroon gaan precederen, en het gezamenlijke MR-signaal zich versterkt (Figuur 1.7). We spreken hierbij van een „RF-echo" of een „spin-echo".

Ruwweg gesproken zijn er twee benaderingen die kunnen worden gebruikt om informatie te krijgen over de ruimtelijke positie van het MR-signaal: met frequentie of met fase. Beide benaderingen zijn gebaseerd op het verschijnsel dat de precessiefrequentie van waterstofkernen evenredig is met de magnetische veldsterkte. Bij lokale veldsterkte variaties volgt de precessiefrequentie de veldsterkte.

De benadering op basis van frequentie is als volgt. Met een gradiëntspoel wordt ervoor gezorgd dat in één richting de magnetische veldsterkte lineair toeneemt. Dit leidt dan tot een lineair toenemende precessiefrequentie in diezelfde richting. Daarmee is de ruimtelijke positie van elke waterstofkern direct gekoppeld aan zijn frequentie. Door zorgvuldig de RF-pulsen af te stemmen binnen een beperkte frequentieband, worden alleen de kernen met die zelfde frequenties geëxciteerd, die zich dus binnen een beperkt ruimtelijk gebied bevinden (Figuur 1.5). Op deze manier kunnen kernen worden geselecteerd in een relatief dunne plak („plakselectie", Figuur 1.9a) of een groter volume („volumeselectie", Figuur 1.9b).

Gedurende de tijd dat het weefsel van de patiënt een MR-signaal uitzendt, wordt een gradiënt toegepast in één van de richtingen binnen het vlak van het beeld. De lineair toenemende magnetische veldsterkte leidt tot een lineair toenemende precessiefrequentie in deze nieuwe richting en dus tot een lineair toenemende frequentie van het MR-signaal. Zo wordt de positie waar het uitgezonden MR-signaal vandaan komt gecodeerd in zijn frequentie. Dit proces heet frequentiecodering.

Frequentiecodering wordt meestal slechts in één richting toegepast. In de andere richting in het beeldvlak wordt fasecodering gebruikt. Hierbij wordt een gradiënt in die richting maar heel even aangezet, waardoor sommige kernen heel even net iets sneller of iets langzamer precederen dan andere. Met andere woorden, het gradiëntveld geeft de assen van de kernen een zetje, waardoor de fase van bepaalde kernen voorloopt, en de fase van anderen achterloopt, afhankelijk van hun ruimtelijke positie. Op deze manier is de ruimtelijke positie van de kernen in deze richting gecodeerd in hun faseverschuiving. Herhaling van de meting met variërende gradiëntsterktes leidt tot zwakkere en sterkere faseverschuivingen van de kernen. Dit fasecoderingsproces biedt vergelijkbare informatie over waar het MR-signaal vandaan komt als met frequentiecodering kan worden verkregen. In wezen kan fasecodering worden beschouwd als een gediscretiseerde of stapsgewijze variant van frequentiecodering.

Fasecodering is echter wel een langzaam proces, afhankelijk van de vereiste resolutie: in principe moet de meting net zo vaak worden herhaald als het vereiste aantal beeldlijnen.

Bij multi-slice afbeelden (Figuur 1.9a) worden dunne plakken geselecteerd, en wordt fasecodering slechts in één richting in het beeldvlak toegepast, loodrecht op de frequentiecoderingsrichting. Bij 3D afbeeldingen (Figuur 1.9b) wordt een groot volume geselecteerd en wordt fasecodering niet alleen in het beeldvlak toegepast, maar ook in de richting loodrecht op het beeldvlak.

Beeldartefacten door metalen implantaten

Vooral frequentiecodering en de selectie van het weefsel, dat als gevolg van de RF-puls een signaal geeft, zijn sterk afhankelijk van de Larmor frequentie. Voor een betrouwbare Larmor frequentie van alle kernen in de MRI scanner is het essentieel dat het magnetische veld in de gehele tunnel extreem homogeen is. Wanneer echter een patiënt met een metalen implantaat de MRI-scanner in gaat, wordt het magnetische veld lokaal afgebogen door het implantaat (Figuur 2.2), waardoor de veldhomogeniteit significant verslechtert. De resulterende ruimtelijke variatie van het magnetische veld veroorzaakt aanzienlijke afwijkingen in de precessiefrequentie van de kernen. Aangezien deze frequentie wordt gebruikt voor het lokaliseren van het signaal, leiden de frequentieafwijkingen tot misplaatsing van het signaal in het beeld, met name in de frequentiecoderingsrichting. Bij 2D beeldvorming leiden de door het metaal geïnduceerde frequentieafwijkingen bovendien tot verstoring van het plakselectieprofiel dat anders recht zou zijn (Figuur 2.3). Deze verstoringen veroorzaken op hun beurt weer andere artefacten in het beeld, waaronder lichte en donkere vlekken. Fasecodering daarentegen is ongevoelig voor veldsterkte variaties en dus ruimtelijk nauwkeurig zelfs in de buurt van metaal.

Bestaande technieken om metaalartefacten te reduceren

Een aantal algemeen beschikbare technieken kunnen worden gebruikt om metaalartefacten binnen de perken te houden (paragraaf 2.3). Er blijven echter artefacten over en deze zijn vaak te groot om evaluatie van weefsel mogelijk te maken op een halve centimeter afstand van het implantaat. De afgelopen jaren zijn er meer geavanceerde technieken ontwikkeld om metaalartefacten aan te pakken (hoofdstuk 3). Hiertoe behoren de multi-spectrale afbeeldingstechnieken (*Multi-Spectral Imaging,* MSI). MSI technieken reduceren metaalartefacten aanzienlijk, maar ten koste van een langere scantijd. Voorbeelden van MSI technieken zijn SEMAC (*Slice-Encoding for Metal Artifact Correction*) en MAVRIC (*Multi-Acquisition with Variable-Resonance Image Combination*). SEMAC is gebaseerd op een multi-slice signaal acquisitie en lost plakvervorming op met een aantal extra fasecoderingsstappen in de richting loodrecht op het beeldvlak (Figuur 3.3). MAVRIC is gebaseerd op een 3D acquisitie met een beperkte frequentie-inhoud, en herhaalt deze acquisitie voor een aantal aangrenzende frequentiebanden, zogenaamde „*spectral bins*", om het volledige frequentiespectrum af te dekken (Figuur 3.4). In beide MSI technieken wordt dus een conventionele acquisitie techniek meerdere malen herhaald om voldoende informatie te verzamelen over de locatie en de frequentie van MR signalen, met als gevolg een langere scantijd.

Het aantal fasecoderingsstappen in de richting loodrecht op het beeldvlak in MSI technieken is afhankelijk van het materiaal en de afmeting van het implantaat en het ruimtelijke gevoeligheidsprofiel van de ontvangstspoel. Te veel fasecoderingsstappen leiden tot overmatige toename van scantijd, maar te weinig fasecoderingsstappen dekken het MR-signaal niet volledig af, waardoor het MR-signaal zichtbaar wordt op een verkeerde positie in het beeld, of zelfs in het verkeerde beeld („*aliasing* artefacten", Figuur 3.5).

Innovaties in MSI

Hoofdstuk 5 presenteert een nieuwe aanpassing van MSI technieken, genaamd *Off-Resonance Suppression* (ORS, Figuur 5.1). In de oorspronkelijke MSI technieken zijn de excitatiepuls en de daarop volgende refocuseringspulsen uitgelijnd en beïnvloeden beide soorten pulsen dezelfde waterstofkernen. Bij ORS daarentegen verschillen de twee soorten pulsen en overlappen ze slechts gedeeltelijk. Daardoor zijn er slechts een beperkt aantal kernen die zowel de excitatiepuls als de refocuseringspulsen ondervinden en die bijdragen aan het MR-signaal. Kernen met sterke frequentieafwijkingen op grote afstand van het beoogde afbeeldingsgebied ervaren slechts een van beide soorten pulsen en dragen niet bij aan het MR-signaal.

Deze wijziging van het selectieproces maakt een regelbare inperking van het MR-signaal mogelijk, en dus van het vereiste aantal fasecoderingsstappen om het MR-signaal volledig af te dekken. ORS maakt het dus mogelijk om de scantijd en de omvang van het MR-signaal tegen elkaar uit te ruilen zonder het risico op *aliasing* artefacten. ORS kan worden toegepast of verschillende MSI technieken waaronder SEMAC (ORS-SEMAC) en MAVRIC (ORS-MAVRIC). Voorbeelden hiervan zijn gedemonstreerd in fantoom- en vrijwilliger-experimenten (Figuur 5.5, Figuur 5.6, Figuur 5.7, Figuur 5.9).

Een SEMAC-beeld kan signaal van meerdere plakselecties bevatten. Daardoor kan in SEMAC-beelden een resterend artefact voorkomen wanneer overgangen tussen naburige plakselecties zichtbaar worden, hetgeen resulteert in intensiteitsfluctuaties, aangeduid als het *ripple* artefact. In hoofdstuk 6 wordt een analyse van het mechanisme achter dit *ripple* artefact gepresenteerd. De zichtbaarheid van de overgangen tussen plakken wordt extra benadrukt door de signaalverplaatsingen in de frequentiecoderingsrichting (Figuur 6.1). Het gebruik van bredere overlappende plakselecties zorgt voor vloeiender overgangen tussen de plakselecties, en reduceert het *ripple* artefact aanzienlijk (Figuur 6.3, Figuur 6.4). Zowel de analyse van het mechanisme achter het *ripple* artefact en de benadering om het artefact te reduceren zijn geverifieerd met behulp van MRI-simulaties en fantoomexperimenten.

Prototype

Om te evalueren of met MSI technieken uitgebreid met ORS (ORS-MSI) metaalartefacten naar tevredenheid kunnen worden aangepakt, is een software-prototype gebouwd met de MSI en ORS functionaliteit (hoofdstuk 7). Dit prototype is gebaseerd op software die draait op een klinische Philips MRI-scanner, om zo installatie van het prototype op Philips MRI-scanners in ziekenhuizen mogelijk te maken. Klinische eisen aangeleverd door orthopeden en radiologen (hoofdstuk 4) en technische eisen (hoofdstuk 7) hebben de standaard gezet voor het prototype, zodat de verschillende aspecten van de functionaliteit kunnen worden geëvalueerd, waaronder correctie, toepasbaarheid, snelheid en gebruiksvriendelijkheid.

Met behulp van fantoomexperimenten is gecontroleerd of de functionaliteit van het prototype resulteert in de correctie van geometrische verstoringen en afwijkingen in signaalintensiteit die mag worden verwacht op basis van de theorie. Een validatiestudie of de bereikte artefactreductie voldoet aan de klinische behoefte toonde aan dat een goede visualisatie op slechts een halve centimeter afstand van een titanium heupimplantaat mogelijk is (Figuur 8.7). Bij een roestvrijstalen heupimplantaat werd niet aan de klinische behoefte voldaan (Figuur 8.8): de afmeting van het artefact varieerde per locatie, en was aanzienlijk kleiner dan een halve centimeter in de buurt van de heupsteel maar groter dan een centimeter in de buurt van de kop van het implantaat. Niettemin was het artefact aanzienlijk gereduceerd met behulp van de functionaliteit van het prototype in vergelijking met conventionele scantechnieken. Van artefacten nabij massieve roestvrijstalen implantaten mag worden verwacht dat dit de meest uitdagende artefacten zijn om te reduceren. Veel andere implantaten, met kleinere afmeting of gemaakt van andere materialen, zullen kleinere artefacten veroorzaken en voor die implantaten biedt ORS-MSI voldoende artefactreductie binnen klinisch haalbare scantijden. In alle experimenten werden metaalartefacten nooit versterkt door het gebruik van ORS-MSI.

De beschreven methoden voor de verificatie en validatie van het proefontwerp omvatten simulaties en fantoom- en vrijwilligerexperimenten. Evaluatie van de functionaliteit op patiënten in de klinische praktijk is nodig om het klinische nut van de techniek verder aan te tonen. Aan de klinische evaluatie wordt gewerkt. De eerste resultaten tonen voldoende klinisch nut om productontwikkeling van de nieuwe functionaliteit aan te bevelen. Daarmee zal de voorgestelde ORS-MSI functionaliteit voor artefactreductie nabij metalen implantaten binnenkort beschikbaar worden als commercieel product en evaluatie en diagnose van weefsel mogelijk maken in klinisch haalbare scantijden dichter bij metalen implantaten dan elke andere momenteel beschikbare techniek.

D. Acknowledgements

With nearly everything I do, I get the opportunity to thank others for their indispensable contribution and support. The same holds for this thesis, in which I have the opportunity to eternize my acknowledgements. I want to thank you, the reader of these words, for your interest. And I want to acknowledge everyone who contributed directly or indirectly to this thesis.

Although a list is inevitably incomplete, I do want to mention a number of these friends by name. Both my promotors Pieter Wijn and Marcel Breeuwer and my copromotor Clemens Bos I want to thank for their wise and accurate advice and feedback to always guide me in the direction of the next concrete and feasible steps of the project. Clemens, additional thanks to you for the many years of pleasant collaboration that already outlived both our Philips careers and during which I have learned a lot from you about many fascinating and challenging topics. And also for the larger part of this thesis I am much obliged to you for your contribution.

Also to the other members of the promotion committee Herman Clercx, Klaas Nicolaij, Ward Cottaar, Andrew Webb, and Frédéric Lecouvet, I want to express my sincere appreciation for investing their valuable time in this thesis. Frédéric, thank you for the pleasant continuing collaboration and your help to clarify both the benefits and the limitations of the evaluated methods. Ward, without you, I might have never known about the concept of a promotion on technological design.

I am very grateful to all friends at Philips Healthcare who helped create the enjoyable and inspiring environment where this work was possible. Many of them contributed to this technological design. Many thanks go to Mark Limkeman and Liz Moore for giving me many opportunities including the chance to invest in the investigations of metal artifact reduction techniques. Crucial to these investigations and to making the prototype were the major contributions of the co-authors of the articles, Ulrike Blume and Gert van IJperen. Likewise, the support by Ronald Holthuizen for the PRIDE environment was essential. I appreciate very much the instructive and enjoyable collaboration.

I want to acknowledge Johan van den Brink, Ruud de Boer, Paul Folkers, Gwenael Herigault, Alex Dresner, and Dave Hitt for their help to advertise the relevance of the technology within the company. Thanks go to Wim Prins for sharing his knowledge and quite complete contributions for metal robust preparation phases. Wim and Ruud, thank you for your help to make the best images in this thesis look this good. Raymond Habets, thank you for your energetic enthusiasm and for sharing your experience of your promotion on technological design, years ago, which served as a very stimulating example for me. Thank you, Silke Hey and Anne-Sophie Glantenay for our pleasant and constructive collaboration and for taking the technology to the next level. Miha Fuderer, thank you for the constructive conversations and stimulations. The mugs are still being used daily.

To the team of test bay engineers, including Ivar Schretzmeijer, Mattie de Leest, Ber Bovee, Peter Jonkers, and Theo van Roosmalen, I am very grateful for keeping the test bays

functional and available, including even the older software releases I used. Thanks go to Tom Rozijn, Michel Jurrissen, Elwin de Weerdt, Hans Peeters, Kay Nehrke, Peter Börnert, and Mariya Doneva for inspiring conversations on metal artifact reduction that –among others– led to a few patent applications.

I want to thank Shannon Kolind for sharing the first implementation of VAT in the Philips scanner software, which was very helpful for starting this project.

Many thanks go to all members of the musculoskeletal (MSK) team, for the inspiring discussions and exchange of fantastic ideas, and special thanks go to Marius van Meel, Lars van Loon, Wendy Hopkins, and John Pitts, for all contributions on the applications aspects of the scanning techniques. Morten Bruvold, Vincent Denolin, and EunJu Kim, thank you for supporting the clinical evaluations of the scanning techniques.

For carrying out these clinical evaluations I want to express my sincere appreciation to Conny Ström, Jörgen Strinnholm, and Jón Hauksson of Norrlands Universitetssjukhus in Umeå, Sweden, to Frédéric Lecouvet, Bruno Vande Berg, Fabiano Nassar Cardoso, and Patrick Omoumi at UCL St.Luc Hospital in Brussels, Belgium, to Chris Bakker, Gerrit van de Maat, Peter Seevinck, and Koen Vincken at the University Medical Center in Utrecht, the Netherlands, and to the group of Jin-Seok Suh & Young Han Lee of the Yonsei University Severance Hospital in Seoul, Korea. Additionally, I greatly appreciate the valuable time made available by Conny Ström, Jörgen Strinnholm, Volker Ottens, and Kjell Gunnar Nilsson of Norrlands Universitetssjukhus in Umeå, Sweden, and by Stephan Vehmeijer, and Linda van Zeeland of the Reinier de Graaf hospital in Delft, the Netherlands, to supply the clinical information and to explain and quantify the clinical need for visualization of soft tissue near metal.

All colleagues at the Reinier de Graaf hospital I want to acknowledge for their moral support and advice during my doctorate project. Especially Joleen Blok and Vincent Verhoeven, thank you for providing and supporting the opportunity to continue part of this project within the framework of the medical physics training program.

I want to thank my family and friends for their support and for their remaining friendship even though I have not been available lately as much as I would have liked to. Thanks to Karin Stalman-Timmerman, Hanke Griffioen-Kleij and Eric Bohré for their helpful advice on the cover design. Special thanks go to my parents for their feedback and moreover for the education opportunities as well as for many other things. Karine, the most important woman in my life for so many reasons, thank you for your feedback and your stimulating support throughout this project. And above all I thank God, who has shown how much He is able to achieve with me.

E. Curriculum Vitae

Chiel den Harder (Figure 1.1b) was born in Oss, the Netherlands, on April 9th, 1974. He graduated at the Gereformeerde Scholengemeenschap Amersfoort in 1991. From 1991 until 1996, he studied Physics at the University of Utrecht. His master's thesis "Iterative reconstruction for quantitative SPECT" was based on work at the University Medical Center Utrecht (UMCU), at the faculty of Image Processing (today, the Image Sciences Institute, ISI) in close collaboration with the department of Nuclear Medicine. This work led to two publications. After graduating with distinction in 1996, he moved to Enschede to study Mechanical Engineering at the University of Twente. In close collaboration with the rehabilitation center 't Roessingh and Ambroise Holland BV, he designed an extension of the existing UTX leg orthosis for improved frontal stability: the UTX-FS, which was the basis for his graduation in 1998.

After working at the home for the elderly Landscheiding in The Hague for a few months on software for early detection of dementia, he moved to Eindhoven to join Philips Medical Systems (today, Philips Healthcare) in Best in the development and predevelopment of MRI scanner software, first as MR software engineer, and later as MR imaging scientist. He worked in international teams that included scientists, application specialists, and medical doctors, on research and development of technical innovations, clinical evaluation of prototypes and convergence of clinical requirements towards product definition. A number of the technical innovations have led to publications and/or patent applications. In more recent years, one of the major activities was the research on metal artifact reduction techniques in MRI and the development of a prototype to evaluate these techniques on Philips MRI scanners in a clinical setting. That activity eventually led to this thesis.

In 2013, Chiel started as a medical physicist trainee at the Reinier de Graaf hospital in Delft and later at the Leiden University Medical Center.

F. Publications

Journal papers

1. Beekman FJ, den Harder JM, Viergever MA, van Rijk PP. Fully 3D iterative scatter compensation in nonuniform attenuation & media for SPECT. J Nucl Med 1996;V37:216P.
2. Beekman FJ, den Harder JM, Viergever MA, van Rijk PP. SPECT scatter modeling in non-uniform attenuating objects. Phys Med Biol, 1997;V42:1133-1142.
3. Frick M, Paetsch I, den Harder C, Kouwenhoven M, Heese H, Dries S, Schnackenburg B, de Kok W, Gebker R, Fleck E, Manka R, Jahnke C. "Fully automatic geometry planning for cardiac MR imaging and reproducibility of functional cardiac parameters". J Magn Reson Imag 2011 Aug;34(2):457-467.
4. den Harder JC, Blume UA, van Yperen GH, Bos C. Off-resonance suppression for multispectral MR imaging near metallic implants. Magn Reson Med 2014. doi: 10.1002/mrm.25126.
5. den Harder JC, Blume UA, van Yperen GH, Bos C. Ripple Artifact Reduction Using Slice Overlap in Slice Encoding for Metal Artifact Correction. Magn Reson Med. 2014. doi: 10.1002/mrm.25127.

Conference publications

1. Fuderer M, Duijndam AJ, Jones AA, den Harder JM, Rozijn TH. Intensity correction at high field MRI by filtering of the reference scan. In Proceedings of the 19th Annual Meeting of ISMRM, Kyoto, Japan, 2004. p.2145.
2. Moore EA, Hoogenraad FG, Golay X, Petersen ET, Versluis M, den Harder JM, Moerland A. Sub-Minute Arterial Spin Labelling at 3.0T. In Proceedings of the 19th Annual Meeting of ISMRM, Seattle, WA, USA, 2006. p.2690.
3. Pekar V, Bystrov D, Heese H, Dries S, Schmidt S, Grewer R, den Harder C, Bergmans R, Simonetti A, van Muiswinkel A. Automated planning of scan geometries in spine MRI scans. Med Image Comput Comput Assist Interv, 2007;10(Pt 1):601-608.
4. Bergmans R, den Harder C, Simonetti AW, Pekar V, Bystrov D, Grewer R, van Muiswinkel AM. Consistent automated scan planning of spine. In Proceedings of the 15th Annual Meeting of ISMRM, Berlin, Germany, 2007. p.2340.
5. Heese HS, Bystrov D, Pekar V, Dries SP, Grewer R, den Harder CJ, Bergmans R, Simonetti AW, van Muiswinkel AM. Robust anatomy recognition approach for automated scan planning of spine MRI examinations. In Proceedings of the 16th Annual Meeting of ISMRM, Toronto, Ontario, Canada, 2008. p.3171.
6. den Harder CJ, de Jong JW, Bos C, van Meel M, Bystrov D, Heese H, Simonetti AW. Consistent automated scan planning of shoulder. In Proceedings of the 16th Annual Meeting of ISMRM, Toronto, Ontario, Canada, 2008. p.3665.
7. den Harder CJ, Moore EA, van Muiswinkel AM. Consistent automated planning of irregular ROI's for intracranial MRA MIP's. In Proceedings of the 17th Annual Meeting of ISMRM, Honolulu, Hawai'i, USA, 2009. p.1328.

8. Simonetti AW, Holthuizen R, den Harder CJ, Visser M, Limkeman M. 3D breast segmentation for image based shimming, In Proceedings of the 17th Annual Meeting of ISMRM, Honolulu, Hawai'i, USA, 2009. p.2114.
9. Heese HS, Dries SP, Bystrov D, Peters J, Ecabert O, Weese J, den Harder CJ, de Kok W, van Muiswinkel AM. Consistency in automated versus manual definition of MRI scan volume orientations of the human heart. In Proceedings of the 17th Annual Meeting of ISMRM, Honolulu, Hawai'i, USA, 2009. p.4681.
10. Bos C, den Harder C, van Yperen G. MR imaging near orthopedic implants with artifact reduction using View-Angle Tilting and Off-Resonance Suppression. In Proceedings of the 18th Annual Meeting of ISMRM, Stockholm, Sweden, 2010. p.129.
11. Glantenay A-S, den Harder CJ, van den Brink JS, Herigault G, Koonen J. Efficient EPI distortion correction using non-phase encoded reference data. In Proceedings of the 19th Annual Meeting of ISMRM, Montréal, Québec, Canada, 2011. p.846.
12. den Harder CJ, Blume UA, Bos C. MR imaging near orthopedic implants using Slice-Encoding for Metal Artifact Correction & Off-Resonance Suppression. In Proceedings of the 19th Annual Meeting of ISMRM, Montréal, Québec, Canada, 2011. p.3170.
13. van de Maat GH, Blume UA, den Harder CJ, Bos C, Bakker CJ. Macroscopic meets microscopic: the use of Multi Acquisition Variable Resonance Image Combination (MAVRIC) for detection of microscopic objects by means of off-resonance excitation. In Proceedings of the 19th Annual Meeting of ISMRM, Montréal, Québec, Canada, 2011. p.4522.
14. den Harder CJ, Blume UA, Bos C. MR Imaging near metallic implants using Selective Multi-Acquisition with Variable Resonances Image Combination. In Proceedings of the 20th Annual Meeting of ISMRM, Melbourne, Australia, 2012. p.2432.
15. Nielsen T, den Harder C, Bos C, Börnert P. Reduction of breating motion artifacts in shoulder imaging using an orbital navigator as motion sensor. In Proceedings of the 20th Annual Meeting of ISMRM, Melbourne, Australia, 2012. p.2463.
16. Ström C, Strinnholm J, Otten V, Hauksson J, Bruvold M, Blume U, den Harder C, Bos C. Evaluation of Slice Encoding for Metal Artifact Correction in Patients with Recalled Orthopedic Hip Implants. In Proceedings of the 20th Annual Meeting of ISMRM, Melbourne, Australia, 2012. p.3333.
17. Huang F, Lin W, Beck G, den Harder C, Bos C, Duensing R, Reykowski A. A Reconstruction Method for Non-rigid Motion Compensation in Brain MRI. In Proceedings of the 20th Annual Meeting of ISMRM, Melbourne, Australia, 2012. p.3410.
18. Huang F, Lin W, den Harder C, Bos C, Duensing R, Reykowski A. Advantages of Channel by Channel Artifact Detection and Correction. In Proceedings of the 20th Annual Meeting of ISMRM, Melbourne, Australia, 2012. p.3434.
19. Huang F, Lin W, Beck G, den Harder C, Bos C, Duensing R, Reykowski A. MRI Using Sharable Information Among Images With Different Contrasts: Motion Compensation. In Proceedings of the 20th Annual Meeting of ISMRM, Melbourne, Australia, 2012. p.3435.

20. den Harder CJ, Blume UA, van IJperen G, Bos C. On the relation of the ripple artifact in Multi-Spectral Imaging and susceptibility induced field gradients. In Proceedings of the 21st Annual Meeting of ISMRM, Salt Lake City, UT, USA, 2013. p. 2562.
21. Ström C, Strinnholm J, Crnalic S, Bruvold M, Blume U, den Harder C, Bos C. Evaluation of T2-weighted Slice Encoding for Metal Artifact Correction in Patients with Recalled Orthopedic Hip Implants. In Proceedings of the 21st Annual Meeting of ISMRM, Salt Lake City, UT, USA, 2013. p.3486.

Patents

1. den Harder JM, van Muiswinkel A, Young S, inventors; Koninklijke Philips Electronics N.V., applicant. Method, apparatus, and computer program product for acquiring medical image data. US Patent US8634616. October 22, 2013.
2. Bergmans CJFM, Bystrov D, Heese HS, Kouwenhoven M, den Harder JM, Simonetti AW, de Kok W, inventors; Koninklijke Philips Electronics N.V., applicant. Automated sequential planning of MR scans. US Patent US8565505. January 21, 2014.

Patent applications

1. Holthuizen RFJ, den Harder JM, de Kok W, inventors; Koninklijke Philips Electronics N.V., applicant. Apparatus and method for acquiring diagnostic information. US Patent Application WO2011036613. March 31, 2011.
2. den Harder JM, Bos C, Blume UA, inventors; Koninklijke Philips Electronics N.V., applicant. Restriction of the imaging region for MRI in an inhomogeneous magnetic field. US Patent Application WO2012123830. September 20, 2012.
3. Wenzel F, Truyen R, Ermes JPFAM, den Harder JM, inventors; Koninklijke Philips Electronics N.V., applicant. Image processing system and method. US Patent Application WO2012137113. October 11, 2012.
4. Holthuizen RFJ, den Harder JM, inventors; Koninklijke Philips Electronics N.V., applicant. Medical image system and method. US Patent Application WO2012153222. November 15, 2012.
5. Nehrke K, Boernert P, den Harder JM, Rozijn TH, inventors; Koninklijke Philips Electronics N.V., applicant. Metal resistant MR imaging reference scan. US Patent Application WO2014053927. April 10, 2014.
6. Jurrissen MPJ, den Harder JM, Blume UA, de Weerdt E, van IJperen GH, inventors; Koninklijke Philips Electronics N.V., applicant. Metal resistant MR imaging. International Patent Application WO2014115043. July 31, 2014.

G. Abbreviations and Symbols

2D	Two-Dimensional
3D	Three-Dimensional
AAOS	American Academy of Orthopaedic Surgeons
AP	Anterior-Posterior
B_0	main magnetic field strength
B_1	RF pulse amplitude
b-SSFP	Balanced Steady State Free Precession
BW	Bandwidth
BW_{EX}	Excitation Bandwidth
BW_{REF}	Refocusing Bandwidth
BW_{SEL}	Selection Bandwidth
CPMG	Carr-Purcell-Meiboom-Gill
CT	Computed Tomography
DBS	Deep Brain Stimulation
DICOM	Digital Image and COmmunications in Medicine
EPI	Echo-Planar Imaging
f_0	spin precession frequency
$F(\omega_n)$	Spectral response of the n-th selection
FID	Free Induction Decay
FFE	Fast Field Echo
FSE	Fast Spin Echo (see also TSE)
FOV	Field of View
FWHM	Full Width at Half Maximum
Gd	Gadolinium
G_{EX}	Excitation Gradient
G_{PE}	Phase Encoding Gradient
G_{READ}	Read-out Gradient or frequency encoding gradient
G_{REF}	Refocusing Gradient
G_{SEL}	Selection Gradient
G_{VAT}	View Angle Tilting Gradient
H	Applied magnetic field strength
Hz	Hertz
IR	Inversion Recovery
kg	KiloGram
kHz	KiloHertz
kx,ky,kz	K-space coordinates or time domain coordinates
M	Magnetization
MAVRIC	Multi-Acquisition with Variable-Resonance Image Combination
MARS	Metal Artifact Reduction Sequence
MHz	MegaHertz
MIP	Maximum Intensity Projection
M_{xy}	Transverse Magnetization
M_z	Longitudinal Magnetization
m	Meter

mm	MilliMeter
m,p,s	image space coordinates: *measurement*, *phase encoding*, *slice selection*
MOM	Metal-On-Metal
MR	Magnetic Resonance
MRI	Magnetic Resonance Imaging
ms	MilliSecond
MSK	MusculoSKeletal
mT	MilliTesla
n.a.	Not Applicable
NSA	Number of Signals Averaged
ORS	Off-Resonance Suppression
ORS-SEMAC	Off-Resonance Suppressed Slice-Encoding for Metal Artifact Correction
ORS-MAVRIC	Outer-Region Suppressed Multi-Acquisition with Variable-Resonance Image Combination
PDw	Proton Density weighted
PET	Positron Emission Tomography
PNS	Peripheral Nerve Stimulation
ppm	Parts Per Million
PRIDE	Philips Research Image Development Environment
RF	Radio Frequency
RFE	Radio Frequency pulse Echo
ROM	Range Of Motion
s	Second
SAR	Specific Absorption Rate
SE	Spin Echo
SEMAC	Slice-Encoding for Metal Artifact Correction
SENSE	SENSitivity Encoding
SNR	Signal to Noise Ratio
SPAIR	SPectral Attenuated Inversion Recovery
S_{PE}	Phase Encoded Image Thickness
SPI	Single Point Imaging
SPECT	Single Photon Emission Computed Tomography
SPIR	Spectral Presaturation with Inversion Recovery
SPRITE	Single-Point Ramped Imaging withT1-Enhancement
STIR	Short TI Inversion Recovery
STK	Slice Thickness
SVD	Singular Value Decomposition
SWIFT	SWeep Imaging with Fourier Transform
T	Tesla
t	Time
T1	spin-lattice relaxation time constant
T1w	T1 weighted
T2	spin-spin relaxation time constant
T2w	T2 weighted
t.b.d.	To Be Determined
TE	Echo Time
TR	Repetition Time

TSE	Turbo Spin Echo (see also FSE)
UI	User Interface
US	UltraSound
UTE	Ultrashort Echo Time
VAT	View-Angle Tilting
VOB	Versioned Object Base
VS-3D-MSI	Volume Selective 3D Multi-Spectral Imaging
W	Watt
XML	Extensible Markup Language
x,y,z	MRI scanner coordinates
β	view angle
γ	gyromagnetic ratio
ΔB_0	main magnetic field deviation
Δf_0	spin precession frequency deviation
Δm	signal displacement in the measurement direction
Δs	slice distortion
µs	MicroSecond
µT	MicroTesla
φ	spin phase
χ	magnetic volume susceptibility